# Threat of Rising Sea Level & Water Tables to Texas Coastal Septic Systems: An Integrated Study

## FINAL REPORT

GLO Contract Number: 21-155-009-C881 Jan 10, 2025

## Prepared by

Dorina Murgulet, Ph.D., Principal Investigator
David Felix, Ph.D., and Vikram Kapoor, Ph.D. Co-Investigators
Roya Narimani, Ph.D., Postdoctoral Fellow

Texas A&M University-Corpus Christi 6300 Ocean Dr., Unit 5864 Corpus Christi, Texas 78412 Phone: 361-825-2309

Email: Dorina.murgulet@tamucc.edu

Submitted to: Texas General Land Office 1700 Congress Ave. Austin, TX 78701-1495

This report was funded in part through a grant from the Texas General Land Office (GLO) providing Gulf of Mexico Energy Security Act of 2006 funding made available to the State of Texas and awarded under the Texas Coastal Management Program. The views contained herein are those of the authors and should not be interpreted as representing the views of the GLO or the State of Texas.





# TABLE OF CONTENTS TABLE OF FIGURES 7 TASK 1: GROUNDWATER-SEAWATER INTERACTION ASSESSMENT.......16 3.4.2. Data analysis: statistical summary, correlations, and distributions of groundwater 3.4.5. Depth to groundwater and implications for water table flooding and subsurface infrastructure damage 53 3.5. 3.5.1. 3.5.2. Groundwater levels predictive model ......57 3.6. 3.7. References 60 TASK 2: MEASUREMENT OF FECAL INDICATOR BACTERIA ......64 4.1. Executive Summary .......64 4.2. Background 64 4.3.2. Enterolert Test 65

4.3.5. I	Data Analysis	66
4.3.6. (	Quality Assurance/Quality Control	67
4.4. Resu	lts and Discussion	67
4.4.1. I	Performance of qPCR assays	67
4.4.2. I	Detection of Culture-based Enterococci	67
4.4.3. I	Detection of Fecal Contamination using MST Markers	72
4.5. Conc	lusion/Recommendation	84
4.6. Refe	rences	85
5. TASK	3: QUANTIFICATION AND SOURCE TRACKING OF NUTRIENT INPUTS	S 86
5.1. Exec	utive Summary	86
5.2. Back	groundground	87
5.3. Meth	ods	92
5.3.1. \$	Sample Collection	92
5.3.2. \$	Sample Analysis	92
5.3.3. I	sotope Mixing Model	95
5.4. Resu	lts	97
5.4.1.	Nitrate Spatial and Temporal Variations	98
5.4.2.	Ammonium Spatial and Temporal Variations	106
5.4.3.	DON Spatial and Temporal Variations	111
5.4.4.	Ancillary Data	115
5.5. Disci	ussion	118
5.5.1.	Nitrate	118
5.5.2.	Ammonium	122
5.5.3. I	OON	124
5.5.4 N	Vitrogen Species, Water Levels, and Implications	126
	GRATED ASSESSMENT: GROUNDWATER TRACERS, BACTERIA, AND INTERACTIONS	136
6.1. Anal	ysis of FIB Behavior in the Studied Environments	136
6.1.1. \$	Surface water relationships	136
6.1.2. 0	Groundwater relationships	140
6.1.3. I	Porewater relationships	143
6.1.4. 0	Combined groundwater, porewater, and surface water relationships	144
6.2. Anal	ysis of Chemical Data Using Deep Learning and Principal Component Analyses	144
	tionships Between Bacteria Levels, Groundwater Elevation, and Environmental sing Machine Learning Techniques	149
	3	

	6.3.1. Analysis of environmental and hydrological datasets, preprocessing of data, and variables selection for machine learning models	. 149
	6.3.2. Surface water bacteria level predictions using machine learning techniques	. 157
6	5.4 References	.160
7.	OVERALL CONCLUSION	. 163
8.	TASK 4: EDUCATION AND OUTREACH	.166
8	3.1. List of all Communications	. 166
8	3.2. List of Student Training Opportunities	. 166
8	3.3. List of Conferences, Publications, and Public Presentations	. 167

## TABLE OF TABLES

Table 3.1. Environmental and hydrological variables with temporal resolutions and data sources	
<b>Table 3.2.</b> Monthly water sample data (2021–2023).2 <b>Table 3.3.</b> Statistical summary of water quality variables in groundwater samples (Nov 2021-May 2023).2	0
<b>Table 3.4.</b> Statistical summary of water quality variables in porewater samples (Nov 2021-May 2023)	7
Table 3.5. Statistical summary of water quality variables in surface water samples (Nov 2021-May 2023).	
<b>Table 4.1.</b> Primers/probes for the PCR assays used in the study.       6 <b>Table 4.2.</b> Average standard curve qPCR amplification efficiencies and R2 values obtained through BioRad CFX Manager 3.1 software.       6	
<b>Table 4.3.</b> Spatial Detection frequency of Enterococci enumerated by IDEXX Enterolert kit in well Samples	8
Table 4.4. Spatial Detection frequency of Enterococci enumerated by IDEXX Enterolert in Surface Samples.         6       6	
<b>Table 4.5.</b> Spatial Detection frequency of Enterococci enumerated by IDEXX Enterolert in Pore Samples	8
Table 4.6. Temporal Detection frequency of Enterococci enumerated by IDEXX Enterolert in well water Samples.         7	0
<b>Table 4.7.</b> Temporal Detection frequency of Enterococci enumerated by IDEXX Enterolert in surface water Samples	0
<b>Table 4.8.</b> Temporal Detection frequency of Enterococci enumerated by IDEXX Enterolert in pore water Samples.       7	1
<ul> <li>Table 5.1. Potential sources of nitrogen and their corresponding isotopic values. These unique isotope signatures can be used to determine pollutant contributions in affected waters 8</li> <li>Table 5.2. Nitrogen processes and their corresponding enrichment factors</li></ul>	00 ,
Table 5.4. Isotope effects used for the SIMMR model according to sample matrix	
<ul> <li>Table 5.6. Nitrate isotopic composition (‰) and % source contribution to nitrate in surface waters by season and site. SS, dg, wd, mar is the % contribution from sewage/septic dog waste/gull guano. wet deposition and Gulf of Mexico waters, respectively</li></ul>	0

<b>Table 5.8.</b> Nitrate isotopic composition (‰) and % source contribution to nitrate in ground waters by season and site. SS, dg, wd, soil is the % contribution from sewage/septic dog waste/gull guano. wet deposition and soil, respectively
<b>Table 5.9.</b> Correlation matrix for surface water. Numbers in each cell represent the correlation
coefficient "R" and a positive or negative relationship. DTW is depth to water and DO is
dissolved oxygen
<b>Table 5.10.</b> Probability (p) value correlation significance matrix for surface water. Numbers in
each cell represent the p-value of the correlation. Numbers in each cell represent the p-
value of the correlation. Light blue to dark blue values indicate significant negative
correlations increasing in magnitude with darkness. Light purple to dark purple values
indicate significant positive correlations increasing in magnitude with darkness 116
<b>Table 5.11.</b> Correlation matrix for pore water. Numbers in each cell represent the correlation
coefficient "R" and a positive or negative relationship. DTW is depth to water and DO is
dissolved oxygen
Table 5.12. Probability (p) value correlation significance matrix for pore water. Numbers in each
cell represent the p-value of the correlation. Numbers in each cell represent the p-value of
the correlation. Light blue to dark blue values indicate significant negative correlations
increasing in magnitude with darkness. Light purple to dark purple values indicate
significant positive correlations increasing in magnitude with darkness
<b>Table 5.13.</b> Correlation matrix for groundwater. Numbers in each cell represent the correlation
coefficient "R" and a positive or negative relationship. DTW is depth to water and DO is
dissolved oxygen
<b>Table 5.14.</b> Probability (p) value correlation significance matrix for groundwater. Numbers in
each cell represent the p-value of the correlation. Numbers in each cell represent the p-
value of the correlation. Light blue to dark blue values indicate significant negative
correlations increasing in magnitude with darkness. Light purple to dark purple values
indicate significant positive correlations increasing in magnitude with darkness 117
<b>Table 5.15.</b> Seasonal surface, pore, and groundwater nitrate $\delta$ 15N vs $\delta$ 18O plot characteristics
including number of samples (n), correlation coefficient (R), probability value (p) and
likely nitrate processes associated with these characteristics

## **TABLE OF FIGURES**

_	<b>2.1.</b> Map of the study area showing the locations of monitoring wells, surface water, and porewater sampling locations
	<b>2.2.</b> Land use map of sampling area along Texas barrier islands using the Esri 2020 Land Cover dataset. Sample sites are shown in black
Figure	<b>3.1.</b> Photos of selected monitoring wells for the research
<b>Figure</b>	<b>3.2.</b> Flow chart of the research methodology
Figure	<b>3.3.</b> Key steps in data preprocessing
	<b>3.4.</b> Wind Direction Rose Diagram for Seven Stations: Visual representation of wind
	direction frequencies across all stations. Each diagram highlights the dominant wind
	patterns, with the length of each bar indicating the proportion of time the wind blew from
	a particular direction, aiding in understanding regional wind trends and their
	environmental impact
<b>Figure</b>	<b>3.5.</b> Soil texture depth profile by well. Note the persistence of sands for most of the
	sedimentary facies except for well #1, which is located inland and not included in the
	analyses
<b>Figure</b>	<b>3.6.</b> (a) Heatmap of correlation coefficients between groundwater levels at different
	wells. (b) Line chart showing groundwater level variations over time for the selected
	wells
<b>Figure</b>	<b>3.7.</b> Violin plot for groundwater parameters
	<b>3.8.</b> Violin plot for pore water parameters
<b>Figure</b>	<b>3.9.</b> Violin plot for surface water parameters
Figure	<b>3.10.</b> Darcy's Law calculated SGD rates using freshwater heads from groundwater and Gulf of Mexico nearshore water levels. The negative values indicate that when the static groundwater level was measured in the month, the seawater level was higher, resulting in
	a negative/reverse gradient when seawater may intrude the water table aquifer, and
	negligible groundwater discharge will occur
<b>Figure</b>	<b>3.11.</b> Groundwater discharge rates (velocity rates) over time for all locations
	corresponding to the monitoring wells in regions 3 and 4 (See Figure 2.1 for a location
	map)
<b>Figure</b>	<b>3.12.</b> Groundwater discharge rates (velocity rates) across all locations corresponding to
	the monitoring wells in regions 3 and 4 (See Figure 2.1 for a location map)
<b>Figure</b>	<b>3.13.</b> Groundwater discharge rates (velocity rates) across months correspond to the
	monitoring wells in regions 3 and 4 (See Figure 2.1 for a location map)
<b>Figure</b>	<b>3.14.</b> Radium-224 derived SGD rates using the shallow groundwater/water table as the
	source/endmember
<b>Figure</b>	<b>3.15.</b> Radium-224 derived SGD rates using the porewater as the source/endmember 40
	<b>3.16.</b> Radium-223 derived SGD rates using the shallow groundwater/water table as the
	source/endmember
<b>Figure</b>	<b>3.17.</b> Radium-223 derived SGD rates using the shallow groundwater/water table as the
	source/endmember
Figure	<b>3.18.</b> Radium-226 derived SGD rates using the shallow groundwater/water table as the
_	source/endmember
Figure	<b>3.19.</b> Radium-224 derived SGD rates using the shallow groundwater/water table as the
_	source/endmember 44

<b>Figure 3.20.</b> Performance of the Groundwater Level Prediction Model for Wells	
and 13 (Area 3).	
Figure 3.21. Performance of the Groundwater Level Prediction Model for Wells	
(Area 4).	
<b>Figure 3.22.</b> Feature importance for area 3: the top 20 most important features be weight metric for predicting groundwater elevation at multiple wells. Each corresponds to one well, with features ordered by their contribution to red model's error. Bars represent the importance of each feature, and values of indicate their relative importance score.	h subplot ucing the on the bars
<b>Figure 3.23.</b> Feature importance for area 4: the top 20 most important features be weight metric for predicting groundwater elevation at multiple wells. Each corresponds to one well, with features ordered by their contribution to red error. Bars represent the importance of each feature, and values on the bar relative importance score.	h subplot auce the model's as indicate their
<b>Figure 3.24.</b> The spatial distribution of stations monitoring environmental factors study area.	
<b>Figure 3.25.</b> Depth to water continuous measurements in monitoring wells for are <b>Figure 2.1</b> for geographic locations). The ground surface is the reference meters)	point at 0
<b>Figure 4.1.</b> Spatial variation of enterococci concentration using MST marker Ent the study period	ero1 throughout
<b>Figure 4.2.</b> Temporal variation of enterococci concentration using MST marker I the study sites.	Entero1 across
<b>Figure 4.3.</b> Spatial variation of Human fecal contamination using MST marker H throughout the study period.	IF183
<b>Figure 4.4.</b> Temporal variation of Human fecal contamination using MST market throughout the study period.	r HF183
<b>Figure 4.5.</b> Spatial variation of Canine fecal contamination using MST marker B throughout the study period.	acCan
Figure 4.6. Temporal variation of Canine fecal contamination using MST marker study sites	BacCan across
<b>Figure 4.7.</b> Spatial variation of Gull fecal contamination using MST marker GFD study period.	throughout the
Figure 4.8. Temporal variation of Gull fecal contamination using MST marker G study sites	FD across
Figure 5.1. Temporal trends of water sample enterococci concentrations along the water	91
<b>Figure 5.2.</b> Surface water NO3- concentrations by month	
Figure 5.3. Surface water NO3- concentrations by site	inge triangle),
November 2021- April 2023.	*

Figure 5.5. Surface water NO3- estimated source % contribution	s throughout duration of
sampling and for each season.	101
<b>Figure 5.6.</b> Porewater NO3- concentrations by month	
<b>Figure 5.7.</b> Porewater NO3- concentrations by site	
Figure 5.8. Porewater NO3- estimated source % contributions th	roughout duration of sampling
and for each season.	
Figure 5.9. Groundwater average NO3- concentrations by month	n 104
Figure 5.10. Groundwater average NO3- concentrations by site a	
apportionment for high nitrate concentration wells	
Figure 5.11. Ground water NO3- estimated source % contribution	
sampling and for each season.	
<b>Figure 5.12.</b> Surface water average NH4+ concentrations by mo	
Figure 5.13. Surface water average NH4+ concentrations by site	
<b>Figure 5.14.</b> Porewater average NH4+ concentrations by month.	
<b>Figure 5.15.</b> Porewater average NH4+ concentrations by site	
Figure 5.16. Groundwater average NH4+ concentrations by more	
not pictured.	
<b>Figure 5.17.</b> Groundwater average NH4+ concentrations by site.	
not pictured.	The state of the s
Figure 5.18. Surface water average DON concentrations by mon	
<b>Figure 5.19.</b> Surface water average DON concentrations by mon	
Figure 5.19. Surface water average DON concentrations by site.	
•	· ·
Figure 5.21. Porewater average DON concentrations by month s	
Figure 5.22. Groundwater average DON concentrations by mont	
Figure 5.23. Groundwater average DON concentrations by site.	
<b>Figure 5.24.</b> Surface water $1/[DON]$ vs $\delta15N$ -DON plot portray	0.1
summer	124
<b>Figure 6.1.</b> Monthly bacteria contamination levels in surface Wa	iter. The average bacteria levels
across various monitoring locations are shown with color	
markers represent higher contamination levels	
<b>Figure 6.2.</b> Monthly bacteria levels in groundwater. Higher cond	
the blue, orange, and red colors.	
<b>Figure 6.3</b> . Monthly bacteria levels in porewater. Higher concen	
blue, orange, and red colors.	
<b>Figure 6.4.</b> Results of the Variational Autoencoder (VAE) for su	
original Bacteria dataset. (a) The relationship between La	
Latent Dimension 3 (25.39%), with red arrows highlighti	
than 0.05. (b) Contribution of each variable to the respect	
* /	
<b>Figure 6.5.</b> Results of the Variational Autoencoder (VAE) for su	-
log-transformed Bacteria dataset, focusing on the highest	
relationship between Latent Dimension 3 (28.18%) and L	
with red arrows highlighting variables with a p-value less	
each variable to the respective latent dimensions	
<b>Figure 6.6.</b> Results of the Variational Autoencoder (VAE) for po	
original Bacteria dataset, focusing on the highest latent di	mensions. (a) The relationship

between Latent Dimension 1 (35.41%) and Latent Dimension 3 (42.18%), with red arrows highlighting variables with a p-value less than 0.05. (b) Contribution of each variable to the respective latent dimensions.
Figure 6.7. Results of the Variational Autoencoder (VAE) for pore sample chemicals with log-
transformed Bacteria dataset, focusing on the highest latent dimensions. (a) The
relationship between Latent Dimension 3 (44.46%) and Latent Dimension 4 (40.45%),
with red arrows highlighting variables with a p-value less than 0.05. (b) Contribution of
each variable to the respective latent dimensions
Figure 6.8. Results of the Variational Autoencoder (VAE) for ground sample chemicals with the
original Bacteria dataset, focusing on the highest latent dimensions. Results of the
Variational Autoencoder (VAE) for ground sample chemicals with the original Bacteria
dataset, focusing on the highest latent dimensions. (a) The relationship between Latent
, , , , , , , , , , , , , , , , , , , ,
Dimension 3 (20.64%) and Latent Dimension 4 (73.59%), with red arrows highlighting
variables with a p-value less than 0.05. (b) Contribution of each variable to the respective
latent dimensions. 148
Figure 6.9. Results of the Variational Autoencoder (VAE) for ground sample chemicals with
log-transformed Bacteria dataset, focusing on the highest latent dimensions. (a) The
relationship between Latent Dimension 3 (38.81%) and Latent Dimension 4 (50.74%),
with red arrows highlighting variables with a p-value less than 0.05. (b) Contribution of
each variable to the respective latent dimensions
<b>Figure 6.10.</b> Analysis of Environmental Factors and Bacteria in Area 4 in different months: (a)
2021-12; (b) 2022-02; (c) 2022-03; (d) 2022-06; (e) 2022-08; (f) 2022-10; (g) 2022-11;
(h) 2022-12; (i) 2023-01; (j) 2023-02; (k) 2023-04
Figure 6.11. Area 1: Normalized Bacteria in surface water and significant environmental factors:
(a) original bacteria data; (b) log-transformed bacteria data
Figure 6.12. Area 2: Normalized Bacteria in surface water and significant environmental factors:
(a) original bacteria data; (b) log-transformed bacteria data
Figure 6.13. Scatter plot of the model's predictions for both areas using transformed log bacteria
data
<b>Figure 6.14.</b> Feature importance for (a) Area 3 and (b) Area 4, illustrating the top 30 most
(a) original bacteria data; (b) log-transformed bacteria data

### 1. EXECUTIVE SUMMARY

This study underscores the essential role of an interdisciplinary approach in tackling the hydrological and ecological challenges facing the Texas Gulf Coast—insights that have direct implications for coastal management. By integrating groundwater monitoring, sediment analysis, microbial source tracking (MST), radium isotope analysis, and predictive modeling, we are able to illuminate the complex interactions between regional hydrological systems and localized coastal dynamics. A significant conclusion from our research is the impact of upstream streamflow on groundwater recharge. This establishes a vital link between mainland watersheds and the water tables of barrier islands. Seasonal peaks, particularly during winter and spring, lead to increased water table levels, heightening the risk of flooding on these islands and affecting both human populations and natural ecosystems. This interconnection highlights the urgent need for coordinated management strategies that consider upstream water flow and its broader effects on coastal systems.

Flooding of the water table on barrier islands is most pronounced in late winter and early spring, times when both rainfall and upstream contributions are at their highest. In sandy, permeable areas, these shallow water tables significantly increase the potential for flooding, resulting in contamination risks from failing septic systems and sewage backflow. During such events, fecal indicator bacteria, which can originate from both human and canine sources, may be transported into nearshore waters, creating serious public health risks and compromising recreational safety. Coastal managers face the challenge of monitoring these conditions, as elevated levels of bacteria necessitate public advisories to protect beachgoers. Moreover, nutrient inflows from failing septic systems contribute to eutrophication, potentially leading to harmful algal blooms and the degradation of coastal ecosystems. Our findings emphasize the critical need for robust monitoring frameworks that can effectively capture the dynamic nature of water table fluctuations and associated microbial contamination.

In addition, this study sheds light on the transport and ecological effects of nutrients like nitrogen and phosphorus, which are often associated with sewage and septic system failures during periods of water table flooding. Elevated nutrient concentrations can destabilize marine habitats, fueling algal blooms, depleting oxygen levels, and disrupting aquatic food webs. Coastal areas with consistently shallow water tables are particularly susceptible, acting as conduits for the transport of nutrients and contaminants. Our use of radium isotopes as tracers for submarine groundwater discharge (SGD) has identified hotspots of nutrient-rich groundwater discharge, coinciding with times of high water table levels and flooding. These processes further highlight the interconnectedness of coastal water quality with regional hydrology and infrastructure resilience. For coastal managers, understanding these patterns is vital to designing effective interventions that safeguard both recreational and ecological resources.

Ultimately, this research outlines tangible pathways for coastal managers to minimize these risks and bolster resilience. The predictive modeling tools developed during this study offer valuable insights for forecasting water table behavior and identifying high-risk periods for flooding and microbial contamination. Such tools facilitate the implementation of early warning systems, enabling managers to issue timely advisories and proactive strategies. Additionally, our findings advocate for improvements in septic systems and sewage infrastructure in vulnerable

regions, coupled with targeted land-use policies aimed at reducing nutrient and contaminant inputs. By integrating upstream hydrological management with localized coastal interventions, this study promotes a holistic approach to addressing the intertwined challenges of public health and ecological degradation, ensuring sustainable management of Gulf Coast resources amid ongoing climate and development pressures.

#### 2. STUDY AREA

This study focuses on the dynamic barrier island systems and adjacent coastal environments of Galveston, Matagorda, and Brazoria Counties along the Texas Gulf Coast (Figure 2.1). These regions, shaped by dynamic geological processes, support diverse ecosystems and play a critical role in protecting inland areas from storm surges while serving as hubs for tourism, recreation, and fishing industries. The Texas Gulf Coast, with its 3,359 miles of shoreline, features extensive barrier islands, bays, tidal rivers, and creeks that have been heavily influenced by natural and anthropogenic factors over time (NOAA, 2020). Barrier islands, which constitute about 10% of Earth's continental shorelines, are significant landforms along the Texas coast. The Texas barrier islands form a chain of long, sandy islands that separate the coastal bays from the Gulf of Mexico, protecting these bays from severe waves and currents. Galveston Island, 43 kilometers long, is associated with the Trinity-San Jacinto Estuary, while Follet's Island, 21 kilometers long, is associated with the Christmas Bay Estuary. Sargent Beach and Matagorda Beach, located on the Matagorda Peninsula, shield Matagorda and East Matagorda Bays. The Galveston Coast Guard Station monitors weather conditions, reporting that the wet season is from June to September (highest rainfall in September: 124.5 mm), and the dry season is from October to May (driest month: March, 81.3 mm). These islands, comprised primarily of fine sands, are prone to flooding, with land use dominated by industry or recreational housing (Figure 2.2Error! Reference source not found.). The lithology of Galveston, Matagorda, and Brazoria Counties highlights the interplay between high-energy barrier island environments and low-energy estuarine, lagoonal, and marsh systems. Barrier islands are predominantly composed of fine- to medium-grained sands deposited and shaped by wave and tidal forces. Meanwhile, back-barrier areas comprise organic-rich silty clays formed in tidal wetlands, transitioning inland to coarser clay, sand, and gravel deposits in older terraces and river systems. Galveston County includes Galveston Island and the Bolivar Peninsula, dominated by Holocene barrier island deposits of well-sorted, fine- to medium-grained sands formed by wave and tidal processes. Behind the barrier islands lie back-barrier environments with lagoonal and marsh deposits composed of silty clays rich in organic content, reflecting low-energy tidal settings. Galveston Bay, the largest estuary in Texas, plays a vital ecological role but faces challenges such as urbanization and industrial pollution, particularly in areas like the Houston Ship Channel and Clear Lake (Ward and Armstrong, 1992).

Matagorda County features the Matagorda Peninsula, a prominent barrier island system protecting the expansive Matagorda Bay estuary from Gulf storm activity. The peninsula's sediments are dominated by fine sands deposited by high-energy waves and wind. At the same time, the adjacent bay contains mud, fine sand, and shell fragments characteristic of low-energy estuarine environments. Freshwater inflows from the Tres Palacios Creek watershed are critical to Matagorda Bay's ecological balance but have been identified as a source of E. coli contamination from septic systems, agricultural runoff, and wildlife waste (TCEQ, 2018). Brazoria County's coastal environment is heavily influenced by the Brazos River, which has deposited sand, silt, and clay in its floodplain and deltaic systems. Coastal areas feature prominent sand layers, while marshes and low-lying plains contain finer clay and mud deposits typical of low-energy environments. However, these regions face challenges such as moderate salinity levels and periodic flooding, impacting both ecosystems and land management practices (Texas Geological Survey, 2022).

Hydrologically, the region interacts with significant groundwater systems, including the

Chicot and Evangeline aquifers. The Chicot Aquifer, composed of unconsolidated sands and silts with interbedded clay layers, reflects fluvial and deltaic processes. At the same time, the deeper Evangeline Aquifer transitions to marine-origin finer-grained deposits, indicative of historical sea-level changes. These aquifers are vital resources for the coastal plain but face challenges from salinity intrusion, over-extraction, and surface contamination (Texas Geological Survey, 2022). Water quality concerns arise from natural processes and human activities, such as nutrient loading, bacterial contamination, and urban runoff. For example, in Galveston Bay, urban and industrial activities have increased nutrient and bacterial pollution, impacting marine habitats and public health. In Matagorda Bay, agricultural runoff and waste discharges alter nutrient and contaminant concentrations. In Brazoria County, bacterial contamination is associated with septic system failures, industrial activities, and urbanization (Powers et al., 2021).

This research addresses these critical water quality and hydrological challenges through field monitoring, modeling studies, and machine-learning approaches. Objectives include determining chemical concentrations in groundwater and surface water, identifying drivers of bacterial and nutrient contamination, and assessing nutrient and bacterial transport between the Gulf of Mexico and surrounding watersheds. The research will also evaluate groundwater dynamics, which play a significant role in exacerbating contamination linked to failing septic systems.

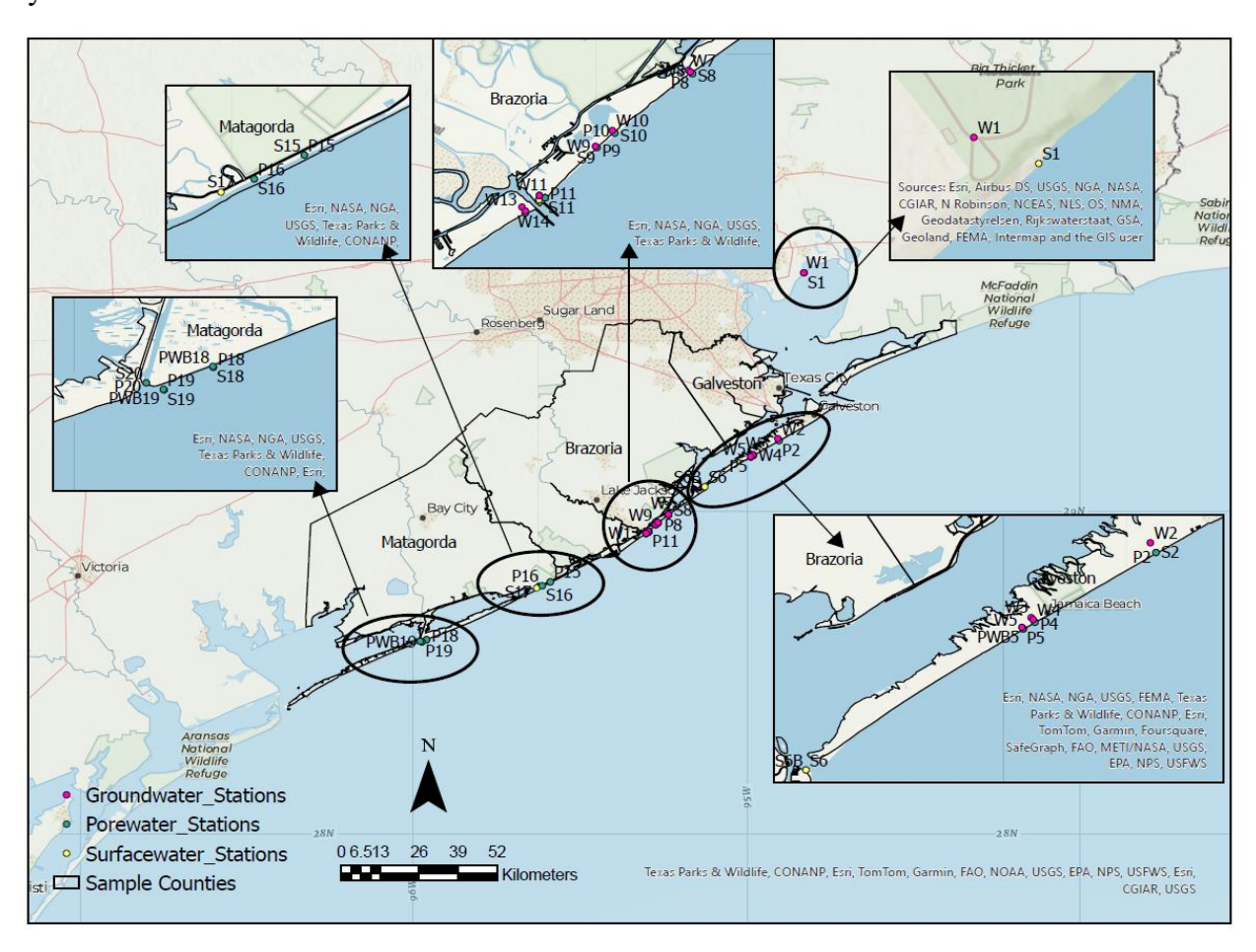


**Figure 2.1.** Map of the study area showing the locations of monitoring wells, surface water, and porewater sampling locations.

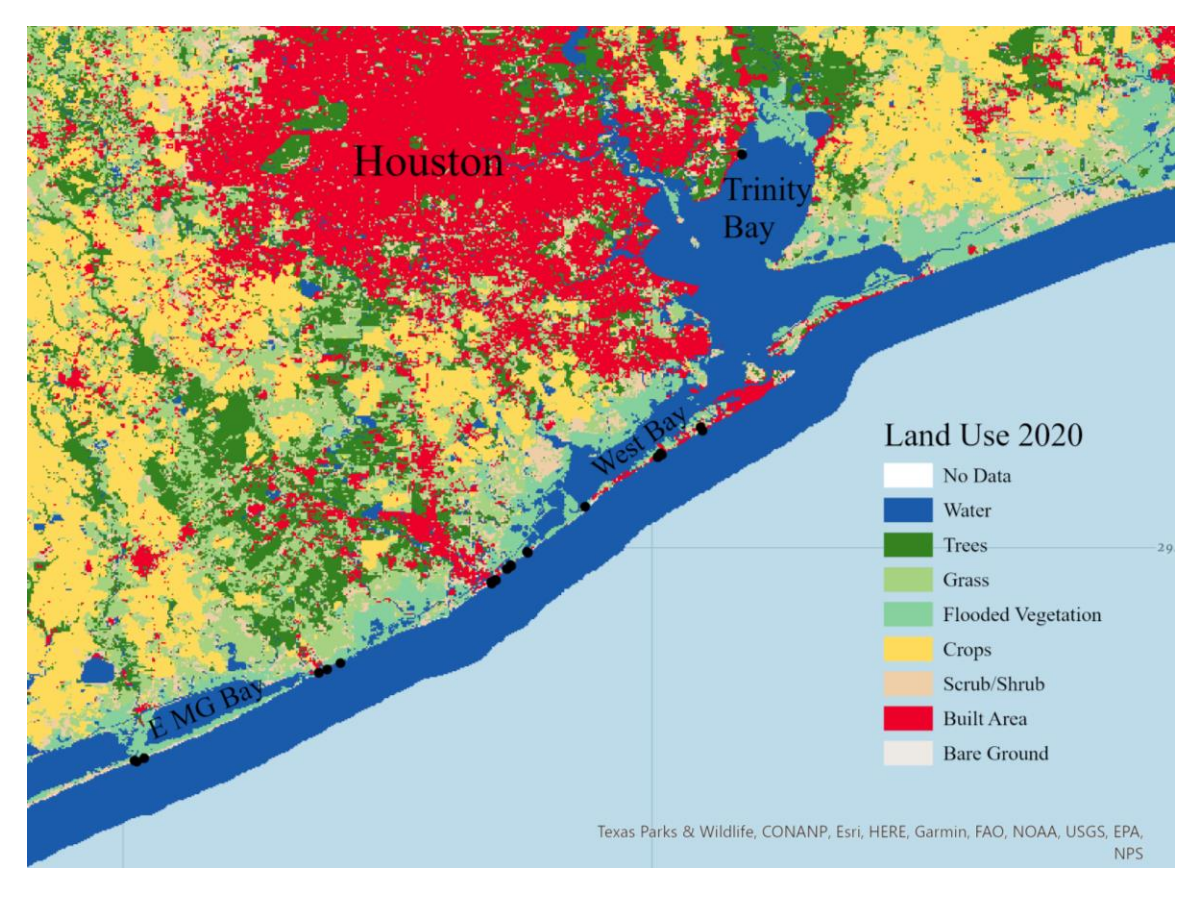


Figure 2.2. Land use map of sampling area along Texas barrier islands using the Esri 2020 Land Cover dataset. Sample sites are shown in black.

### 2.1 References

Powers, N.C., Pinchback, J., Flores, L., Huang, Y., Wetz, M.S. and Turner, J.W., (2021). Long-term water quality analysis reveals correlation between bacterial pollution and sea level rise in the northwestern Gulf of Mexico. Marine Pollution Bulletin, 166, p.112231.

NOAA Office for Coastal Management (2020). Shoreline Mileage of the United States. National Oceanic and Atmospheric Administration.

TCEQ (2018). Matagorda Bay Basin Highlights Report. Texas Commission on Environmental Quality.

Texas Geological Survey (2022). Geological Maps of Texas Coastal Regions.

Ward, G.H. and Armstrong, N.E., (1992). Data bases on ambient water and sediment quality of Galveston Bay.

#### 3. TASK 1: GROUNDWATER-SEAWATER INTERACTION ASSESSMENT

Prepared by Roya Narimani, Ph.D., Dorina Murgulet, Ph.D., Cody Lopez, and Joy Brown

## 3.1. Executive Summary

This study examines groundwater dynamics across coastal areas of the Texas barrier islands, focusing on four distinct regions between Quintana Park and the Heritage Preserve. Key findings highlight the spatial and seasonal variability in hydrology, influenced by sediment composition, recharge events, and tidal forcing. Coastal areas exhibit permeable sediments that facilitate rapid groundwater flow and discharge, while inland areas have finer sediments that reduce permeability. Seasonal depth-to-water (DTW) trends reveal higher flooding risks during late winter and early spring in coastal areas, with DTW approaching or exceeding the ground surface, particularly in regions closer to the Gulf of Mexico. Inland regions consistently show deeper DTW values, reducing their vulnerability to flooding. Submarine groundwater discharge (SGD) rates are significantly higher in coastal regions during cooler months due to rainfalldriven recharge and aquifer flushing, while warmer months see seawater intrusion and reduced SGD rates. Predictive modeling, achieving high accuracy ( $R^2 > 0.93$ ), identifies streamflow, rainfall, and soil moisture as key drivers of groundwater fluctuations. These insights emphasize the interconnected dynamics of groundwater behavior, SGD, and infrastructure vulnerability, providing a foundation for adaptive coastal resource management strategies, flood risk mitigation, and sustainable water resource planning.

## 3.2. Background

Groundwater is critical in coastal ecosystems as a pathway for nutrient and contaminant transport via submarine groundwater discharge (SGD). SGD contributes significantly to coastal nutrient loading, delivering solutes such as nitrate, ammonium, and dissolved organic carbon, which can exacerbate eutrophication and algal blooms (Knee et al., 2011; Bianchi et al., 2014). This process, often driven by anthropogenic activities, introduces pollutants from urban development, agriculture, and septic systems, affecting the ecological and economic stability of coastal regions (Burnett et al., 2003; Bianchi et al., 2014). Radon-222 and radium isotopes are essential natural tracers for detecting and quantifying groundwater contributions to coastal contamination. Radon-222, with its short half-life, is a reliable indicator of recent SGD, marking areas of active discharge (Burnett et al., 2003; Knee et al., 2011). Radium isotopes, on the other hand, provide a longer-term perspective on interactions between fresh and saline water, mapping the pathways of contaminants from land-based sources to coastal waters (Burnett et al., 2003; Moore, 1996). In Texas coastal bays, seasonal and spatial variations in SGD rates have been linked to changes in nutrient concentrations, particularly ammonium and nitrate, which are key indicators of septic system leachate and agricultural runoff (Murgulet et al., 2016).

In environments where surface water inputs are not a substantial part of the water budget to coastal waters, SGD emerges as a primary nutrient source, particularly through the release of nutrients like nitrate and ammonium, which are often linked to septic system leachate, agricultural runoff, and decaying organic matter (Hu et al., 2006; Kroeger and Casey, 2007). The biogeochemical processing within subterranean estuaries (STEs) further modifies these solutes, resulting in SGD with unique chemical signatures and significant ammonium fluxes under anoxic conditions (Charette and Sholkovitz, 2006; Roy et al., 2010). Such nutrient-rich discharges can stimulate algal productivity or contribute to harmful algal blooms (HABs) in coastal ecosystems (Kroeger et al., 2007; Santos et al., 2012). SGD is also a significant source of

bacterial pathogens such as E. coli, which pose risks to public health and marine ecosystems (EPA, 2020; Smith et al., 2020). Stable isotopes of nitrogen and oxygen in nitrate further elucidate the transformations and origins of nutrients, helping to trace contamination pathways and identify pollution sources (Xue et al., 2009). This integration of groundwater tracers with bacterial and nutrient source tracking provides a detailed understanding of how SGD contributes to nutrient and pathogen loading in coastal environments.

This research underscores the importance of integrating radium and radon tracers with bacteriological data to analyze groundwater-surface water interactions. By investigating SGD's role in transporting nutrients and contaminants such as E. coli to Texas Gulf Coast estuaries, this study provides critical insights into the management of water quality in vulnerable coastal regions. These findings directly affect public health, ecosystem functions, and sustainable watershed management (Smith et al., 2020; Texas Water Resources Institute, 2017). By identifying and addressing the sources of bacterial and nutrient pollution, this research supports the development of remediation strategies that enhance water quality, protect biodiversity, and promote resilience within coastal communities (Jones et al., 2019; TCEQ, 2018).

### 3.3. Methods

## 3.3.1. Hydroparameter and water sample collection

Groundwater, porewater, and surface water samples were collected monthly, starting with November 2021 to May 2023. Field parameters, which were collected before sampling, including salinity, dissolved oxygen (DO), pH, and specific conductivity, were measured using a multi-probe YSI ProDSS. Groundwater was sampled at the wellhead using a peristaltic pump after purging three well volumes and after field parameters stabilized. Surface water samples were collected approximately one foot below the air-water interface in knee-depth waters along the shoreline (TCEQ 2012). Porewater was sampled at the same locations with surface water at approximately 0.2 m below the sediment-water interface with a push-piezometer sampler attached to a peristaltic pump after stabilization of field parameters (RCRA SOP 2009). All water samples were collected in 1 L HPDE bottles previously acid-washed with 20% hydrochloride acid, rinsed with 18.2 M $\Omega$  cm water, and finally triple-rinsed with sample water, were placed in ice until transported back to the lab and filtered through 0.2  $\mu$ m pore-sized polycarbonate membranes within 24-48 hours. Samples were then frozen until analysis.

### 3.3.2. Submarine groundwater discharge estimates

SGD rates were calculated using Darcy's law and radium activities, as described below.

### 3.3.2.1. Darcy discharge rate estimates

Darcy's law estimates of groundwater velocity (v, Darcy's Law formulas below) of "local" shallow, brackish to hypersaline SGD were derived using water level data from the groundwater monitoring wells. Hydraulic conductivity data was estimated from a series of well/sediment core data collected at the installation of each monitoring site. This field analysis provided knowledge about how grain size, sorting, composition, and porosity changed with depth. With these categories and an idea of where the water table lies, base hydraulic conductivity values ranged between  $10^{-2}$  to  $10^{-7}$  cm/s, as dependent on the sedimentary make-up of the conductive saturated layer using standard values from Fetter (2001).

Darcy's Law analysis was performed using the true or seepage velocity formula:  $v = K \cdot i \cdot /n$ ; where K is the hydraulic conductivity, i is the hydraulic gradient, and n is effective porosity. The distance used to calculate the hydraulic gradient is the distance between the monitoring wells and the water line along the shoreline. The tidal activity was subtracted from the groundwater level at each well to get a true idea of the water's change in head. An effective porosity ranging from 0.05 to 0.15 was used for velocity estimates. The saltwater heads of the groundwater and seawater levels were converted to freshwater heads using estimated water densities based on the temperature and salinity of the water.

### 3.3.2.2. Radium mass balance and SGD rates

Surface water samples for radium (radium-224 [<sup>224</sup>Ra], radium-226 [<sup>226</sup>Ra]) analysis were collected in 20L jugs (approximately 19 to 21 L total volume) at each of the sampling sites by wading into the water and rinsing and filling the bottle in the wave zone. Samples from the monitoring wells and porewaters were collected in 10L collapsable cubes. The radium was extracted by processing the samples through ~15g manganese dioxide, MnO<sub>2</sub>, impregnated acrylic fibers at a flow rate <1 L·min<sup>-1</sup> (Kim, Burnett et al. 2001, Dimova, Burnett et al. 2007). The Mn-fibers were then rinsed thoroughly with Ra-free water to eliminate any salts or particulates and then pressed to a water-to-fiber ratio of 0.3-1g (i.e., 20-30g wet weight) (Sun and Torgersen 1998). The fibers were tested for <sup>224</sup>Ra (half-life: 3.6 days) on a Radium Delayed Coincidence Counter (RaDeCC). Activities of <sup>224</sup>Ra were measured within three days of collection, given the short half-life (Moore 2006). After the short-lived isotope measurements, the fibers were flushed with nitrogen gas and sealed for >21 days to reach secular equilibrium before measuring the <sup>226</sup>Ra (half-life: 1,600 years) on a RAD-7 with measurements corrected to a calibration curve determined from 5 standards (Moore 1996).

Following Null et al. (2014), a mass balance for each Ra isotope was developed using Moore's (1996) method. Brackish SGD fluxes were estimated by assessing excess Ra activities within the coastal zone up to approximately 50 m from the water line. The area was segmented into four areas, as shown in **Figure 2.1**. Our Ra mass balance model quantifies only brackish SGD into the coastal zone, excluding freshwater discharge due to Ra's salinity dependence (Webster Hancock and Murray, 1995; Null et al., 2014). The selected endmembers for the box model calculation were the average Ra activities from porewater and monitoring wells at each corresponding surface water location of the four regions. Fluxes of SGD to the gulf (*D*) were calculated with a modified version of Eq. (1) from Moore (1996):

$$D(m^3 \cdot d^{-1}) = \frac{(V_{box})(A_{box} - A_{offshore})}{\tau \times A_{gw}}$$
 Eq. 1

where  $V_{box}$  is the volume of the nearshore segment (e.g., the area from sites 2 to 5, the area from sites 7 to 14, the area for sites 15 to 16, the area for sites 18 to 19: 2.0 x 10<sup>6</sup>, 1.8 x 10<sup>6</sup>, 5.5 x  $10^5$  and 2.9 x  $10^5$  m<sup>3</sup> respectively),  $\tau$  is the area's water flushing time (Area for sites 2 to 5:  $\bar{x}$ = 5.3 and 25.5; Area for sites 7 to 14:  $\bar{x}$ = 4.5 and 25.5; Area for sites 15 to 16:  $\bar{x}$ = 5.5 and 16.5; Area for sites 18 to 19:  $\bar{x}$ = 5.2 and 10.6 days for <sup>223</sup>Ra and <sup>226</sup>Ra based calculations respectively),  $A_{box}$  is the excess Ra activity in the box area, offshore Ra ( $A_{offshore}$ ), and groundwater or porewater endmember Ra. Volumetric rates were normalized to each respective area (Area for sites 2 to 5: 1.0 x  $10^6$  m<sup>2</sup>, Area for sites 7 to 14: 9.2 x  $10^5$  m<sup>2</sup>, Area for sites 15 to 16: 2.8 x  $10^5$  m<sup>2</sup>, Area for sites 18 to 19: 1.5 x  $10^5$  m<sup>2</sup>) to derive advective SGD rates (m·d<sup>-1</sup>). This step is necessary to accurately determine the discharge rate per unit area and compare different regions of the study area, especially when comparing the regions of different sizes.

## 3.3.3. Groundwater level prediction: data preparation and analysis

## 3.3.3.1. Data preparation: acquisition and sampling

In this study, two distinct categories of datasets were used: Data obtained from online repositories and field samples collected from monitoring wells. Each dataset type plays a critical role in the overall analysis and is described in detail in the subsequent sections. The collected data encompasses continuous, observational measurements, while the sampled data refers to targeted, point-in-time observations. These two categories provide complementary insights, and their distinct characteristics are essential for developing a comprehensive understanding of the phenomena under investigation. Detailed explanations of the methodologies and data handling for both categories are provided in the following sections.

## Data acquisition

The datasets utilized in this study comprised key hydrological and environmental variables: wind speed, wind direction, wind gust, water temperature, air temperature, tide level, rainfall, streamflow, Terrestrial water storage, baseflow runoff, storm surface runoff, root zone soil moisture, soil moisture content, GPM\_3IMERGHHI, MRMS rainfall, and sea level pressure. These variables were downloaded across multiple locations (**Table 3.1**) to assess their relationships with bacteria levels and nutrient concentrations. By analyzing these environmental and hydrological factors, the study aims to identify potential correlations and better understand the drivers influencing bacterial and nutrient dynamics in the given areas.

*Table 3.1.* Environmental and hydrological variables with temporal resolutions and data sources.

Variables	Temporal Resolution	Download Link
Streamflow	Hourly	https://waterdata.usgs.gov/
Tide level	Hourly	https://tidesandcurrents.noaa.gov/
GPM_3IMERGHHI	30 minutes	https://giovanni.gsfc.nasa.gov/giovanni/
Wind speed Wind direction Wind gust Air temperature	Hourly	https://tidesandcurrents.noaa.gov/
Precipitation	Daily	https://www.ncdc.noaa.gov/
Terrestrial water storage	Daily	https://giovanni.gsfc.nasa.gov/giovanni/
Baseflow runoff	Daily	https://giovanni.gsfc.nasa.gov/giovanni/
Storm surface runoff	Hourly	https://giovanni.gsfc.nasa.gov/giovanni/
Root zone soil moisture	Hourly	https://giovanni.gsfc.nasa.gov/giovanni/
Soil moisture content	Hourly	https://giovanni.gsfc.nasa.gov/giovanni/
MRMS rainfall	Hourly	https://mtarchive.geol.iastate.edu/
Sea level pressure	Hourly	https://giovanni.gsfc.nasa.gov/giovanni/

Sampled data: data preparation and laboratory analysis: processing and evaluation

Twelve monitoring wells (**Figure 3.1**) were installed along the shoreline and at the bay/river outlet to collect groundwater samples, pore water, and surface water samples. Between

November 2021 and May 2023, 843 samples were collected. **Table 3.2** presents the number of samples collected each month for surface, pore, and groundwater, along with the total samples for that month. Each well was equipped with a pressure transducer that continuously recorded the water table elevation every 15 minutes.

Table 3.2. Monthly water sample data (2021–2023).

Year	Month	Surface Pore G		Ground	<b>Total Samples</b>
2021	November	16	11	12	39
2021	December	18	13	12	43
2022	January	19	13	12	44
2022	February	25	16	14	55
2022	March	19	15	12	46
2022	April	19	11	12	42
2022	May	18	10	12	40
2022	June	19	12	12	43
2022	July	19	12	12	43
2022	August	18	12	12	42
2022	September	19	12	12	43
2022	October	19	15	12	46
2022	November	19	13	12	44
2022	December	19	14	12	45
2023	January	19	15	12	46
2023	February	19	15	12	46
2023	March 19		15	12	46
2023	April	19	15	12	46
2023	May	18	15	11	44
Total		360	254	229	843

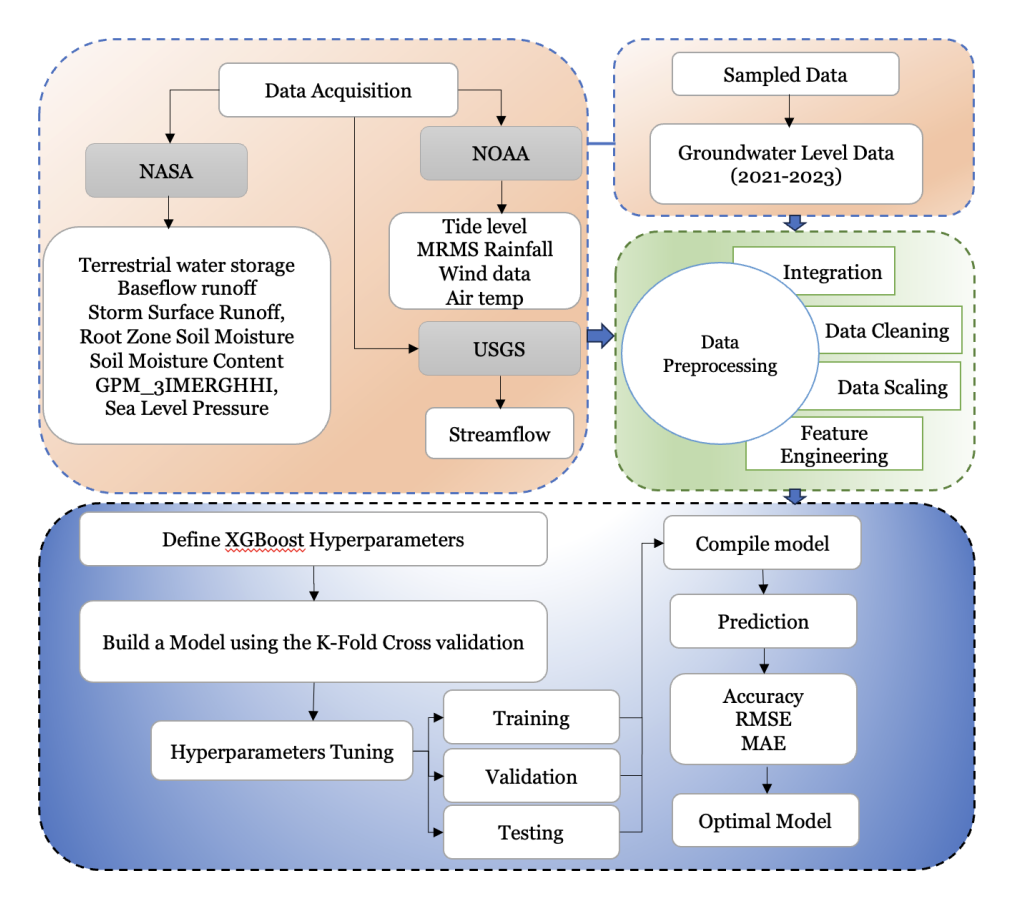


Figure 3.1. Photos of selected monitoring wells for the research.

## 3.3.3.2. Modeling framework: development and validation

**Figure 3.2** outlines the systematic framework for groundwater level prediction, focusing on data preprocessing, model development, and validation. After multi-source data retrieval, the preprocessing phase ensures data quality and consistency through integration, noise removal, outlier correction, and standardization. Feature engineering further enhances the dataset by extracting meaningful attributes to improve model performance. The model development phase employs the XGBoost algorithm, chosen for its computational efficiency and ability to handle structured data. Optimal hyperparameters are defined, and the model is trained using K-Fold Cross-Validation to improve generalizability and mitigate overfitting. Hyperparameter tuning fine-tunes the balance between bias and variance, while the iterative training, validation, and

testing process ensure robust model refinement. Finally, the compiled model undergoes performance evaluation, where prediction accuracy is measured using Root Mean Square Error (RMSE), R<sup>2</sup>, and Mean Absolute Error (MAE). This rigorous process identifies the optimal model, delivering reliable groundwater level predictions for effective resource management.



*Figure 3.2.* Flow chart of the research methodology.

## 3.3.3.2.1. Data preprocessing

After the dataset is collected, a thorough cleaning process is conducted to ensure quality and relevance for modeling. Missing values are addressed using K-Nearest Neighbors (KNN) imputation, noisy data is mitigated through filtering or transformations, and irrelevant images and datasets unsuitable for the model are removed. This systematic approach enhances data integrity and prepares it for the modeling phase. **Figure 3.3** illustrates a summary of the preprocessing steps undertaken.

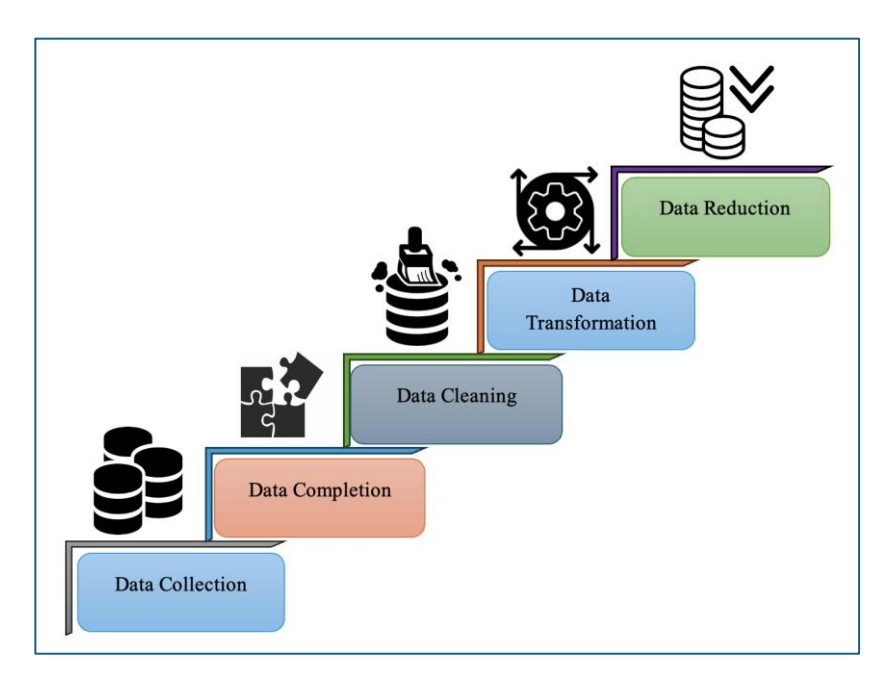


Figure 3.3. Key steps in data preprocessing.

## 3.3.3.2.2. Variational Auto-Encoder (VAE) and Principal Component Analysis (PCA)

In this study, two distinct approaches were utilized to explore relationships within the chemical dataset: Principal Component Analysis (PCA), a statistical technique for uncovering underlying patterns and reducing dimensionality, and Variational Auto-Encoder (VAE), a deep learning-based method for identifying complex, non-linear interactions among the variables. However, PCA was insufficient for capturing the intricate relationships in the dataset, as it is a traditional technique that may not fully account for the complexity of water chemistry.

Variational Auto-Encoder (VAE) is an artificial neural network architecture introduced by Diederik P. Kingma and Max Welling (Kingma and Welling, 2014), and it is an extension of the traditional autoencoder that adds a probabilistic approach to the learning process. In a Variational Autoencoder (VAE), the encoder maps the input data into a probabilistic distribution (typically Gaussian) instead of a fixed representation, enabling a more adaptable data representation. Rather than learning a specific code, the VAE models a distribution over the latent variables, allowing for sampling from this distribution during the decoding process. The decoder then reconstructs the data from this latent space, attempting to generate output that closely resembles the original input but using the probabilistic representation. Below are the results of applying deep learning techniques to the chemistry dataset using the original and transformed data.

## 3.3.3.2.3. Transformation techniques

The scale of bacteria levels in the dataset varies significantly, with some days showing extremely high values. To address this, logarithmic and Box-Cox transformations were applied to normalize the data and mitigate the impact of outliers. These transformations enhanced the correlation between the bacteria data and the chemistry dataset, making the relationships more interpretable and reliable for analysis. In addition, environmental and hydrological factors were incorporated into the analysis by employing various data transformation techniques, such as

lagging data, normalization, cumulative sums, differencing, logarithmic transformations, smoothing techniques, polynomial features, categorical encoding, and feature selection. These methods helped refine the dataset and improve the robustness of the modeling approach.

Modeling bacteria levels based on wind direction is challenging because wind direction is a physical phenomenon influenced by meteorological conditions. In contrast, bacteria levels are typically driven by environmental factors like water quality, temperature, or contamination sources. However, relationships might exist indirectly, such as wind patterns influencing bacteria transport or dispersal. To address this, wind direction was transformed to account for its circular nature, incorporating additional axes to align with local environmental patterns (Wolfe et al., 2023). **Figure 3.4** illustrates the wind speed and wind direction rose diagrams for the seven stations utilized in this study. Each diagram provides insight into the dominant wind directions and their corresponding speeds at each location.

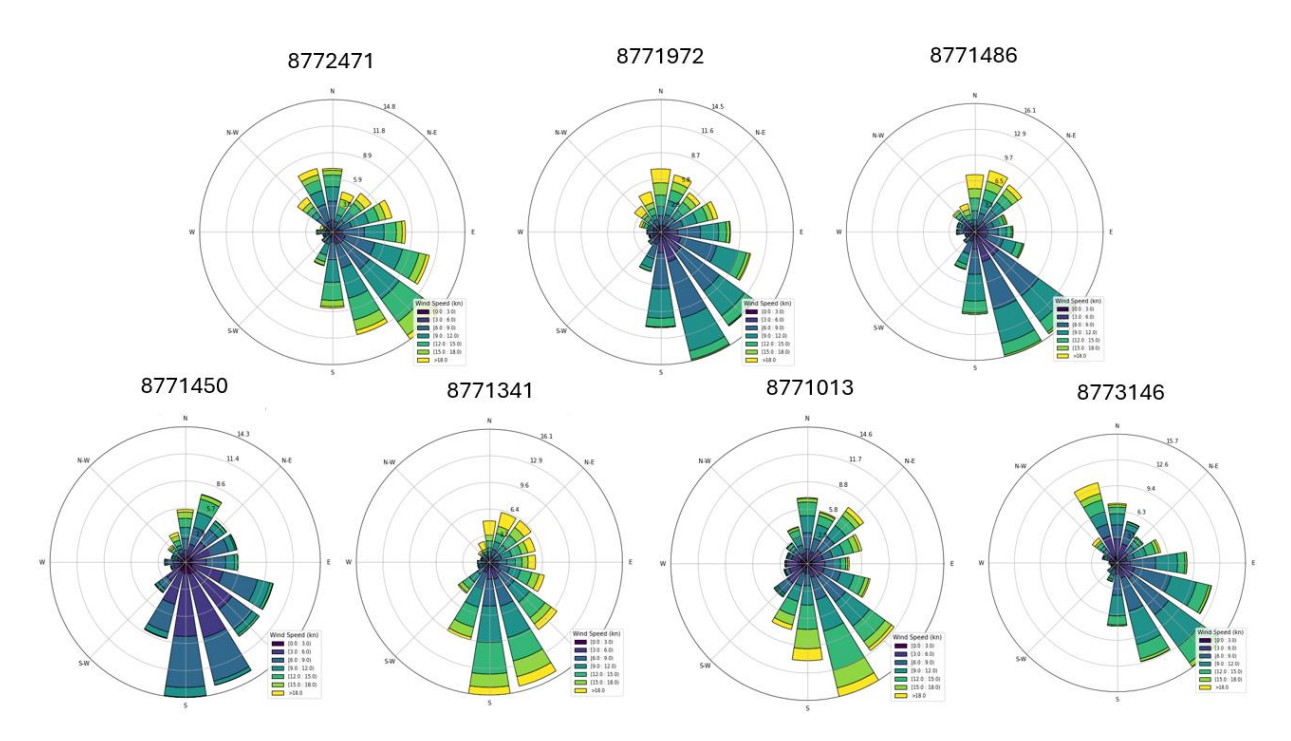


**Figure 3.4.** Wind Direction Rose Diagram for Seven Stations: Visual representation of wind direction frequencies across all stations. Each diagram highlights the dominant wind patterns, with the length of each bar indicating the proportion of time the wind blew from a particular direction, aiding in understanding regional wind trends and their environmental impact.

## 3.3.3.2.4. GIS-Ensemble model and validation

A machine learning model was developed in this research to predict groundwater elevations by integrating transformed environmental and hydrological factors. Among the various machine learning and deep learning techniques tested—such as Multilayer Perceptron (MLP), Random Forest, and Long Short-Term Memory (LSTM)—the XGBoost model demonstrated superior performance. XGBoost model, a gradient boosting machine learning technique known for its high performance in predictive tasks. The model is trained using the

preprocessed data, along with hourly groundwater levels collected from 11 monitoring wells between November 2021 and May 2023. Geographic Information System (GIS) tools were used to extract and organize data based on specific watersheds, enabling a more precise spatial analysis of groundwater dynamics. Hyperparameters are defined and optimized using K-fold cross-validation to improve model accuracy. The model is then trained on the dataset, followed by hyperparameter tuning to refine its performance. The final trained model is evaluated using performance metrics like RMSE, MAE, and R<sup>2</sup> to assess its predictive capability for groundwater levels.

#### 3.4. Results

#### 3.4.1 Sediment core characterization

The following provides a detailed description of the sediment cores, and the observed layered heterogeneity based on depth intervals, sediment type, and grain size, as represented in **Figure 3.5** below. A summary of the sediment core analyses by well is as follows:

Well #1: The sediment core is dominantly characterized by clay with silt and sand lenses interspersed at various depths. Between 400 and 600 cm, the layers consist of compacted clay with minimal moisture, indicative of drier, consolidated material. Deeper layers transition to wetter conditions, with intervals of sandy silt and clay-silt mixtures, reflecting a finer-grained sediment composition.

Well #2: This sediment core consists primarily of clay-silt mixtures, with some organic content observed near the surface. Layers of sandy clay appear at various depths, interbedded with finer silts. Sediments are predominantly wet, with intervals exhibiting varying plasticity that correlates to changes in clay content and compaction.

Wells #3 and #4: The sediment cores display complex layering of fine silt, clay, and sandy textures. Notably, the sediments at these locations contain distinct intervals of sandy silt interbedded with clay layers. Colors range from gray and olive gray to brown, suggesting organic material and mineral variations. Sediments maintain wet conditions throughout, indicating consistent water retention.

Well #5: This sediment core exhibits alternating layers of sandy silt, clay, and sand, with surface intervals containing sand, silt, and plant roots. Deeper sections are dominated by fine clay and clay-sand mixtures, which appear more compact and drier. The varying textures suggest episodic shifts in depositional energy.

Wells #7 and #8: These wells display significant variability:

- Well #7: The upper layers are predominantly gravel and sand, transitioning to fine clay and gravelly silt at depth. Sediment colors range from yellow-orange to olive-gray, reflecting mineralogical changes. Moisture levels vary from slightly moist to saturated, with deeper clay layers indicating high plasticity.
- Well #8: This core contains sandy clay, with interbedded clay and silt layers, maintaining a generally wet condition. Some intervals include sand and gravel, indicative of coarsergrained depositional events.

Well #9: This core is primarily comprised of sand. Deeper intervals exhibit higher sand content and maintain wet, loose conditions. Sediment colors range from white-gray to olive-gray, suggesting variations in mineral composition.

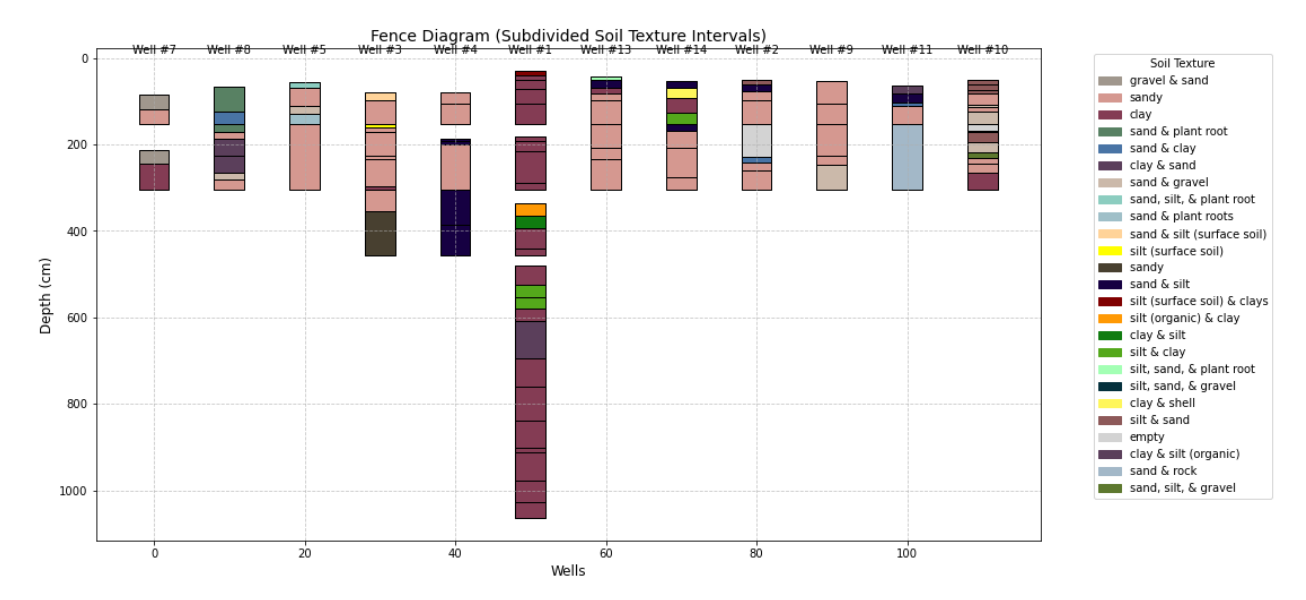


**Figure 3.5.** Soil texture depth profile by well. Note the persistence of sands for most of the sedimentary facies except for well #1, which is located inland and not included in the analyses.

Well #10: The sediment core consists predominantly of fine silt and clay, with interbedded sand and gravel lenses occurring sporadically. Sediments are predominantly wet, with certain intervals of sandy clay reflecting higher depositional energy. Deeper sections show clay dominance, with high plasticity observed in finer-grained zones.iWell #11: At this location, the sediment layers of fine clay mixed with silt and sand, with a higher organic content near the surface. The moisture levels fluctuate between ilightly plastic and saturated, with deeper sections containing loose, wet silts. This variability suggests changes in sediment deposition and compaction.

Wells #13 and #14: At these locations, sediments exhibit alternating fine sand, silt, and clay layers. Shallow intervals (0–100 cm) are dominated by fine silt and clay mixtures, transitioning to sandy clay at depth. Moisture levels range from dry to saturated, with certain intervals showing varied plasticity and silt-dominated textures.

These sediment cores, collected from coastal and near-coastal environments, highlight a diverse range of sedimentological features influenced by hydrological processes, depositional history, and depth-related compaction. The sediment textures—ranging from clay and silt to sand, gravel, and plant roots—reflect variability in depositional energy and water table dynamics.

# 3.4.2. Data analysis: statistical summary, correlations, and distributions of groundwater elevations

#### 3.4.2.1. Statistical summary

The statistical summaries for the variables of interest, categorized by parameter, are presented in the tables below. **Table 3.3**, **Table 3.4**, **Table 3.5** provide detailed statistical descriptions for surface, pore, and groundwater samples, respectively.

**Table 3.3.** Statistical summary of water quality variables in groundwater samples (Nov 2021-May 2023).

Column	Mean	Min	Max	Variance	Standard Deviation	Coefficient of Variation (CV)
DO	3.1	0.2	8.5	4.3	2.1	66.5
Sal	3.0	0.3	14.3	16.0	4.0	132.3
pН	7.1	5.4	8.6	0.2	0.5	6.7
ORP	-18.0	-205.8	272.7	12293.4	110.9	-615.7
Rn	3404.4	0.0	30141.1	21821125.6	4671.3	137.2
Ra223	46.8	-0.8	577.1	5390.9	73.4	156.7
Ra224	1108.8	22.7	7813.2	1554661.6	1246.9	112.5
Ra226	254.2	69.8	878.0	34166.0	184.8	72.7

**Table 3.4.** Statistical summary of water quality variables in porewater samples (Nov 2021-May 2023).

Column	Mean	Min	Max	Variance	Standard Deviation	Coefficient of Variation (CV)
DO	2.9	0.5	10.2	2.5	1.6	55.6
Sal	26.7	0.9	38.1	35.4	5.9	22.3
pН	7.6	6.4	8.6	0.1	0.4	4.7
ORP	40.4	-331.0	317.2	11696.1	108.1	267.9
Rn	1420.2	0.0	6646.6	1065431.3	1032.2	72.7
Ra223	165.7	0.0	1705.9	25791.5	160.6	96.9
Ra224	3046.8	23.2	13037.9	3909267.3	1977.2	64.9
Ra226	491.9	147.0	1887.0	84489.6	290.7	59.1

**Table 3.5.** Statistical summary of water quality variables in surface water samples (Nov 2021-May 2023).

Column	Mean	Min	Max	Variance	Standard Deviation	Coefficient of Variation (CV)
DO	7.6	1.9	12.3	1.6	1.3	16.8
Sal	26.4	0.6	36.0	32.0	5.7	21.4
pН	8.0	7.0	8.9	0.1	0.3	3.4
ORP	92.9	-123.5	289.2	5369.9	73.3	78.9
Rn	29.0	0.0	644.2	3211.7	56.7	195.5

Ra223	36.9	0.0	660.6	1939.9	44.0	119.4
Ra224	546.3	59.2	7477.4	323877.3	569.1	104.2
Ra226	250.1	43.9	945.5	24673.0	157.1	62.8

The raw groundwater level data were carefully cleaned to remove noise and inconsistencies, ensuring reliable input for analysis. This step included filtering out errors to produce a high-quality dataset. The heatmap displays the correlation coefficients between groundwater levels across various wells. As shown in **Figure 3.6a**, Wells 3 and 5 exhibit a high correlation (~0.97), suggesting similar patterns in their groundwater level fluctuations, while Wells 2 and 9 show a lower correlation (~0.42), indicating differences in their behavior. **Figure 3.6b** illustrates the data trends over time for the selected wells, highlighting variations that likely reflect a combination of local environmental and hydrological factors, as well as differences in slope, elevation, and watershed characteristics. These variations influence groundwater elevation changes at different locations, which may respond similarly or differently depending on the location. This affects the observed fluctuation patterns across wells, reflecting the unique responses to hydrological processes such as flow and recharge.

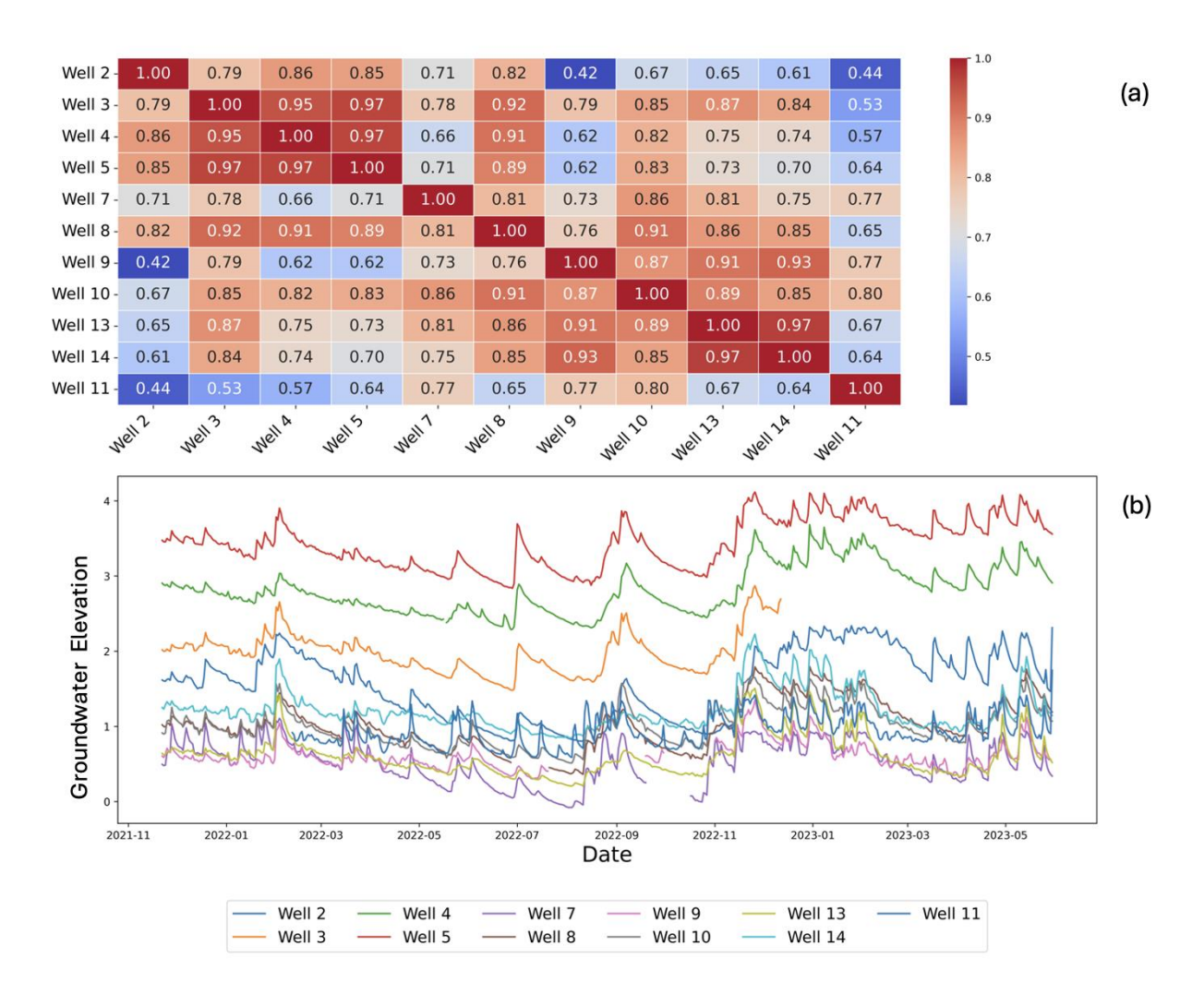


**Figure 3.6.** (a) Heatmap of correlation coefficients between groundwater levels at different wells. (b) Line chart showing groundwater level variations over time for the selected wells.

#### 3.4.2.2. Radium activities

### Radium-224 activities

Porewater exhibited the highest mean <sup>224</sup>Ra activity (3,047 Bq/m³), with a maximum of 13,038 Bq/m³ observed at station P14 in May 2023. This peak indicates intense radium mobilization from sediments, possibly driven by episodic geochemical or hydrological events, such as increased SGD discharge or sediment disturbances and mobilization due to increases in salinity within the groundwater-surface water freshwater-seawater interface. The lowest <sup>224</sup>Ra activity in porewater was 23 Bq/m³, recorded in September 2022 at P14, where reduced SGD or sediment interactions have occurred. Temporal trends in porewater activities showed consistently high levels, with peaks during May 2023 and July 2022, aligning with seasonal SGD patterns. Stations P10 and P14 also exhibited substantial variability, with periodic spikes exceeding 6,000 Bq/m³.

Surface water displayed much lower mean activity (547 Bq/m³), with a maximum of 7,477 Bq/m³ recorded in March 2022 at station S5, expected to result from large SGD inputs

derived from nearby sources. The minimum activity of 59 Bq/m³ occurred at S20 in February 2022, indicative of dilution by offshore Gulf waters and/or reduced SGD inputs. Like porewater, August 2022 was a notable month for elevated surface water activities, particularly at stations S1, S10, and S17, where radium-enriched groundwater discharges influenced the observed spikes. Stations S6B and S12, by contrast, maintained relatively stable activities, with levels ranging between 195 and 225 Bq/m³, showing minimal interaction with groundwater and limited porewater fluxes.

Groundwater samples showed moderate variability, with a mean <sup>224</sup>Ra activity of 1,071 Bq/m³. The highest activity (7,813 Bq/m³) was recorded at station W9 in November 2021, potentially linked to deeper aquifer inputs rich in radium. However, long residence times and increased salinities due to prolonged saltwater intrusion (e.g., high tides) events allow for radium dissolution from sediments. The lowest <sup>224</sup>Ra activity (23 Bq/m³) was observed at W7 in May 2022, indicating limited radium mobilization or mixing or recent recharge from precipitation. Darcy's groundwater discharge rates in this location indicate potential saltwater intrusion, thus causing dilution of ambient aquifer activities with the depleted seawater. Temporal patterns in groundwater showed elevated activity during November 2021, February 2022, May 2023, and August 2022. Station W10 mirrored patterns seen in porewater, with consistent peaks correlating with SGD pulses during the late summer.

All three sample types showed elevated <sup>224</sup>Ra activity in August 2022, suggesting strong SGD contributions during the late summer months. Porewater and groundwater exhibited complementary peaks, indicating that interactions between these systems are substantial. Stations S5 and P14 displayed significant peaks across surface and porewater, respectively, underscoring their roles as hotspots for SGD-driven radium mobilization. Station W7 showed similar behavior for groundwater, particularly in November 2021. Stations S15 and S20 in surface water, W5 in groundwater, and P4 in porewater maintained relatively consistent <sup>224</sup>Ra activity, reflecting minimal influence from episodic or seasonal variations. All sample types showed a general pattern of higher activities during summer months (e.g., August 2022 and July 2022) and lower levels during late winter (e.g., March 2022), emphasizing the seasonal influence on SGD dynamics and sediment-water interactions.

## Radium-223 activities

Activities of <sup>223</sup>Ra are generally much lower than those of <sup>224</sup>Ra, given the lower abundance of the parent isotope in sediments along the Gulf Coast Aquifer. Thorium-227 is part of the decay chain of Uranium-235 and is a precursor to <sup>223</sup>Ra. This relationship is relevant in environmental and geochemical studies, as radium isotopes like <sup>223</sup>Ra are often used to trace SGD or to study sediment-water interactions (Moore and Arnold, 1996). Thorium-227 tends to be particle-reactive and binds to sediment particles. From there, it decays into <sup>223</sup>Ra, which can be more mobile in porewater or released into the overlying water column.

Notable spatial and temporal variability in <sup>223</sup>Ra activities is observed among porewater, surface water, and groundwater samples along the coast. Porewater samples showed the highest mean <sup>223</sup>Ra activity at 168 Bq/m³, with a peak of 1,706 Bq/m³ in February 2023 at station P2. Like <sup>224</sup>Ra, this may reflect strong geochemical interactions and possibly substantial radium mobilization near the sediment-water interface. Other notable peaks in porewater occurred in July 2022 (1,042 Bq/m³ at P14), suggesting episodic inputs from terrestrial groundwater enriched in radium.

Surface water samples exhibited much lower mean activity (37 Bq/m³), with a maximum of 661 Bq/m³ observed in March 2022 at station S5, which stands out compared to increased nearshore groundwater inputs during the late summer months with associated higher surface radium. Temporal trends in surface water are generally more stable, but slight elevations in activity occurred in January 2022 (274 Bq/m³ at S6). Moderate variability was observed in groundwater, with activities ranging from 0.1 Bq/m³ (at W4 in December 2022) to a peak of 577 Bq/m³ recorded in November 2021 at W9. The November peak corresponds to the time of increased terrestrial input or mixing dynamics likely linked to seasonal (e.g., late summer-fall) recharge (see Darcy's SGD section). Other minor peaks occurred in May 2023 (322 Bq/m³ at W11), aligning with similar trends seen in porewater.

Monthly averages indicate dynamic interactions between groundwater-porewater-surface water. For instance, porewater activities, which were consistently higher than groundwater and surface water, are likely a source of radium to surface water and potentially to groundwater at times of low water table and saltwater intrusion. Porewater had sharp peaks in February 2023 and December 2022, while surface water and groundwater showed their most significant increases during January 2022 and November 2021, respectively. From these observations, it can be inferred that porewater is a key reservoir that influences radium dynamics along the barrier island.

#### Radium-226 activities

Like <sup>223</sup>Ra, the peak <sup>226</sup>Ra activity was 8,411 Bq/m<sup>3</sup> in a porewater sample, P19, in October 2022. This significant spike indicates specific localized geochemical conditions that are facilitating the heightened mobilization of radium from sediments located near the shore, among which could be input from deeper or more distant groundwater. On the other end of the spectrum, the lowest <sup>226</sup>Ra activity measured was 42 Bq/m<sup>3</sup>, captured in surface water at S1 in August 2022. These low levels may result from dilution with Gulf of Mexico offshore waters or insignificant terrestrial groundwater discharge. High <sup>226</sup>Ra activities were observed in September and October 2022, with numerous instances exceeding the threshold of 800 Bq/m<sup>3</sup>. These frequent spikes may indicate intensified biogeochemical interactions between sediments and water during these months. Given that <sup>226</sup>Ra does not recoil back into solution as quickly as the short-liver isotopes described above, the impact of salinity changes is not expected to be a large contributor to activity changes from month to month. However, high <sup>226</sup>Ra activities could be the result of both increased SGD from nearby sources (of lower <sup>226</sup>Ra activities) or proportionally lower terrestrial, more distant groundwater discharge that is generally richer in <sup>226</sup>Ra. In groundwater samples, moderate <sup>226</sup>Ra levels were generally detected, with peaks occurring in October 2022 and February 2023. The highest observation occurred in October 2022 (6,031 Bq/m<sup>3</sup>). Surface water activities showed more stable trends overall, with a higher average <sup>226</sup>Ra level in October 2022, similar to groundwater, with a maximum activity of 5,340 Bg/m<sup>3</sup>.

A downward trend in <sup>226</sup>Ra activity was generally observed during June 2022 and December 2021 across all sampling site types, suggesting the influence of seasonal or environmental factors, such as dilution and/or lower groundwater inputs. Levels of <sup>226</sup>Ra above 800 were predominantly recorded in porewater and groundwater. Porewater consistently exhibited high activities, frequently exceeding 800 Bq/m³, particularly notable in October 2022. Similar occurrences occurred in groundwater, where levels peaked above 800 in October 2022. Although surface water exhibited more stable patterns, it also reached a maximum activity of

5,340 Bq/m³ in October 2022, suggesting terrestrial groundwater inputs as significant sources during this time.

Observed fluctuations in <sup>226</sup>Ra levels may result from variable SGD inputs, both in magnitude and sources, or biogeochemical reactions and magnitudes of recirculation within the subsurface transition zone between groundwater and surface water. As with the short-lived radium isotopes, analysis of <sup>226</sup>Ra also highlights significant temporal and spatial variability in activities, especially in porewater, indicating substantial nearshore radium dynamics.

## 3.4.2.3. Measures of dispersion: violin plot

**Figure 3.7**, **Figure 3.8**, and **Figure 3.9** illustrate the distribution and outliers in the dataset using violin plots. The width of each violin plot indicates the density of data points at different values; wider sections signify higher concentrations of data points, while narrower sections suggest lower density. The height of each violin plot represents the range of the data, extending from the minimum to the maximum values, which provides an overview of the data's spread. A taller plot indicates a larger range of values, reflecting greater variability within the dataset. Together, the width and height of the violin plots provide a comprehensive view of the data distribution, highlighting where the majority of data points are concentrated and revealing

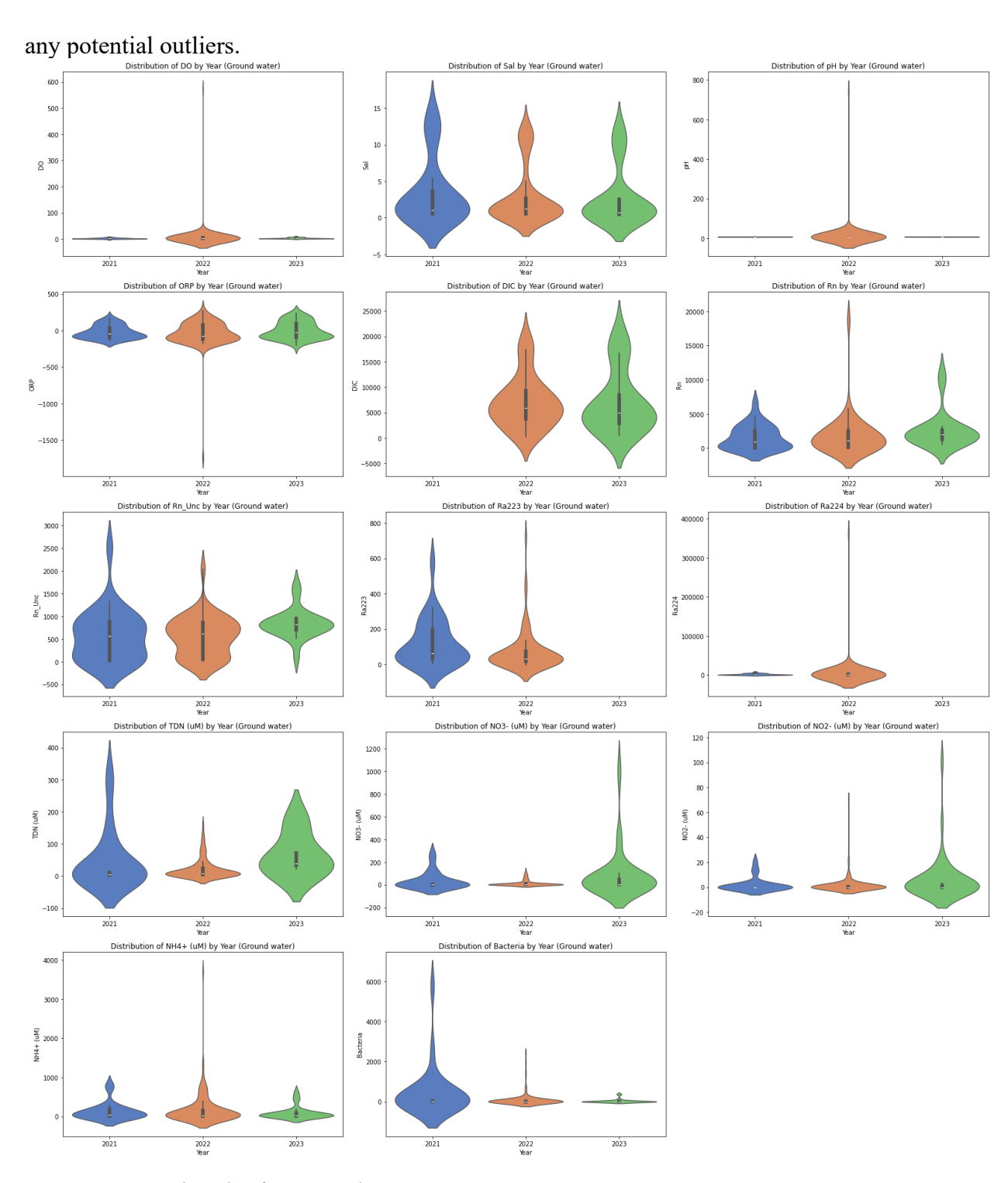


Figure 3.7. Violin plot for groundwater parameters.

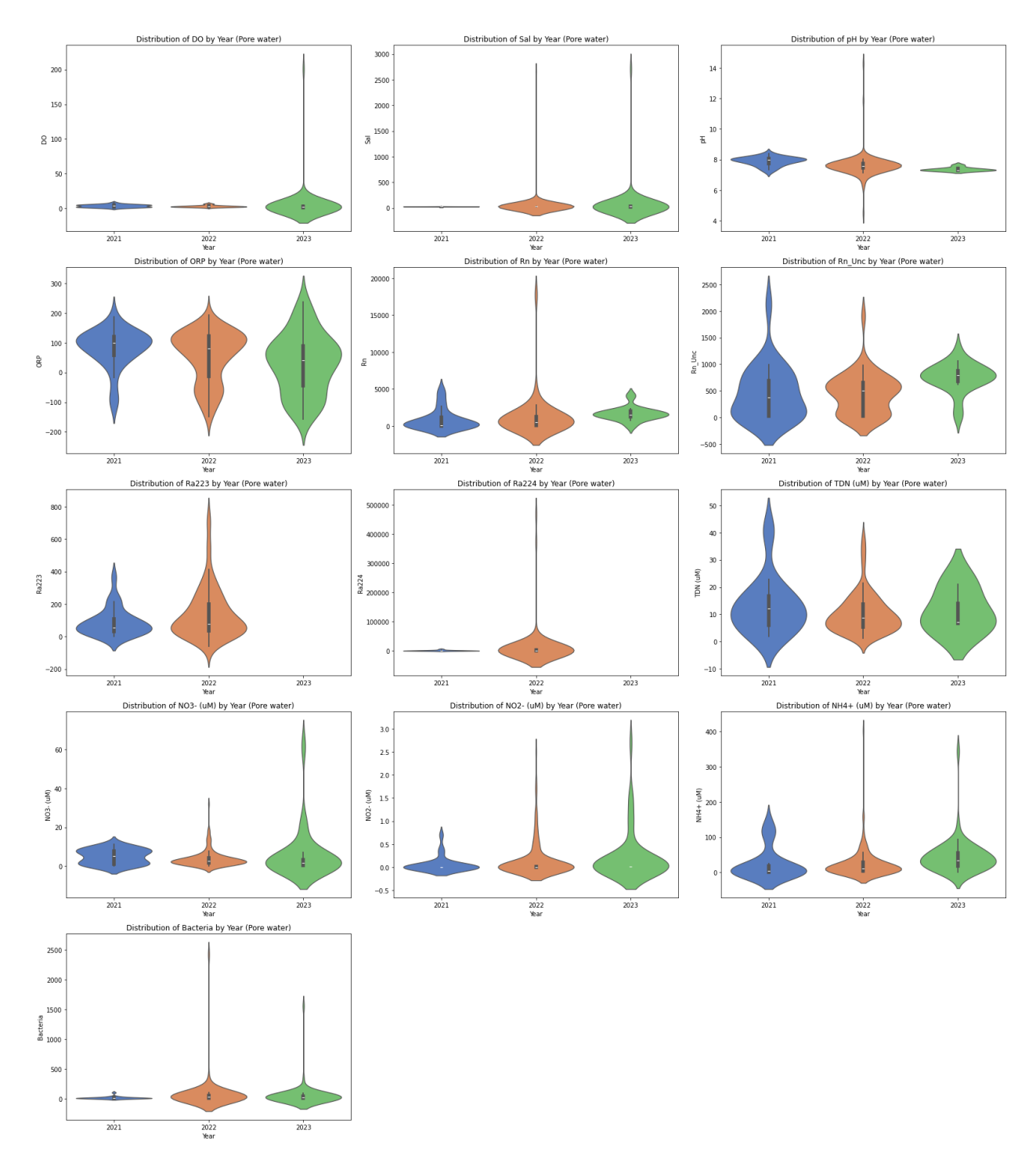


Figure 3.8. Violin plot for pore water parameters.

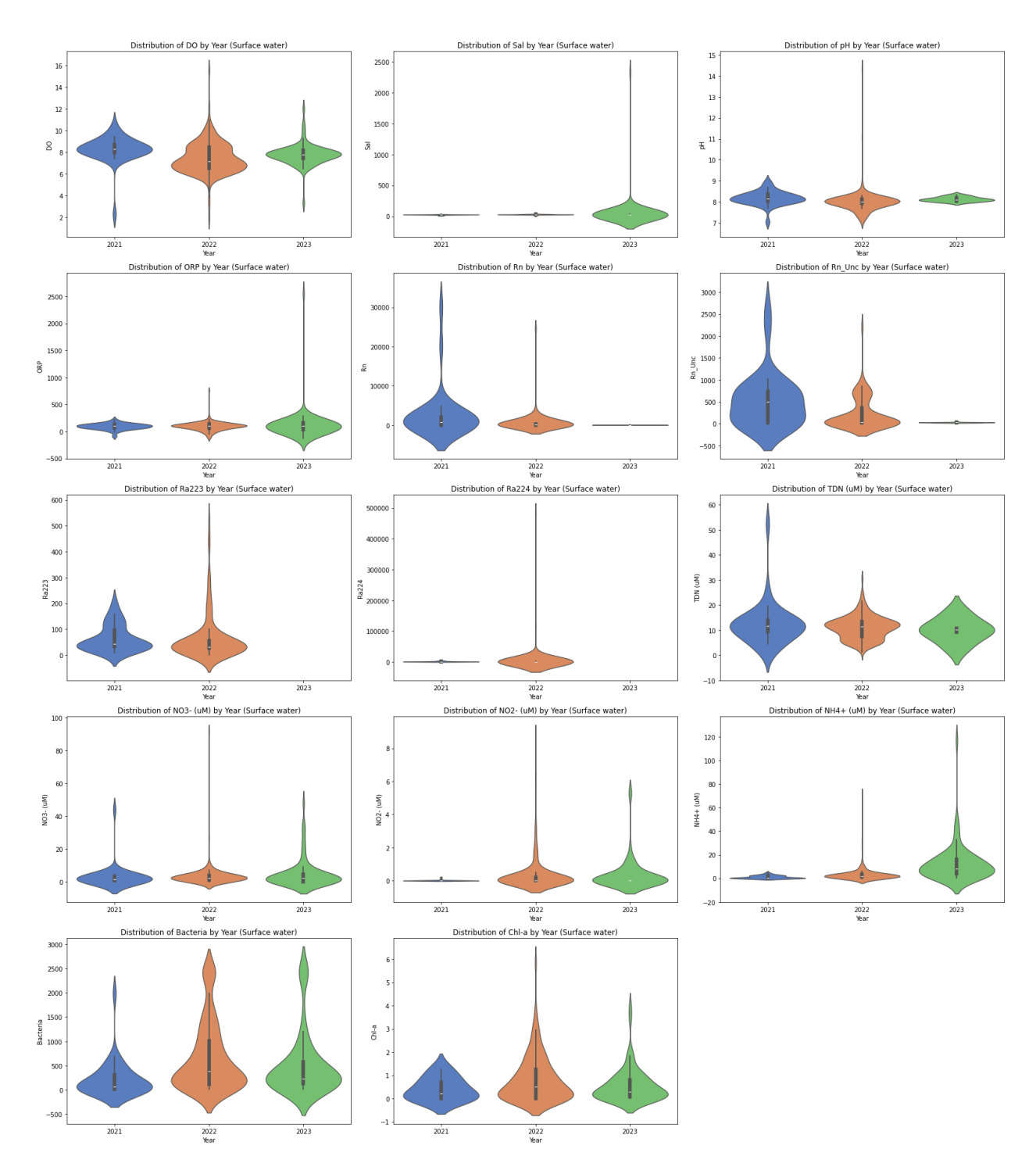
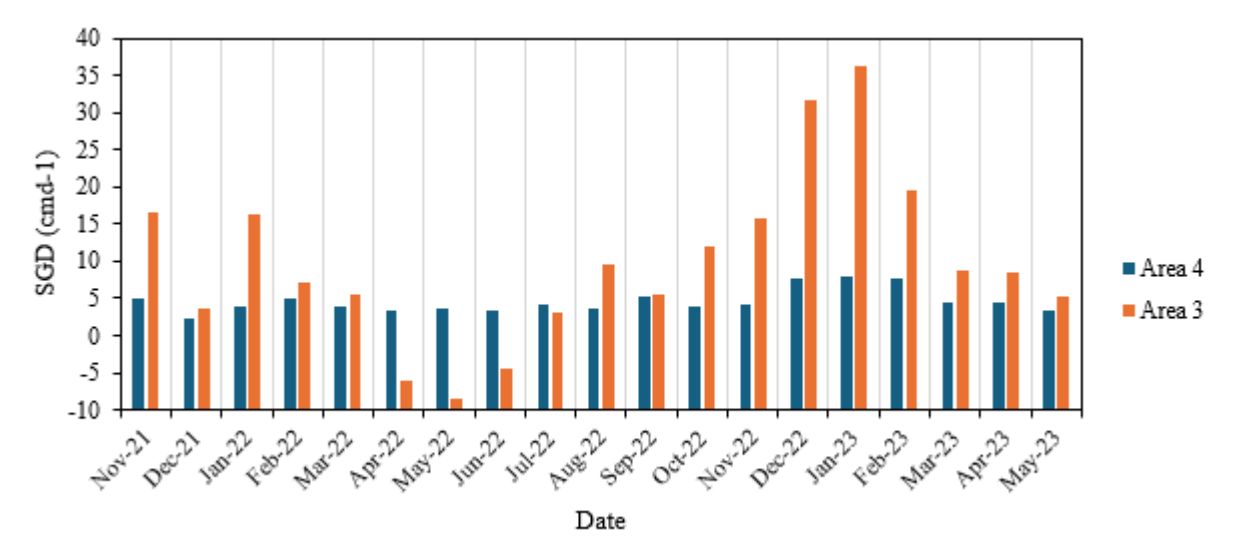


Figure 3.9. Violin plot for surface water parameters.

## 3.4.3. Submarine groundwater discharge

## 3.4.3.1 Darcy's SGD rates

Results from the Darcy's Law calculations show that the average SGD rates from area 3 (wells 7 to 14) are higher than those of area 4 (wells 2 to 5). A seasonal trend is more visible in area 3's data than area 4, but both data sets match, which is that in the colder months (roughly September to March), SGD is at its peak but drops low in the warmer months (March to August). See **Figure 3.10,Figure 3.11**, **Figure 3.12**, and **Figure 3.13**. This seasonal trend is reflected in the velocity data from individual wells, particularly in area 3. The area near well 7 consistently displayed the highest groundwater discharge velocities, peaking at 187 cm/d in January 2023 and 162 cm/d in December 2022 (**Figure 3.11** and **Figure 3.12**). These high velocities align with the peaks in SGD for area 3 during the same months, reinforcing the strong response of this region to seasonal recharge events. In contrast, during the warmer months, negative velocities were recorded near well 7 in April 2022, May 2022, and June 2022, indicating seawater intrusion. This is consistent with the lowest SGD rate for area 3, recorded in May 2022 at -8.5 cm·d<sup>-1</sup>. The negative SGD rate and velocities reflect the influence of tidal reversals, as seawater levels exceeded groundwater elevations. Darcy's Law calculations could only be performed for the area where wells were available as the groundwater elevations of the porewater are unknown.



**Figure 3.**10. Darcy's Law calculated SGD rates using freshwater heads from groundwater and Gulf of Mexico nearshore water levels. The negative values indicate that when the static groundwater level was measured in the month, the seawater level was higher, resulting in a negative/reverse gradient when seawater may intrude the water table aquifer, and negligible groundwater discharge will occur.

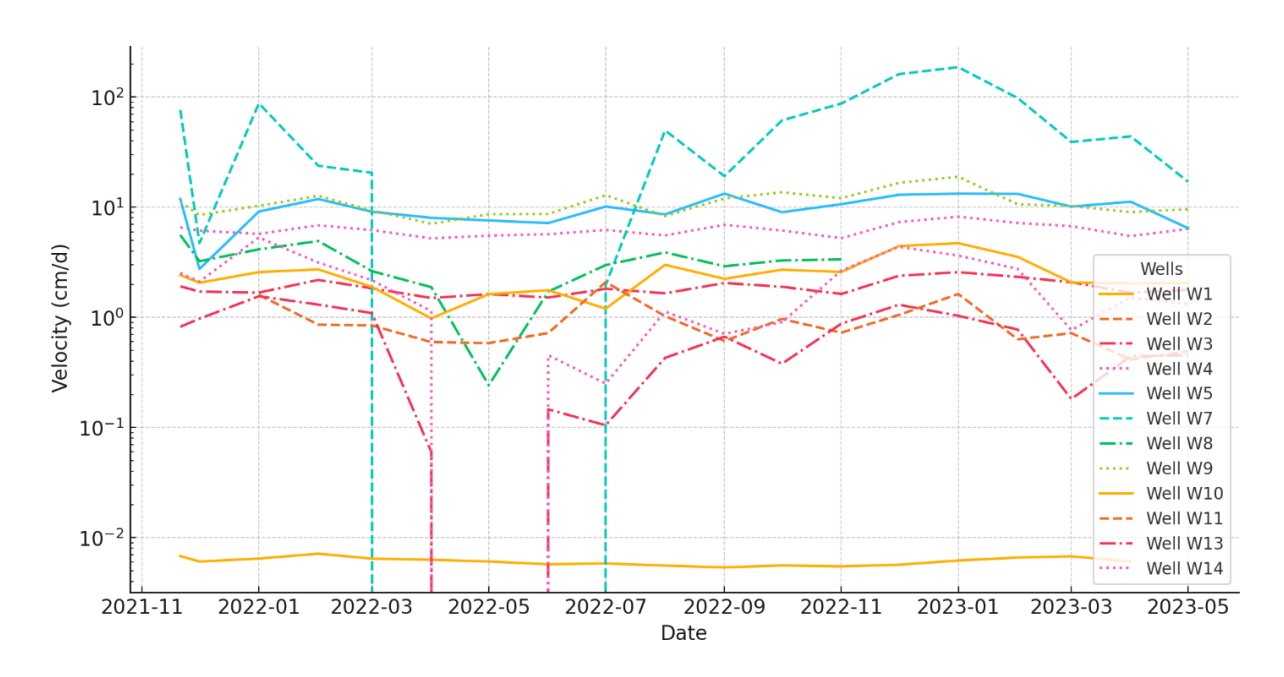


*Figure 3.11.* Groundwater discharge rates (velocity rates) over time for all locations corresponding to the monitoring wells in regions 3 and 4 (See Figure 2.1 for a location map).

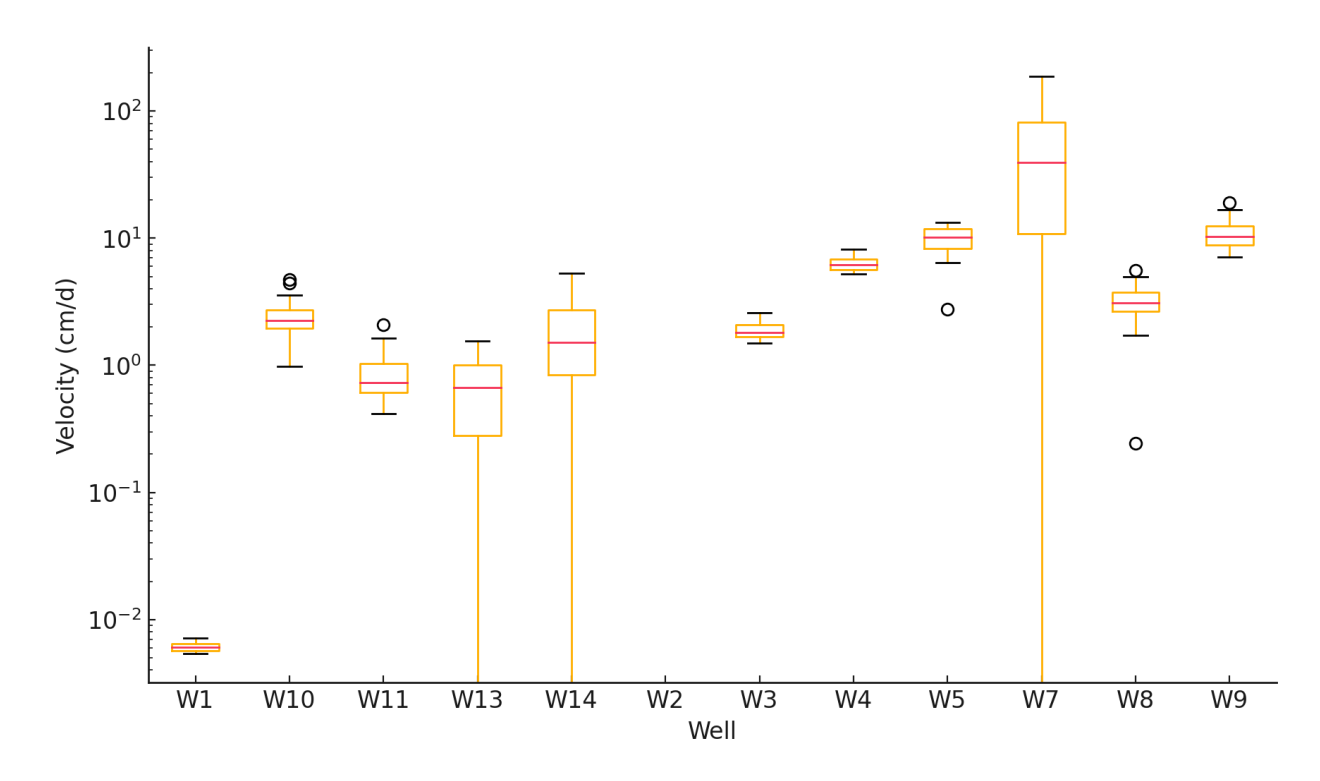


*Figure 3.12.* Groundwater discharge rates (velocity rates) across all locations corresponding to the monitoring wells in regions 3 and 4 (See Figure 2.1 for a location map).

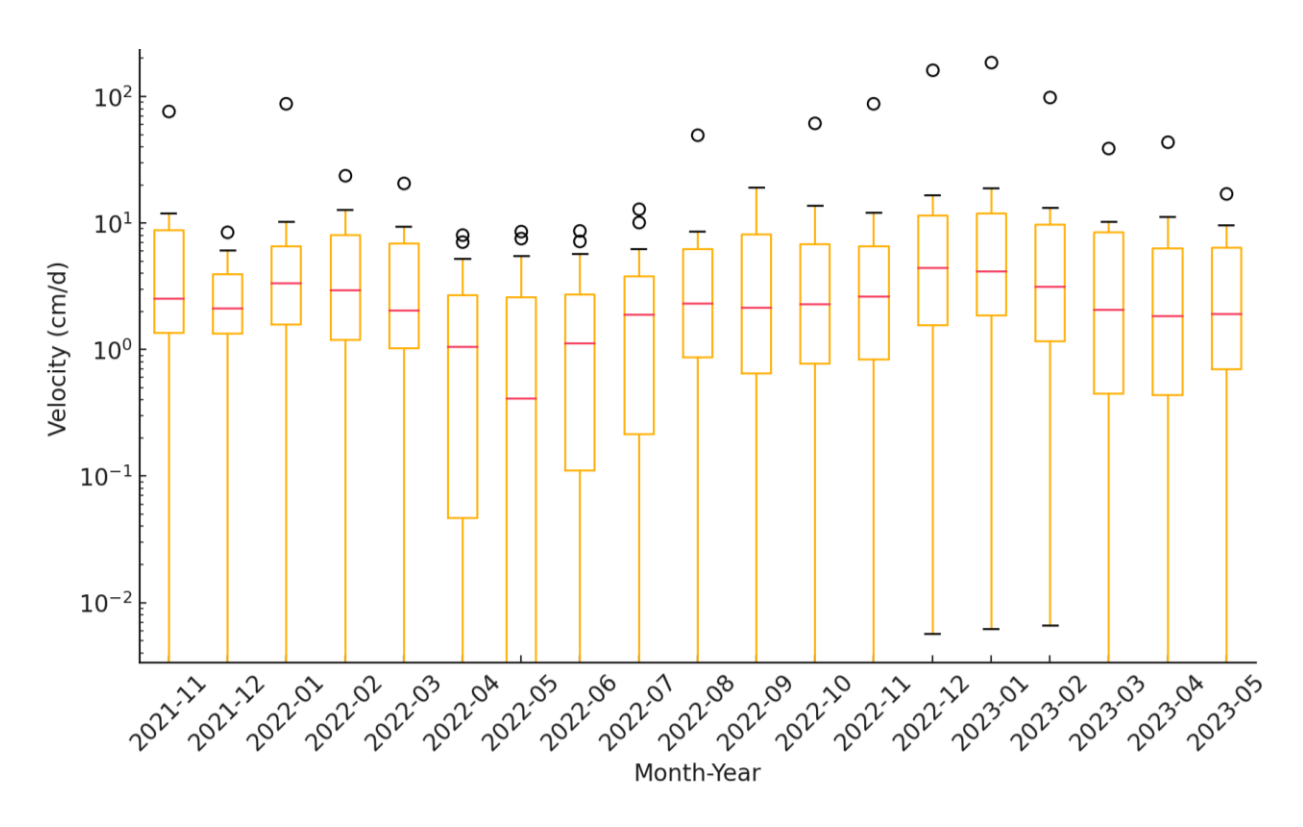


*Figure 3.13.* Groundwater discharge rates (velocity rates) across months correspond to the monitoring wells in regions 3 and 4 (See Figure 2.1 for a location map).

The variability in velocities among different wells highlights the differences between areas 3 and 4. For instance, while area 3 exhibited dynamic responses with high peaks near well 7, area 4 demonstrated more stable velocity patterns. The area near well 3 consistently displayed velocities between 1 and 3 cm/d, with no reverse gradients recorded, indicating localized aquifer stability. Similarly, the area near well 10 peaked at 3.5 cm/d, reflecting limited tidal influence and stable recharge conditions. These patterns correspond to area 4's lower but more consistent SGD rates, which peaked at 8.0 cm·d<sup>-1</sup> in January 2023 and reached a minimum of 2.4 cm·d<sup>-1</sup> in December 2021. The highest peak for area 4 was 8.0 cm·d<sup>-1</sup> in January 2023, the same time that area 3's peak of 36.2 cm·d<sup>-1</sup> was determined. For area 3, a similar peak was also reached in December 2022 of 31.6 cm·d<sup>-1</sup>.

The lowest rate for area 4 was reached in December 2021 with a rate of 2.4 cm·d<sup>-1</sup>, while for area 3, the lowest rate was determined to be in May 2022 with a rate of -8.5 cm·d<sup>-1</sup>. This negative rate from Darcy's Law indicates that some level of seawater intrusion is likely to have occurred as the sea level was higher than the groundwater elevation, causing seawater to intrude into the groundwater. The area near well 2 in area 3 further supports this observation, as reverse gradients were consistently recorded during November 2021, December 2021, and summer 2022, with velocities ranging from -1.4 cm/d to -0.6 cm/d. The swampy conditions and frequent flooding near this well, combined with tidal reversals, create conditions conducive to seawater intrusion.

Overall, area 4 has more consistent but lower SGD rates over the course of the study, while area 3 has more variable rates that reach much higher (**Figure 3.10**) but include times of

seawater intrusion. The seasonal velocity peaks in wells like 7 (area 3) and 5 highlight the dynamic aquifer response to recharge events, particularly during colder months when SGD rates are highest. Conversely, wells in area 4, such as 3 and 10, illustrate stable hydrological conditions contributing to its lower but steady discharge rates. These findings emphasize the contrasting hydrodynamic behaviors of the two areas and their influence on SGD (**Figure 3.10**).

#### 3.4.3.2 Radium-224 SGD rates

Results from the <sup>224</sup>Ra mass balance using the well/shallow groundwater activities as the source/end member show significant spatial and temporal variability in SGD rates (**Figure 3.14**). Shallow groundwater-derived SGD consistently shows the highest rates in region 4, with a peak of 769 cm/day in March 2022. This extremely high discharge rate could be related to a hydrological event, such as seasonal aquifer recharge associated with high rain amounts, which is characteristic of the area in the spring, which elevates water tables and regional groundwater levels, enhancing groundwater discharge towards the Gulf. Another major peak occurred in June 2022 (653 cm/day), further underscoring the dominance of region 4 in large-scale groundwater discharge dynamics. Sustained moderate rates were also observed during January 2023 (345 cm/day) and April 2023 (415 cm/day).

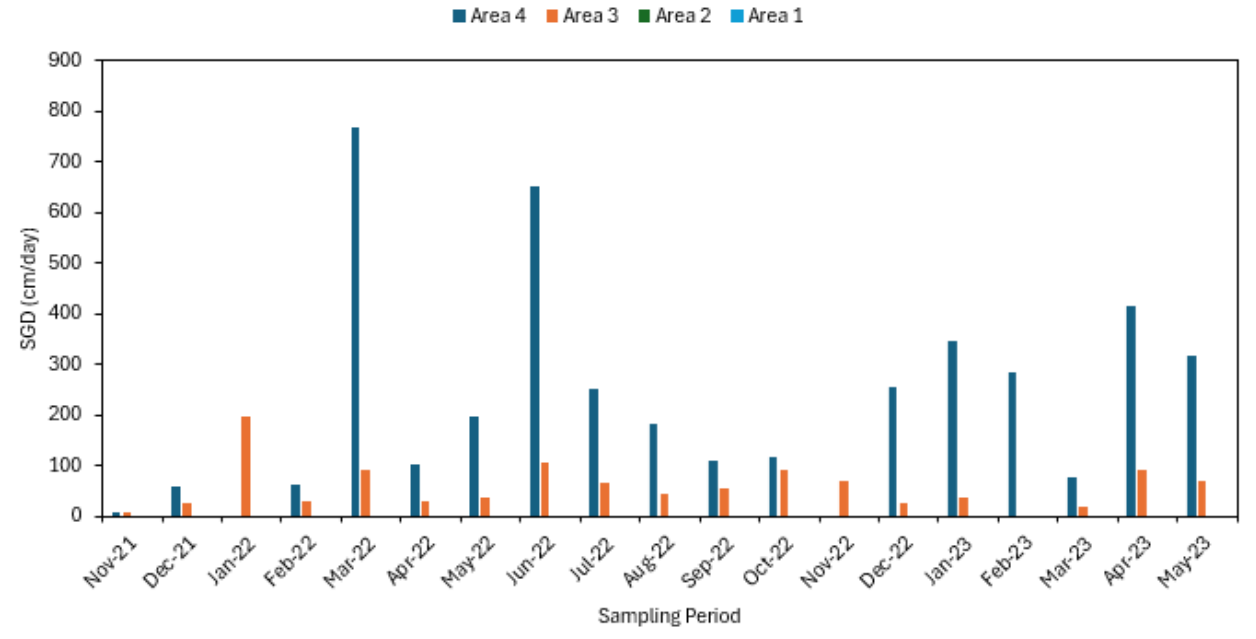


**Figure 3.14.** Radium-224 derived SGD rates using the shallow groundwater/water table as the source/endmember.

In region 3, SGD rates were notably lower than in region 4 but still exhibited important seasonal contributions. The highest rate in this region was recorded in January 2022 (198 cm/day), followed by smaller peaks in March 2022 (93 cm/day) and June 2022 (108 cm/day). These rates indicate sporadic contributions to SGD from region 3, with lower magnitudes than region 4. Groundwater was not monitored in regions 1 and 2. Thus, SGD rates calculated using this endmember are not available.

The SGD results using the porewater endmember reveal a different pattern of SGD compared to those derived using the water table/shallow groundwater endmember, with lower overall values and significant contributions from different areas at specific times (**Figure 3.15**). When using porewater as the endmember, the highest SGD rates were observed in region 1, with a peak value of 232 cm/day in May 2023, marking the largest discharge magnitude for this endmember across all regions and months. Additional elevated rates were noted in July 2022 (141 cm/day) and January 2023 (61 cm/day), reflecting localized benthic flux contributions during these periods. This suggests that region 1, though not validated using the shallow groundwater inputs via water table monitoring, plays a significant role when considering porewater fluxes.

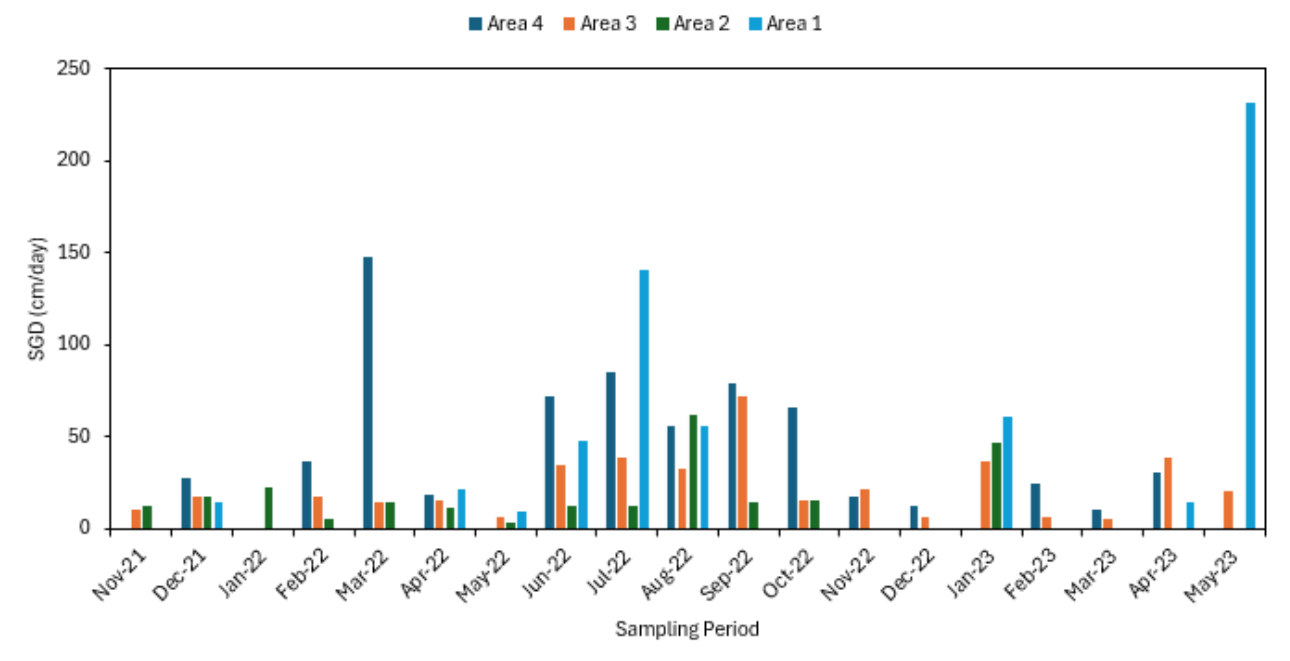


*Figure 3.15.* Radium-224 derived SGD rates using the porewater as the source/endmember.

Region 4 continued to show moderate but consistent SGD contributions with this endmember, with its highest rate recorded in March 2022 (147 cm/day), with other notable peaks in July (85 cm/day) and September 2022 (80 cm/day). However, these values are considerably lower than those observed when using the shallow groundwater endmember, indicating that the terrestrial freshwater inputs are likely higher than the recirculated counterparts. It is also possible that more enriched 224Ra groundwater inputs enter in the nearshore Gulf of Mexico waters rather than mixing in the water table aquifer of the barrier islands. In region 3, porewater-derived SGD exhibited intermittent activity, with peaks of 72 cm/day in September 2022 and 39 cm/day in July 2022. Unlike the shallow groundwater-derived SGD, no significant contributions were observed in March or June 2022, suggesting that SGD processes in this region may be more influenced by localized groundwater/terrestrial inputs rather than benthic interactions. Region 2 displayed sporadic and low-magnitude SGD, with peaks in August 2022 (62 cm/day) and January 2023 (47 cm/day), showing minor contributions relative to other regions.

The comparison between the two endmembers highlights key differences in the source and spatial dynamics of SGD. Region 4 dominated shallow groundwater-derived SGD rates, with discharge values exceeding 700 cm/day during critical months like March and June 2022. In

contrast, lower porewater-derived SGD rates like those in the same region, peaking at 147 cm/day, suggest that deeper groundwater flow pathways are more active in this area. Conversely, region 1 is a dominant contributor from benthic or recirculated sources when using porewater as the endmember, particularly in May 2023, with the highest recorded discharge of 232 cm/day. The absence of overlapping peaks in certain regions and months, such as the lack of porewater-derived SGD peaks in March and July 2022 in region 4, indicates distinct hydrological processes governing discharge patterns. Shallow groundwater-derived SGD reflects aquifer/terrestrial groundwater discharge, while porewater-derived SGD emphasizes more localized fluxes influenced by benthic and sediment interactions (e.g., recirculation).

#### 3.4.3.2 *Radium-223 SGD rates*

Results from the <sup>223</sup>Ra mass balance using the well/shallow groundwater activities as the source/end member show significant spatial and temporal variability in SGD rates (**Figure 3.16**). Shallow groundwater-derived SGD consistently shows the highest rates in region 4, with a peak of 769 cm/day in March 2022. This extremely high discharge rate could be related to a hydrological event, such as seasonal aquifer recharge associated with high rain amounts, which is characteristic of the area in the spring, which elevates water tables and regional groundwater levels, enhancing groundwater discharge towards the Gulf. Another major peak occurred in June 2022 (653 cm/day), further underscoring the dominance of region 4 in large-scale groundwater discharge dynamics. Sustained moderate rates were also observed during January 2023 (345 cm/day) and April 2023 (415 cm/day). In region 3, SGD rates were notably lower than in region 4 but still exhibited important seasonal contributions. The highest rate in this region was recorded in January 2022 (198 cm/day), followed by smaller peaks in March 2022 (93 cm/day) and June 2022 (108 cm/day). These rates indicate sporadic contributions to SGD from region 3, with lower magnitudes than region 4. Groundwater was not monitored in regions 1 and 2. Thus, SGD rates calculated using this endmember are not available.

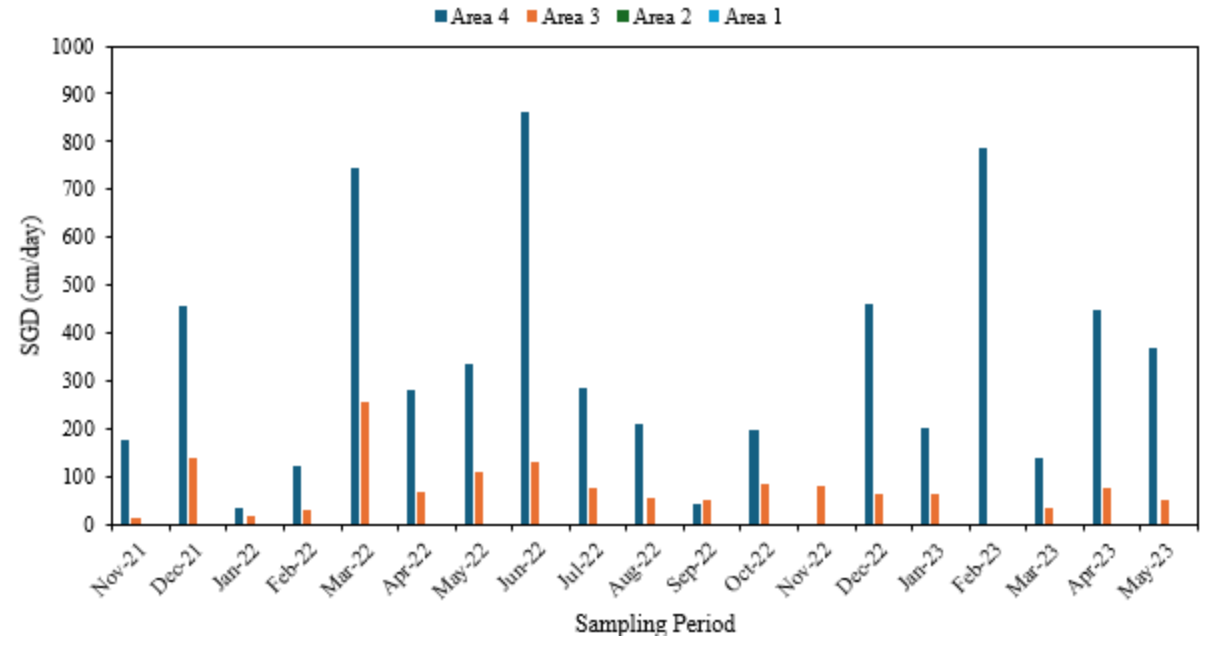


*Figure 3.16.* Radium-223 derived SGD rates using the shallow groundwater/water table as the source/endmember.

The SGD results using the porewater endmember reveal a different pattern of SGD compared to those derived using the water table/shallow groundwater endmember, with lower overall values and significant contributions from different areas at specific times (**Figure 3.17**). When using porewater as the endmember, the highest SGD rates were observed in region 1, with a peak discharge rate of 232 cm/day in May 2023, marking the largest discharge magnitude for this endmember across all regions and months. Additional elevated rates were noted in July 2022 (141 cm/day) and January 2023 (61 cm/day), reflecting localized benthic flux contributions during these periods. This suggests that region 1, though not validated using the shallow groundwater inputs via water table monitoring, plays a significant role when considering porewater fluxes.

Region 4 continued to show moderate but consistent SGD contributions with this endmember, with its highest rate recorded in March 2022 (147 cm/day), with other notable peaks in July (85 cm/day) and September 2022 (80 cm/day). However, these values are considerably lower than those observed when using the shallow groundwater endmember, indicating that the terrestrial freshwater inputs are likely higher than the recirculated counterparts. It is also possible that more enriched 224Ra groundwater inputs enter in the nearshore Gulf of Mexico waters rather than mixing in the water table aquifer of the barrier islands. In region 3, porewater-derived SGD exhibited intermittent activity, with peaks of 72 cm/day in September 2022 and 39 cm/day in July 2022. Unlike the shallow groundwater-derived SGD, no significant contributions were observed in March or June 2022, suggesting that SGD processes in this region may be more influenced by localized groundwater/terrestrial inputs rather than benthic interactions. Region 2 displayed sporadic and low-magnitude SGD, with peaks in August 2022 (62 cm/day) and January 2023 (47 cm/day), showing minor contributions relative to other regions.

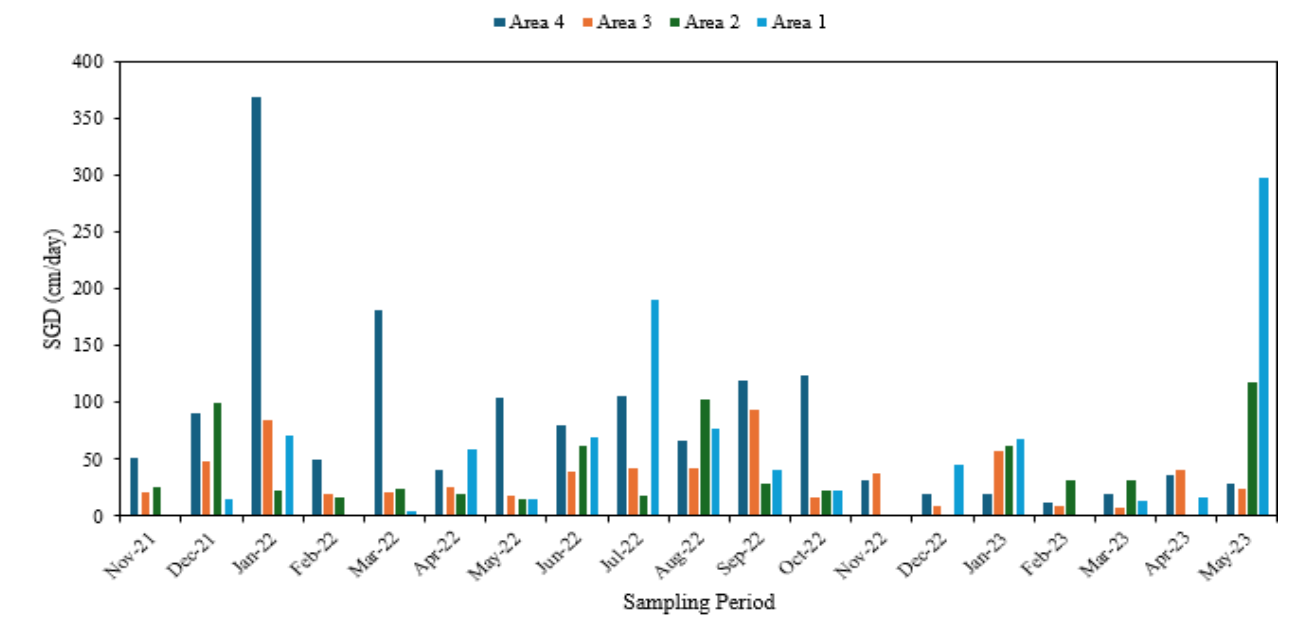


*Figure 3.17.* Radium-223 derived SGD rates using the porewater as the source/endmember.

The comparison between the two endmembers highlights key differences in the source and spatial dynamics of SGD. Region 4 dominated shallow groundwater-derived SGD rates, with discharge values exceeding 700 cm/day during critical months like March and June 2022. In contrast, lower porewater-derived SGD rates like those in the same region, peaking at 147 cm/day, suggest that deeper groundwater flow pathways are more active in this area. Conversely, region 1 is a dominant contributor from benthic or recirculated sources when using porewater as the endmember, particularly in May 2023, with the highest recorded discharge of 232 cm/day. The absence of overlapping peaks in certain regions and months, such as the lack of porewater-derived SGD peaks in March and July 2022 in region 4, indicates distinct hydrological processes governing discharge patterns. Shallow groundwater-derived SGD reflects aquifer/terrestrial groundwater discharge, while porewater-derived SGD emphasizes more localized fluxes influenced by benthic and sediment interactions (e.g., recirculation).

# 3.4.3.3 Radium-226 SGD rates

The analysis of SGD rates derived from <sup>226</sup>Ra reveals notable spatial and temporal variability when using porewater and combined porewater/shallow groundwater averages as endmembers (**Figure 3.18** and **Figure 3.19**). The results emphasize significant discharge contributions in specific regions and time periods.

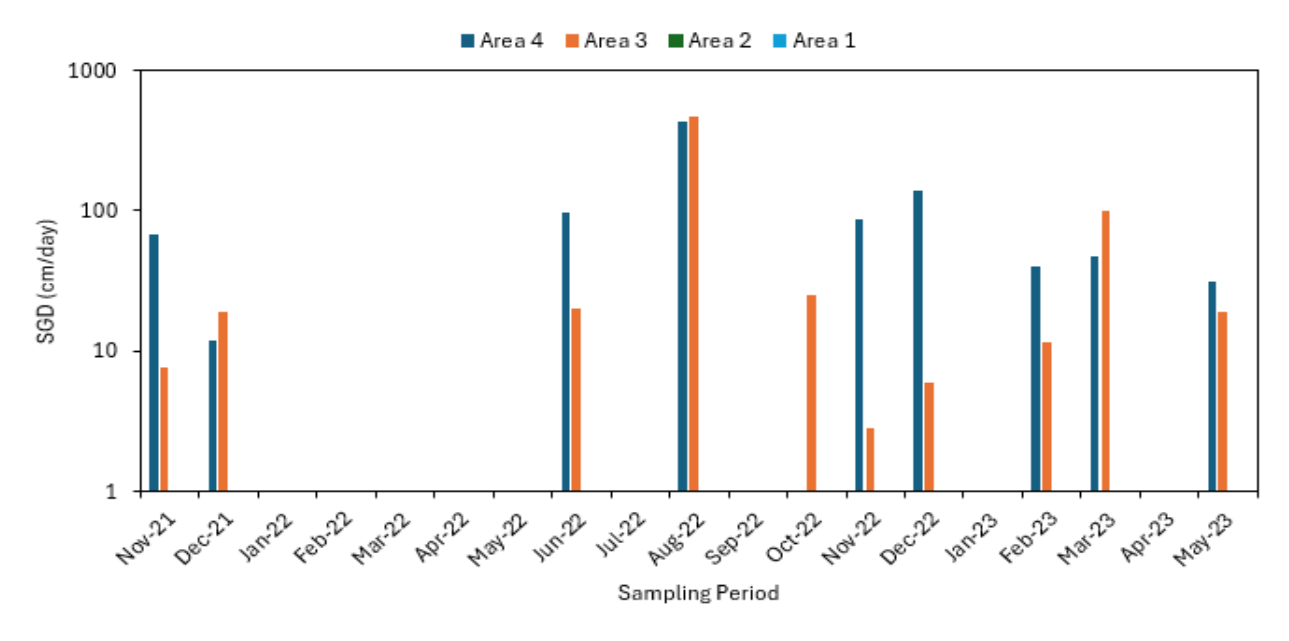


*Figure 3.18.* Radium-226 derived SGD rates using the shallow groundwater/water table as the source/endmember.

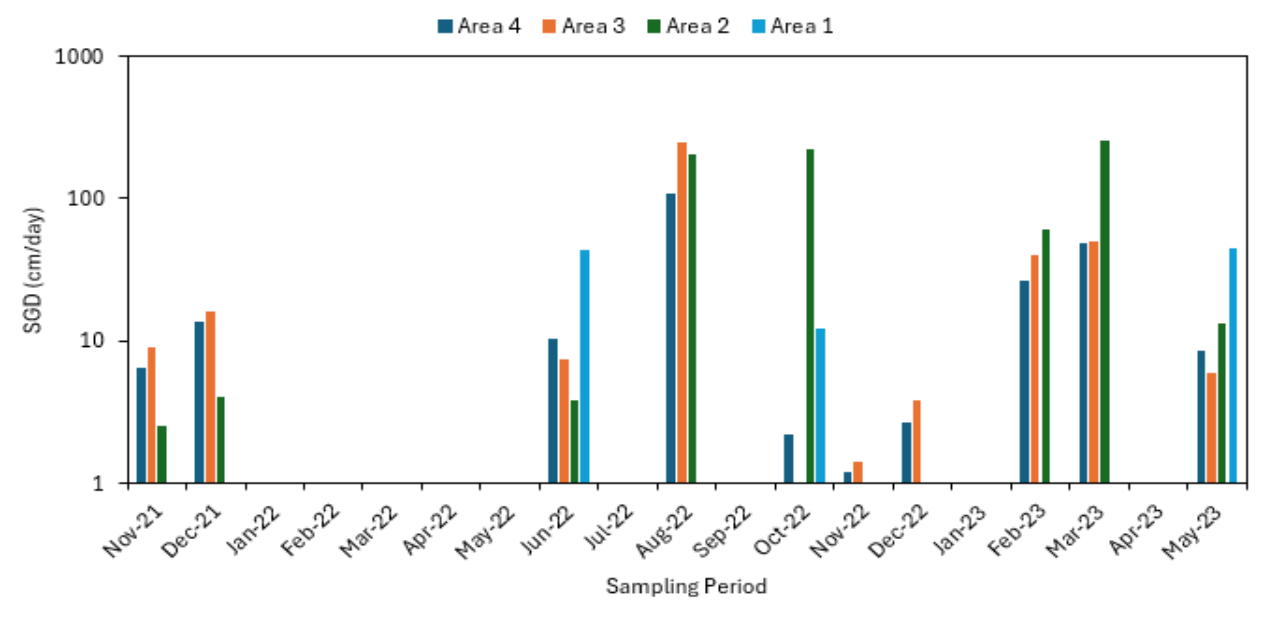


*Figure 3.19.* Radium-224 derived SGD rates using the porewater as the source/endmember.

The highest <sup>226</sup>Ra-derived SGD rate using porewater was observed in region 2, with a peak of 257 cm/day in March 2023. This high magnitude indicates a significant discharge event, possibly driven by seasonal hydrological heights, as explained in the <sup>226</sup>Ra results section. Other notable peaks include region 3, where SGD reached 246 cm/day in August 2022, suggesting high activity during late summer. Using porewater <sup>226</sup>Ra activities as the source of surface water, SGD rates were moderate in region 4, with a maximum of 108 cm/day in August 2023. This region showed consistent, though lower, contributions throughout the study period. Region 1 exhibited the lowest SGD rates overall, with a peak of 45 cm/day in May 2023, reflecting localized and smaller-scale discharge processes compared to other regions.

When considering porewater and shallow groundwater averages, region 3 displayed the highest SGD rate of 269 cm/day in August 2022, aligning with the peak observed in porewater during the same month. This indicates a strong convergence of discharge processes in this region during late summer. Region 4 followed closely with a peak of 266 cm/day in August 2022, suggesting substantial SGD contributions influenced by both shallow groundwater and recirculated/benthic sources. Region 2 showed a tendency for intermittent and elevated discharge events based on porewater-derived SGD rates. Regions 2 and 3 show the highest SGD rates, particularly in August 2022 (region 3) and March 2023 (region 2). These months reflect critical periods of high discharge, likely tied to seasonal aquifer recharge or enhanced SGD pathways. Region 4, on the other hand, has consistently moderate SGD rates, with sustained activity observed during months such as January 2023 and August 2022. While its peaks were lower than those in regions 2 and 3, region 4 remained a stable source of groundwater discharge over time. Region 1 exhibited the lowest overall discharge rates, with occasional peaks such as in May 2023 (45 cm/day), emphasizing its limited but localized benthic/recirculated fluxes compared to the other regions. The use of combined porewater/shallow groundwater averages highlights August 2022 as a key period of SGD activity in regions 3 and 4, with values exceeding 265 cm/day. In contrast, porewater-derived SGD underscores March 2023 (region 2) and August 2022 (region 3) as critical discharge events. While region 4 exhibited consistent discharge across both methods, regions 1 and 2 showed intermittent contributions, depending on the endmember used. These findings emphasize the importance of regional and temporal dynamics in SGD processes, with specific regions like 2 and 3 playing dominant roles during high-activity periods. The choice of endmember—porewater or combined averages—significantly influences the interpretation of discharge patterns.

## 3.4.4. Groundwater level prediction: model development and evaluation

Predicting groundwater levels is critical for managing water resources, mitigating environmental risks, and ensuring infrastructure integrity. Fluctuations in groundwater levels can significantly impact environmental systems and public health. For instance, rapid changes in groundwater levels may lead to groundwater contamination, especially when these changes reach buried infrastructure such as pipelines, septic systems, or utility corridors. This can facilitate the spread of bacteria and other contaminants, increasing the risk of waterborne diseases and ecological damage. XGBoost emerged as the best-performing model, demonstrating its robustness and adaptability to the complex, multivariate dataset. and **Figure 3.21** present the line charts for the model developed to predict groundwater levels in areas 3 and 4. Notably, in this study, we incorporated various latent variables that do not directly correlate with groundwater levels. Despite this, the performance of the model remains acceptable, with an RMSE of 0.061, R<sup>2</sup> value of 0.93, and an MAE of 0.04 for area 3, as well as an RMSE of 0.05, R<sup>2</sup> value of 0.97, and an MAE of 0.03 for area 4, which demonstrates the model's robustness and predictive capability.

The model successfully captures the overall trend and changes in groundwater levels, even when considering factors that indirectly influence them. This indicates that the model generalizes well to unseen data and provides reliable predictions for future groundwater level variations. Such predictive accuracy is essential for proactive water management and minimizing risks associated with fluctuating groundwater levels, including bacterial contamination and potential harm to buried infrastructure.

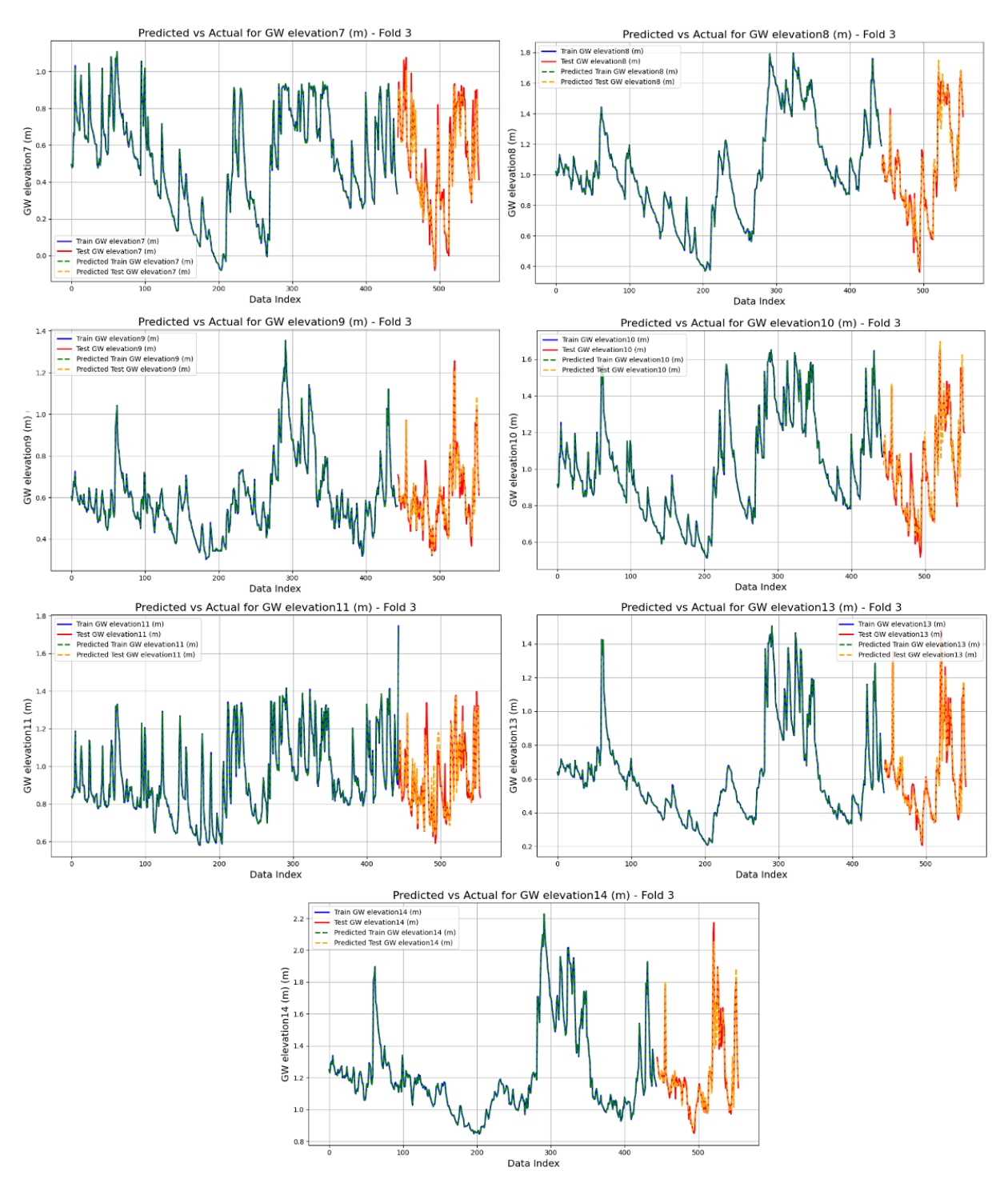


*Figure 3.20.* Performance of the Groundwater Level Prediction Model for Wells 7, 8, 9, 10, 11, and 13 (Area 3).

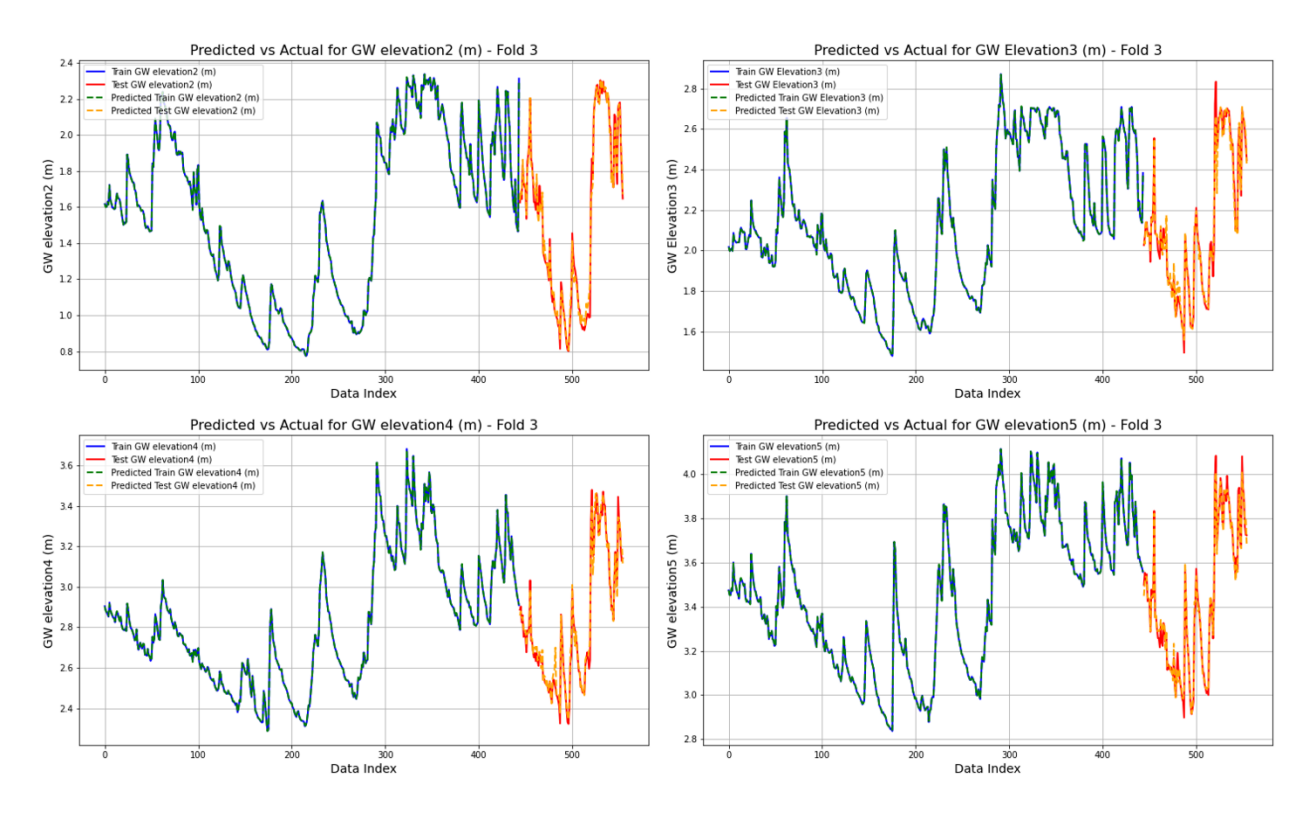


*Figure 3.21.* Performance of the Groundwater Level Prediction Model for Wells 2, 3, 4, and 5 (Area 4).

In this research, feature importance was computed to understand how different environmental and hydrological factors influence groundwater levels at various wells. The model used to predict groundwater levels (e.g., XGBoost) provided feature importance scores that helped to identify which factors are most influential at each groundwater monitoring location. As shown in **Figure 3.22**, groundwater levels in the Well 7 area are strongly influenced by streamflow, rainfall, and soil moisture. These factors play a particularly significant role during heavy rain and tidal fluctuations when their combined effects on water recharge and groundwater levels are most pronounced. In contrast, well 11 shows a higher sensitivity to rainfall and soil moisture, with smaller contributions from tide and streamflow. The results indicate that the shallow groundwater levels at different locations are influenced by distinct environmental conditions. By identifying the key factors that influence each well, predictions can be made more efficiently and accurately, ultimately saving time and resources. These findings highlight the importance of considering local environmental and hydrological factors when developing predictive groundwater-level models.

Due to the heterogeneity and complexity of dynamic processes in groundwater systems, suitable methods are essential for accurately capturing their temporal and spatial variations. While numerous techniques have been explored to quantify groundwater variations across temporal and spatial scales, each with its own strengths and limitations, this study introduces a data-driven predictive model to predict daily regional groundwater levels in distinct watersheds. The study area was divided into four distinct locations based on their watersheds. This approach allowed the developed model to capture the unique characteristics of each region, which improved the accuracy of groundwater level predictions. By taking into account localized

hydrological variations and site-specific factors, the model provided more reliable results, which can help tailor management strategies to the specific characteristics of an area. Temporal variability in groundwater is primarily driven by hydro-meteorological conditions, as demonstrated in previous studies (Chang et al., 2016). Our analysis shows that the proposed advanced machine learning model could capture temporal-spatial variations and provide reliable predictions for the given dataset, demonstrating high correlation coefficients and low RMSE values.

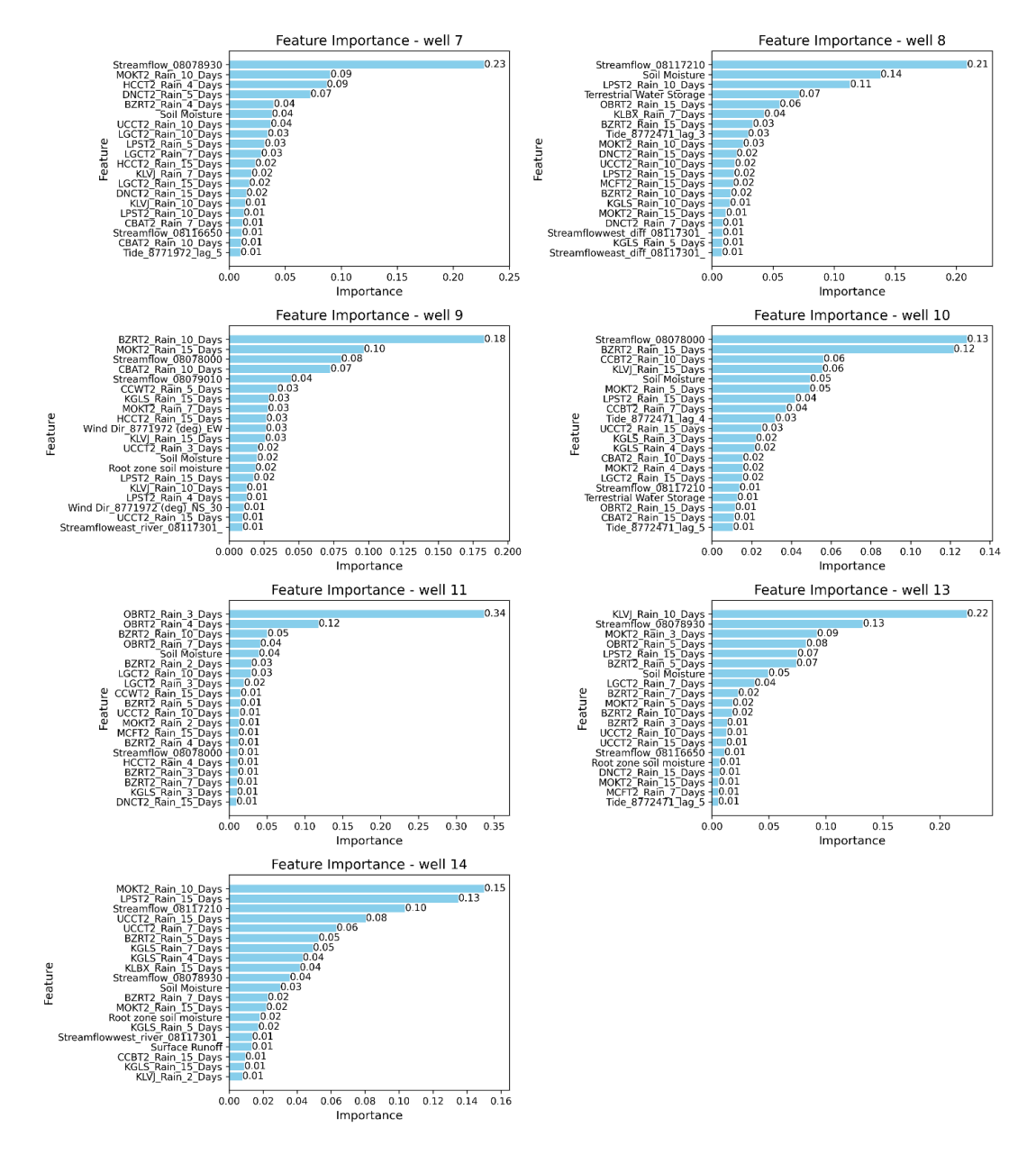


**Figure 3.22.** Feature importance for area 3: the top 20 most important features based on the weight metric for predicting groundwater elevation at multiple wells. Each subplot corresponds to one well, with features ordered by their contribution to reduce the model's error. Bars represent the importance of each feature, and values on the bars indicate their relative importance score.

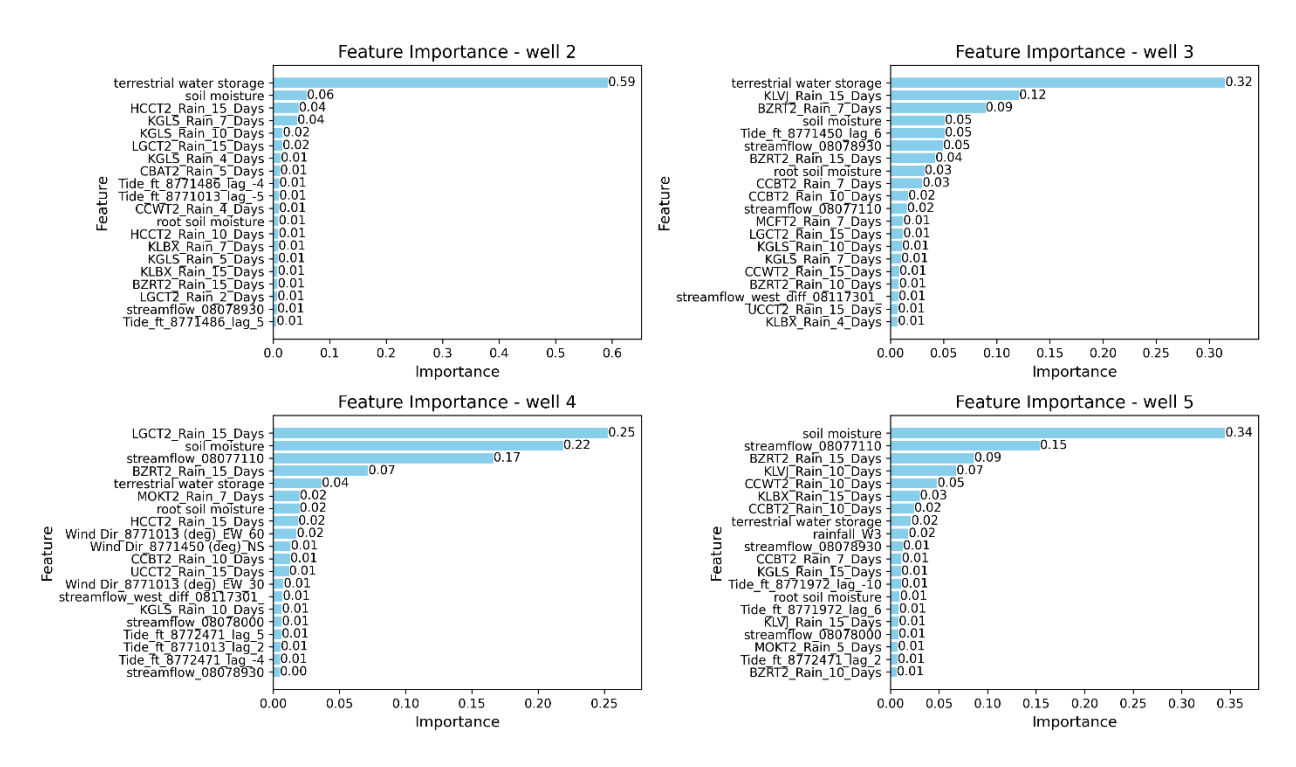


**Figure 3.23.** Feature importance for area 4: the top 20 most important features based on the weight metric for predicting groundwater elevation at multiple wells. Each subplot corresponds to one well, with features ordered by their contribution to reduce the model's error. Bars represent the importance of each feature, and values on the bars indicate their relative importance score.

The model assigns importance scores to various factors based on how much they contribute to predicting groundwater elevation. Areas 3 and 4 are located in Watershed 11 (**Figure 3.24**) Area 3, which includes wells 7, 8, 9, 10, 11, 13, and 14, is influenced by factors such as streamflow and soil moisture. In contrast, Area 4, which includes wells 2, 3, 4, and 5, is primarily affected by terrestrial water storage and rainfall. The following presents a detailed description of the factors correlated with groundwater elevation in each well, as indicated by the model results:

Well #2: Average territorial water storage holds the highest significance with a score of 0.59, followed by average soil moisture at 0.06. Other key factors include cumulative rainfall from station HCCT2 over 15 days (0.04), and from station KGLS (**Figure 3.24**) over 7 days (0.04), as well as combined cumulative rainfall from KGLS and LGCT2 over 10 and 15 days, respectively (0.02). Additionally, tidal influences at stations 8771486 with lags of -4 and 5 days, and 8771013 with lags of -5 and 4 days, along with cumulative rainfall from KGLS station over 5 days, CBAT2 rainfall station over 5 days, average root soil moisture for the area 4, and streamflow at station 08078930, all show a contribution of 0.01 in the model (**Figure 3.23**). This demonstrates that the model can uncover latent variables, allowing for a deeper understanding and accurate prediction of groundwater elevation. Well #3: Average territorial water storage holds the highest significance with a score of 0.32, followed by the KLVJ rainfall station with 15-day cumulated rainfall (0.12), and BZRT2 rainfall with 7-day cumulated rainfall (0.09). Additionally, average soil moisture, tidal influence at station 8771450 with a lag of 6 days,

streamflow at station 08078930, all have an importance score of 0.05. Rainfall from BZRT2 station with 15-day cumulated rainfall (0.04), average root soil moisture, and rainfall from CCBT2 station for 7 days contribute 0.03. Streamflow at station 08077110 also holds a score of 0.02. Other key factors, as shown in **Figure 3.23**, have an importance score around 0.01 in the model.

Well #4: The highest significance is held by the LGCT2 rainfall station with a 15-day cumulative value (0.25), followed by average soil moisture (0.22), and streamflow at station 08077110 (0.17). Factors include BZRT2 rainfall station with a 15-day cumulative value and average territorial water storage, showing scores of 0.07 and 0.04, respectively. MOKT2 rainfall station with a 7-day cumulative value, average root soil moisture, and HCCT2 with a 15-day cumulative value, wind direction at station 8771013 (EW\_60) all contributing 0.02. Additionally, tidal influences at stations 8772471, 8771013 with lag times along with streamflow at station 08117301, all have an importance score of 0.01.

Well #5: The highest significance is held by average soil moisture for the area 4 (0.34), followed by streamflow at station 08077110 (0.15). Other key factors include BZRT2 rainfall station with a 15-day cumulative value (0.09), KLVJ rainfall station with a 10-day cumulative value (0.07), CCWT2 with a 10-day cumulative value (0.05), and KLBX rainfall station with a 15-day cumulative value (0.03). Additionally, MRMS rainfall located in Well 3, average territorial water storage, and CCBT2 rainfall station with a 10-day cumulative value, all show a contribution of 0.02. Other factors, such as streamflow at station 08078930, average root soil moisture, and tidal influences at station 8772471, have values less than 0.01.

Well #7: Streamflow at station 08078930 has the highest significance with a score of 0.23. MOKT2 rainfall station for 10 days and HCCT2 rainfall station for 4 days are both 0.09, followed by DNCT2 rainfall station for 5 days at 0.07. Average soil moisture, BZRT2 rainfall for 4 days, and UCCT2 rainfall for 10 days are all 0.04. Additionally, LGCT2 for 10 days, LPST2 for 5 days, and LGCT2 for 7 days contribute 0.03. HCCT2 rainfall for 15 days, KLVJ rainfall for 7 days, LGCT2 rainfall for 15 days, and DNCT2 rainfall for 15 days have a value of 0.02. Other factors, such as streamflow at station 08116650, other rainfall stations, and tide level at station 8771972 with a lag of 5 days, show 0.01.

Well #8: Streamflow at station 08117210 has the highest significance at 0.21, followed by average soil moisture at 0.14, and LPST2 rainfall for 10 days at 0.11. Other key factors include average terrestrial water storage (0.07), OBRT2 rainfall for 15 days (0.06), and KLBX rainfall for 7 days (0.04). Additionally, tide level at station 8772471 with a lag of 3 days contributes 0.03, while BZRT2 and MOKT2 with 15-day and 10-day accumulations, respectively, both show a value of 0.03. MOKT2, UCCT2, and BZRT2 all with 10-day accumulations, along with DNCT2, LPST2, and MCFT2 with 15-day accumulations, are all 0.02.

Well #9: BZRT2 rainfall station for 10 days has the highest significance at 0.08, followed by MOKT2 rainfall station for 15 days at 0.10, and streamflow at station 08078000 at 0.08. Other key factors include CBAT2 rainfall station for 10 days (0.07), streamflow at station 08079010 (0.04), and CCWT2 rainfall station for 5 days, KGLS rainfall station for 15 days, MOKT2 rainfall station for 7 days, HCCT2 rainfall station for 15 days, KLVJ rainfall station for 15 days, and wind direction at station 8771972 (EW) all contributing 0.03. Additionally, average soil moisture and average root zone soil moisture both show a value of 0.02. Other factors, such

as wind direction at station 8771972 (NS-30) and streamflow at East River station 08117301, along with other factors, are 0.01 or less.

Well #10: Streamflow at station 08078000 has the highest significance at 0.13, followed by BZRT2 rainfall for 15 days at 0.12. Other key factors include CCBT2 rainfall with a 10-day cumulative value (0.06), and KLVJ rainfall for 15 days (0.06). Additionally, average soil moisture and MOKT2 rainfall for 5-day accumulative values are both 0.05, while LPST2 rainfall for 15 days and CCBT2 for 7 days contribute 0.04. Tide level at station 8772471 with a lag of 4 days is 0.03, and UCCT2 rainfall for 15 days is 0.03. Furthermore, KGLS rainfall for 3 days and 4 days, CBAT2 for 10 days, MOKT2 for 4 days, and LGCT2 for 15 days are all 0.02. Other factors, such as average terrestrial storage, streamflow at station 08117210, tide level at 8772471 with a lag of 5 days, and other rainfall stations, are 0.01.

Well #11: Rainfall at OBRT2 station with a 3-day cumulative value is 0.34, and a 4-day cumulative value is 0.12. Rainfall at station BZRT2 for 10 days contributes 0.05, while average soil moisture and rainfall at OBRT2 station both show values of 0.04. Additionally, rainfall at BZRT2 and LGCT2 stations with 2-day and 10-day accumulative values, respectively, are both 0.03, and LGCT2 rainfall for 3 days is 0.02. Other rainfall stations and streamflow at station 08078000 have values 0.01.

Well #13: KLVJ rainfall station with a 10-day cumulative value is 0.22, followed by streamflow at station 08078930 (0.13). Rainfall from MOKT2 for 3 days, OBRT2 for 5 days, LPST2 for 15 days, and BZRT2 for 5 days contribute 0.09, 0.08, 0.07, and 0.07, respectively. Average soil moisture shows a value of 0.05, while LGCT2 rainfall station for 7 days is 0.04. Additionally, BZRT2, MOKT2, and BZRT2 rainfall stations with 7-day, 5-day, and 10-day cumulative values are 0.02. Other factors show values of 0.01 or less.

Well #14: MOKT2 rainfall for 10 days has the highest significance at 0.15, followed by LPST2 rainfall for 15 days at 0.13. Streamflow at station 08117210 contributes 0.10, and UCCT2 rainfall for 15 days and 7 days shows values of 0.08 and 0.06, respectively. BZRT2 rainfall for 5 days and KGLS rainfall for 7 days are both 0.05. Additionally, KGLS for 4 days, KLBX rainfall for 15 days, and streamflow at station 08078930 are 0.04. Average soil moisture contributes 0.03, while BZRT2 rainfall for 7 days, MOKT2 rainfall for 15 days, average root zone soil moisture, and KGLS rainfall for 5 days are all 0.02. Other factors, such as average surface runoff, streamflow at station 08117301, and other rainfall stations, show values of 0.01.

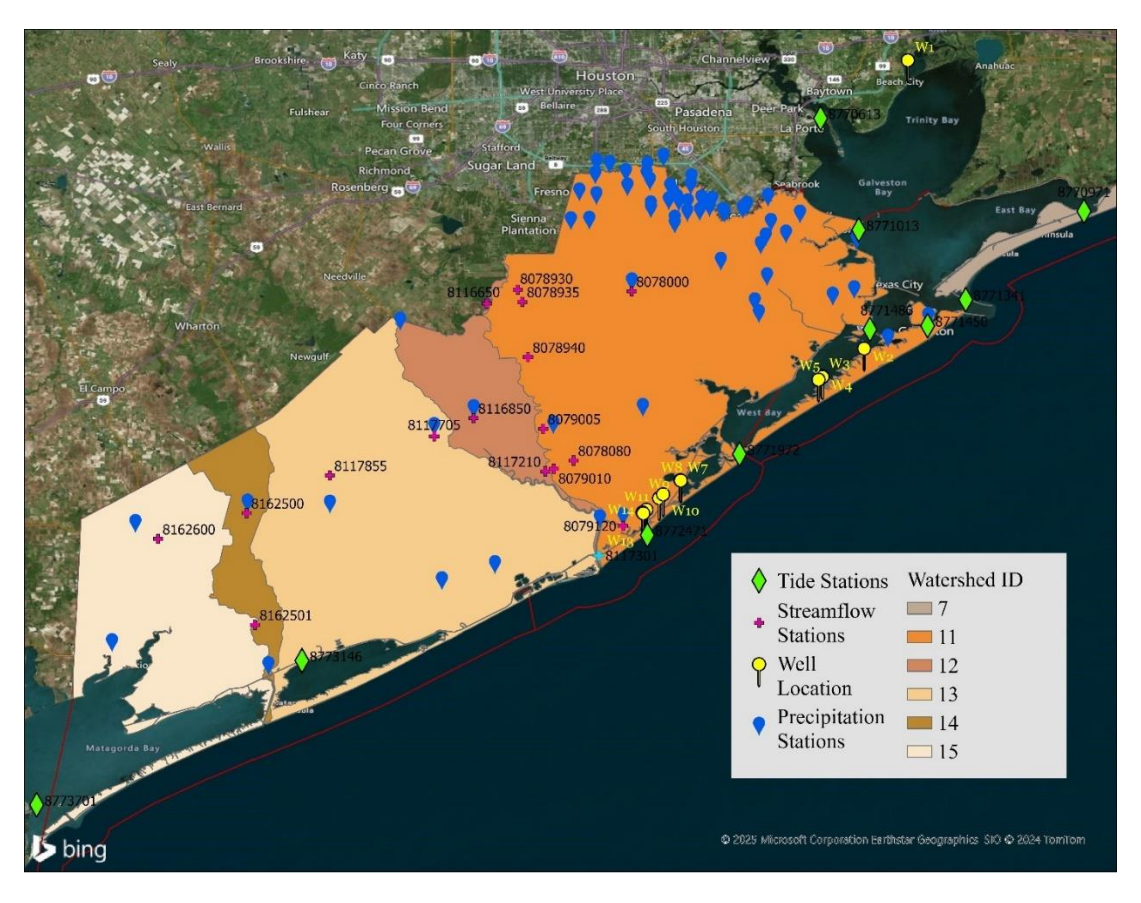


*Figure 3.24.* The spatial distribution of stations monitoring environmental factors within the study area.

According to **Figure 3.23**, Wells 4 and 5 are near Jamaica Beach, suggesting a stronger connection with the tidal and coastal hydrological processes. This is why more tidal stations are among the top 20 most important features. On the other hand, Wells 2 and 3 are located farther north and are likely shielded from direct tidal influences by land features. Area 4 is most significantly impacted by terrestrial water storage and rainfall. Variations in terrestrial water storage can directly influence groundwater levels and indirectly alter flood risk (Asoka and Mishra., 2020). Being closer to the coast, wells 4 and 5 are more influenced by surface hydrological factors like tidal fluctuations, direct rainfall, and streamflow. The higher importance of soil moisture and streamflow (**Figure 3.23**) indicates that groundwater at these locations is influenced by watershed hydrology including surface and near-surface processes. The high significance of soil moisture (0.22 for Well 4 and 0.34 for Well 5) and streamflow highlights the role of coastal surface processes. This is supported by rainfall contributions from nearby stations and the influence of tidal lags.

Located farther inland, groundwater in the areas near wells 2 and 3 is less affected by direct tidal or surface interactions. The dominance of terrestrial water storage reflects subsurface hydrological processes like groundwater recharge and storage within the watershed, which are more critical in areas farther from immediate surface water bodies. The importance of terrestrial water storage (scores of 0.59 and 0.32) aligns with their inland position, where recharge and subsurface flow govern groundwater dynamics.

Area 3 is primarily influenced by streamflow, with the highest importance placed on streamflow at station 08078930 in well 7 in Oyster Creek. Average soil moisture, rainfall, and tidal influences also play significant roles, with factors such as rainfall for 10 days (0.09) at station MOKT2 and streamflow at station 08117210 (0.21) contributing to groundwater elevation predictions. The model captures local hydrological processes, including variations in rainfall across different stations (BZRT2, MOKT2, LGCT2) and their cumulative effects over various time periods. For well #8, streamflow and soil moisture are significant due to potential lateral water movement and water retention capacity in the soil. The prominence of these factors suggests a linkage to groundwater recharge through these mechanisms. Well #9 is influenced by both recent rainfall and longer-term streamflow conditions. This implies a mix of immediate rainfall effects and the cumulative impact of water movement through the watershed affecting groundwater levels. Well #10 appears to be more influenced by streamflow and cumulative rainfall, with a strong dependence on both short-term and longer-term hydrological inputs. Well #11's top feature indicates a significant dependency on recent rainfall events, suggesting rapid groundwater recharge and vulnerability to immediate hydrological changes. Well #13's strong reliance on cumulative rainfall over 10 days, combined with streamflow, reflects its dependency on sustained terrestrial hydrological inputs over time. Well #14 demonstrates a balance between cumulative rainfall over 10 days and streamflow influences, with moderate contributions from soil moisture and tide levels.

The varying top features (**Figure 3.23** and **Figure 3.24**) across wells reflect differences in their hydrological sensitivities. Wells closer to Gulf or with a higher connectivity to surface water sources, like streamflow, show higher significance for immediate water inputs. Conversely, wells that integrate longer-term cumulative rainfall and soil moisture suggest a more prolonged hydrological response. These variations indicate distinct local hydrological conditions influencing groundwater levels, causing the differences in top features.

# 3.4.5. Depth to groundwater and implications for water table flooding and subsurface infrastructure damage

In area 3, which encompasses wells 2, 3, 4, and 5, depth-to-water (DTW) patterns over the observed period reveal significant seasonal variability (**Figure 3.25**). During late winter to early spring (e.g., early 2023), the DTW is generally lower, reflecting a water table closer to the ground surface, typically approaching 0 meters or less for Wells 4 and 5, increasing the likelihood of flooding. Conversely, in the summer months, the DTW increases, indicating a deeper water table farther below the ground surface. Among these wells, well 3 consistently exhibits the greatest DTW (deepest water table) throughout the monitoring period, with values regularly exceeding 1.5 to 2 meters, particularly during summer and decreasing starting with December 2022. This fluctuation highlights periods when the water table near well 3 is least likely to experience water table flooding, even during wetter seasons. Wells 4 and 5, located near the Gulf of Mexico dune system in the tidal zones, are more prone to flooding during high tide or

storm surges, especially during late winter and early spring when the water table is naturally higher.

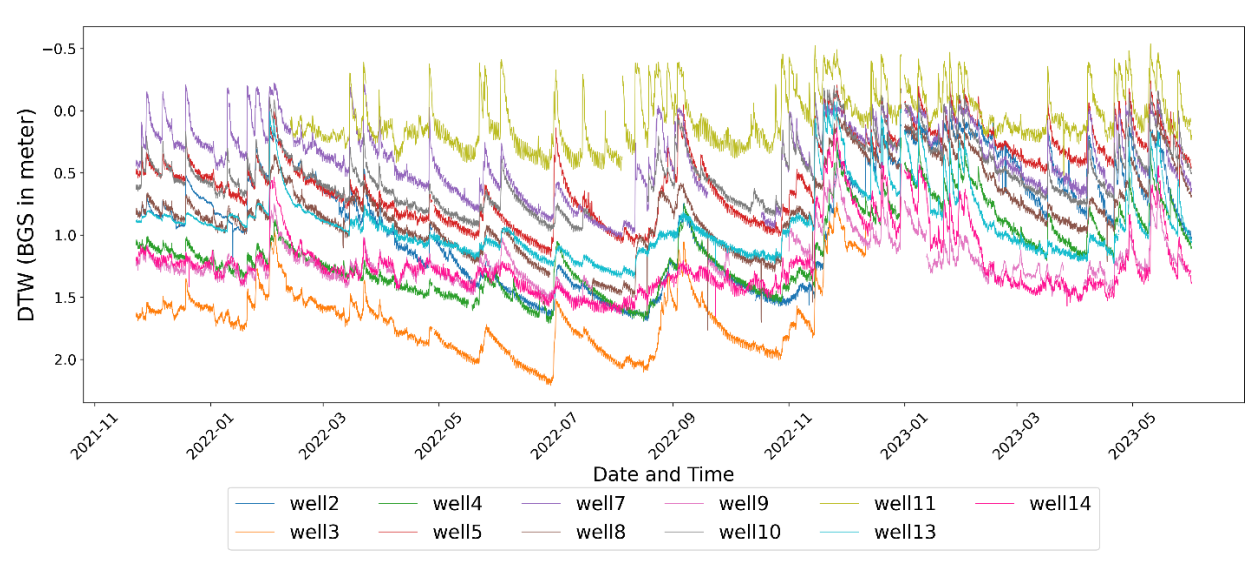


Figure 3.25. Depth to water continuous measurements in monitoring wells for areas 3 and 4 (see Figure 2.1 for geographic locations). The ground surface is the reference point at 0 meters).

In area 4, which includes wells 7, 8, 9, 10, 11, 13, and 14, a similar examination of DTW patterns reveals shallow water tables during late winter to early spring and deeper water tables during the summer months. Wells 7, 8, and 9 are particularly noteworthy, as their DTW values often approach or fall below 0.5 meters in late winter to early spring, indicating a high risk of water table flooding during recharge events or storms. Conversely, wells 10, 13, and 14 exhibit greater seasonal fluctuations, with DTW values dropping to between 1- and 1.5 meters during summer and rising closer to 0.5 meters in late winter and early spring. In particular, well 11 is consistently near or above the ground surface, with the highest and most frequent risk of flooding of underground infrastructure. The risk of water table flooding is most pronounced for wells 7 and 8 during late winter and early spring due to their persistently shallow DTW. In contrast, wells 10 and 13, despite generally deeper DTW, could experience localized flooding during heavy recharge events.

The susceptibility of septic systems and sewage lines to failure is an additional concern in both areas. In area 3, the area near wells 4 and 5, with DTW values below 1 meter during late winter and early spring, faces increased risks of water infiltration and contamination, particularly during heavy rainfall or tidal surges. The area near Well 3, with consistently deeper DTW values, poses the lowest risk for septic systems and sewage lines in this area. In area 4, Wells 7, 8, and 11 are at the highest risk for compromised septic systems and sewage lines due to their persistently shallow DTW values, often nearing or below 0.5 meters during late winter to early spring or storm surges. While Wells 14, 9 and 13 demonstrate deeper DTW values, suggesting lower susceptibility, localized recharge events during extreme conditions (e.g., late winter 2022-spring 2023) will likely compromise infrastructure performance.

#### 3.5. Discussion

## 3.5.1. Submarine groundwater discharge dynamics in barrier islands

The sediment characterization and hydrological data collected from the barrier islands in this study between Quintana Park and the Heritage Preserve provide critical insights into the spatial and temporal variability of groundwater behavior and its interaction with nearshore Gulf of Mexico waters. This section reveals the complex interplay between subsurface sediment makeup of the water table aquifer, groundwater discharge dynamics, and radium isotopes as tracers for SGD, shedding light on the processes influencing the shallow/water table aquifer systems in the barrier islands.

## Sediment Core Characteristics and Their Implications

The sediment cores reflect substantial variability in texture, composition, and moisture across the study area, highlighting distinct depositional environments shaping the barrier island shallow groundwater system. Sediments near the coastline, such as those at wells 7, 8, and 9, are dominated by coarser materials like sandy silt and gravel, indicative of higher depositional energy. These permeable layers facilitate significant groundwater movement, as evidenced by high Darcy velocities and SGD rates in these locations. In contrast, inland cores, such as well 1, exhibit fine-grained clay and silt layers with minimal sand content, which contribute to reduced permeability and slower groundwater movement. This sediment composition aligns with observed DTW patterns, as coastal wells (e.g., wells 7, 8, and 9) consistently exhibit shallow water tables during late winter and early spring, increasing risks of water table flooding. Conversely, inland wells, such as Well 3 in area 3, maintain deeper DTW values year-round, reducing their susceptibility to water table surges.

# Groundwater Dynamics and SGD Variability

The groundwater elevation data reveal clear spatial patterns and temporal variability, strongly influenced by hydrogeological and environmental conditions. Wells in areas 3 and 4 displayed distinct hydrodynamic behaviors:

Area 3: In area 3, which encompasses wells 2, 3, 4, and 5, DTW patterns over the observed period reveal significant seasonal variability (Figure 3.25). During late winter to early spring (e.g., early 2023), the DTW is generally lower, reflecting a water table closer to the ground surface, typically approaching 0 meters or less for Wells 4 and 5, increasing the likelihood of flooding. Conversely, in the summer months, the DTW increases, indicating a deeper water table farther below the ground surface. Among these wells, well 3 consistently exhibits the greatest DTW (deepest water table) throughout the monitoring period, with values regularly exceeding 1.5 to 2 meters, particularly during summer and decreasing starting with December 2022. This fluctuation highlights periods when the water table near well 3 is least likely to experience water table flooding, even during wetter seasons. wells 4 and 5, located near the Gulf of Mexico dune system in the tidal zones, are more prone to flooding during high tide or storm surges, especially during late winter and early spring when the water table is naturally higher. Additionally, wells in area 3, particularly near well 7, exhibited highly dynamic responses to seasonal recharge events. High groundwater velocities in winter months (e.g., 187

cm/day in January 2023) correspond to peaks in SGD rates, underscoring the influence of rainfall and aquifer recharge (as indicated by the streamflow predictive variable in the ML model results). Negative gradients recorded in warmer months reflect reduced groundwater flow toward the coast from the watershed, which facilitates seawater intrusion, a result of higher tides and lower groundwater elevations (Qiu et al., 2012; Saba et al., 2024). The strong correlation between streamflow and groundwater levels in area 3 highlights the regional connectivity between surface water and aquifer systems. The variability in sediment permeability in this area amplifies these dynamics, with sandy layers promoting rapid groundwater flow and discharge.

**Area 4**: In area 4, which includes wells 7, 8, 9, 10, 11, 13, and 14, a similar examination of DTW patterns reveals shallow water tables during late winter to early spring and deeper water tables during the summer months. Wells 7, 8, and 9 are particularly noteworthy, as their DTW values often approach or fall below 0.5 meters in late winter to early spring, indicating a high risk of water table flooding during recharge events or storms. Conversely, wells 10, 13, and 14 exhibit greater seasonal fluctuations, with DTW values dropping to between 1- and 1.5-meters during summer months and rising closer to 0.5 meters in late winter and early spring. In particular, well 11 is consistently near or above the ground surface, with the highest and most frequent risk of flooding of underground infrastructure. The risk of water table flooding is most pronounced for wells 7 and 8 during late winter and early spring due to their persistently shallow DTW, while wells 10 and 13, despite generally deeper DTW, could experience localized flooding during heavy recharge events. Groundwater in area 4 was more stable, with lower but consistent SGD rates compared to area 3. Sediments in this area are dominated by clay and silt, which reduce permeability and buffer against rapid fluctuations. Peaks in groundwater velocity (e.g., 8.0 cm/day in January 2023) align with seasonal recharge, although the magnitude of SGD rates remains lower due to the less permeable substrate.

#### Radium Isotope Insights into SGD Patterns

This study finds radium isotopes as a powerful tool for tracing SGD, revealing both seasonal and spatial variability in groundwater discharge processes along the nearshore Gulf of Mexico. For instance, <sup>224</sup>Ra activities in porewater were highest in areas with significant groundwater-surface water interactions, such as stations P14 and S5, where SGD fluxes were amplified by seasonal recharge events. Similarly, <sup>223</sup>Ra peaks in porewater (e.g., 1,706 Bq/m³ at P2) and surface water (e.g., 661 Bg/m<sup>3</sup> at S5) indicate localized sediment-water interactions and episodic SGD pulses. The temporal alignment of these peaks with Darcy velocity data confirms the role of hydrological events, such as heavy rainfall, local and distant aquifer recharge, and regional groundwater inputs nearshore or tidal forcing, in driving SGD dynamics. The long-lived isotope <sup>226</sup>Ra showed more stable patterns across the study area, with higher activities in porewater and groundwater during fall months (e.g., October 2022). which are also supported by Darcy's velocity estimates, which peak in the fall months. These peaks likely reflect sustained groundwater discharge from deeper aquifers, where prolonged residence times facilitate radium mobilization. The higher activities in region 3 during late summer further underscore the importance of seasonal recharge and aquifer flushing in this dynamic area and the potential for impacting nearshore water table dynamics.

Coastal areas near wells 4 and 5 in area 3 and wells 7, 8, and 11 in area 4 are particularly susceptible to the compounded effects of rainfall, tidal forcing, and aquifer recharge. These factors amplify groundwater discharge, posing potential risks of nutrient and contaminant transport into nearshore Gulf waters, as well as increasing risks to underground infrastructure such as septic systems and sewage lines. The high SGD rates in area 3 during colder months and the associated radium peaks indicate intense sediment-water interactions and nutrient fluxes, which could influence coastal ecosystems and the buried infrastructure. The potential for seawater intrusion during warmer months further emphasizes the need for monitoring and management strategies to protect freshwater resources and maintain the ecological balance of the Gulf of Mexico. The findings significantly advance the understanding of how water table patterns influence infrastructure vulnerability and SGD processes along the Texas barrier islands.

# 3.5.2. Groundwater levels predictive model

The analysis of groundwater predictors highlights the complex interplay between environmental and hydrological factors driving water table fluctuations in areas 3 and 4. These fluctuations are influenced by streamflow, rainfall, soil moisture, terrestrial water storage, and tidal dynamics, with each factor contributing uniquely based on the spatial and temporal characteristics of the groundwater systems in these areas (MDNR, 2020; Wei et al., 2024). This study demonstrates the importance of understanding these drivers to predict groundwater behavior and mitigate associated risks effectively. In area 4, terrestrial water storage emerged as the most significant predictor of groundwater levels, revealing the critical role of subsurface hydrological processes, particularly groundwater recharge and long-term water storage within the watershed. Based on the model results in this area, groundwater is largely shielded from the direct impacts of tidal and surface hydrology, resulting in more stable water table fluctuations. However, it remains vulnerable to prolonged upstream recharge events, where sustained rainfall and increases in aquifer storage can lead to gradual yet significant rises in water levels. This sensitivity to subsurface dynamics highlights the need for long-term monitoring and management strategies tailored to inland aquifers.

Coastal areas within the study, particularly those near wells 4 and 5 in area 4, exhibited a stronger connection to surface hydrological processes, including tidal influences, rainfall, and soil moisture. Groundwater in these regions is more susceptible to rapid fluctuations due to the proximity to tidal zones and the influence of near-surface hydrology (Wei et al., 2023). High soil moisture and lagged tidal effects suggest strong interactions between rainfall-driven recharge and tidal cycles. This dynamic interplay makes coastal groundwater systems particularly vulnerable during high tides or storm surges when water levels can rise quickly, increasing the risk of groundwater flooding and contamination from surface water or seawater intrusion (Allen et al., 2019). Effective coastal management must account for these interactions to reduce risks associated with water table fluctuations.

In area 3, groundwater near wells 7, 8, and 13 was predominantly influenced by streamflow and soil moisture, with rainfall also playing a significant role. For example, streamflow at station 08078930 was the most important predictor for groundwater levels in this region, illustrating the strong connectivity between streamflow and groundwater recharge (Healy and Scanlon, 2010). These groundwater systems displayed dynamic responses to hydrological events, such as rapid recharge during heavy rainfall or upstream runoff. However, this dynamic

nature also makes them more prone to sharp water table fluctuations, which could exacerbate flooding risks during storm events or periods of high streamflow (Bowes et al., 2019; Serafin et al., 2019). Additionally, groundwater systems influenced by soil moisture and rainfall, as observed in areas near wells 8 and 13, may experience compounding effects of prolonged wet conditions, amplifying groundwater level rises. The compounded effects of multiple predictors, such as rainfall, upstream recharge, and tidal influences, present significant challenges in managing groundwater in these areas. Coastal groundwater systems face heightened risks when high tides coincide with heavy rainfall, leading to rapid water table surges (Jang and Chang, 2022; Lian et al., 2017; Jalili Pirani and Najafi, 2020). Similarly, inland groundwater may experience delayed yet substantial rises from sustained upstream recharge (Neri-Flores et al., 2019), increasing the potential for downstream coastal flooding due to increased hydraulic gradients towards the coast (Pietrafesa et al., 2019). These findings underscore the interconnected nature of groundwater systems, where localized and regional hydrological processes interact to influence water table dynamics in barrier islands.

#### 3.6. Conclusion/Recommendation

Conclusions

The findings from this study provide essential insights into the hydrological dynamics that influence the water table along the Texas barrier islands, specifically between Quintana Park and the Heritage Preserve (see **Figure 2.1**).

- 1. Sediment Characterization and Groundwater Dynamics:
- Sediment cores reveal significant heterogeneity across different wells, demonstrating variability and permeability in depositional environments. Coastal wells (e.g., wells 7, 8, and 9) predominantly feature sandy and gravelly textures, facilitating high groundwater flow. In contrast, inland wells (e.g., wells 1 and 10) show finer-grained sediments (clay and silt), characteristically lower permeability, and slow down groundwater movement.
- Seasonal variability in groundwater discharge is evident, with higher discharge rates occurring during cooler months due to rainfall and aquifer recharge. Conversely, seawater intrusion is more pronounced during warmer months, driven by tidal influences and reduced groundwater gradients.
- DTW patterns highlight seasonal trends in water table behavior. In area 3, wells 4 and 5 show shallow water tables during late winter and early spring, with DTW values approaching 0 meters, increasing the likelihood of flooding. Conversely, well 3 exhibits the greatest DTW (deepest water table), consistently exceeding 1.5–2 meters, particularly in the summer, which reduces its vulnerability to flooding. In area 4, wells 7, 8, and 11 display persistently shallow DTW values during late winter and early spring, often approaching or falling below 0.5 meters, highlighting a high risk of water table flooding and compromised infrastructure.
  - 2. Submarine Groundwater Discharge (SGD) and Radium Dynamics:
- Radium isotopes (224Ra, 223Ra, and 226Ra) are effective indicators of groundwater discharge, revealing peaks in SGD during periods of increased recharge and aquifer flushing. For instance, elevated 224Ra levels in porewater and surface water correlate with enhanced SGD, underscoring the role of hydrological events in facilitating groundwater-surface water exchanges.

- The variability in SGD highlights the interplay between sediment composition, tidal forcing, and seasonal recharge. Coastal regions, in particular, are more vulnerable to rapid water table fluctuations, which can lead to nutrient and contaminant transport into nearshore ecosystems.
- Areas with shallow DTW, such as wells 4, 5, 7, and 8, are more prone to flooding during late winter and early spring recharge. In these regions, the interplay of tidal influences, precipitation, and aquifer recharge amplifies SGD rates and their associated impacts on coastal ecosystems and infrastructure.

## 3. Groundwater Level Prediction and Key Drivers:

- Predictive modeling identifies streamflow, rainfall, soil moisture, terrestrial water storage, and tidal dynamics as key drivers of water table fluctuations. In area 3, the strong influence of streamflow and soil moisture indicates dynamic responses to surface hydrology, while the predominance of terrestrial water storage in area 4 reflects subsurface hydrological processes.
- The dynamic nature of coastal groundwater systems increases the risks of flooding and seawater intrusion during high tides or storm surges. The DTW patterns further emphasize these risks, with coastal wells in both areas showing shallow water tables and high flooding vulnerability during late winter and early spring recharge periods. Inland wells with deeper DTW values, such as well 3 in area 3, demonstrate reduced susceptibility to such risks.

#### Recommendations

# 1. Monitoring and Data Collection:

- Implement long-term monitoring programs that focus on groundwater levels, tidal cycles, and precipitation patterns. Enhanced spatial and temporal data resolution will improve model accuracy and help identify critical periods of vulnerability, especially during seasonal transitions.
- Expand radium isotope sampling to more comprehensively track SGD and sediment-water interactions under diverse hydrological conditions.
- Integrate DTW monitoring into existing programs, focusing on wells with high flooding vulnerability (e.g., wells 4, 5, 7, 8, and 11). This will provide critical insights into seasonal and event-driven risks to water table dynamics and infrastructure.

#### 2. Coastal and Groundwater Management:

- Develop adaptive groundwater management strategies to mitigate the risks of seawater intrusion and groundwater flooding in coastal areas, especially during high tides and storm surges. Targeted interventions like recharge wells or tidal barriers can help stabilize water table fluctuations.
- Emphasize sustainable water use and storage strategies in inland regions, focusing on recharge zones to maintain aquifer levels during prolonged dry spells or periods of high withdrawal.
- Prioritize interventions in areas with shallow DTW during high-risk periods (e.g., late winter and early spring) to protect septic systems and underground infrastructure from water infiltration and contamination.

#### 3. Model Development and Application:

- Incorporate site-specific features, such as sediment composition and aquifer geometry, into predictive models to enhance their utility for localized decision-making. Additionally, integrating climate projections can help anticipate future hydrological shifts and their impacts on groundwater dynamics.
- Utilize the predictive model to design early-warning systems for water table rises and flooding risks, enabling proactive response measures during hydrological extremes.
- Refine the model to account for the seasonal variability in DTW, particularly in high-risk wells, to improve predictions of infrastructure vulnerability and flooding risks.
  - 4. Ecosystem and Infrastructure Protection:
- Conduct vulnerability assessments for critical coastal ecosystems and infrastructure exposed to fluctuating groundwater levels and SGD-induced nutrient transport. Develop policies to minimize ecological impacts while protecting infrastructure integrity.
- Focus on wells 7, 8, and 11 in area 4 and wells 4 and 5 in area 3 for infrastructure protection, as these areas consistently exhibit shallow DTW values during high-risk periods. Strategies to mitigate flooding and contamination risks should prioritize these locations.
- Promote interdisciplinary approaches that combine hydrology, geology, and coastal management to tackle the complex challenges groundwater dynamics present in barrier island environments.

These conclusions and recommendations lay the groundwork for sustainable groundwater and coastal resource management, enhancing the region's resilience against environmental and hydrological stressors.

#### 3.7. References

AcreValue. (2023). Soil Survey Maps and Data.

- Allen, T. R., Crawford, T., Montz, B., Whitehead, J., Lovelace, S., Hanks, A. D., Christensen, A. R., & Kearney, G. D. (2019). Linking water infrastructure, public health, and sea level rise: Integrated assessment of flood resilience in coastal cities. *Public Works Management & Policy*, 24(1), 110-139. <a href="https://doi.org/10.1177/1087724X18798380">https://doi.org/10.1177/1087724X18798380</a>
- Asoka, A., & Mishra, V. (2020). Anthropogenic and climate contributions on the changes in terrestrial water storage in india. *Journal of Geophysical Research*. *Atmospheres*, 125(10), n/a. <a href="https://doi.org/10.1029/2020JD032470">https://doi.org/10.1029/2020JD032470</a>
- Bianchi, T. S., Allison, M. A., & Cai, W. (2014). *Biogeochemical dynamics at major river-coastal interfaces: Linkages with global change* (1st;1; ed.). Cambridge University Press. https://doi.org/10.1017/CBO9781139136853
- Bowes, B. D., Sadler, J. M., Morsy, M. M., Behl, M., & Goodall, J. L. (2019). Forecasting groundwater table in a flood prone coastal city with long short-term memory and recurrent neural networks. *Water*, 11(5), 1098. <a href="https://doi.org/10.3390/w11051098">https://doi.org/10.3390/w11051098</a>
- Burnett, W. C., Bokuniewicz, H., Huettel, M., Moore, W. S., & Taniguchi, M. (2003). Groundwater and pore water inputs to the coastal zone. *Biogeochemistry*, 66(1-2), 3-33. https://doi.org/10.1023/b:biog.0000006066.21240.53
- Chang, F., Chang, L., Huang, C., & Kao, I. (2016). Prediction of monthly regional groundwater levels through hybrid soft-computing techniques. *Journal of Hydrology (Amsterdam)*, 541, 965-976. https://doi.org/10.1016/j.jhydrol.2016.08.006

- Charette, M. A., & Sholkovitz, E. R. (2006). Trace element cycling in a subterranean estuary; part 2, geochemistry of the pore water. *Geochimica Et Cosmochimica Acta*, 70(4), 811-826. <a href="https://doi.org/10.1016/j.gca.2005.10.019">https://doi.org/10.1016/j.gca.2005.10.019</a>
- Dimova, N., Burnett, W. C., Horwitz, E. P., & Lane-Smith, D. (2007). Automated measurement of 224Ra and 226Ra in water. *Applied Radiation and Isotopes*, 65(4), 428-434. https://doi.org/10.1016/j.apradiso.2006.10.005
- EPA (2020). *National Water Quality Inventory Report to Congress: 2017*. United States Environmental Protection Agency.
- Fetter, C. W. (2001). Applied hydrogeology (4th;4; ed.). Prentice Hall.
- Healy, R. W., & Scanlon, B. R. (2010). *Estimating groundwater recharge* (1st ed.). Cambridge University Press. <a href="https://doi.org/10.1017/CBO9780511780745">https://doi.org/10.1017/CBO9780511780745</a>
- Hu, C., Muller-Karger, F. E., & Swarzenski, P. W. (2006). Hurricanes, submarine groundwater discharge, and florida's red tides. *Geophysical Research Letters*, *33*(11). https://doi.org/10.1029/2005GL025449
- Jalili Pirani, F., & Najafi, M. R. (2020). Recent trends in individual and multivariate compound flood drivers in canada's coasts. *Water Resources Research*, 56(8). https://doi.org/10.1029/2020WR027785
- Jang, J., & Chang, T. (2022). Flood risk estimation under the compound influence of rainfall and tide. *Journal of Hydrology, 606*, 127446. <a href="https://doi.org/10.1016/j.jhydrol.2022.12744">https://doi.org/10.1016/j.jhydrol.2022.12744</a>
- Jones, D., Smith, R., & Wang, H. (2019). Waterborne pathogens in coastal environments: Sources, impacts, and mitigation. *Journal of Coastal Research*, 35(2), 275-289.
- Kim, G., Burnett, W. C., Dulaiova, H., Swarzenski, P. W., & Moore, W. S. (2001). Measurement of 224Ra and 226Ra activities in natural waters using a radon-in-air monitor. *Environmental Science & Technology*, 35(23), 4680-4683. https://doi.org/10.1021/es010804u
- Kingma, D. P., & Welling, M. (2022). *Auto-encoding variational bayes*. Cornell University Library, arXiv.org
- Knee, K., & Paytan, A. (2011). 4.08 submarine groundwater discharge: a source of nutrients, metals, and pollutants to the Coastal Ocean. *Treatise Estuarine and Coastal Science*, 4, 205-234. <a href="https://doi.org/10.1016/B978-0-12-374711-2.00410-1">https://doi.org/10.1016/B978-0-12-374711-2.00410-1</a>
- Kroeger, K. D., Swarzenski, P. W., Greenwood, W. J., & Reich, C. (2007). Submarine groundwater discharge to tampa bay; nutrient fluxes and biogeochemistry of the coastal aquifer. *Marine Chemistry*, 104(1-2), 85-97. <a href="https://doi.org/10.1016/j.marchem.2006.10.012">https://doi.org/10.1016/j.marchem.2006.10.012</a>
- Kroeger, T., & Casey, F. (2007). An assessment of market-based approaches to providing ecosystem services on agricultural lands. *Ecological Economics*, 64(2), 321-332. https://doi.org/10.1016/j.ecolecon.2007.07.021
- Lian, J., Xu, H., Xu, K., & Ma, C. (2017). Optimal management of the flooding risk caused by the joint occurrence of extreme rainfall and high tide level in a coastal city. *Natural Hazards*, 89(1), 183-200. https://doi.org/10.1007/s11069-017-2958-4
- MDNR (2020). *Why Groundwater Levels Change*. Missouri Department of Natural Resources. <a href="https://dnr.mo.gov/document-search/why-groundwater-levels-change-pub2884/pub2884">https://dnr.mo.gov/document-search/why-groundwater-levels-change-pub2884/pub2884</a>
- Moore, W. S. (1996). Large groundwater inputs to coastal waters revealed by 226Ra enrichments. *Nature*, 380(6575), 612-614. https://doi.org/10.1038/380612a0

- Moore, W. S., & Arnold, R. (1996). Measurement of 223Ra and 224Ra in coastal waters using a delayed coincidence counter. *Journal of Geophysical Research: Oceans, 101*(C1), 1321-1329. https://doi.org/10.1029/95JC03139
- Murgulet, D., Douglas, A. R., Spalt, N., & Lee, L. (2016). Using geochemical tracers and radium isotopes to investigate groundwater and surface water interactions and nutrient fluxes to coastal embayments. *Marine Chemistry*, 182, 77–89.
- Murgulet, D., Runnels, B., Spalt, N., & Smith, E. (2022). Spatial variability of nutrient and freshwater inputs into estuaries of the northwest Gulf of Mexico. *Science of the Total Environment*, 819, 152022.
- Neri-Flores, I., Moreno-Casasola, P., Peralta-Peláez, L. A., & Monroy, R. (2019). Groundwater and river flooding: The importance of wetlands in coastal zones. *Journal of Coastal Research*, 92(sp1), 44-54. https://doi.org/10.2112/SI92-006.1
- Null, K. A., Knee, K. L., Crook, E. D., de Sieyes, N. R., Rebolledo-Vieyra, M., Hernandez-Terrones, L., & Paytan, A. (2014). Composition and fluxes of submarine groundwater along the caribbean coast of the yucatan peninsula. *Continental Shelf Research*, 77, 38-50. <a href="https://doi.org/10.1016/j.csr.2014.01.011">https://doi.org/10.1016/j.csr.2014.01.011</a>
- Pietrafesa, L., Zhang, H., Bao, S., Gayes, P., & Hallstrom, J. (2019). Coastal flooding and inundation and inland flooding due to downstream blocking. *Journal of Marine Science and Engineering*, 7(10), 336. <a href="https://doi.org/10.3390/jmse7100336">https://doi.org/10.3390/jmse7100336</a>
- Qiu, C., Zhu, J., & Gu, Y. (2012). Impact of seasonal tide variation on saltwater intrusion in the changjiang river estuary. *Journal of Oceanology and Limnology*, 30(2), 342-351. https://doi.org/10.1007/s00343-012-1115-x
- Roy, M., Martin, J. B., Cherrier, J., Cable, J. E., & Smith, C. G. (2010). Influence of sea-level rise on iron diagenesis in an east florida subterranean estuary. *Geochimica Et Cosmochimica Acta*, 74(19), 5560-5573. https://doi.org/10.1016/j.gca.2010.07.007
- Saba, J. A., Ash, K., & Napton, D. (2024). Assessing the vulnerability of cape coral, florida, to sea level rise using principal component analysis (2020–2050). International Journal of Disaster Risk Reduction, 115, 105014. <a href="https://doi.org/10.1016/j.ijdrr.2024.105014">https://doi.org/10.1016/j.ijdrr.2024.105014</a>
- Santos, I. R., Eyre, B. D., & Huettel, M. (2012). The driving forces of porewater and groundwater flow in permeable coastal sediments; a review. *Estuarine, Coastal and Shelf Science*, 98, 1-15. https://doi.org/10.1016/j.ecss.2011.10.024
- Serafin, K. A., Ruggiero, P., Parker, K., & Hill, D. F. (2019). What's streamflow got to do with it? A probabilistic simulation of the competing oceanographic and fluvial processes driving extreme along-river water levels. *Natural Hazards and Earth System Sciences*, 19(7), 1415-1431. <a href="https://doi.org/10.5194/nhess-19-1415-2019">https://doi.org/10.5194/nhess-19-1415-2019</a>
- Smith, T. A., Johnson, L. A., & Davis, P. (2020). Septic systems as a source of bacterial contamination in rural watersheds. *Water Quality Research Journal*, 55(1), 1-12.
- Smith, V. H., Tilman, G. D., & Nekola, J. C. (1999). Eutrophication; impacts of excess nutrient inputs on freshwater, marine, and terrestrial ecosystems. *Environmental Pollution*, 100(1-3), 179-196. https://doi.org/10.1016/S0269-7491(99)00091-3
- TCEQ (2018). *Matagorda Bay Basin Highlights Report*. Texas Commission on Environmental Quality.
- Texas Geological Survey (2022). Geological Maps of Texas Coastal Regions.
- TWRI (2017). Texas Bays and Estuaries. Texas Water Resources Institute.
- TWRI (2017). Tres Palacios Creek Watershed Protection Plan. Texas Water Resources Institute.

- USDA Natural Resources Conservation Service (2023). *General Soil Map of Texas*. Natural Resources Conservation Service.
- USGS (2022). Geologic and Lithologic Mapping of Coastal Plains. U.S. Geological Survey.
- Webster, I. T., Hancock, G. J., & Murray, A. S. (1995). Modelling the effect of salinity on radium desorption from sediments. *Geochimica Et Cosmochimica Acta*, 59(12), 2469-2476. https://doi.org/10.1016/0016-7037(95)00141-7
- Wei, Y., Chen, Y., Cao, X., Xiang, M., Huang, Y., & Li, H. (2024). A critical review of groundwater table fluctuation: Formation, effects on multifields, and contaminant behaviors in a soil and aquifer system. *Environmental Science & Technology*, 58(5), 2185-2203. https://doi.org/10.1021/acs.est.3c08543
- Wei, Y., Xu, X., Zhao, L., & Cao, X. (2023). Numerical modeling investigations of colloid facilitated chromium migration considering variable-density flow during the coastal groundwater table fluctuation. *Journal of Hazardous Materials*, 443, 130282-130282. https://doi.org/10.1016/j.jhazmat.2022.130282
- Wolfe, W. W., Murgulet, D., Gyawali, B., & Sterba-Boatwright, B. (2023). Modeling time series radon inventory and constraints on the submarine groundwater discharge mass balance of a well-mixed, highly dynamic estuary. *Journal of Hydrology (Amsterdam)*, 625, 130065. https://doi.org/10.1016/j.jhydrol.2023.130065
- Xue, D., Botte, J., De Baets, B., Accoe, F., Nestler, A., Taylor, P., Van Cleemput, O., Berglund, M., & Boeckx, P. (2009). Present limitations and future prospects of stable isotope methods for nitrate source identification in surface- and groundwater. *Water Research*, 43(5), 1159-1170. <a href="https://doi.org/10.1016/j.watres.2008.12.048">https://doi.org/10.1016/j.watres.2008.12.048</a>

#### 4. TASK 2: MEASUREMENT OF FECAL INDICATOR BACTERIA

Prepared by Dipti Anik Dhar, Kiran Kumar Vadde, and Vikram Kapoor, Ph.D.

## 4.1. Executive Summary

The purpose of the study/Task-2 was to apply microbial source tracking (MST) approaches to evaluate fecal pollution inputs along the Texas Gulf Coast. Quantitative PCRbased methods were applied for one general fecal marker (Entero1), two animal-associated assays (BacCan and GFD), and one human-associated marker (HF183). For comparison, one conventional fecal indicator bacteria (Enterococci) was measured by following a culture-based quantification method. Culture-based enterococci was present in all surface water samples in high concentration, whereas well and pore water samples showed low detection frequency with low concentration. 79% of surface water samples exceed the safe condition for marine recreational water. Among 4 qPCR markers, Entero1 showed comparatively higher concentration and detection frequency in wells, surface water, and pore water (88% of samples). The sole use of these general markers doesn't give us a clear understanding of the hosts and sources of fecal pollution in the Texas Gulf Coast. Among the host-specific markers, the highest level of gull markers, GFD, was observed, suggesting a higher percentage of fecal pollution was coming from the bird population on the coast. The next predominant marker was BacCan, which can be introduced by unrestrained dogs along the coast. Human-derived fecal pollution was detected as well though the level and detection of the marker was lowest.

# 4.2. Background

Identifying the types of sources that contribute to bacteria in water systems is key when developing strategies to reduce bacteria and other pollution levels in surface and groundwater, as well as evaluating their potential impact on the environment. In coastal regions where sources are not easily known or understood, microbial source tracking (MST) techniques can provide an opportunity to analyze water samples in a way that identifies the source of fecal bacteria in the sample, from simply identifying whether the source is human or animal to, at times, identifying the source down to the species (e.g., cow, dog, deer). The molecular methods used for MST most commonly include the analysis of genetic material (e.g., deoxyribonucleic acid [DNA] or ribonucleic acid [RNA]) to determine the source (human or animal) that contributed to the fecal bacteria observed in the water sample. The underlying assumption of these types of MST methods is that there are genetic sequences unique to bacteria from a particular host that can be used to identify where the bacteria originated.

As an integral part of the project, Task 2 sought quantitative data on fecal pollution to provide a comprehensive view of the study area. We were looking to identify the potential sources of fecal contamination such as (1) humane waste/ runoff through on-site sewage facilities (OSSFs), (2) animal waste (domesticated and unrestrained animals regarding recreation), and (3) wildlife waste (Seagulls and birds). The potential impact of microbial contamination was assessed by conventional fecal indicator bacteria and advanced molecular MST markers. Culturable Enterococci, as well as general qPCR assay Entero1 (General Enterococcus) and host-specific qPCR assays such as HF183 (human), BacCan (Canine), GFD (Gull), were used to identify the presence and the abundance of fecal contamination along the Texas Gulf Coast. The information from Task 2 will be integrated with other project tasks to develop a comprehensive

scenario with detailed geological and environmental factors that influence the sources, abundance, and transport of fecal contamination along the Texas Gulf Coast.

## 4.3. Methods

## 2.3.1. Sampling Sites and Sample Collection

The present study was conducted at twenty locations along the Texas Gulf Coast in Chambers, Brazoria, Galveston, and Matagorda County, Texas, USA. Each location has a different combination of well, surface, and pore water samples. Water samples were collected for 19 months from November 2021 to May 2023 from each site and analyzed for Fecal Indicator Bacteria (FIB) and Microbial Source Tracking (MST) markers. Water samples were collected in sterile 1 Liter Nalgene bottles (Rochester, NY) as previously mentioned (Hinojosa et al., 2020) and transferred to UTSA Laboratory in ice coolers where the water samples were immediately processed for Enterolert test and filtration.

#### 4.3.2. Enterolert Test

Enterolert Test kit by IDEXX (Westbrook, Maine) was used to enumerate Enterococci levels in water samples. 100 ml of water sample was transferred in 250 ml sterile Erlenmeyer Flask using sterile serological pippete. The reagent was added to samples and mixed properly by shaking the flasks until the powder dissolved completely. The sample mixtures were poured into QuantiTray/2000 and sealed with QuantiTray Sealer Plus. The trays were incubated at  $41 \pm 0.5$  °C for 24 hrs. After incubation, the trays were marked under UV light. The wells with blue fluorescence were marked as positive, whereas no fluorescence indicated negative. The number of positive large and small wells were counted, and the MPN Table provided with Quanti Tray/2000 was referred to obtain the concentration of enterococci in MPN/100ml.

#### 4.3.3. Filtration and DNA Extraction

300 ml of each water sample was filtered in duplicate on a vacuum manifold through 0.45-µm-pore-size, 47 mm diameter polycarbonate membranes (Pall Corporation, Ann Arbor, Michigan) and immediately stored at -80°C until DNA extraction. Sterile de-ionized water controls were filtered with each sampling event to check for cross-contamination during sample processing. Before DNA extraction, the filtered samples were thawed on ice. The genomic DNA was extracted using DNeasy PowerLyzer PowerSoil Kit (Qiagen, Hilden, Germany) according to the manufacturer's protocol. Extraction blank was processed with all batches of extraction to check carryover contamination. DNA concentration and purity were checked with a Nanodrop spectrophotometer (Thermo Scientific, Wilmington, DE). All extracted DNA samples were stored in -20°C until further qPCR analysis.

#### 4.3.4. qPCR analysis

The presence and distribution of four MST markers (3 TaqMan assays and 1 SYBR Green assay) were measured to identify fecal contamination in Texas Gulf Coast waters. Extracted DNA from collected coastal water samples were analyzed as the templates (**Table 4.1**) for following MST markers using previously developed qPCR assays; human-associated Bacteroidales (HF183), canine-associated Bacteroidales (BacCan), Enterococcus (Entero1), and avian-associated fecal markers (GFD). All the qPCR assays were carried out using CFX96 Touch Real-Time PCR Detection System (Bio-Rad, Hercules, CA) and all qPCR reactions were performed with 20  $\mu$ L as reaction volume. HF183 and Entero1 were probe-based and each qPCR

reaction mixture contained 10  $\mu$ L of iTaq<sup>TM</sup> Universal Probes Supermix (Bio-Rad, Hercules, CA), 1  $\mu$ M each of respective forward and reverse primers, 80 nM of the respective probe and 2  $\mu$ L of template DNA. Probe-based assay BacCan has same reaction mixture except it contains 0.4  $\mu$ M each of respective forward and reverse primers. GFD is a SYBR Green based assay where the reaction mixture contains 10  $\mu$ L of SsoAdvanced Universal SYBR® Green Supermix (Bio-Rad, Hercules, CA), 0.1  $\mu$ L each of forward and reverse primers and 2  $\mu$ L of template DNA. The qPCR reaction was run in duplicate for all DNA templates. The thermal protocol of qPCR amplification was performed following an initial denaturation at 95 °C for 2 min, followed by 40 cycles of 15 s at 95 °C and 60 s at 60 °C (except Entero1 and GFD, which were performed at 54 °C and 57 °C respectively). The GFD assay involved conducting a melting curve analysis, where the temperature was increased from 60 °C to 95 °C at a rate of approximately 0.4 °C per minute. This analysis was performed after qPCR amplification to confirm the specificity of the amplified products. Samples were considered positive if their melting points matched the melting point of the qPCR standards within a tolerance of 0.5 °C.

A standard curve with concentrations spanning the range from 10<sup>6</sup> to 10<sup>1</sup> gene copies per reaction, with two duplicates was prepared by using serially diluted plasmids standards containing the target sequence for each assay purchased from Integrated DNA Technologies (IDT, Skokie, IL). The qPCR data were analyzed using Bio-Rad's CFX Manager Software (version 3.1). Based on standard curve, the targeted marker copy number per 100 mL of water was calculated for all samples. Cross contamination was checked by including extraction blanks and three no template controls (NTC) in qPCR each plate. The amplification efficiency for each run was calculated as per instrument manufacturer's instructions (Bio-Rad). The absolute gene copies of the markers were determined by calculating the average concentration of duplicate reactions and expressing the results as log<sub>10</sub> gene copies per 100 mL of water.

<b>Table 4.1.</b> 1	Primers/i	probes i	for the	PCR assa	vs used	in th	he study.

Assay	Primer/probe Sequence (5'-3')	Reference
Human-specific Bacteroidales (HF183)	HF183: ATCATGAGTTCACATGTCCG BacR287: CTTCCTCTCAGAACCCCTATCC BacP234MGB: 6FAMCTAATGGAACGCATCCC-MGB	Green et al., 2014
Dog Bacteroidales (BacCan)	BacCan- 545f: GGAGCGCAGACGGGTTTT BacUni-690r: CAATCGGAGTTCTTCGTGATATCTA BacUni-656p: 6-FAM-TGGTGTAGCGGTGAAA-TAMRA-MGB	Kildare et al., 2007
Avian-associated marker (GFD)	F: TCGGCTGAGCACTCTAGGG R: GCGTCTCTTTGTACATCCCA	Green et al., 2012
General Enterococcus (Entero1)	ECST748F: AGAAATTCCAAACGAACTTG ENC854R: CAGTGCTCTACCTCCATCATT GPL813TQ: 6FAM- TGGTTCTCCCGAAATAGCTTTAGGGCTA-TAMRA	Ludwig & Schleifer, 2000

## 4.3.5. Data Analysis

All bacteria data was transformed into log<sub>10</sub> scale to generate normally distributed data sets and reduce the influence of broad range of observation. Cultured enterococci enumerated with IDEXX has Limit of Detection (LOD) as <1 MPN/100ml and above detection limit as >2419.6 MPN/100ml which have been reported as 0 and 2419.6 MPN/100ml respectively. We

maintained Limit of Quantification (LOQ) as 10 copies/100ml per qPCR reaction for all four MST markers. The values below 10 copies/100ml were reported as no detection and were assigned a value of one before log transformation. Statistical analyses were performed in R-studio (version 2024.04.1) software. Based on non-normality of datasets, a Kruskal-Wallis test was run to determine if differences between marker concentrations among sampling sites were statistically significant. Analyses were considered significant at alpha level of 0.05 (95% of confidence level). Boxplots were constructed in GraphPad Prism (Version 10.3.0(507)). Lower and upper box boundaries indicate the first and third quartiles. The median is given as the horizontal black line within the box. Upper and lower whiskers represent the maximum and minimum value respectively.

# 4.3.6. Quality Assurance/Quality Control

All environmental samples were collected and handled according to procedures outlined in the EPA field sample collection protocol - EPA Method 1669 (USEPA, 1996), including labeling of containers and logging of sample information on field logs. All samples were transported on ice and were accepted in good condition, according to protocol. Samples were logged in upon arrival at the laboratory, and a unique sample number was given for identification purposes. The following quality control activities were conducted during the PCR laboratory analysis: filtration, positive controls, no template controls, method accuracy, and specificity.

#### 4.4. Results and Discussion

## 4.4.1. Performance of qPCR assays

Each qPCR plate contained a standard curve in duplicate generated from a serial dilution of known target copies per reaction, which were used to determine the amplification efficiencies and linear ranges of the qPCR assays. The linear range of quantification for all qPCR assays was between 10<sup>1</sup> and 10<sup>6</sup> copies per reaction. The qPCR amplification efficiencies for all the assays ranged from 85.8 to 114.9 %, and the R2 values were greater than 0.941 (**Table 4.2**). DNA extraction controls and no template controls (three per qPCR plate) were run to check crosscontamination, and the absence of contamination in the qPCR experiments was confirmed.

**Table 4.2.** Average standard curve qPCR amplification efficiencies and R2 values obtained through BioRad CFX Manager 3.1 software.

Assay	Amplification Efficiency (%)	$\mathbb{R}^2$
Human-associated Bacteroidales (HF183)	98.60	0.989
Dog-associated Bacteroidales (BacCan)	94.78	0.979
Avian-associated marker (GFD)	99.79	0.984
General Enterococcus (Entero1)	100.4	0.985

# 4.4.2. Detection of Culture-based Enterococci

Enterococci was enumerated from all type of water samples (207 well water samples, 335 surface water, and 226 pore water samples) collected from December 2021 to May 2023. **Table** 

**4.3**, **Table 4.4**, and **Table 4.5** show the spatial detection frequency of enterococci and **Table 4.6**, **Table 4.7**, and **Table 4.8** show the temporal detection frequency of enterococci with similar categories published in the beach monitoring website Texas Beach Watch managed by Texas General Land Office (TGLO). The website has color coded Beach Advisory levels; Low, Medium and High with the criteria of less than 35 MPN/100ml, 35 to 104 MPN/100mL, and more than 104 MPN/100 mL, respectively. High Level denotes that the concentration of enterococci exceeds the EPA recreational water quality standard. The samples from well, surface and pore water had considerably different detection patterns throughout the study. Enterococci was detected in all surface water samples with high concentration whereas well and pore samples had low concentration with low detection frequency.

**Table 4.3.** Spatial Detection frequency of Enterococci enumerated by IDEXX Enterolert kit in well Samples.

Sites		W1	W1 W2 W3 W4 W5 W7 W8 W9 W10 W11 W13 W							W14			
No. of Samp	oles	17	15	18	18	18	18	13	18	18	18	18	18
Beach Advisory Level	Criteria (MPN/ 100mL)	Perce	Percentage of positive samples fall in the criteria										
Low	<35	94	6	100	94	100	6	54	78	94	83	94	72
Medium	35 to 104	6	6 27 0 6 0 44 8 22 6 0 0 17								17		
High	>104	0	67	0	0	0	50	38	0	0	17	6	11

**Table 4.4.** Spatial Detection frequency of Enterococci enumerated by IDEXX Enterolert in Surface Samples.

Sites	Trans	S1	S2	S4	S5	S6	S6B	S8	<b>S</b> 9	S10	S11
No. of Sam	ples	17	18	18	18	17	17	18	18	18	18
Beach Advisory Level	Criteria (MPN/ 100mL)	Percen	tage of po	ositive sa	mples fal	l in the cı	riteria		•	•	
Low	<35	29	0	6	6	0	6	0	6	0	0
Medium	35 to 104	6	33	28	28	53	41	28	28	17	17
High	>104	65	67	66	66	47	53	72	66	83	83
Sites		S12	S12B	S14	S15	S16	S17	S18	S19	S20	
No. of Sam	ples	18	16	18	18	18	18	17	17	18	
Beach Advisory Level	Criteria (MPN/ 100mL)	Percen	tage of po	ositive sa	mples fal	l in the cr	riteria				
Low	<35	0	0	0	0	0	0	0	0	0	
Medium	35 to 104	0	6	17	6	6	0	6	24	11	
High	>104	100	94	87	94	94	100	94	76	89	

**Table 4.5.** Spatial Detection frequency of Enterococci enumerated by IDEXX Enterolert in Pore Samples.

Sites		P2	P4	P5	PWB5	P8	P9	P10	P11
No. of Sample	es	18	18	18	9	18	18	18	18
Beach Advisory Level	Criteria (MPN/ 100mL)	Percenta	ge of positi	ve sample	s fall in the	criteria			

Low	<35	78	61	72	56	50	67	67	56
Medium	35 to 104	16	33	28	44	44	33	28	39
High	>104	6	6	0	0	6	0	5	5
Sites		P14	P15	P16	P18	PWB18	P19	PWB19	
No. of Sample	es	18	11	14	17	9	15	7	
Beach	Criteria								
Advisory	(MPN/	Percenta	ge of positi	ve sample	s fall in the	criteria			
Level	100mL)								
Low	<35	28	73	50	65	67	74	72	
Medium	35 to 104	61	18	29	23	33	13	14	
High	>104	11	9	21	12	0	13	14	

Less contamination was observed with IDEXX Enterolert Kit in well water samples than surface and pore water samples throughout the study. The concentration of enterococci ranged from below detection limit (< 1 MPN/100 mL) to above detection limit (> 2419.6 MPN/100 mL). Statistically significant difference in enterococci concentration across the study sites was found (Kruskal-Wallis test; p < 0.05). Most of the samples (154 out of 207) fell into Low level of enterococci from different well sites. 48 out of 207 well water samples (23%) showed no detection or < 1 MPN/100 mL of enterococci. The samples from W1, W3, W4, W5, W9, and W10 fell into low and medium level which indicates these sites never exceeded the recreational water quality throughout the study. The concentration of enterococci in these sites ranged from < 1 MPN/100 mL to 65 MPN/100 mL. W3 and W5 contained 100% of the samples in low level for 18 months. High percentage of detection in High level or above recreational water quality was observed in W2, W7, and W8 (67%, 50%, and 38% respectively). Similarly, W11, W13, and W14 showed low percentage of frequency in High level of enterococci (17%, 6%, and 11% respectively). Out of 7 well samples in Brazoria County, all well sites contained enterococci concentration in High level except W9 and W10 indicating the wells encountered fecal contamination. Well sites in Galveston turned out less contaminates except W2 which has highest detection frequency in High Level. Chambers county has only one well site and it is comparatively less contaminated.

100% of samples collected from Surface water sites were tested positive for cultured enterococci (Table 3(b)). There was statistically significant difference in enterococci concentration across the study sites for surface water samples (Kruskal-Wallis test; p < 0.05). Unlike well and pore water samples, surface water samples showed higher concentration of enterococci in all sites throughout the study period ranging from 11.8 MPN/100 mL to above detection limit (> 2419.6 MPN/100 mL). Only 21% of samples (71 out of 335 surface samples) met the threshold for marine recreational water. Elevated detection frequency (47% to 100%) was observed for High criteria of Beach Advisory Level indicating regular heavy fecal contamination throughout the study period. Site S12 and S17 were the most contaminated sites as they did not meet the criteria over 18 months of sampling event. S12B, S15, S16, and S18 exhibited high fecal contamination due to showing only one day of safe condition for swimming in Medium Criteria. Overall, the surface water sites in Chambers County, Galveston County and Brazoria County showed lower percentage of detection frequency in High criteria of Beach Advisory Level comparing with Matagorda County and the sites near Quintana Park in Brazoria County.

Enterococci was detected in 98% of the samples from pore water sites ranging from below detection limit (< 1 MPN/100 mL) to above detection limit (> 2419.6 MPN/100 mL). There was no statistically significant difference among pore water sites (Kruskal-Wallis test; p > 0.05). Unlike well water samples, only 2% of pore water samples showed no detection or below detection limit throughout the study period. For all sites, higher detection frequency was observed in Low (28 % to 78%) and Medium (13% to 61%) level of contamination The samples from P5, PWB5, P9, and PWB18 did not exceed the maximum acceptable level for enterococci in recreational water with a concentration ranging from < 1 MPN/100 mL to 100.6 MPN/100 mL. Only 1 sample throughout the study period exceeded the maximum allowable level in site P2, P4, P8, P10, P11, P15, and PWB19B. P14, P16, P18, and P19 had more than one sample which did not meet the acceptable water quality for recreational marine water.

**Table 4.6.** Temporal Detection frequency of Enterococci enumerated by IDEXX Enterolert in well water Samples.

water samples.										
Sampling		Dec 21	Jan 22	Feb 22	Mar 22	Apr 22	May 22	Jun 22	Jul 22	Aug 22
No. of Samples		12	12	12	12	12	12	12	12	12
Beach Advisory Level	Criteria (MPN/ 100mL)	Percentage of positive samples fall in the criteria								
Low	<35	50	59	67	75	75	75	92	83	75
Medium	35 to 104	17	8	8	0	8	8	8	17	17
High	>104	33	33	25	25	17	17	0	0	8
Sampling		Sep 22	Oct 22	Nov 22	Dec 22	Jan 23	Feb 23	Mar 22	Apr 22	May 22
No. of Samples		12	12	12	10	10	10	11	12	10
Beach Advisory Level	Criteria (MPN/ 100mL)	Percentage of positive samples fall in the criteria								
Low	<35	83	67	67	80	90	90	73	67	80
Medium	35 to 104	17	25	0	10	10	10	9	17	10
High	>104	0	8	33	10	0	0	18	17	10

**Table 4.7.** Temporal Detection frequency of Enterococci enumerated by IDEXX Enterolert in surface water Samples.

Sampling		Dec 21	Jan 22	Feb 22	Mar 22	Apr 22	May 22	Jun 22	Jul 22	Aug 22
No. of Samples		17	19	19	19	19	18	19	19	18
Beach Advisory Level	Criteria (MPN/ 100mL)	Percer	ntage of p	positive s	samples fa	all in the	criteria	•	•	•
Low	<35	0	0	5	5	0	0	0	0	6
Medium	35 to 104	18	26	32	26	26	11	11	0	22
High	>104	82	74	63	69	74	89	89	100	72
Compling		Sep	Oct	Nov	Dec	Jan	Feb	Mar	Apr	May
Sampling		22	22	22	22	23	23	22	22	22
No. of Samples	•	19	19	18	19	19	19	18	19	18

Beach Advisory Level	Criteria (MPN/ 100mL)	Percent	tage of p	ositive sa	amples fa	ll in the o	criteria			
Low	<35	11	0	0	5	0	5	6	5	0
Medium	35 to 104	21	0	28	32	16	32	22	11	0
High	>104	68	100	72	63	84	63	72	84	100

**Table 4.8.** Temporal Detection frequency of Enterococci enumerated by IDEXX Enterolert in

pore water Samples.

pore water Samp	ies.		1		1		1		1	1
Sampling		Dec	Jan	Feb	Mar	Apr	May	Jun	Jul	Aug
Samping		21	22	22	22	22	22	22	22	22
No. of Samples		12	13	14	15	11	10	12	12	12
Beach Advisory Level	Criteria (MPN/ 100mL)	Percen	Percentage of positive samples fall in the criteria							
Low	<35	84	77	57	73	55	20	83	42	66
Medium	35 to 104	8	23	29	27	45	70	17	33	17
High >104		8	0	14	0	0	10	0	25	17
C1:		Sep	Oct	Nov	Dec	Jan	Feb	Mar	Apr	May
Sampling		22	22	22	22	23	23	22	22	22
No. of Samples		13	14	10	9	15	15	12	13	14
Beach Advisory Level	Criteria (MPN/ 100mL)	Percentage of positive samples fall in the criteria								
Low	<35	54	57	50	56	60	40	75	85	64
Medium	35 to 104	38	29	50	44	27	53	25	15	29
High	8	14	0	0	13	7	0	0	7	

Detection frequency in well, surface, and pore water samples was considered for temporal pattern in this study throughout the study period (Tables 4a, 4b, 4c). There was no statistically difference of the concentration of Enterococci in 18 months of well samples water (Kruskal-Wallis test; p > 0.05). All well samples contained enterococci under the threshold value in June 2022, July 2022, September 2022, April 2022, February 2023. The other 13 months of samples contained varied frequency in High Criteria of Enterococci (8% to 33%). Surface water sites showed statistically significant difference within 18 months of samples (Kruskal-Wallis test; p < 0.05). Elevated detection frequency was observed in High criteria (63% to 100%) in every month throughout the study period indicating all the sites had unsafe level of enterococci concentration. In July 2022, October 2022, and May 2022, 100% samples from 19 surface water sites contained enterococci concentration higher than the maximum allowable level for recreational marine water. There was statistically significant difference in enterococci concentration across 18 months of pore water samples (Kruskal-Wallis test; p < 0.05). The higher percentage of detection frequency in Low and Medium criteria for pore water samples was an indication of less fecal contamination throughout the study period. Safe level of enterococci was detected in all pore water samples from the month January 2022, March 2022, April 2022, June 2022, November 2022, December 2022, March 2023, and April 2023.

## 4.4.3. Detection of Fecal Contamination using MST Markers

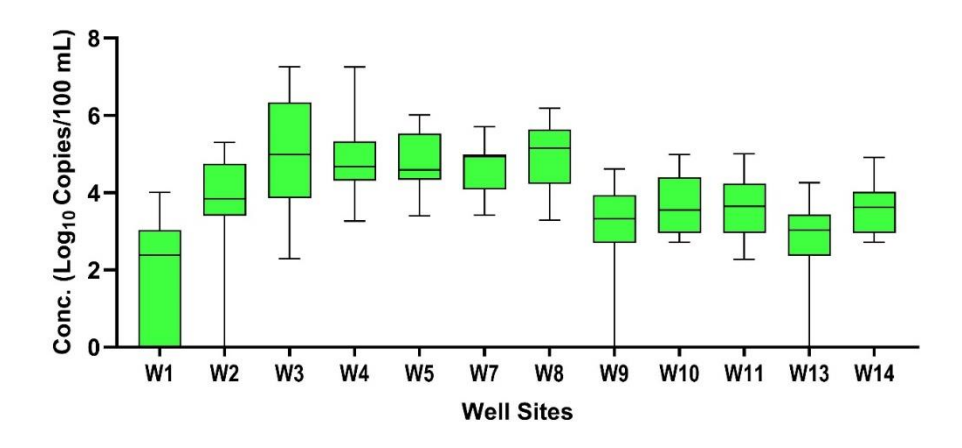
From November 2021 to May 2023, 807 water samples from different well, surface and pore water sites were analyzed for four MST markers to characterize fecal pollution sources and trends along Texas Gulf coast. Among four MST markers, enterococci were found most frequently (89% of samples) using Entero1 assay. Among host-specific markers, human feces associated marker HF183 was detected in less than 5% of samples, whereas avian marker GFD was found in majority of the samples (88% of samples). 23% samples were positive for canine fecal marker BacCan indicating that the study area received fecal pollution from dog sources throughout the study period. Detailed findings for each marker are presented and discussed below.

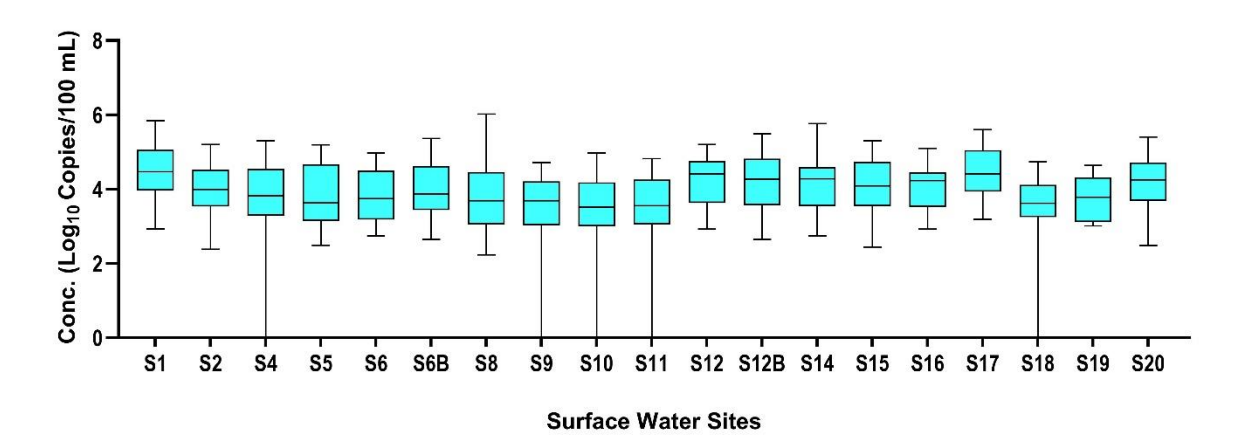
## 4.4.3.1. Detection of general fecal marker

Enterococci showed the highest concentration among all the qPCR markers across the sampling sites (**Figure 4.1**). Entero1 was detected in 206 out of 219 well water samples collected from 12 well water sites. The concentration of enterococci using the marker Entero1 in well samples was statistically different (Kruskal-Wallis test; p < 0.05) with a range of 2.27 Log10 Copies/100 ml to 7.26 Log10 Copies/100 ml. The mean value fluctuated from 1.7 Log10 Copies/100 ml to 4.93 Log10 Copies/100 ml. 100% samples were positive for the marker in W3, W4, W5, W7, W8, W10, W11 and W13. Several samples from W1 did not show the presence of Entero1.

There was statistically significant difference in the concentration of Entero1 detected in surface water in different surface water sites along Texas Gulf Coast (Kruskal-Wallis test; p < 0.05). **Figure 4.2** shows the concentration of Entero1 with 98% presence in surface water samples (345 out of 351 surface water samples). Mean value of Entero1 varied in a close range from 3.32 Log10 Copies/100 ml to 4.47 Log10 Copies/100 ml. The minimum and maximum positive value for Entero1 were 2.23 Log10 Copies/100 ml and 6.02 C both collected from S8.

The samples yielded significantly different amplification for Entero1 across the pore water sites (Kruskal-Wallis test; p < 0.05). 167 out of 237 pore water samples (70%) were positive for Entero1 throughout the study. The abundance of Entero1 varied from 2.23 Log10 Copies/100 ml to 6.99 Log10 Copies/100 ml. P2, P14, and P16 frequently showed high abundance of Entero1 with more than 80% detection frequency.





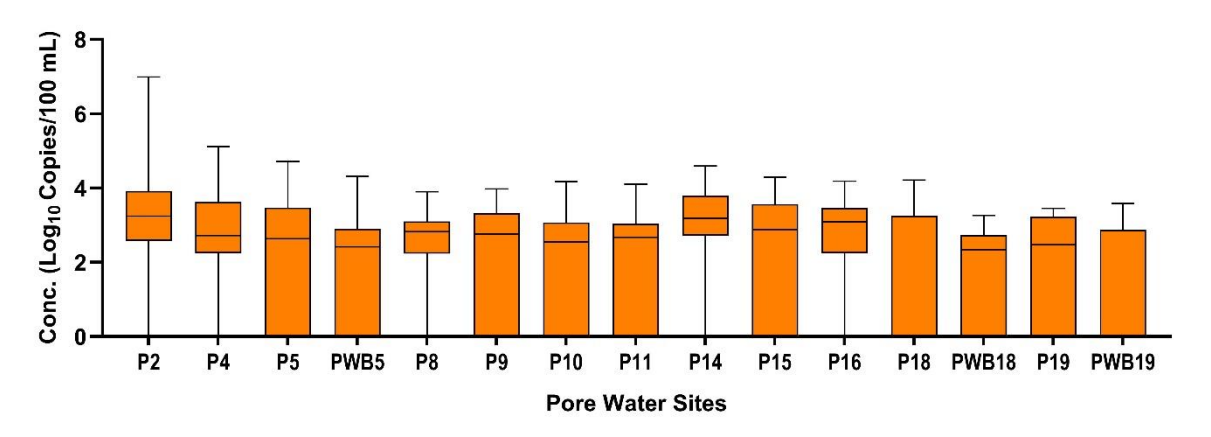
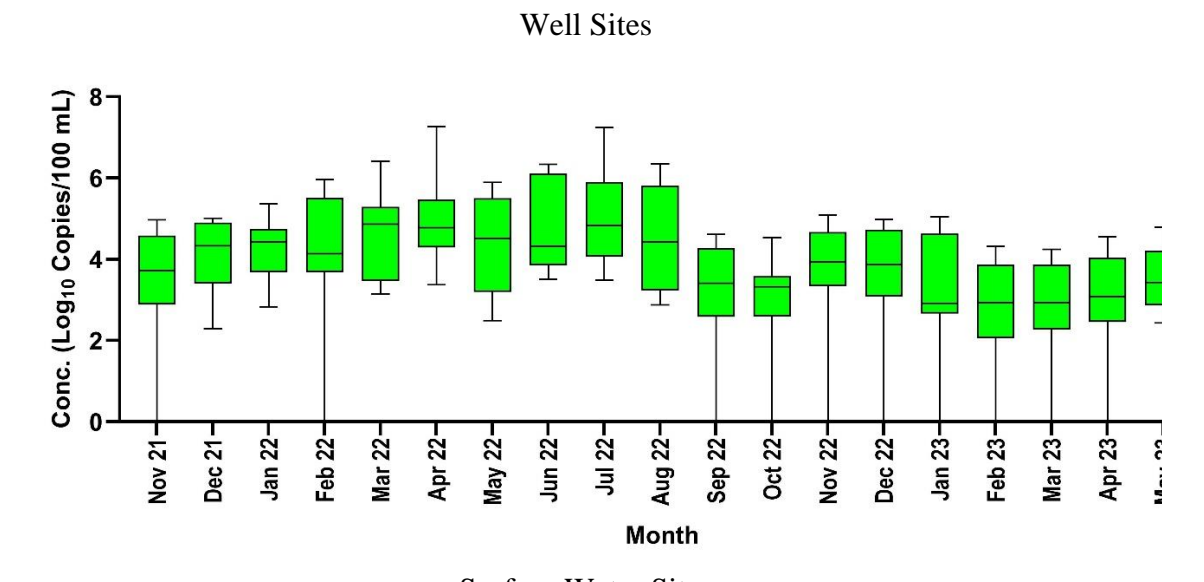


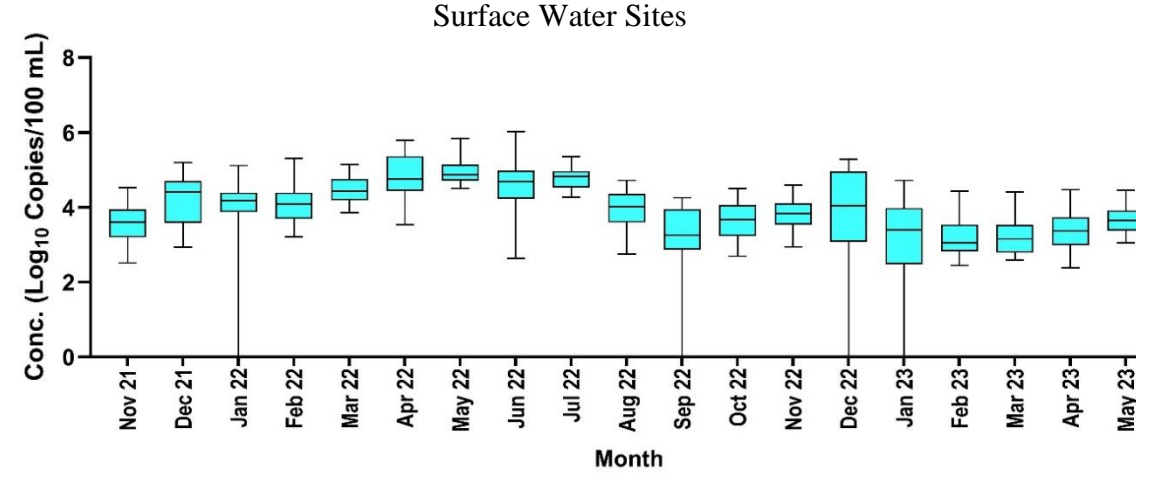
Figure 4.1. Spatial variation of enterococci concentration using MST marker Enterol throughout the study period.

The temporal distribution of Entero1 in well, surface water, and pore water is presented in **Figure 4.2**. A statistically significant difference was found throughout 19 months of the study period while analyzing well water samples, surface water samples, and pore water samples separately (Kruskal-Wallis test; p < 0.05). The concentration of Entero1 found higher in summertime while they are lower in winter and spring time. The highest

mean abundance of Entero1 (5.05 Log10 Copies/100 ml) in well samples was found in July 2022 whereas the lowest mean (2.72 Log10 Copies/100 ml) occurred in February 2023. The lowest and highest average value of Entero1 in surface water were 3.00 and 4.96 occurred in January 2023 and July 2022 respectively. In pore water, lowest mean (0.81 Log10 Copies/100 ml) of Entero1 concentration occurred in March 2023 and highest mean (3.99 Log10 Copies/100 ml) was detected in April 2022.

Overall, high detection frequency of general fecal marker Entero1 indicates the presence of fecal contamination at all types of sites along Texas Gulf Coast. Enterococci has been reported to survive and grow outside of human and animal gastrointestinal system in a wide variety of environments. Therefore, presence of Entero1 doesn't give us sufficient information of specific source of fecal contamination.





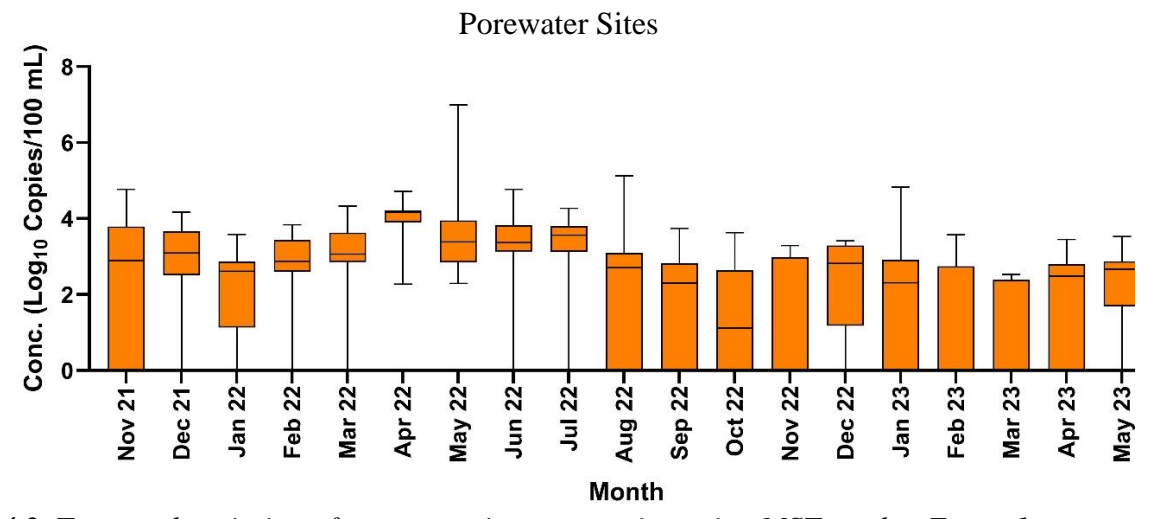


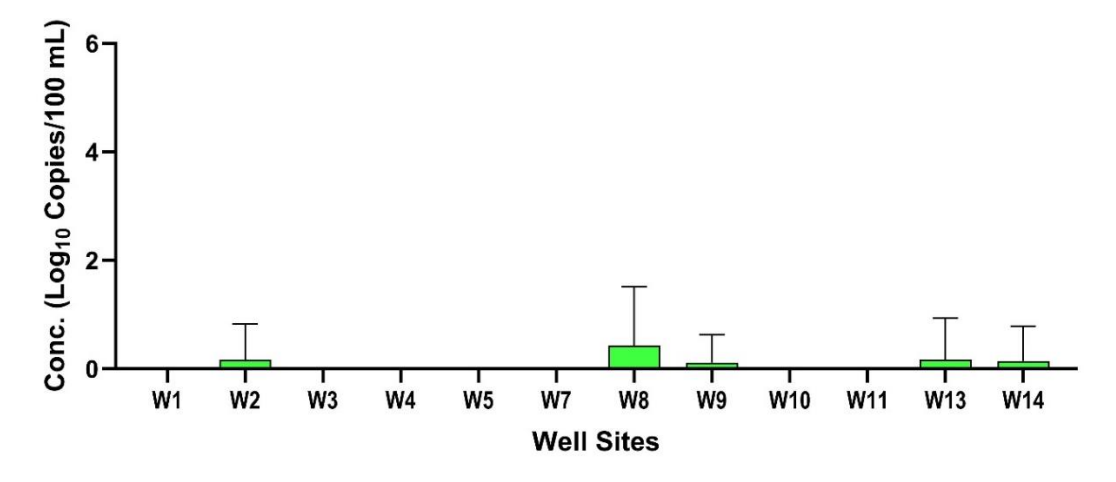
Figure 4.2. Temporal variation of enterococci concentration using MST marker Entero1 across the study sites.

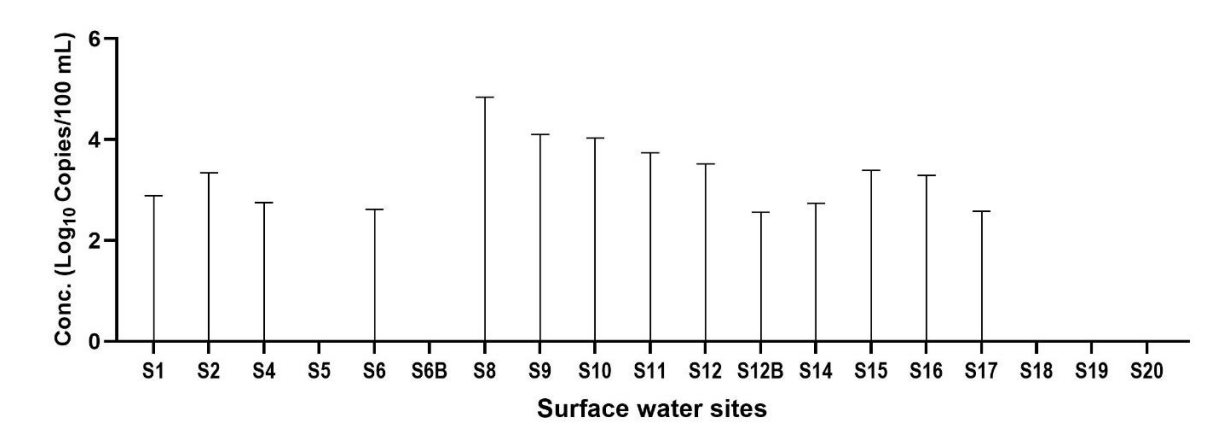
#### 4.4.3.2. Detection of human-associated marker

Human waste can be introduced in various aquatic environments from old and failing onsite sewage systems (OSSS), stormwater runoff, public portable washrooms adjacent to beach access, boat and fishing ramps, RV camp sides. Among three host-associated MST markers, human-associated marker HF183 was detected least frequently across Texas Gulf Coast throughout the study. 34 out of 807 water samples (4%) collected from collected from well, surface, and pore water sites contained HF183. The spatial and temporal distribution of HF183 is shown in Figure 4.3 and Figure 4.4. The abundance of HF183 was not statistically significant in well, surface water, and pore waters (Kruskal-Wallis test; p > 0.05). The marker HF183 was more prevalent in surface water (7%) than well (3%) and pore (1%) water. The concentration varied from 2.24 Log10 Copies/100 ml to 3.32 Log10 Copies/100 ml in well water. W1, W3, W4, W5, W7, W10, and W11 never showed any detection of HF183. For surface water, S10 showed highest detection frequency (21%) for HF183. The concentration of HF183 ranged from 2.38 Log10 Copies/100 ml to 4.84 Log10 Copies/100 ml in site S8. Surface water site S5, S6B, S18, S19, and S20 never displayed the presence of HF183. All surface water sites from Brazoria were positive for human associated marker. HF183 was detected only once in each site of P2 and PWB5 and the mean value of the concentration was 2.49 Log10 Copies/100 ml. No detection in other pore water sites indicated no human fecal contamination in pore water.

No month particularly showed statistically significant difference in abundance of HF183 for well water and pore water samples (Kruskal-Wallis test; p > 0.05). 19 months sampling exhibited significant difference in concentration of HF183 for surface water (Kruskal-Wallis test; p < 0.05). In well samples, HF183 was detected mostly during winter and spring/early spring which could be contributed by septic systems of rental houses near Gulf Coast during vacation periods. Abundance of HF183 in surface water did not show any significant pattern. All six months from December 2022 to May 2023 could be a concerning event. Higher detection frequency in surface water was found in July 2022, April and May 2023. Overall, majority of the

samples exhibited no detection of human-specific markers suggesting human fecal pollution was not severe compared to other hosts.





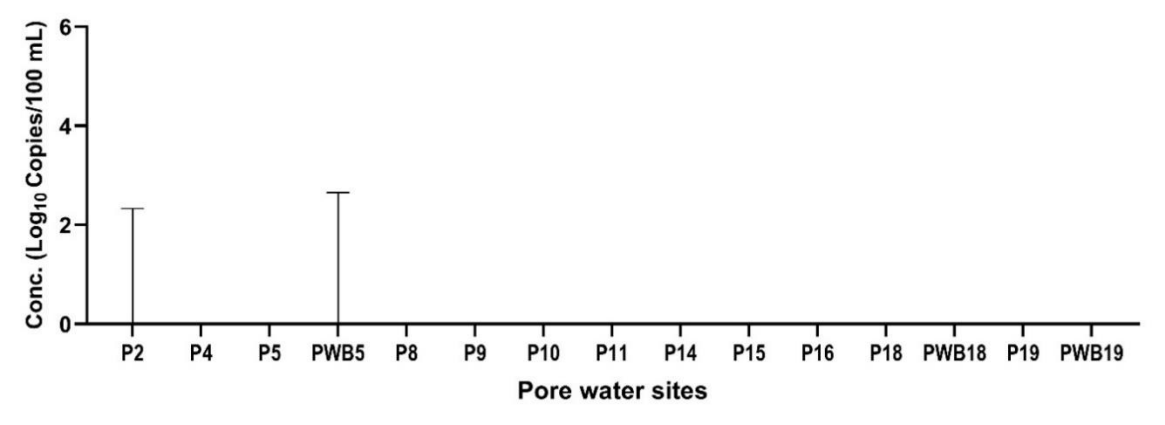
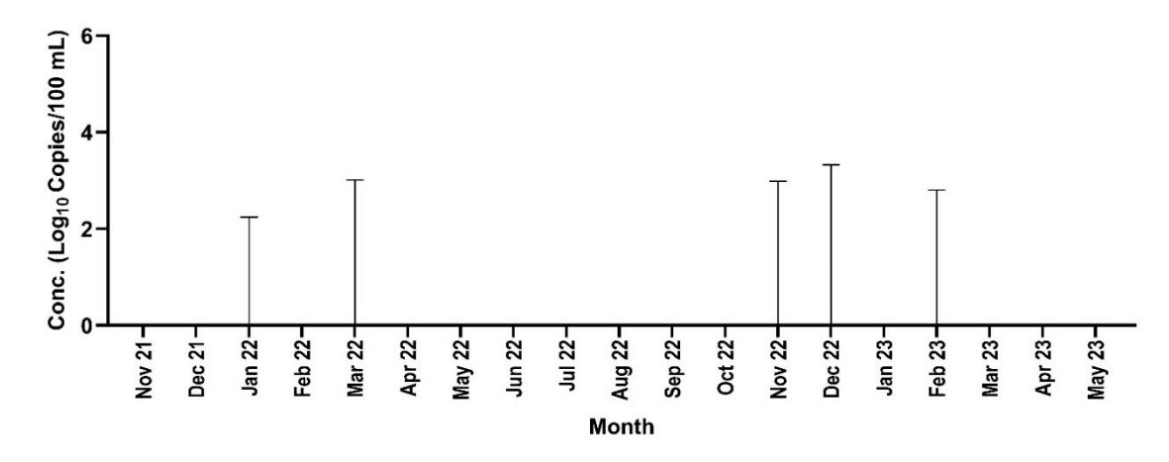
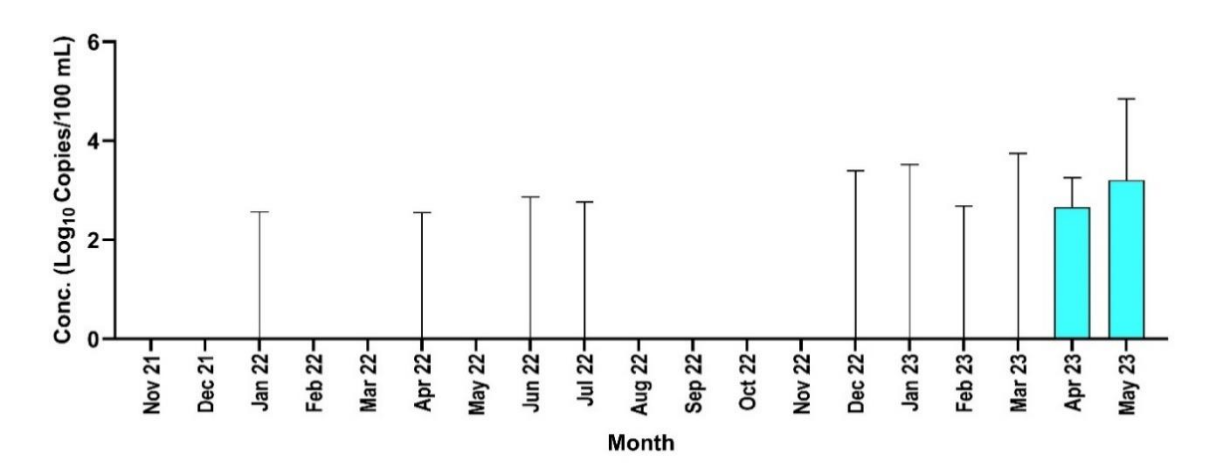


*Figure 4.3.* Spatial variation of Human fecal contamination using MST marker HF183 throughout the study period.





# Surface Water Sites



# Porewater Sites

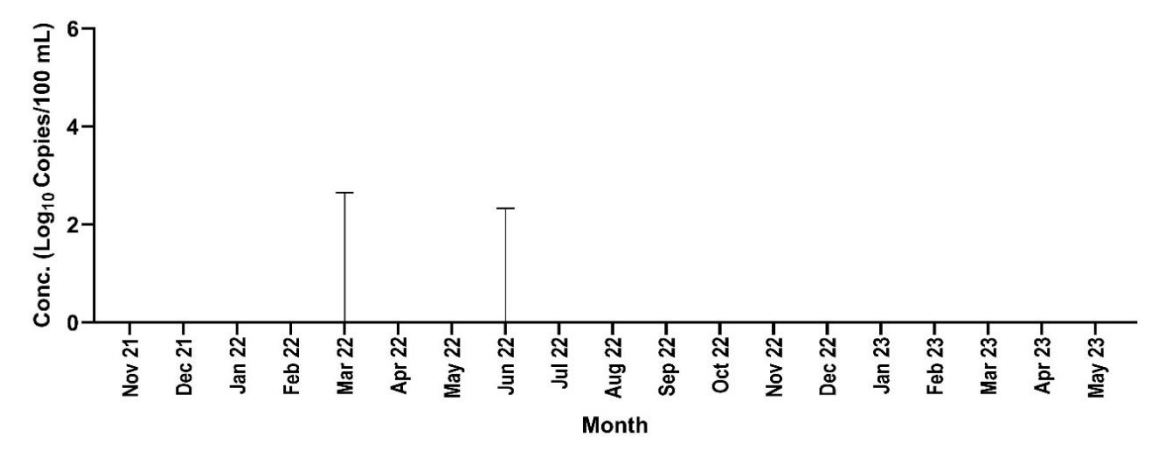


**Figure 4.4.** Temporal variation of Human fecal contamination using MST marker HF183 throughout the study period.

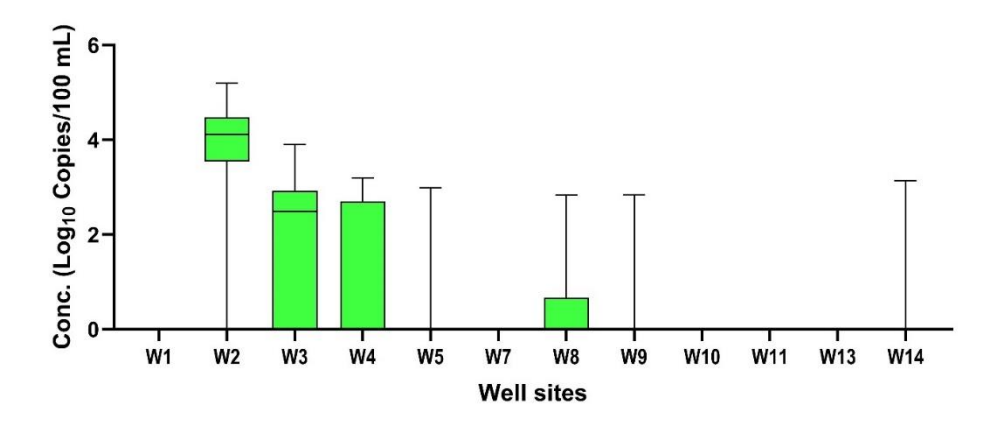
# 4.4.3.3. Detection of canine-associated marker

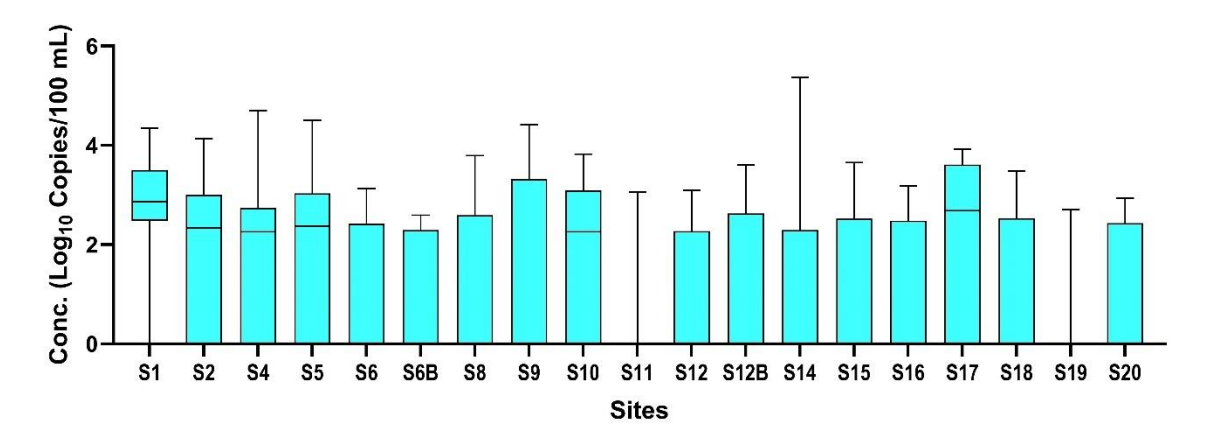
Similar to other markers, Canine fecal marker BacCan was detected for frequently in surface water (40% of samples) than well (19%) and pore water (3%) (**Figure 4.5**). The variation of the concentration of BacCan was statistically significant in well water samples (Kruskal-Wallis test; p < 0.05) with a range from 2.30 Log10 Copies/100 ml and 5.19 Log10 Copies/100 ml. Most contaminated wells were W2, W3, and W4 located in Galveston County. W2 encountered consistent dog pollution with a mean concentration of 3.85 Log10 Copies/100 ml. W1, W7, W10, W11, W13 were most clean well sites with no detection of BacCan throughout the study.

All surface water sites received dog pollution in various detection frequency (11% to 89%) at some point throughout the study period. Statistically significant difference was found in the level of BacCan marker in surface water sites (Kruskal-Wallis test; p < 0.05). The concertation of BacCan varied from 2.22 Log10 Copies/100 ml to 5.37 Log10 Copies/100 ml. The most frequent dog fecal contamination occurred in S2 with a mean value of 2.71 Log10 Copies/100 ml. Considerable contamination was detected in S2, S4, S5, S10, and S17 with more than 50% detection of BacCan marker.

No significant difference in the level of BacCan marker was yielded in pore water samples (Kruskal-Wallis test; p > 0.05). The marker was detected only once in P2, P4, P5, PWB5, P8, and PWB19 with a range from 2.25 Log10 Copies/100 ml to 4.22 Log10 Copies/100 ml.

Unlike well and pore water samples, the concertation of BacCan in surface water varied significantly over 19 months of sampling (Kruskal-Wallis test; p < 0.05). Relatively high concentration for BacCan was observed in Spring and winter time in all type of sites (**Figure 4.6**). Surface water encountered dog contamination more frequently in Winter months. In Texas, the outside temperature is more favorable during these times. Pet owners might spend recreational time at rental houses and at the beach. High levels of dog fecal waste in Texas Gulf Coast could be associated with large number of unrestrained dog population visiting and engaging seasonal recreational activities.





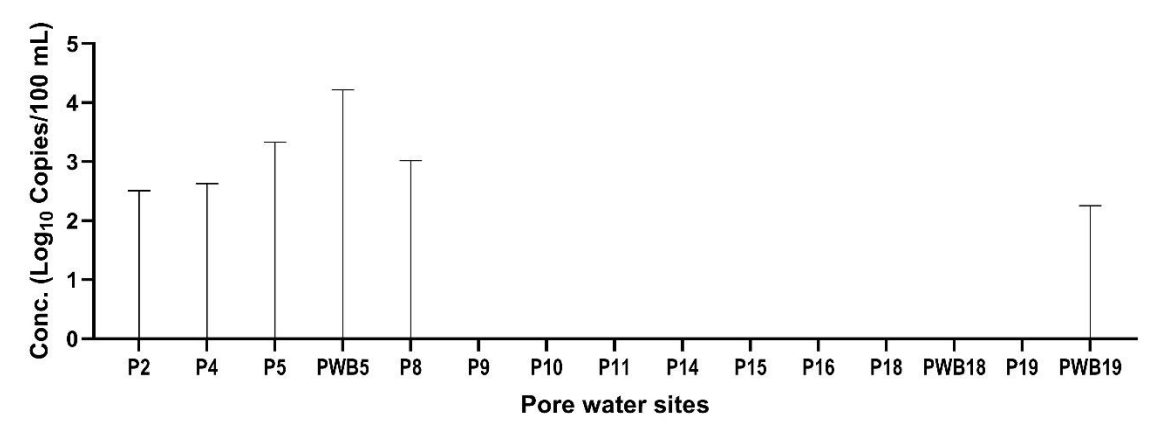


Figure 4.5. Spatial variation of Canine fecal contamination using MST marker BacCan throughout the study period.

## Well Water Sites Conc. (Log<sub>10</sub> Copies/100 mL) Apr 23-May 23-Dec 21-Jan 22-Feb 22-Apr 22-May 22-Jun 22-Jul 22-Sep 22-Oct 22-Jan 23-Feb 23-Mar 23-Mar 22-Aug 22-Nov 22-Conc. (Log<sub>10</sub> Copies/100 mL) Surface water Nov 21-Dec 21-Apr 22-Jun 22-Aug 22-Oct 22-Jan 22-Feb 22-Mar 22-May 22-Jul 22-Sep 22-Nov 22-Dec 22-Jan 23-Feb 23-Mar 23-Apr 23-May 23-Conc. (Log<sub>10</sub> Copies/100 mL) Porewater Sites



Jul 22-

Aug 22-

Month

Sep 22-

Oct 22-

Nov 22-

Dec 22-

Jan 23-

Feb 23-

Mar 23-

Apr 23-

May 23-

Nov 21-

Dec 21-

Jan 22-

Feb 22-

Mar 22-

Apr 22-

May 22-

Jun 22-

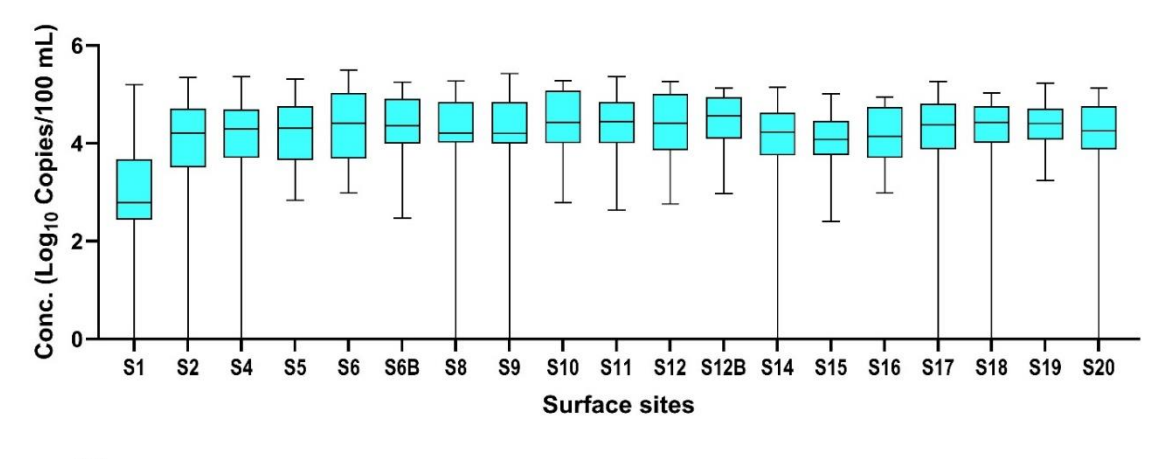
# 4.4.4.4. Detection of avian-associated marker

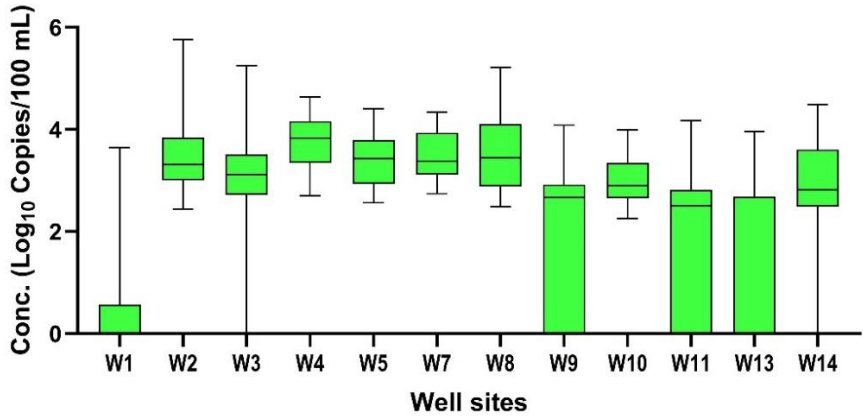
Among the host-specific fecal markers, GFD was consistently present in all types of sites (**Figure 4.7**). Texas is in the migratory route for various species of birds flying during fall/winter seasons, especially in coastal areas due to humid weather. Texas is a residence for all season birds; therefore, the GFD marker was detected frequently throughout the study. However, the MST marker GFD is designed for detecting *Helicobacter* sp., which is present in a wide range of avian species, including seagulls, waterfowls, and other birds. The concertation of the GFD marker was observed to be relatively higher in surface water than in well and pore water, indicating gull feces as a potential source of concern in the Texas Gulf Coast (**Figure 4.7**). Temporal concentration varied in a statistically significant manner (Kruskal-Wallis test; p < 0.05) in all types of samples for 19th-month sampling (**Figure 4.8**).

The concentration of GFD varied significantly across different well sites (Kruskal-Wallis test; p < 0.05) with a range of concentration from 2.25 Log10 Copies/100 ml to 5.76 Log10 Copies/100 ml. The mean concentration of the GFD marker ranged from 0.66 Log10 Copies/100 ml to 3.77 Log10 Copies/100 ml. W2, W4, W5, W7, W8, and W10 were the most contaminants well sites by gull fecal marker showing 100% detection of GFD.

No significant variation in GFD abundance was found in surface water samples (Kruskal-Wallis test; p > 0.05). High detection frequency was observed in all surface water sites (83% to 100%). The concentration varied from 2.39 Log10 Copies/100 ml to 5.49 Log10 Copies/100 ml in surface water samples. Except for S1, the concentration of the GFD marker was consistently prevalent, with a mean concentration of 3.99 Log10 Copies/100 ml to 4.44 Log10 Copies/100 ml.

Statistically significant variation was not observed in pore water samples for the GFD marker (Kruskal-Wallis test; p > 0.05). The lowest and highest concentrations of GFD were found both in P18 (2.23 Log10 Copies/100 ml and 5.09 Log10 Copies/100 ml). The mean concentration of GFD in pore water varied from 1.91 Log10 Copies/100 ml to 3.16 Log10 Copies/100 ml.





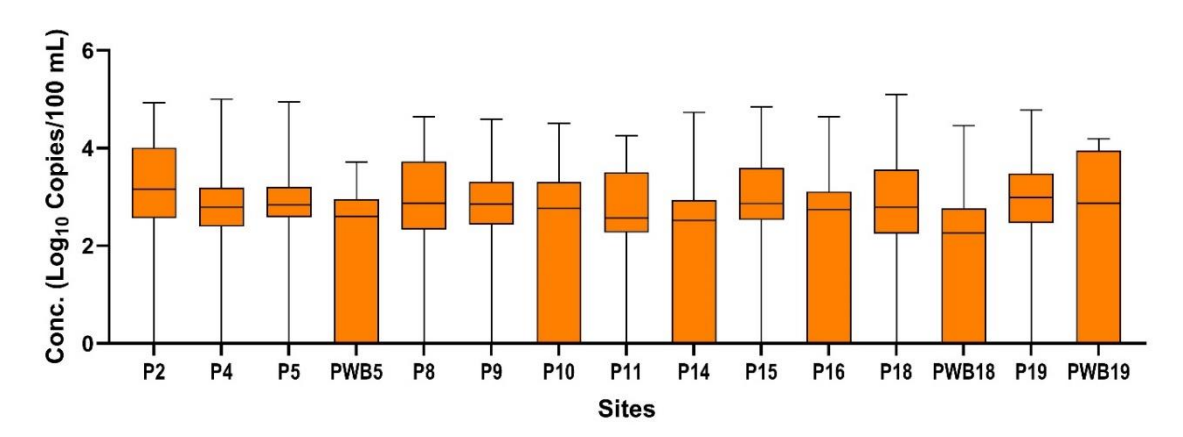


Figure 4.7. Spatial variation of Gull fecal contamination using MST marker GFD throughout the study period.

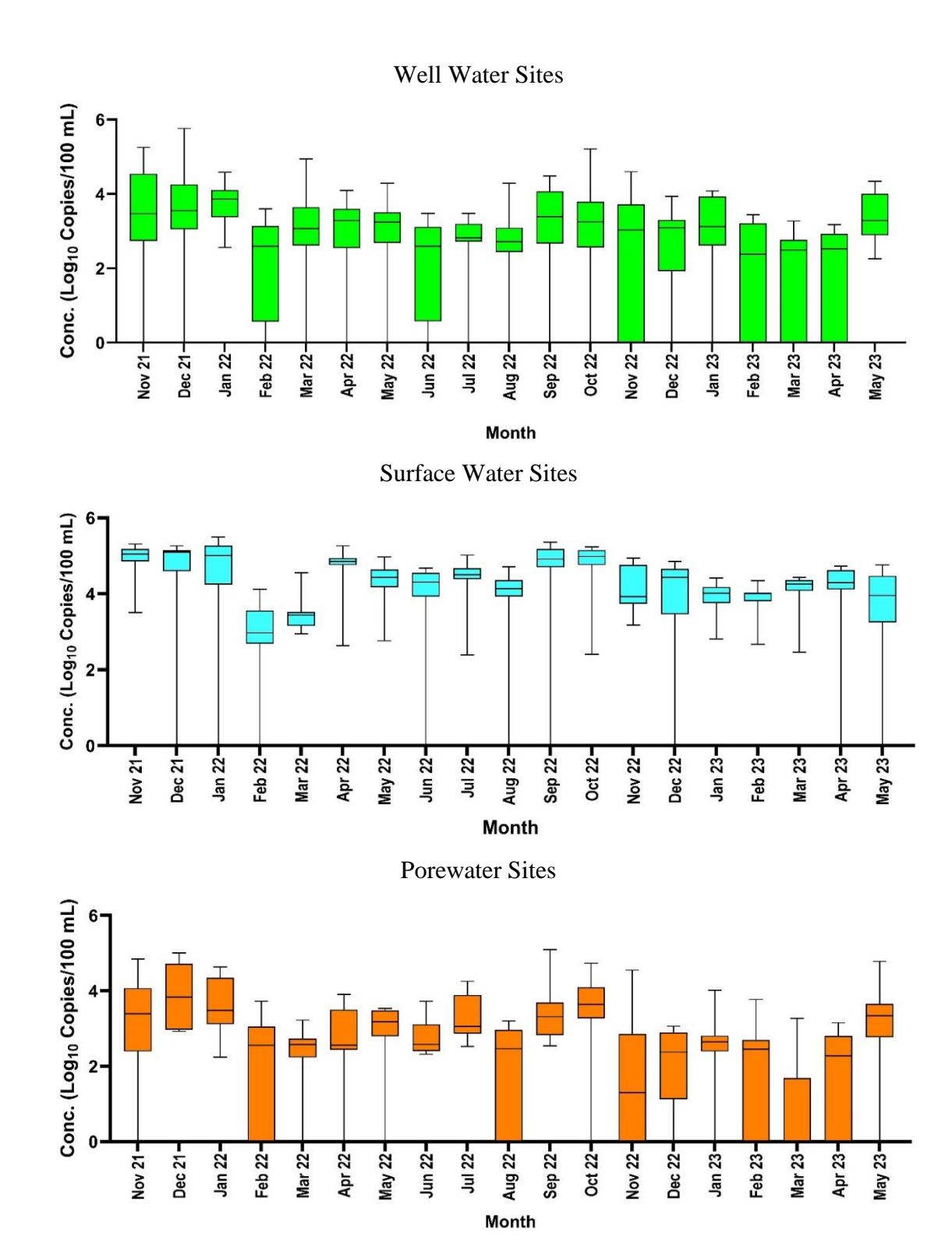


Figure 4.8. Temporal variation of Gull fecal contamination using MST marker GFD across study sites.

#### 4.5. Conclusion/Recommendation

The following conclusions have been drawn from this study for the study area:

- The general marker (enterococci) exhibited highest levels and a similar spatial distribution pattern across the sampling sites. Among the host-associated markers, low levels were observed for the human-associated markers and the highest levels for GFD, suggesting a higher percentage of fecal pollution to be coming from the large bird populations in the study area.
- The predominant sources of fecal contamination identified in the study area were, in ranked decreasing order of presence: avian including gull, ducks etc., dog and humanderived.
- The concentrations of the GFD genetic marker were relatively higher at all surface water sites and well water sites suggesting that bird fecal pollution is a major source of concern for Texas Gulf coast. The canine marker was consistently higher in the surface water sites as compared to well water sites.
- BacCan exhibited higher concentrations during the end of fall and winter and were all lowest during the summer months.
- Data from this study have established a baseline for fecal pollution sources in the study area and can be used for the recommendation and implementation of best management practices that can accurately and cost effectively prevent, control, and remediate fecal pollution events and maintain water quality.

#### Recommendations for the Texas GLO include:

- Secure resources/funding to implement necessary improvements in management programs and enforcement mechanisms that will mitigate the public health risk by reducing animal and human-derived sources and other readily controllable sources of fecal contamination, including:
  - Domestic Pet Waste Education and outreach to homeowners regarding proper disposal of domestic pet waste.
  - Bird Fecal Waste Identify birds that are polluting the water and develop bird relocation efforts to reduce hazards associated with large bird populations.
  - On-Site Septic Systems
    - Ongoing homeowner education regarding septic system maintenance and homeowner inspections of septic systems.
    - Investigate, identify, and repair or replace problematic septic systems in the contributing zone.
- Improve storm water management programs, including the promotion of Low Impact Development (LID) such as the reduction of effective impervious surfaces, dispersion of storm water runoff to vegetated areas, and Best Management Practices that are appropriate to the site-specific conditions.
- Use the results from this study to evaluate current wastewater infrastructure and on-site septic system management programs and water quality monitoring plans in the recharge and contributing zones. Re-examine implementation strategies and modify if necessary to achieve long-term water quality objectives.
- Implement a change in drainage architecture which supports a more diverse biological habitat around the creeks that could produce a reduction in downstream bacterial input. For example, pouring of concrete channels around the creek to avoid runoff from directly

- entering the stream.
- Continue outreach (including dissemination of related study results) to the public about nonpoint source pollutant sources and steps that can be taken to mitigate those sources that are human-derived and controllable through improved management programs and enforcement mechanisms that will benefit ecosystem and public health.
- Continue emphasis on improving MST methodologies, including efforts that will encourage accessibility and use of these tools in a streamlined and cost-effective manner.

#### 4.6. References

- Green, H.C., Dick, L.K., Gilpin, B., Samadpour, M. and Field, K.G. 2012. Genetic markers for rapid PCR-based identification of gull, Canada goose, duck, and chicken fecal contamination in water. Appl Environ Microbiol 78(2), 503-510.
- Green, H.C., Haugland, R.A., Varma, M., Millen, H.T., Borchardt, M.A., Field, K.G., Walters, W.A., Knight, R., Sivaganesan, M., Kelty, C.A. and Shanks, O.C. 2014. Improved HF183 quantitative real-time PCR assay for characterization of human fecal pollution in ambient surface water samples. Appl Environ Microbiol 80(10), 3086-3094.
- Hinojosa, J., Green, J., Estrada, F., Herrera, J., Mata, T., Phan, D., Pasha, A.B.M.T., Matta, A., Johnson, D. and Kapoor, V. 2020. Determining the primary sources of fecal pollution using microbial source tracking assays combined with land-use information in the Edwards Aquifer. Water Research 184, 116211.
- Kildare, B.J., Leutenegger, C.M., McSwain, B.S., Bambic, D.G., Rajal, V.B. and Wuertz, S. 2007. 16S rRNA-based assays for quantitative detection of universal, human-, cow-, and dog-specific fecal Bacteroidales: a Bayesian approach. Water Res 41(16), 3701-3715.
- Ludwig, W. and Schleifer, K.-H. 2000. How Quantitative is Quantitative PCR with Respect to Cell Counts? Systematic and Applied Microbiology 23(4), 556-562.

# 5. TASK 3: QUANTIFICATION AND SOURCE TRACKING OF NUTRIENT INPUTS

# Prepared by: Erin Taylor and J. David Felix, Ph.D.

#### 5.1. Executive Summary

This study examines nitrogen loading to coastal waters from Matagorda to Galveston Island, utilizing stable isotope techniques to identify the sources and processes driving nitrogen contamination. Over an 18-month period (November 2021 to April 2023), monthly water samples were collected to measure nitrate, ammonium, and dissolved organic nitrogen concentrations, along with their isotopic composition, in surface, pore, and groundwater. Nitrate concentrations in surface  $(3.4 \pm 5.2 \,\mu\text{M})$  and porewaters  $(4.3 \pm 7.1 \,\mu\text{M})$  were consistent with typical environmental conditions reported in previous studies. In comparison, nitrate concentrations in groundwater (34.4  $\pm$  113.5  $\mu$ M) were notably higher than expected background levels (11 µM). Isotope mixing models indicated that nitrate in all water matrices was predominantly sourced from septic/sewage systems, with contributions exceeding 50% in all cases. During the summer, there was a rise in nitrate contributions from septic and sewage systems, likely reflecting increased tourist activity. Interestingly contributions from combined dog/gull waste increased in winter, aligning with avian migratory patterns. Dual isotope trends revealed seasonal changes in nitrate processing across sample matrices. Surface waters exhibited competition between denitrification, assimilation, and nitrification, while porewaters primarily reflected denitrification and dissimilatory nitrate reduction to ammonia (DNRA) in most seasons, with denitrification dominant in summer. Groundwater with high nitrate concentrations showed competition between anammox, denitrification, and nitrification, while groundwater with low nitrate concentrations predominantly experienced denitrification and nitrification.

Surface water NH<sub>4</sub><sup>+</sup> concentrations averaged  $4.9 \pm 9.4 \mu M$ , which are higher than typical open ocean levels, with seasonal trends showing a decrease in summer due to assimilation processes. In porewater, NH<sub>4</sub><sup>+</sup> was the dominant nitrogen species, with an average concentration of  $27.7 \pm 40.6 \,\mu\text{M}$ , exhibiting seasonal peaks in spring and summer, likely driven by increased microbial remineralization and DNRA. Groundwater in the region showed unusually high NH<sub>4</sub><sup>+</sup> concentrations, averaging  $158.9 \pm 345.2 \,\mu\text{M}$ , which likely indicates a direct NH<sub>4</sub><sup>+</sup> source. Groundwater NH<sub>4</sub><sup>+</sup> concentrations were categorized into three tiers based on concentration levels: the highest tier (wells 5 and 7) had concentrations of  $507.8 \pm 335.8 \,\mu\text{M}$ ; the middle tier (wells 3, 10, and 11) had concentrations of  $118.4 \pm 108.1$  µM; and the lowest tier (wells 1, 2, 4, 8, 9, 13, and 14) had concentrations of  $41.7 \pm 123.4 \,\mu\text{M}$ .  $NH_4^+$  concentrations were inversely related to  $\delta^{15}$ N-NH<sub>4</sub><sup>+</sup> values of:  $6.8 \pm 5.1\%$  for the highest tier,  $10.5 \pm 8.8\%$  for the middle tier, and  $15.0 \pm 8.1\%$  for the lowest tier. Wastewater effluent (3.9 ± 2.8%) had a  $\delta^{15}$ N-NH<sub>4</sub><sup>+</sup> value similar to the highest tier, suggesting direct septic source contamination with minimal processing in high-concentration wells. Microbial processing of NH<sub>4</sub><sup>+</sup> preferentially uses the lighter <sup>14</sup>N isotope, leading to an increase in the remaining  $\delta^{15}$ N-NH<sub>4</sub><sup>+</sup>, which explains the higher  $\delta^{15}$ N values in lower concentration wells that have undergone more processing before reaching the water table.

Surface water had an average DON concentration of  $7\pm5~\mu M$ , with higher concentrations observed in fall ( $10\pm4~\mu M$ ) and summer ( $9\pm4~\mu M$ ), likely due to increased organic matter input and microbial activity. A significant correlation between inverse DON concentrations and  $\delta^{15}$ N-DON values indicated source mixing, leading to higher DON levels in summer and fall, potentially from marine and wastewater-derived DON, with a minimal yet

greater contribution from wastewater in summer compared to fall. Porewater DON concentrations averaged  $7\pm8~\mu M$ , with no significant seasonal variations. Correlations between DON concentrations and  $\delta^{15}N\text{-NH}_4^+$  supported  $NH_4^+$  production via remineralization in the sediments. Groundwater DON concentrations averaged  $21\pm58~\mu M$ , with higher concentrations  $(48\pm123~\mu M)$  observed in wells 5 and 7, located near septic systems, suggesting potential contributions from septic effluent. However, the low  $\delta^{15}N\text{-DON}$  values in groundwater imply additional processing or source contributions, such as soil-derived organic matter.

Rising water tables reduce the amount of unsaturated soil available for wastewater filtration, thereby diminishing the effectiveness of on-site sewage facilities OSSFs. This trend is supported by findings from this study, where [NO<sub>3</sub>] was positively (though insignificant) correlated with depth to water (DTW),  $\delta^{15}$ N-NO<sub>3</sub> was positively correlated with DTW, [NH<sub>4</sub><sup>+</sup>] was negatively correlated (p = 0.0026) with DTW, and  $\delta^{15}$ N-NH<sub>4</sub><sup>+</sup> was positively correlated with DTW. Septic discharge typically contains 70-90% NH<sub>4</sub><sup>+</sup>, and when there is more space between the septic discharge field and the water table (i.e., greater DTW), there is more opportunity for  $NH_4^+$  to be nitrified to  $NO_3^-$ , which can then be denitrified to harmless  $N_{2(g)}$ . In this scenario, NH<sub>4</sub><sup>+</sup> is processed before it reaches the water table, and any residual NO<sub>3</sub><sup>-</sup> that is not denitrified to  $N_2$  would enter the groundwater with high  $\delta^{15}N-NO_3$  values due to partial denitrification. In contrast, when DTW is low, septic discharge may directly reach the water table, causing unprocessed NH<sub>4</sub><sup>+</sup> to enter the groundwater at high concentrations with an isotopic signature reflective of the septic source. This scenario likely explains the high NH<sub>4</sub><sup>+</sup> concentration wells with low  $\delta^{15}$ N-NH<sub>4</sub>+values, similar to the wastewater NH<sub>4</sub>+ isotopic signature (+3.9 ± 2.8%). The evidence suggests that the high NH<sub>4</sub><sup>+</sup> concentrations, along with the lowest DTW values, indicate compromised OSSFs, likely due to sea level variations, which could be a significant issue in this region.

#### 5.2. Background

Nitrogen is an essential growth-limiting nutrient for primary producers in marine ecosystems, however excessive nutrient inputs caused by anthropogenic activities are negatively affecting coastal waters worldwide (Gotkowska-Płachta et al., 2016; Yang et al., 2019). These inputs can lead to eutrophication, triggering harmful algal blooms that threaten aquatic food and water supplies, as well as the formation of dead zones that result in fish and shellfish mortality. Furthermore, excess nitrogen contributes to greenhouse gas emissions and overall water quality degradation, creating unsafe conditions for recreation and aquaculture (Anderson et al., 2008; Ji et al., 2017).

When assessing nitrogen's effects on ecosystems, it is important to consider its various forms. Total dissolved nitrogen (TDN) in a system consists of both dissolved organic nitrogen (DON) and dissolved inorganic nitrogen (DIN). DIN, which includes nitrite (NO<sub>2</sub>-), nitrate (NO<sub>3</sub>-), and ammonium (NH<sub>4</sub>+), has traditionally been the primary focus in studies of nitrogen loading into water bodies. In contrast, DON is a complex mixture of molecules such as—but not limited to—urea, amino acids, and proteins (Yang et al., 2019). Sources of DIN and DON contamination from anthropogenic activities include animal waste, fertilizers, wastewater outfalls, septic tanks, and stormwater runoff (Davidson et al., 2014; Gotkowska-Płachta et al., 2016; Middelburg et al., 2001). Co-occurring pollutants can help identify the primary sources of nitrogen loading. For example, fecal indicator bacteria (FIB) can serve as a marker for contamination from human or animal waste, aiding in pinpointing the sources impacting water bodies.

According to the National Oceanic and Atmospheric Administration (NOAA), approximately 40% of the U.S. population resides in coastal counties, and this number continues

to grow. As urbanization expands in these areas, the need for water quality monitoring and public notification programs becomes increasingly critical. Fecal indicator bacteria are commonly used to assess the sanitary quality of water for recreational, industrial, and water supply purposes. Data from the National Water Quality Council reveals that in 2018, around 58% of all beaches analyzed in the United States and Puerto Rico had bacteria levels exceeding the recommended Beach Action Value (104 units per 100 mL water) on at least one occasion. This included exceedances at 85% of Gulf Coast sites and 45% of East Coast beaches (Water Quality Portal). These contamination events are expected to rise nationwide due to climate change-induced factors such as increasing temperatures, extreme weather events, and intensified precipitation, coupled with growing coastal populations (Powers et al., 2021; Elmir, 2018). Addressing this growing issue is challenging, as contamination can stem from a variety of point and nonpoint sources.

Point source pollution originates from a single, identifiable source, such as a pipe, industrial stormwater discharge, or factory smokestack. In contrast, nonpoint source (NPS) pollution arises from diffuse, unconfined areas, making it challenging to pinpoint the exact sources. According to the EPA, NPS pollution typically results from land runoff containing fertilizers and animal wastes, precipitation, drainage, seepage, or malfunctioning septic systems. Faulty septic systems are hypothesized to be a major contributor to elevated fecal indicator bacteria (FIB) levels in coastal areas and may also play a role in excess nitrogen loading (Powers et al., 2021). On-site sewage facilities (OSSFs) are septic systems that treat and dispose of wastewater on the same property where it is generated. These systems are most prevalent in rural areas, barrier islands, and other locations where sewer infrastructure is difficult to establish; approximately 24% of U.S. homes are served by OSSFs (Hoghooghi et al., 2021). A typical OSSF consists of a septic tank for primary wastewater treatment, followed by effluent discharge to the soil, where soil layers act to adsorb, purify, and filter contaminants before the effluent mixes with groundwater. However, improperly installed or failing OSSFs may not provide sufficient residence time or proper conditions to effectively treat nitrate and other pollutants before mixing with groundwater (TGPC, 2019; OSSF Information System). Groundwater seepage contaminated by such effluent can infiltrate porewater, a key medium for solute transport to surface waters in coastal zones or streams. This porewater exchange can directly contribute to nutrient overloading in surface waters, resulting in eutrophication (Anderson et al., 2008; Krause et al., 2009; Sadat-Noori et al., 2019).

Although the contributions of OSSFs to coastal nitrogen loading are not well understood, recent reports indicate that septic system malfunctions are increasingly linked to sea level variations and more frequent heavy precipitation events. These factors have been associated with both fecal and nitrogen pollution (Powers et al., 2021; Elmir, 2018). Rising water tables reduce the amount of unsaturated soil available for wastewater filtration, thereby diminishing the effectiveness of OSSFs. Coastal communities face heightened risks of OSSF failures due to sandy, porous soils, erosion, severe weather events, and the impacts of sea level variations driven by climate change (Mallin, 2013). Additionally, many OSSFs are old or undocumented, as permits were not required before the Clean Water Act of 1972. These aging systems are at greater risk of malfunction, potentially contaminating groundwater and drinking water supplies with pathogens, nutrients, and other harmful substances. While fecal indicator bacteria (FIB) can signal failing systems, it is essential to identify and trace all potential sources of contamination, including OSSFs, to better understand their role in nonpoint source pollution. One effective

method for this is the analysis of stable nitrogen isotopes in co-migrating nitrogen species within affected waters, which can help determine the contribution of OSSFs to nutrient pollution.

In nature, nitrogen exists as two stable isotopes:  $^{14}N$  and  $^{15}N$ , having a mass of either 14 atomic mass units (amu) or 15 amu, respectively (Middelburg et al., 2001). Organisms generally prefer incorporating  $^{14}N$  over  $^{15}N$ , due to its lower atomic mass and lower energy requirements (Craine et al., 2015). This causes  $^{15}N$  and  $^{14}N$  to have different reaction rates, resulting in fractionation. The ratio of these isotopes ( $^{15}N/^{14}N$ ) can be unique for each nitrogen source and serve as a "source signature". The isotopic composition ( $\delta^{15}N$ ) of these sources is determined by comparing their nitrogen isotope ratios to the nitrogen international reference standard, atmospheric  $N_2$ , which is reported as 0% by definition (Junk and Svec, 1958). Isotopic composition is expressed in terms of a delta ( $\delta$ ) value expressed in permil (%) units difference from this reference standard:

 $\delta$ =(R<sub>sample</sub>/R<sub>standard</sub> -1) x 1000 where "R" is the ratio of the heavy to light isotope.

These unique stable isotope ratios of nitrogen have been used for tracing sources in the environment (**Table 5.1**). For example, sources of nitrate such as septic/wastewater influent ( $\delta^{15}N = +14.9\% \pm 3.5\%$ ) and animal waste ( $\delta^{15}N = +15\% \pm 10\%$ ) are often more enriched in <sup>15</sup>N than other sources such as fertilizers ( $\delta^{15}N = -0.9\% \pm 1.9\%$ ), wet deposition ( $\delta^{15}N = -1.9 \pm 3.5\%$ ), and soil ( $+5\% \pm 2\%$ ) (Kendall et al., 2007; Cox, *in prep*; Qiu et al., 2024; Xue et al., 2009). Ammonium sources from untreated sewage have  $\delta^{15}N$  values of +5 to +9%, while fertilizers have a range of  $\delta^{15}N = -3.9\% \pm 0.3\%$ , livestock waste values are  $+7.4 \pm 3.8\%$ , and wet deposition values range from  $-3.1\% \pm 4.0\%$  (Choi et al., 2007; Qiu et al., 2024; Cole et al., 2006; Maeda et al., 2016). Organic nitrogen sources include fertilizers ( $\delta^{15}N = 0.3\% \pm 0.2\%$ ), wet deposition ( $\delta^{15}N = -7.0\%$  to +13.1%), sewage/septic ( $\delta^{15}N = +22.3\% \pm 7.9\%$ ), and livestock waste ( $\delta^{15}N = +7.8 \pm 0.6\%$ ) (Liu et al., 2021; Liu et al., 2017; Qiu et al., 2024).

**Table 5.1.** Potential sources of nitrogen and their corresponding isotopic values. These unique isotope signatures can be used to determine pollutant contributions in affected waters.

Source	$\delta^{15}$ N-NO <sub>3</sub>	δ <sup>18</sup> O-NO <sub>3</sub> -	$\delta^{15}$ N-NH <sub>4</sub> <sup>+</sup>	δ <sup>15</sup> N-DON
Synthetic	$-0.9\%$ $\pm 1.9\%$	$22\%0 \pm 3\%0$	$-3.9\% \pm 0.3\%$	$0.3\% \pm 0.2\%$
Fertilizer	(Kendall et al., 2007)	(Jung et al., 2020)	(Choi et al., 2007)	(Liu et al., 2021)
Wet	$-1.9\%$ $\pm 3.5\%$	$+64.6\% \pm 7.8\%$	$-3.1\%$ $\pm 4.0\%$	-7.0% to $+13.1%$
Deposition	(Qiu et al., 2024)	(Qiu et al., 2024)	(Qiu et al., 2024)	(Liu et al., 2017;
				Qui et al., 2024)
Sewage/Septic	$+14.9\%$ $\pm 3.5\%$	$+19.3\% \pm 2.6\%$	$+3.9 \pm 2.8\%$	$+22.3\%$ $\pm 7.9\%$
	(Cox, 2023)	(Cox, 2023)	(Cox 2023)	(Qiu et al., 2024)
Livestock	$+15\%$ $\pm 10\%$	+4‰ ± 4‰ (Maeda	$+7.4\%$ $\pm 3.8\%$	+7.8%0 ± 0.6%
Waste	(Xue et al., 2009)	et al., 2016)	(Maeda et al.,	(Liu et al., 2021)
			2016)	
Soil	$+5\%$ $\pm 2\%$	$5.2\% \pm 0.4\%$ (Nikolei	nko et al., 2018)	
	(Nikolenko et al., 2018)			

While many nitrogen sources have unique isotopic signatures, different biological processes of the nitrogen cycle can have fractionation effects that alter the original isotopic composition (**Table 5.2**). Strong fractionation is associated with dissimilatory processes, while weak fractionation is associated with assimilatory processes such as primary production (Ryabenko, 2013). Dissimilatory processes include denitrification, reduction of nitrate to

ammonium (DNRA) in suboxic to anoxic conditions, nitrification, and anaerobic oxidation of ammonium (anammox) (Ribot et al., 2017). In denitrification, nitrate is used to oxidize organic matter, causing the production of N<sub>2</sub>O, NO<sub>x</sub>, and N<sub>2</sub>. This is considered a net loss of DIN if these compounds leave as gases; otherwise, these will remain as inorganic N compounds. A competing nitrate reduction process, DNRA, is the anaerobic reduction of nitrate to nitrite, and then to ammonium. Research suggests that DNRA starts to be favored over denitrification with rising salinity and increasing temperature. This is also the case with a high DOC:NO<sub>3</sub><sup>-</sup> ratios (Giblin et al., 2013; Gao et al., 2021). Nitrification is the oxidation of ammonium to nitrate and is used to meet energy demands of plants. Nitrification has been shown to increase with ammonium concentrations, especially in streams receiving wastewater effluents (Ribot et al., 2017). Other processes include anammox, where nitrite is combined with ammonium to produce nitrogen gas under anaerobic conditions, and remineralization, where organisms consume organic nitrogen and convert some of it back to ammonium (Kartal et al., 2010; Möbius, 2013).

Nitrification is associated with a fractionation of -35 to 0‰, while denitrification is associated with an effect of +5 to + 25‰ (Granger and Wankel, 2016). Other processes and their corresponding enrichment factors are  $NO_3^-$  uptake (5.9‰ ± 3.7‰),  $NH_4^+$  uptake (9.4‰ ± 6.6‰), anammox (– 31‰), remineralization/ammonification (-2.3 to 0‰), and nitrogen fixation (–3 to + 1‰) (Denk 2017; Brunner, et al., 2019; Kendall et al., 2007; Yu et al., 2021) (**Table 5.2**). Nitrogen isotope ratio data can also help discern if a reaction is complete; for example, incomplete nitrification of ammonium would cause lower  $\delta^{15}N$ - $NO_3^-$  than that of the initial ammonium  $\delta^{15}N$  value (Murgulet and Tick, 2013). It is important to take these processes and unique source signatures into account to determine nitrogen inputs and cycling in different regions and ecosystems.

*Table 5.2.* Nitrogen processes and their corresponding enrichment factors.

Process	<b>Enrichment Factor (ε)</b>	Reference
Nitrification	-35‰ to 0‰	Granger and Wankel, 2016
Denitrification	+5‰ to +25‰	Granger and Wankel, 2016
NO <sub>3</sub> Uptake	$5.9\%$ $\pm 3.7\%$	Denk et al., 2017
NH <sub>4</sub> <sup>+</sup> Uptake	$9.4\% \pm 6.6\%$	Denk et al., 2017
Anammox	31‰	Brunner et al., 2013
Remineralization/Ammonification	-2.3‰ to +1‰	Yu et al., 2021; Mobius 2013;
		Kendall et al., 2007
Nitrogen Fixation	-3% to $+1%$	Kendall et al., 2007
DNRA	unknown	Inamdar et al., 2024

While nitrogen has been used to fingerprint sources of nitrate contamination and to analyze the effects of nitrogen processes, the identification of nitrogen sources and cycles using only  $\delta^{15}N$  values is limited because of overlapping values from the different nitrate sources. Analysis can therefore be combined with  $\delta^{18}O$  to reduce the uncertainty of nitrogen isotopes in identifying nitrate source contributions (Jung et al., 2020). The predictable changes in composition of both nitrogen and oxygen isotopes in nitrate in water can also help determine the extent to which a source has experienced nitrification (nitrate formation), assimilation (nitrate removal) and/or denitrification (nitrate removal) (Snow, 2018). These dual isotopes can then be plotted vs each other to identify sources and processing and also used in Bayesian-type mixing models to estimate source apportionment (Kendall et al., 2007; Zhang et al., 2018).

Identifying sources of contamination is becoming increasingly critical in regions like the Texas Gulf Coast, where the Texas Beach Watch program has reported rising levels of fecal indicator bacteria (FIB) over the past decade (**Figure 5.1**). From 2009 to 2019, the Texas General Land Office (TGLO) documented that, on average, 21.90% of water samples in Matagorda County exceeded the United States Environmental Protection Agency's (US EPA) Beach Action Value (104 MPN). Similarly, Brazoria County reported an average exceedance rate of 11.93%, while Galveston County averaged 7.09% exceedances during the same period (Powers et al., 2021). Brazoria and Matagorda Counties are particularly concerning, as 2019 enterococci concentrations were statistically higher than in other Texas coastal counties and showed a significant increase compared to previous years. Since there are relatively few point sources of FIB in these areas, it is suspected that nonpoint sources (NPS), particularly from on-site sewage facilities (OSSFs), are the primary contributors. According to the Texas Groundwater Protection

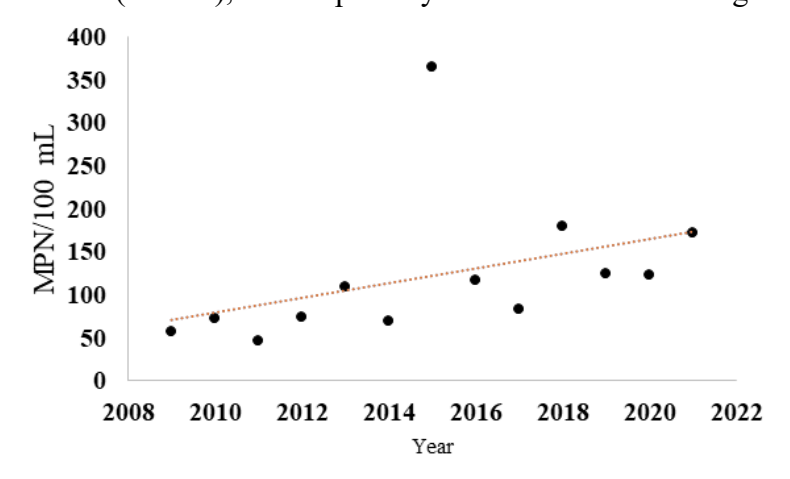


Figure 5.1. Temporal trends of water sample enterococci concentrations along Texas Gulf Coast beaches from 2009 to 2021 (Texas BeachWatch; Powers et al., 2021).

Committee (TGPC), approximately one in five homes in Texas relies on an OSSF for wastewater treatment and disposal, with numbers rapidly increasing along the Gulf Coast. Given the rapid growth of housing and OSSFs in this region, the Texas Commission on Environmental Quality (TCEQ) and Texas AgriLife regularly conduct inventories of septic systems in selected counties within the Coastal Zone of Texas. These inventories are essential for identifying malfunctioning OSSFs as part of

coastal NPS pollution control efforts. Many systems uncovered during these assessments are old or undocumented, placing them at the highest risk for malfunctions and associated water quality impacts.

Given the rising concerns about OSSF malfunctions and contamination, along with the lack of nutrient and DON data along the increasingly vulnerable Texas Gulf Coast, it is critical to identify the sources and drivers of nitrogen loading in Texas coastal waters. For Task 3, we employed stable isotope techniques to investigate the sources and processing of nitrogen loading to sandy barrier islands and coastal waters from Matagorda to Galveston Island. Groundwater elevations were continuously monitored throughout the project to assess whether water table fluctuations were associated with changes in nitrogen loading. The  $\delta^{15}$ N and nitrogen concentration data collected in this study provide valuable insights into the sources with the greatest impacts on water quality throughout the year in these coastal regions. The findings aim to inform the development of effective mitigation strategies to prevent water contamination, harmful algal blooms, and eutrophication. Additionally, monitoring the effects of sea level variations on nitrogen loading will equip stakeholders, landowners, and policymakers in coastal communities with the knowledge needed to prepare for varying sea levels and the broader impacts of climate change in the years to come.

#### 5.3. Methods

#### 5.3.1. Sample Collection

Samples were collected from various sites along the coast of Matagorda, Brazoria, and Galveston counties monthly from November 2021-May 2023 (Figure 4). Groundwater samples from wells are located within 200 meters from the shoreline at predetermined locations near septic systems. Corresponding pore and surface water sites (denoted by matching numbers in Figure 4) are located along a straight transect that was the closest distance from the well to the shore. Pore and surface water samples were collected ~6 m from the shoreline.

On-site physical and chemical properties of water collected included temperature, salinity, pH, conductivity, dissolved oxygen, and oxidation/reduction potential by a multi-probe YSI series six sonde. Surface water was collected at 20 cm below the air-water interface. Porewater was sampled from the sediment with a piezometer sampler attached to a peristaltic pump after the water ran clear (free from sand).

For groundwater sampling, before samples were collected, the well was purged by 3 well volumes. To determine the amount of stagnant water necessary to purge, the amount of standing water was first calculated by measuring the diameter of the well (2 inches for this project), total depth of the water in the well (25 feet for this project), and the water level at the time of sampling. The water level at the time of sampling was calculated by subtracting the depth of water from the top of the casing (taken in the field with measuring tape).

Groundwater was sampled at the wellhead using a peristaltic pump after all YSI readings were stable. All water samples were placed in ice and brought back to the lab in 1L HPDE bottles, which had been rinsed with acid, MQ water, and finally triple rinsed with sample water. Samples were filtered through a  $0.2~\mu m$  GF/F and frozen before analysis. Before each concentration analysis section outlined below, frozen samples were completely thawed in a room-temperature water bath. After the needed amount of thawed samples was taken, the samples were immediately placed back in the freezer.

#### 5.3.2. Sample Analysis

# 5.3.2.1. $NH_4^+$ , $NO_2^-$ , $NO_3^-$ , TDN and DON concentration Analysis

The concentration of NH<sub>4</sub><sup>+</sup> was measured using the o-phthalaldehyde (OPA) fluorometric method (Holmes et al., 1999). The working reagent was prepared by mixing 5 mL OPA solution (1 g of reagent grade OPA in 25 mL of ethanol), 0.5 mL borate solution (10 g of reagent grade sodium tetraborate in 250 mL MQ water), and 94.5 mL sodium sulfite solution (0.8 g of reagent grade sodium sulfite in 100 mL MQ water). Samples were measured with 5 standards of NH<sub>4</sub><sup>+</sup> (0, 1.0, 10.0, 20.0, and 50 μm). For each sample and standard, 0.25 mL was added into individual cuvettes, followed by 1 mL of the working reagent. Then each cuvette was shaken and placed in the dark to react for 3 hours. After 3 hours, cuvettes were analyzed for raw fluorescence (RFU) using a Trilogy® Laboratory Fluorometer with the UV/Ammonium module. The NH<sub>4</sub><sup>+</sup> concentrations were then calculated through the calibration curve produced from the RFU values of the standards, with an R<sup>2</sup> value of at least 0.999.

## 5.3.2.2. NO<sub>2</sub> Concentration Analysis

The NO<sub>2</sub><sup>-</sup> concentration was measured using a colorimetric method (Tsikas, 2007). The color producing reagent was made by mixing the sulfanilamide solution (8 g sulfanilamide, 70 mL of phosphoric acid, and 30 mL of MQ water) and the NEDA solution (0.56 g N-(1-Napthyl)-

ethylenediamine dihydrochloride in 100 mL MQ water) in a 10:1 ratio. Samples were measured with 5 standards NO<sub>2</sub><sup>-</sup> (0, 1.0, 10.0, 30.0, and 50.0 µm). For each sample and standard, 1 mL was added into individual cuvettes, followed by 0.25 mL of the color producing reagent. Then cuvettes were shaken and placed in the refrigerator to react for 30 minutes, followed by 20 minutes at room temperature for equilibration. Cuvettes were then analyzed for absorbance using a Trilogy® Laboratory Fluorometer with the Absorbance/N module. The NO<sub>2</sub><sup>-</sup> concentrations were calculated through the calibration curve produced from the absorbance values of the standards with an R<sup>2</sup> value of at least 0.999.

## 5.3.3.3 NO<sub>3</sub> Concentration Analysis

To measure NO<sub>3</sub><sup>-</sup> the cadmium reduction method was used to reduce it to NO<sub>2</sub><sup>-</sup> (Tsunogai et al., 2008). The reductant, spongey cadmium, was made by adding 8-10 zinc sticks in 11 g cadmium chloride dissolved in around 400 mL of MQ water. After sitting overnight but before 24 hours, the zinc sticks were removed from the spongey cadmium and 3 drops of 6 N HCl were added to acidify the cadmium. The remaining solution was drained, and the solid cadmium was submerged in a 6 N HCl solution. A small spatula was used to break the cadmium into small pieces to increase surface area, and also activate the cadmium in the HCl solution. The HCl solution was then drained, and the cadmium was rinsed with MQ water until the pH was neutral (7) or lower.

Nitrate standards were prepared for analysis along with the samples (30.0, 50.0, and 70.0 µM). An ammonium chloride buffer was mixed by dissolving 3.74 g of ammonium chloride in 80 mL HPLC grade water in a 150 mL HDPE plastic bottle. Then 0.5 mL of 6 M NaOH was added to adjust the pH to 8.5, and the buffer was diluted with an additional 20 mL HPLC grade water. 1 mL of this buffer was added to each 5 mL sample/standard in a 15 mL centrifuge tube. Next, 0.3 g of the cadmium was added to each centrifuge tube, and samples were placed on a shaker table for 90 minutes to ensure the NO<sub>3</sub><sup>-</sup> is reduced to NO<sub>2</sub><sup>-</sup>. Then, the concentration of NO<sub>3</sub><sup>-</sup> + NO<sub>2</sub><sup>-</sup> was calculated via the colorimetric method explained under the NO<sub>2</sub><sup>-</sup> concentration analysis section, taking into account the dilution of the sample/standard with the ammonium chloride buffer by multiplying the concentration of each sample by 6/5, and using the standards to ensure a conversion of NO<sub>3</sub><sup>-</sup> to NO<sub>2</sub><sup>-</sup> of at least 90% (Tsikas, 2007).

## 5.3.3.4. NH<sub>4</sub><sup>+</sup> Removal for TDN Concentration Analysis

The DON concentration was calculated as the difference between TDN and DIN concentrations. In this case TDN is equal to DON + NO<sub>3</sub>-/NO<sub>2</sub>- since NH<sub>4</sub>+ was removed in the previous step. The concentration of TDN was measured by oxidizing the TDN to NO<sub>3</sub>- by the persulfate method, followed by reduction to NO<sub>2</sub>- by the cadmium method (Tsunogai et al., 2008). The oxidizer, persulfate solution, was made by adding 1 g persulfate into 1.17 mL 6 N NaOH followed by dilution to a final volume of 20 mL using HPLC water. The persulfate solution (0.15 mL) was added to 10 mL of each sample and shaken well before putting into the autoclave for two 30-minute cycles. Then these oxidized samples were reduced to NO<sub>2</sub>- by the cadmium method mentioned in the NO<sub>3</sub>- concentration analysis section. DON standards (e.g., urea, glycine, EDTA, N-acetyl-D-glucosamine) were oxidized and reduced with samples to make sure at least 90% conversion of TDN to NO<sub>2</sub>- was achieved.

# 5.3.3.5. TDN and DON Concentration Analysis

The DON concentration was calculated as the difference between TDN and DIN concentrations. In this case TDN is equal to  $DON + NO_3^-/NO_2^-$  since  $NH_4^+$  was removed in the

previous step. The concentration of TDN was measured by oxidizing the TDN to NO<sub>3</sub><sup>-</sup> by the persulfate method, followed by reduction to NO<sub>2</sub><sup>-</sup> by the cadmium method (Tsunogai et al., 2008). The oxidizer, persulfate solution, was made by adding 1 g persulfate into 1.17 mL 6 N NaOH followed by dilution to a final volume of 20 mL using HPLC water. The persulfate solution (0.15 mL) was added to 10 mL of each sample and shaken well before putting into the autoclave for two 30-minute cycles. Then these oxidized samples were reduced to NO<sub>2</sub><sup>-</sup> by the cadmium method mentioned in the NO<sub>3</sub><sup>-</sup> concentration analysis section. DON standards (e.g., urea, glycine, EDTA, N-acetyl-D-glucosamine) were oxidized and reduced with samples to make sure at least 90% conversion of TDN to NO<sub>2</sub><sup>-</sup> was achieved.

5.3.3.6. 
$$\delta^{15}N$$
 and  $\delta^{18}O$  of  $NO_3^-$ ,  $\delta^{15}N$ - $NH_4^+$ ,  $\delta^{15}N$ -DON Analysis

The isotopic ratios of  $NO_3^-$  and  $NO_2^-$  were measured by the denitrifier bacteria method (Sigman et al., 2001). The  $NO_3^-$  and  $NO_2^-$  in the sample were converted to  $N_2O$  by denitrifier bacteria and the nitrogen isotopic composition was measured by injecting the  $N_2O$  into a continuous flow isotope ratio mass spectrometer (CF-IRMS). Internationally recognized standards (USGS34, USGS32, IAEA-N3 and USGS35) were measured during sample analysis to provide a known  $\delta^{15}N$ - $NO_3^-$  reference for data corrections. Nitrite was not removed but on average was only 5% of the total  $NO_3^- + NO_2^-$  concentration so  $\delta^{15}N$ - $NO_3^-/\delta^{15}N$ - $NO_2^-$  is assumed to represent  $\delta^{15}N$ - $NO_3^-$  for purposes of investigation and discussion. The nitrogen isotopic ratio was calculated using the equation below and was reported in conventional delta ( $\delta$ ) notation in permil (%):

$$\delta^{15}N - NO_2^-/NO_3^- = \frac{(^{15}N/^{14}N)\text{sample} - (^{15}N/^{14}N)\text{standard}}{(^{15}N/^{14}N)\text{standard}} x \ 1000$$

# 3.3.3.7. $\delta^{15}N$ -NH<sub>4</sub><sup>+</sup> Analysis

The NH<sub>4</sub><sup>+</sup> was oxidized to NO<sub>2</sub><sup>-</sup> via bromate/bromide oxidation method (Felix et al., 2013; Zhang et al., 2007), and then the nitrogen isotopic ratio of DIN (NH<sub>4</sub><sup>+</sup>, NO<sub>2</sub><sup>-</sup> and NO<sub>3</sub><sup>-</sup>) was measured using the denitrifier bacteria method. If the concentration was > 10  $\mu$ M then the sample was diluted with MQ water to 10  $\mu$ M before undergoing oxidation. The Br/Br stock solution was made by adding 0.6 g sodium bromate and 5 g sodium bromide in 250 mL MQ water. Then the Br/Br working reagent was made by adding 1 mL of the stock solution to 50 mL Milli-Q water and 6 mL of 6 N HCl. The mixture was left to react in the dark for 5 minutes, after which the working reagent was diluted to a volume of 100 mL with 6 N NaOH. The working reagent (1 mL) was added into samples and shaken vigorously before being put on the shaker for 90 minutes to make sure the NH<sub>4</sub><sup>+</sup> was oxidized. Internationally recognized standards (USGS34, USGS32, IAEA-N3 and USGS35) were measured during sample analysis to provide a known  $\delta^{15}$ N-NO<sub>3</sub><sup>-</sup> reference for data corrections. Additionally, USGS isotope standards (USGS 25 ammonium sulfate and USGS 26 ammonium sulfate) were oxidized along with the samples and included as reference samples during isotope analysis in order to check for oxidation efficiency and to correct for any interference due to reagent blank effects. The  $\delta^{15}$ N-NH<sub>4</sub><sup>+</sup> was calculated:

$$\delta^{15}N - DIN = f_{NH_4^+} \times \delta^{15}N - NH_4^+ + f_{NO_2^-/NO_3^-} \times \delta^{15}N - NO_2^-/NO_3^-$$

where  $f_{\rm NH4^+}$  stands for the fraction of the concentration of NH<sub>4</sub><sup>+</sup> contributing to DIN of the sample and  $f_{\rm NO_2^-/NO_3^-}$  stands for the fraction of the concentration of NO<sub>2</sub><sup>-</sup> and NO<sub>3</sub><sup>-</sup> contributing to DIN of the sample.

5.3.3.8.  $\delta^{15}$ N-DON Analysis

The  $\delta^{15}$ N-DON was calculated:

$$\delta^{15}N - \text{TDN} = f_{\text{DON}} \times \delta^{15}N - \text{DON} + f_{\text{NO}_{2}^{-}/\text{NO}_{3}^{-}} \times \delta^{15}N - \text{NO}_{2}^{-}/\text{NO}_{3}^{-}$$

where  $f_{DON}$  stands for the fraction of the concentration of DON contributing to TDN of the sample and  $f_{NO_2^-/NO_3^-}$  stands for the fraction of the concentration of DIN contributing to TDN of the sample. The error of back-calculated  $\delta^{15}$ N-DON was reported to be over 1.5‰ when DON was less than 20% of TDN pool (Cao et al., 2021). Thus, only samples that had DON higher than 20% of TDN (in this case DON = TDN –  $NO_2^-/NO_3^-$ ) underwent  $\delta^{15}$ N-TDN analysis.

Here the  $NH_4^+$  was removed from the sample and only  $NO_2^-$  and  $NO_3^-$  were left in the DIN pool to reduce the error due to back calculation. This was done through  $NH_4^+$  diffusion. NaOH (5 M) was added to raise the pH above 10 and remove the  $NH_4^+$ . After  $NH_4^+$  was removed, the DIN pool only contained  $NO_2^-$  and  $NO_3^-$  and the  $\delta^{15}N$ -DIN was measured as specified above. In order to measure  $\delta^{15}N$ -TDN, the TDN was oxidized to  $NO_3^-$  using the persulfate method and then the isotopic ratios could be measured using the denitrifier bacteria method (Knapp et al., 2005).

#### 5.3.3. Isotope Mixing Model

A dual isotope mixing model for NO<sub>3</sub><sup>-</sup> source contributions was developed for groundwater using source signatures of sewage/septic, atmospheric deposition, dog waste/gull guano, and soil and soil was replaced with Gulf of Mexico (GOM) NO<sub>3</sub><sup>-</sup> sourced for pore and surface water. Nitrogen isotope signatures of potential sources are shown in **Table 5.3**. Contamination can originate from various sources, but a primary source was hypothesized to be septic systems throughout the study area due to most well sites being located in relatively close proximity to an OSSF. In addition, there are about 1,223 documented OSSFs on the barrier islands of this study area. Of these, 978 are either over 10 years old or have an undocumented age, which poses an increased risk for failure or malfunction (Houston-Galveston Area Council OSSF Information System; Bonaiti et al., 2017).

Fertilizers and animal manure are not likely contaminants to these areas, as lands are herbaceous wetlands or highly urbanized (Houston-Galveston Area Council). However, bacteria marker data indicates dog and gull waste (Kapoor personal communication/this report), as a prominent source of bacteria and have been included in this mixing model as a potential significant source of nitrogen. In addition, there have been documented cases of contamination of beaches from dogs and gulls in beaches of California and Florida (Goodwin et al., 2016; Converse et al., 2012). The  $\delta^{15}N$  value for these sources overlaps and were combined for a value of  $7.9 \pm 2.1\%$  (Mizota 2009; 2009a; Hixon et al., 2022). Another possible nitrogen source is atmospheric deposition. Atmospheric deposition affects biogeochemistry in the upper ocean, and the coastal bend of Texas is considered a humid subtropical climate (U.S. Climate Data). The Galveston Coast Guard Station, located on Galveston Island, monitors weather conditions and reports that the wet season is from June-September, while the dry season is from October-May. The last source included in this model was soil. Sandy soils comprise the majority of the study area; these types of soils are documented as hotspots for organic matter mineralization, as sands are highly permeable (Zhou et al., 2023).

The mixing model was completed by the Stable Isotope Analysis in R (SIAR) that uses a Bayesian framework. The following equations were used:

$$\delta^{15}\text{N-N}_{\text{gulf}} = f_{\text{ss}} \times (\delta^{15}\text{N-N}_{\text{ss}} + \varepsilon) + f_{\text{dg}} \times (\delta^{15}\text{N-N}_{\text{dg}} + \varepsilon) + f_{\text{soil or mar}} \times (\delta^{15}\text{N-N}_{\text{soil or mar}} + \varepsilon) + f_{\text{wd}} \times (\delta^{15}\text{N-N}_{\text{wd}} + \varepsilon)$$

where  $\delta^{15}$ N-N<sub>gulf</sub> is the nitrogen isotopic composition of NO<sub>3</sub><sup>-</sup> of Gulf samples and  $f_{\text{sep}}$ ,  $f_{\text{gull}}, f_{\text{soil}}, f_{\text{mar}}$  and  $f_{\text{wd}}$  are the contribution of sewage/septic, dog waste/gull guano, soil, Gulf of Mexico and wet deposition, respectively.  $\delta^{15}$ N-N<sub>ss</sub> is the nitrogen isotopic ratio of NO<sub>3</sub><sup>-</sup> from sewage/septic.  $\delta^{15}$ N-N<sub>gull</sub> is the nitrogen isotopic ratio of NO<sub>3</sub> from dog waste/gull guano.  $\delta^{15}$ N- $N_{\text{soil}}$  is the nitrogen isotopic ratio of  $NO_3^-$  from soil.  $\delta^{15}N-N_{\text{wd}}$  is the nitrogen isotopic ratio of  $NO_3$  from wet deposition and  $\delta^{15}N-N_{mar}$  is the nitrogen isotopic ratio of from the Gulf of Mexico waters.  $\varepsilon$  is the isotope effect applied to each source. To determine the isotope effect,  $\varepsilon$ , of NO<sub>3</sub> in porewater  $\ln NO_3^- \text{ vs } \delta^{15} \text{N-NO}_3^-$  was but the relationship was insignificant (p = 0.74), however for 90% of the data yields a significant correlation (p < 0.0001) with a slope indicating an  $\varepsilon$  of 4.9\%. The porewater  $\delta^{18}$ O-NO<sub>3</sub> vs  $\delta^{15}$ N- NO<sub>3</sub> slope (1.16) which is close to a theoretical 1:1 slope of denitrification and was considered the primary fractionation process albeit with contributions from other processes leading to deviations from the 1:1 line (e.g., DNRA nitrification, anammox). A literature porewater denitrification fractionation effect of 5% was similar to the  $\varepsilon$  of 4.9% associated with 90% of the data and was applied to porewater  $\delta^{15}$ N-NO<sub>3</sub> values (Sigman and Fripiat 2019) a fractionation correction factor. To determine isotope effect occurring in groundwaters,  $\delta^{15}$ N vs  $\delta^{18}$ O was plotted and it was observed that the trend for samples with  $\delta^{15}N$  values over 30% was indicating a different fractionation process than those samples under 30%. The under 30% samples did not have a significant correlation between ln  $NO_3^-$  and  $\delta^{15}N-NO_3^-$  but the  $\delta^{15}N$  vs  $\delta^{18}O$  had a slope of 0.89 which was indicative of a primarily denitrification process and the literature porewater denitrification isotope effect of 5‰ was applied. The <sup>15</sup>N vs <sup>18</sup>O slope for the >30% samples was very low (0.13) which is indicative of the competing production of nitrate through oxidation and the loss of nitrate through reduction. Since the wells have low DO levels, the oxidation process is likely anammox which has been shown as a significant oxidation pathway in aquifers (Clark et al., 2008; Erler et al., 2008; Robertson et al., 2012; Granger and Wankel 2016). This pathway can account for large fractionation explaining the high  $\delta^{15}$ N values. Brunner et al., 2013 suggest nitrate production associated with anammox displays an inverse kinetic fractionation effect of -31% which was be applied here to groundwater samples with  $\delta^{15}$ N-NO<sub>3</sub> values >30%. Surface water  $\delta^{15}$ N-NO<sub>3</sub> values are likely a product of nitrification, denitrification and assimilation. To determine the overall  $\varepsilon$ , surface ln NO<sub>3</sub> vs <sup>15</sup>N- NO<sub>3</sub> was plotted without eight high concentration outliers. The result was a highly significant relationship (p = 0.0005) with a slope of 3.3 which is the  $\varepsilon$  factor applied to the surface water samples (Kendall et al., 2007).

**Table 5.3.** Nitrate nitrogen isotopic signatures used for the SIAR mixing model. When possible, source signatures as local to the study region were used. Sewage/Septic values are from three wastewater treatment plants in the Texas Coastal Bend, wet deposition values are from a station south of the study region located on the Texas coast and marine values are from Gulf of Mexico waters.

Source	δ <sup>15</sup> N-NO <sub>3</sub> -	Reference
Wet Deposition	$-1.9\%$ $\pm 3.5\%$	Qiu et al., 2024
Sewage/Septic	$+14.9\%$ $\pm 3.5\%$	Cox, in prep
Dog/Gull guano	+7.9%0 ± 2.1%0	Mizota, 2009; 2009a; Hixon et al., 2022

Soil	$+5\% \pm 2\%$	Nikolenko et al., 2018	
	$+4.7\% \pm 0.9\%$		
Marine		Howe et al., 2020	

*Table 5.4.* Isotope effects used for the SIMMR model according to sample matrix.

Sample Matrix	15 <sub>E</sub>	Reference
Groundwater $\delta^{15}N > 30$	31‰	Granger and Wankel, 2016; Brunner et al., 2013
Groundwater $\delta^{15}N < 30$	5‰	Sigman and Fripiat 2019
Surface water	3.3‰	Empirical data from this work
Porewater	5‰	Sigman and Fripiat 2019

#### 5.4. Results

Surface, pore, and groundwater samples were analyzed for  $NO_3^-$ ,  $NO_2^-$ ,  $NH_4^+$ , and DON concentrations, as well as  $\delta^{15}$ N-NO $_3^-$ ,  $\delta^{18}$ O-NO $_3^-$ ,  $\delta^{15}$ N-NH $_4^+$ , and  $\delta^{15}$ N-DON values (**Table 5.5**). When reporting seasonal trends, fall is September 2022, October 2022, November 2021, 2022; winter is December 2021-February 2022; spring is March-May 2022, 2023; and summer is June-July 2022. Three outlier  $\delta^{15}$ N-DON were within the %DON of TDN for valid isotope back calculation but were high outliers and were not included in averages (i.e., 1/2022 W5 (75.7‰) 1/2022 W9 (81.6‰) and 3/2023 W9 (105.3‰).

**Table 5.5.** Nutrient concentration averages ( $\mu$ M),  $\delta$ 15N, and  $\delta$ 18O averages (‰) (November 2021- April 2023) for surface, pore, and groundwater samples. n = # of samples. Isotope data is only available for samples with a concentration  $\geq 3 \mu$ M of the analyte of interest.

Sample Type	NO <sub>3</sub> · (μM)	NO <sub>2</sub> - (μM)	NH <sub>4</sub> <sup>+</sup> (μM)	DON (µM)	δ <sup>15</sup> N- NO <sub>3</sub> -	δ <sup>18</sup> O-NO <sub>3</sub> ·	δ <sup>15</sup> N- NH <sub>4</sub> <sup>+</sup>	δ <sup>15</sup> N- DON
Surface	3.4±5.2	0.3±1.0	4.9±9.4	7±5	13.5±3.2	17.3±4.7	13.1±6.1	5±5
	(n=300)	(n=300)	(n=300)	(n=300)	(n=107)	(n=107)	(n=66)	(n=208)
winter	$5.2\pm7.2$	$0.3\pm1.0$	$3.8\pm3.8$	5±5	$12.6\pm3.0$	$17.4 \pm 5.5$	11.2±6.3	4±4
	(n=101)	(n=101)	(n=101)	(n=101)	(n=54)	(n=54)	(n=28)	(n=47)
spring	$2.6\pm2.3$	$0.6\pm1.5$	$3.0\pm2.7$	7±6	$13.8\pm3.0$	$16.8 \pm 3.1$	$13.4\pm6.3$	6±8
	(n=83)	(n=83)	(n=83)	(n=83)	(n=28)	(n=28)	(n=21)	(n=63)
summer	$2.9 \pm 1.1$	$0.2\pm0.3$	$2.2\pm2.0$	9±4	$15.4\pm3.2$	$18.4 \pm 3.6$	$14.1 \pm 3.6$	7±3
	(n=50)	(n=50)	(n=50)	(n=50)	(n=22)	(n=22)	(n=7)	(n=38)
fall	$2.0\pm5.3$	$0.1\pm0.2$	$2.4\pm2.3$	10±4	$13.0\pm3.1$	$10.7 \pm 1.8$	$16.7\pm4.0$	4±3
	(n=66)	(n=66)	(n=66)	(n=66)	(n=3)	(n=3)	(n=10)	(n=60)
Pore	$4.3\pm7.1$	$0.2\pm0.4$	$27.7 \pm 40.6$	7±8	$14.7\pm4.3$	$12.9\pm5.7$	$10.6\pm6.3$	5±5.
	(n=192)	(n=192)	(n=192)	(n=192)	(n=77)	(n=77)	(n=138)	(n=113)
winter	$7.6\pm12.5$	$0.3\pm1.4$	$27.3\pm33.4$	8±10	$14.0\pm6.8$	$12.5\pm6.8$	$11.4\pm6.2$	6±7
	(n=52)	(n=52)	(n=52)	(n=52)	(n=32)	(n=32)	(n=43)	(n=24)
spring	$2.7\pm2.5$	$0.2\pm0.2$	$31.5\pm28.3$	7±8	$15.3\pm4.8$	$13.7 \pm 4.4$	$7.8 \pm 7.3$	5±5
	(n=53)	(n=53)	(n=53)	(n=53)	(n=16)	(n=16)	(n=47)	(n=31)
summer	$3.1\pm1.6$	$0.3\pm0.5$	$32.9\pm70.0$	7±7	$16.3\pm2.7$	$14.6\pm4.3$	$11.6 \pm 3.8$	5±6
	(n=47)	(n=47)	(n=47)	(n=47)	(n=19)	(n=19)	(n=21)	(n=28)

fall	2.6±2.5	0.2±0.3	18.6±26.4	8±8	13.2±2.3	9.7±4.0	13.7±3.6	6±4
	(n=40)	(n=40)	(n=40)	(n=40)	(n=10)	(n=10)	(n=27)	(n=30)
Ground	34.4±113.5	$2.7 \pm 10.1$	$158.9 \pm 345.2$	21±58	29.3±14.3	20.5±6.3	$10.9\pm8.3$	3±11
	(n=207)	(n=207)	(n=207)	(n=207)	(n=78)	(n=78)	(n=116)	(n=95)
winter	69.1±191.5	$4.3\pm11.9$	127.4±194.4	29±71	32.0±13.0	$22.2\pm7.9$	$10.3\pm 9.4$	6±17
	(n=64)	(n=64)	(n=64)	(n=64)	(n=23)	(n=23)	(n=42)	(n=26)
spring	$22.5\pm40.4$	$3.4\pm3.7$	172.1±506.5	$30\pm77$	27.3±15.8	$18.5 \pm 5.3$	$7.6 \pm 7.8$	2±5
	(n=59)	(n=59)	(n=59)	(n=59)	(n=24)	(n=24)	(n=33)	(n=31)
summer	$10.6\pm18.4$	$1.3\pm2.6$	$257 \pm 378.7$	7±11	26.8±12.6	$23.2\pm3.0$	$13.0\pm5.7$	1±8
	(n=36)	(n=36)	(n=36)	(n=36)	(n=19)	(n=19)	(n=14)	(n=13)
fall	$19\pm53.2$	$0.9\pm3.5$	111.3±199.2	8±10	32.1±16.1	$16.9 \pm 6.1$	$14.9 \pm 6.2$	2±11
	(n=48)	(n=48)	(n=48)	(n=48)	(n=12)	(n=12)	(n=27)	(n=25)

# 5.4.1. Nitrate Spatial and Temporal Variations

# 5.4.1.1. Nitrate Surface Water

The average  $NO_3^-$  concentrations of surface water samples overall were  $3.4 \pm 5.2 \,\mu\text{M}$  (n =300). Concentrations were significantly higher in the winter ( $5.2 \pm 7.2 \,\mu\text{M}$ , n=101; p=0.002). than fall ( $2.0 \pm 5.3 \,\mu\text{M}$ , n = 66), spring ( $2.6 \pm 0.23 \,\mu\text{M}$ , n=83; p = 0.03), and summer ( $2.9 \pm 1.1 \,\mu\text{M}$ , n=50; p=0.03)(ANOVA). Winter, spring, and summer were statistically similar (**Figure 5.2**) and while most months were statistically similar averaging  $2.8 \pm 3.3 \,\mu\text{M}$  (n = 284), January 2023 was distinctly higher  $14.7 \pm 13.8 \,\mu\text{M}$  (n =16). For most sites there were no significant differences in average concentrations (p > 0.05; ANOVA) (**Figure 5.3**) with sites 1, 12, 14, and 19 being observably higher than the average.

Average  $\delta^{15}$ N-NO<sub>3</sub><sup>-</sup> values were  $13.5 \pm 3.2\%$  (n = 108) and average  $\delta^{18}$ O-NO<sub>3</sub><sup>-</sup> values were  $17.3 \pm 4.7\%$  (n = 108).  $\delta^{15}$ N values (15.4 ± 3.2%) in summer were significantly higher than in fall and winter (p < 0.001). Fall  $\delta^{18}$ O values (10.7 ± 1.8%) were significantly lower than all other seasons (p < 0.01). Most sites' average  $\delta^{15}$ N and  $\delta^{18}$ O values were not significantly different from each other. Site 5 had the highest  $\delta^{15}$ N average (16.0 ± 2.9%) and site 17 had the lowest (10.1 ± 0.8%) with the two being significantly different (p = 0.001). Site 5 had the highest  $\delta^{18}$ O average (20.0 ± 4.8%) and site 12 had the lowest (13.3 ± 3.7%) with the two being significantly different (p = 0.002). Plotting both  $\delta^{15}$ N and  $\delta^{18}$ O data in a dual isotope plot allows for preliminary differentiation between sources with similar or overlapping  $\delta^{15}$ N values although isotope fractionation must ultimately be accounted for when deducing source apportionment. The slope of the line (and the resulting  $\delta^{15}$ N: $\delta^{18}$ O ratio) produced from the plot provides insight to the fractionation processes that are occurring (**Figure 5.4**) (Kendall et al., 2007). Surface nitrate samples as a whole had a  $\delta^{15}$ N: $\delta^{18}$ O ratio of 0.85.

Sample  $\delta^{15}$ N values were deployed in a SIAR mixing model to estimate source contributions. Overall, source contributions to surface water were estimated as septic/sewage (36  $\pm$  17%), dog/gull guano (32  $\pm$  18%), marine (23  $\pm$  8%), and wet deposition (9  $\pm$  4%) (**Table 5.6**). Septic/sewage was estimated as the primary source of NO<sub>3</sub><sup>-</sup> for all months except fall months, which showed dog waste/gull guano as the primary source of NO<sub>3</sub><sup>-</sup>, however fall months only had 3 samples with concentrations high enough for isotope analysis (**Figure 5.5**). Most sites also showed septic/sewage as the primary source, with the exceptions of S8, S9, and S12 where dog waste/gull guano was the primary source. For all months and sites, septic/sewage and dog waste/gull guano were the estimated dominant sources.

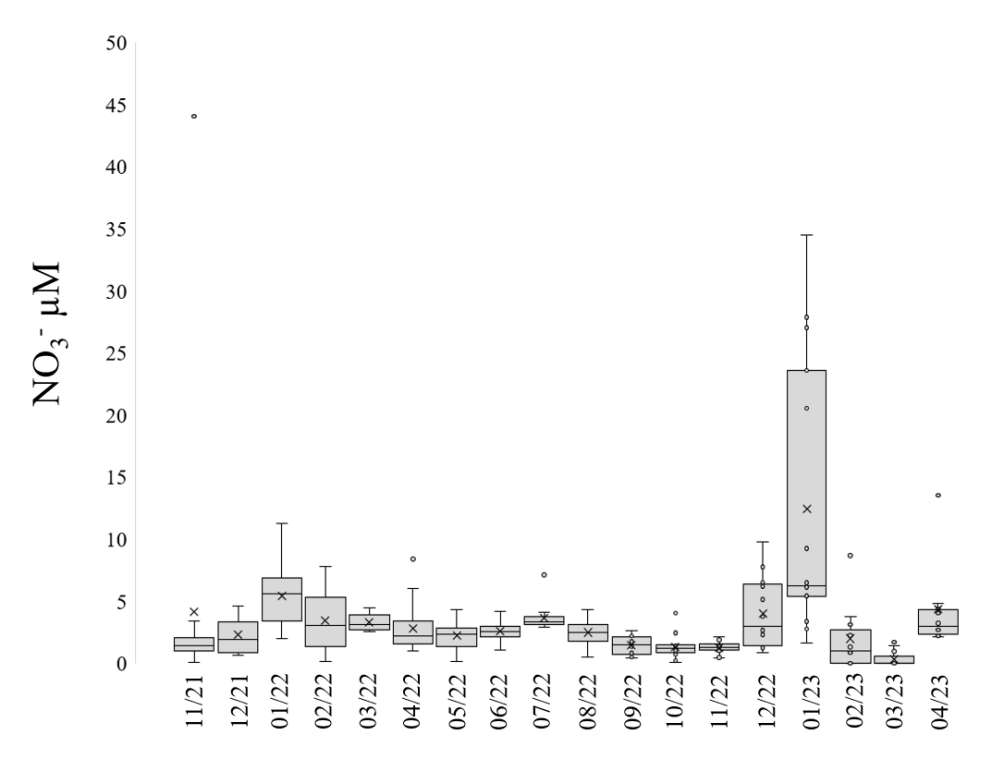


Figure 5.2. Surface water NO3- concentrations by month.

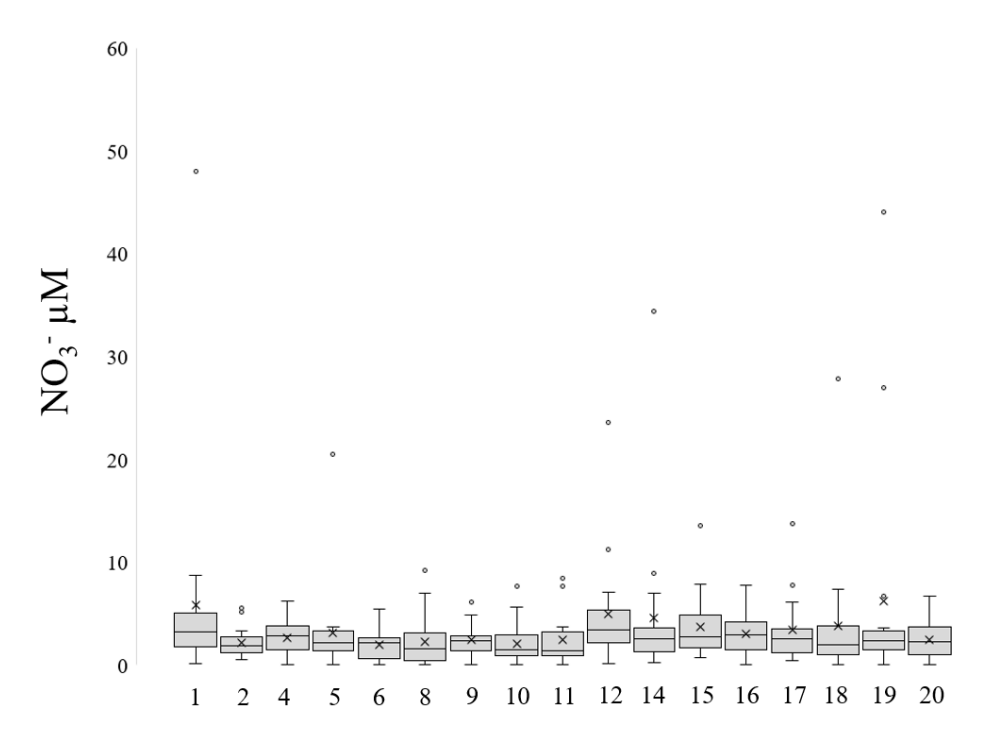
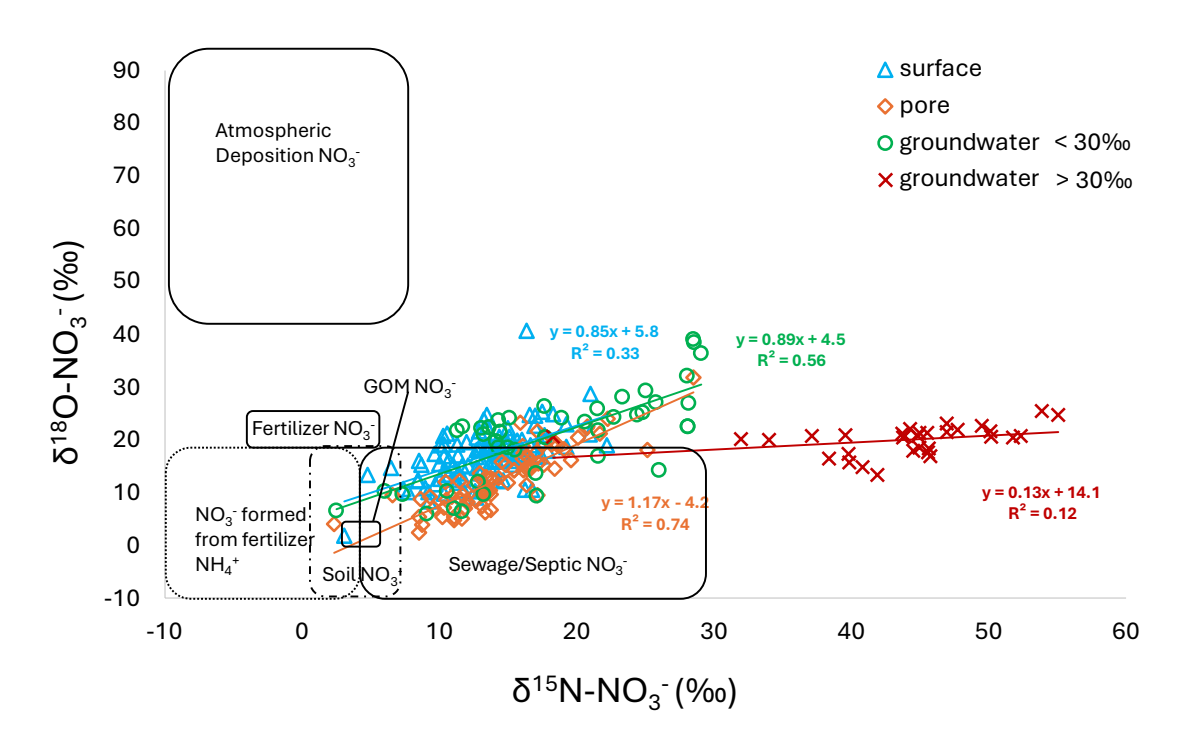


Figure 5.3. Surface water NO3- concentrations by site.



**Figure 5.4.**  $\delta$ 15N-NO3- and  $\delta$ 18O-NO3- data of surface (blue triangle), pore (orange triangle), groundwater < 30% (green circle) and groundwater > 30% (maroon X') samples from November 2021- April 2023.

**Table 5.6.** Nitrate isotopic composition (%) and % source contribution to nitrate in surface waters by season and site. SS, dg, wd, mar is the % contribution from sewage/septic dog waste/gull guano. wet deposition and Gulf of Mexico waters, respectively.

Season/Site	n =	δ <sup>15</sup> N-	δ <sup>18</sup> O-	%	%	%	%	%	%	%	%
		$NO_3$	NO <sub>3</sub>	SS	error	dg	error	wd	error	mar	error
All	107	13.5	17.3	45	17	26	19	13	9	16	11
Winter	54	12.6	17.4	38	17	30	21	14	10	18	12
Spring	28	13.8	16.8	47	16	25	20	12	9	16	11
Summer	22	15.4	18.4	58	15	19	15	11	7	13	9
Fall	3	13.0	10.7	41	17	29	21	14	10	17	12
1	9	14.0	16.5	48	17	25	19	12	8	15	11
2	3	14.1	18.0	48	17	24	19	12	8	16	11
4	7	16.0	17.5	61	14	17	14	10	7	12	9
5	8	16.0	20.4	61	14	17	14	10	7	12	9
6	2	12.2	17.6	36	16	30	20	15	10	20	13
8	5	11.2	13.4	29	15	31	21	17	12	23	15
9	4	10.3	13.4	24	14	31	20	19	12	26	18
10	4	12.7	16.8	39	16	29	20	14	10	18	12
11	6	12.8	18.1	39	16	29	20	14	10	18	12
12	11	11.9	13.1	34	16	31	21	15	10	21	14
14	8	14.4	18.1	51	16	22	18	12	8	15	11
15	9	13.5	18.1	45	17	26	19	12	9	17	12
16	8	14.7	22.9	45	17	26	19	13	9	16	11
17	6	10.1	16.7	23	14	30	20	19	13	28	19

18	6 5 7	14.1	17.6	48	17	24	19	12	8	16	11
19	5	13.6	14.4	45	17	26	19	13	9	16	11
20	7	14.2	18.9	49	16	24	19	12	8	15	10

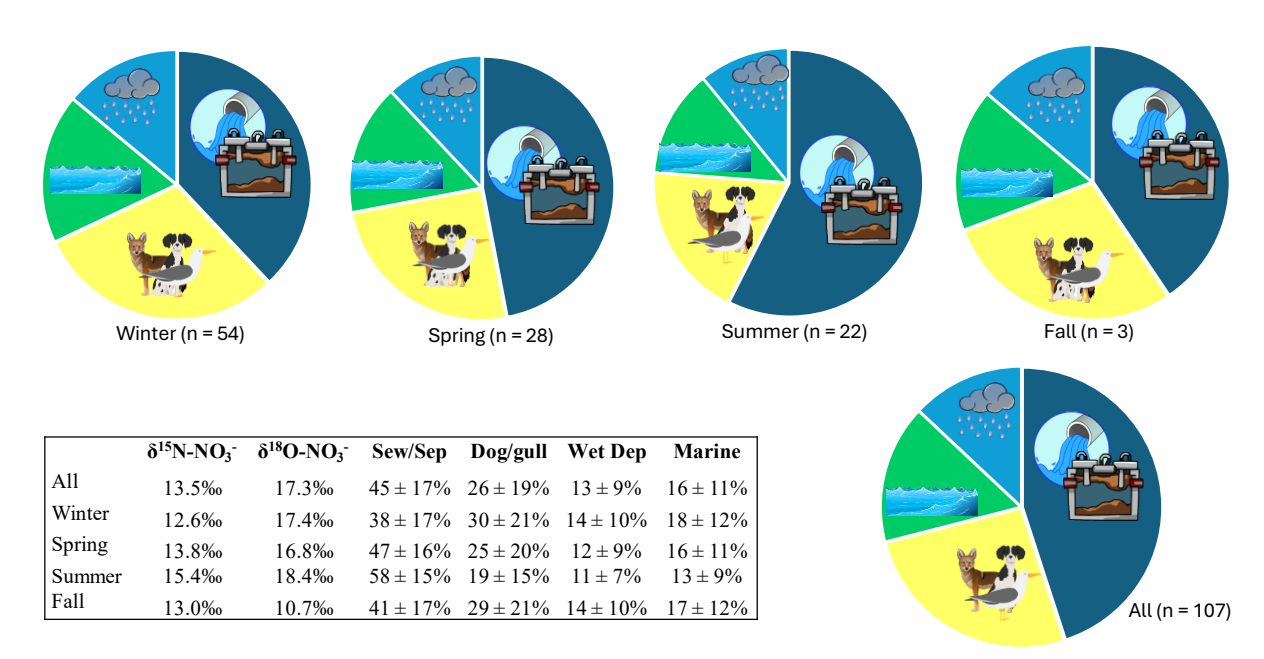


**Figure 5.5.** Surface water NO3- estimated source % contributions throughout duration of sampling and for each season.

## 5.4.1.2. Nitrate Porewater

The overall average porewater  $NO_3^-$  concentration was  $4.3 \pm 7.1 \,\mu\text{M}$  (n=192). There was significant difference between winter  $(7.6 \pm 12.5 \,\mu\text{M})$  and fall  $(3.6 \pm 2.5 \,\mu\text{M})$  (p = 0.03) but his was primarily due to an outlier average in January 2023  $(20.3 \pm 20.2 \,\mu\text{M})$  similar to the trend seen in surface waters (**Figure 5.6**). Average concentration differences across porewater sites were mostly insignificant with sites 9, 10 and 19 being observably higher than the average (**Figure 5.7**).

Average  $\delta^{15}$ N-NO<sub>3</sub> values were  $14.7 \pm 4.3\%$  and average  $\delta^{18}$ O-NO<sub>3</sub> values were  $12.9 \pm 5.7\%$  (n = 77). Season  $\delta^{15}$ N and  $\delta^{18}$ O values were not significantly different with the exception of fall ( $13.2 \pm 2.3\%$ ,  $9.7 \pm 4.0\%$ ) being significantly lower than summer ( $16.3 \pm 2.7\%$ ,  $14.6 \pm 4.3\%$ )(p < 0.009).  $\delta^{15}$ N value averages were lowest at site 8 ( $11.6 \pm 2.6\%$ ) and highest at site 2 ( $17.3 \pm 3.4\%$ ). Samples had a  $\delta^{15}$ N: $\delta^{18}$ O slope of 1.17 (**Figure 5.4**). Overall, isotope mixing models estimate source contributions to porewater were dog waste/gull guano ( $27 \pm 20\%$ ), septic/sewage ( $42 \pm 17\%$ ), soil/marine ( $18 \pm 12\%$ ), and wet deposition ( $14 \pm 9\%$ ) (**Table 5.7**). Septic/sewage was consistently the primary source with it being equal to dog/gull in fall (**Figure 5.8**). For all sites septic/sewage were the estimated dominant sources with the exceptions of sites 8 and 18 where dog/gull was the primary source.

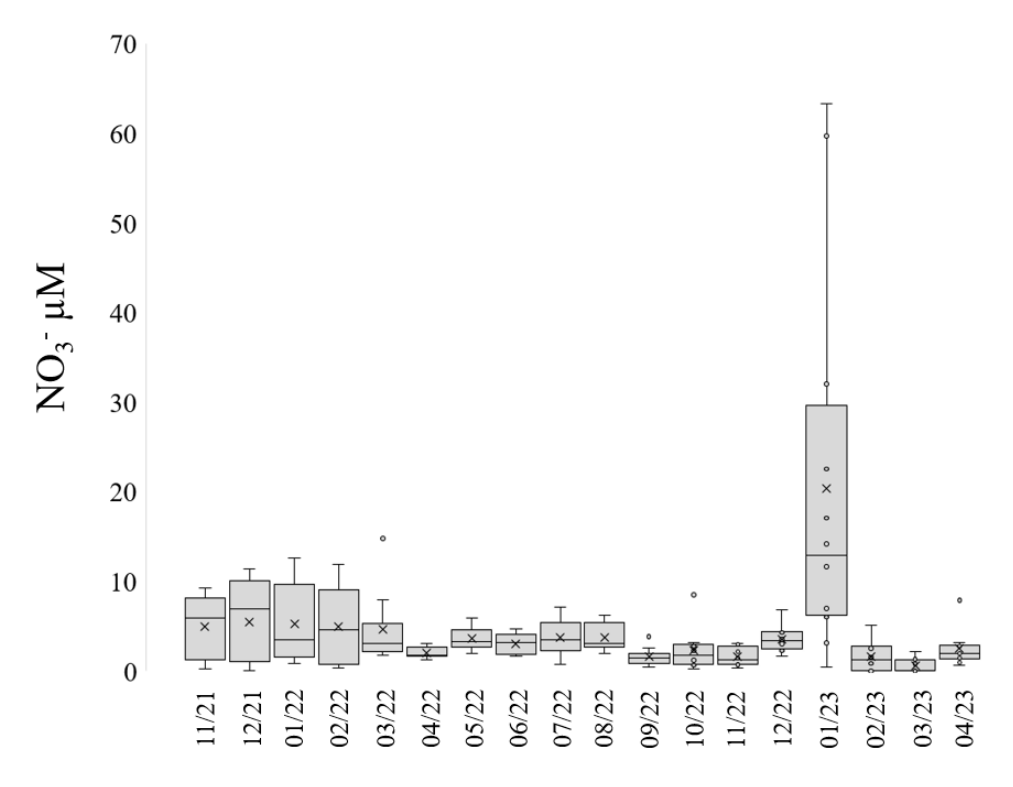


Figure 5.6. Porewater NO3- concentrations by month.

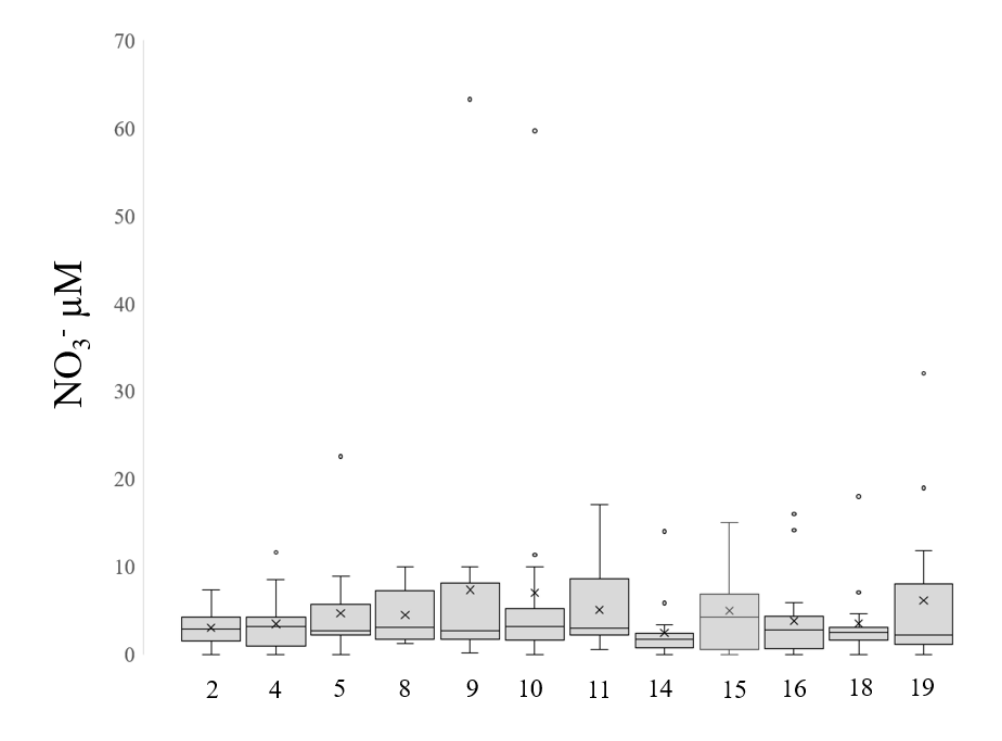
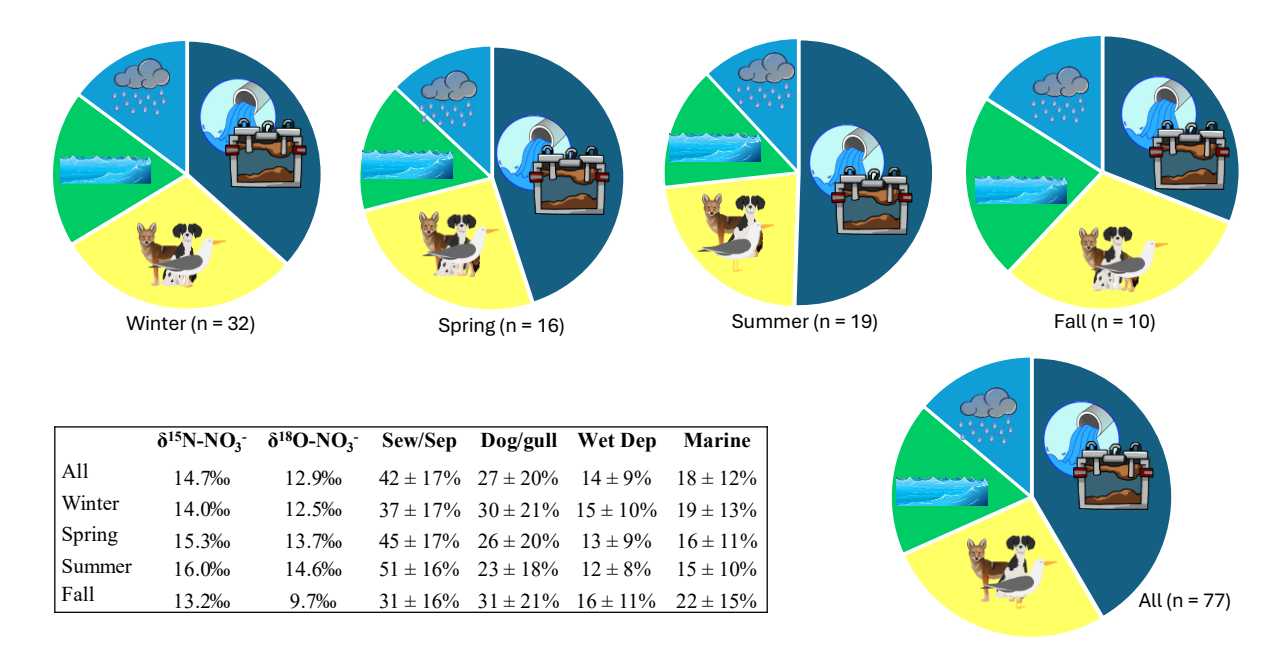


Figure 5.7. Porewater NO3- concentrations by site.

**Table 5.7.** Nitrate isotopic composition (%) and % source contribution to nitrate in pore waters by season and site. SS, dg, wd, soil/marine is the % contribution from sewage/septic dog waste/gull guano. wet deposition and Gulf of Mexico waters, respectively.

Season/Site	n =	δ <sup>15</sup> N-	δ <sup>18</sup> O-	%	%	%	%	%	%	%	%
		$NO_3$	$NO_3^-$	SS	error	dg	error	wd	error	mar	error
All	77	14.7	12.9	42	17	27	20	14	9	18	12
winter	32	14.0	12.5	37	17	30	21	15	10	19	13
spring	16	15.3	13.7	45	17	26	20	13	9	16	11
summer	19	16.0	14.6	51	16	23	18	12	8	15	10
fall	10	13.2	9.7	31	16	31	21	16	11	22	15
2	9	17.3	16.0	58	14	18	14	11	7	13	9
4	9	16.8	14.9	56	15	19	15	11	7	14	9
5	7	15.0	15.4	43	17	27	20	13	9	17	12
8	8	11.6	9.1	22	13	30	20	20	13	29	19
9	7	13.7	11.4	34	16	31	21	15	10	20	14
10	8	13.9	10.4	36	17	30	21	15	10	20	14
11	8	14.1	11.2	37	17	29	21	14	10	20	13
14	1	15.9	23.3	50	16	24	18	12	8	15	10
15	7	13.6	11.6	33	16	31	21	15	11	21	14
16	5	15.3	15.7	45	17	26	20	13	9	16	11
18	2	12.8	11.1	29	15	31	21	17	11	24	16
19	6	15.1	13.0	44	17	27	20	13	9	17	11



*Figure 5.8.* Porewater NO3- estimated source % contributions throughout duration of sampling and for each season.

# 5.4.1.3. Nitrate Groundwater

Overall, average  $NO_3^-$  concentrations of wells were 34.4 ± 113.5  $\mu$ M (n = 207). However, three sites were significantly higher than the others (W1, W9, and W13; these sites will thus be referred to as "high  $NO_3^-$  wells" for the purpose of comparison), and their average

 $NO_3^-$  concentrations were  $115.4 \pm 197.6 \,\mu\text{M}$  (n = 53). (**Figure 5.10**). The rest of the wells had average  $NO_3^-$  concentrations of  $6.0 \pm 32.9 \,\mu\text{M}$  (n = 154). For these high concentration wells, winter had the significantly highest concentrations (223.7 ± 316.6  $\mu$ M), while summer had the significantly lowest (33.0 ± 26.8  $\mu$ M) (ANOVA) (**Figure 5.9**). For the other wells, winter had the significantly highest concentrations (13.2 ± 58.9  $\mu$ M) while fall had the lowest (1.1 ± 0.9  $\mu$ M).

The overall average isotope composition of the groundwater was  $\delta^{15}N = 29.3 \pm 14.3\%$  and  $\delta^{18}O = 20.5 \pm 6.3\%$  (n = 78). It is important to note here the "n" sample number since only samples with high enough concentrations were analyzed. The isotopic composition of the three high  $NO_3^-$  wells were significantly different than the rest of the sites. High  $NO_3^-$  well averages were  $\delta^{15}N = 36.6 \pm 12.7\%$  and  $\delta^{18}O = 18.7 \pm 4.8\%$  while the rest of the wells average was  $\delta^{15}N = 20.7 \pm 10.9\%$  and  $\delta^{18}O = 22.7 \pm 7.2\%$ . For both groups of wells, there was no significant difference among seasons. The slope of the  $\delta^{15}N$ : $\delta^{18}O$  line of high concentration and remaining wells was 0.13 and 0.89, respectively (**Figure 5.4**).

For all months and sites, septic/sewage was estimated as the dominant sources. Source contributions estimates were similar between high and low concentration wells and the overall contribution among wells was dog waste/gull guano (15  $\pm$  12%), wet deposition (10  $\pm$  6%), septic/sewage (63  $\pm$  13%), and soil (12  $\pm$  9%) (**Table 5.8**) (**Figure 5.11**).

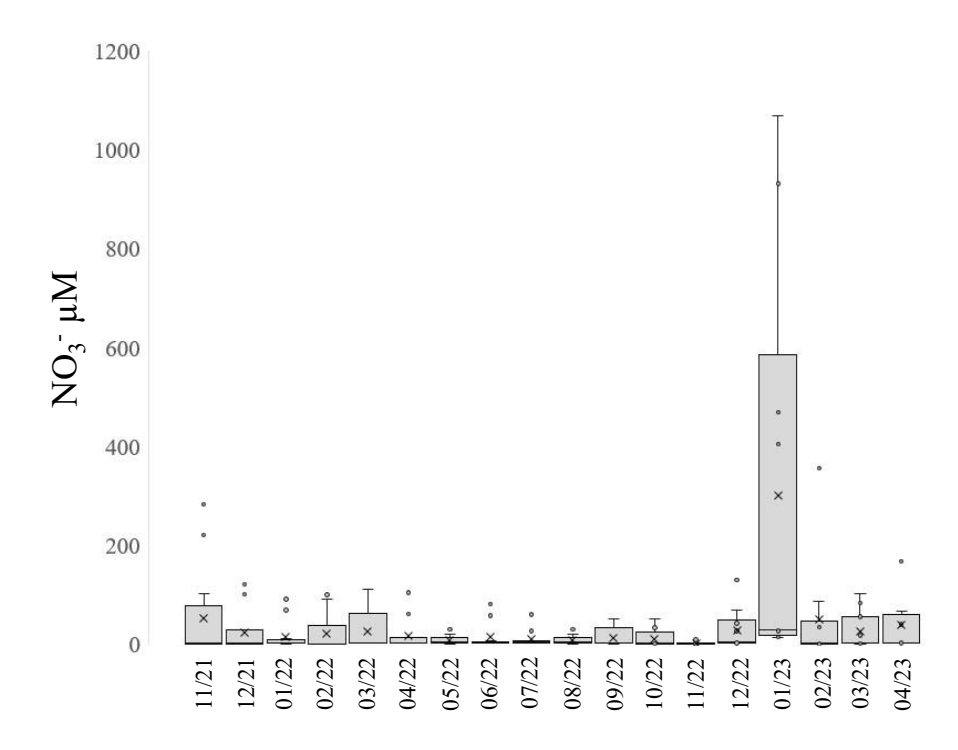


*Figure 5.9.* Groundwater average NO3- concentrations by month.

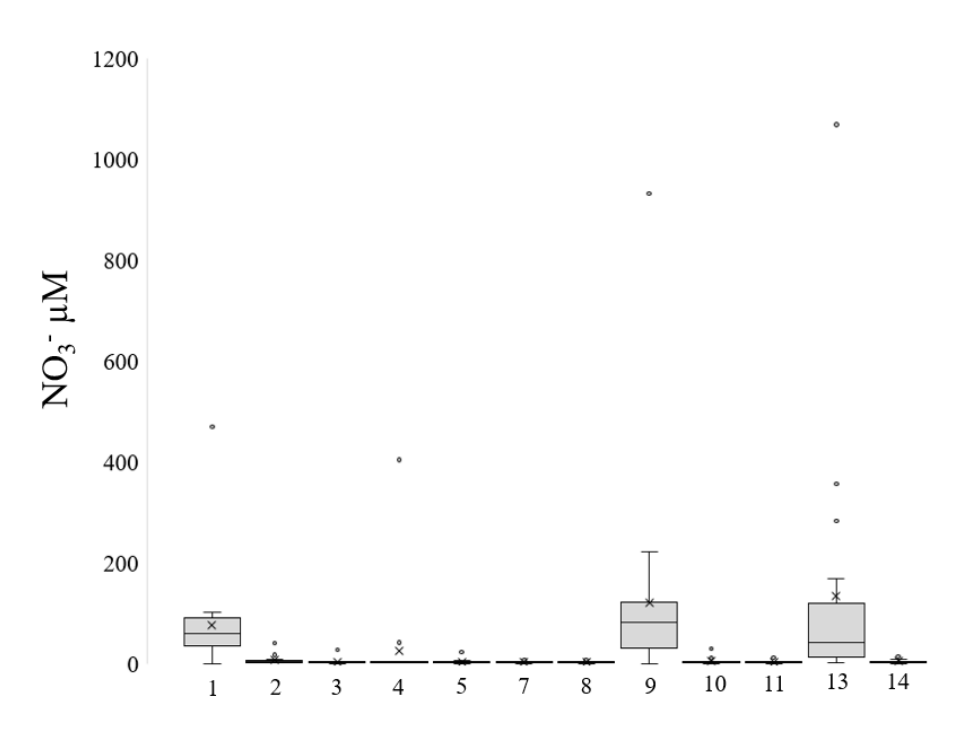


*Figure 5.10.* Groundwater average NO3- concentrations by site and pie chart of source apportionment for high nitrate concentration wells.

**Table 5.8.** Nitrate isotopic composition (‰) and % source contribution to nitrate in ground waters by season and site. SS, dg, wd, soil is the % contribution from sewage/septic dog waste/gull guano. wet deposition and soil, respectively.

Season/Site	n =	δ <sup>15</sup> N-	δ <sup>18</sup> O-	%	%	%	%	%	%	%	%
		$NO_3$	$NO_3$	SS	error	dg	error	wd	error	soil	error
All	78	29.3	20.5	63	13	15	12	10	6	12	9
winter	23	32.0	22.2	69	12	13	10	8	6	10	8
spring	24	27.3	18.5	45	17	26	20	12	9	17	13
summer	19	26.8	23.2	71	11	12	9	8	6	10	7
fall	12	32.1	16.9	67	12	13	10	9	6	11	8
1	17	46.7	20.0	73	10	11	8	7	5	9	7
2	9	22.2	19.5	52	16	21	17	11	8	15	11
3	6	14.5	19.9	38	17	29	21	13	9	20	15
4	1	21.5	21.5	75	10	10	7	7	5	8	6
5	2	14.7	20.0	40	17	27	17	14	10	20	14
7	2	20.3	23.7	72	11	11	8	8	5	9	7
8	2	23.8	24.8	81	8	7	6	5	4	6	5
9	12	35.5	17.4	49	17	23	19	12	8	16	12
10	6	19.5	23.5	69	12	13	10	8	6	10	8
11	1	29.1	29.1	88	5	4	3	3	2	4	3
13	13	24.5	18.0	53	16	21	17	11	8	15	11
14	7	24.9	23.2	75	10	10	7	7	5	8	6

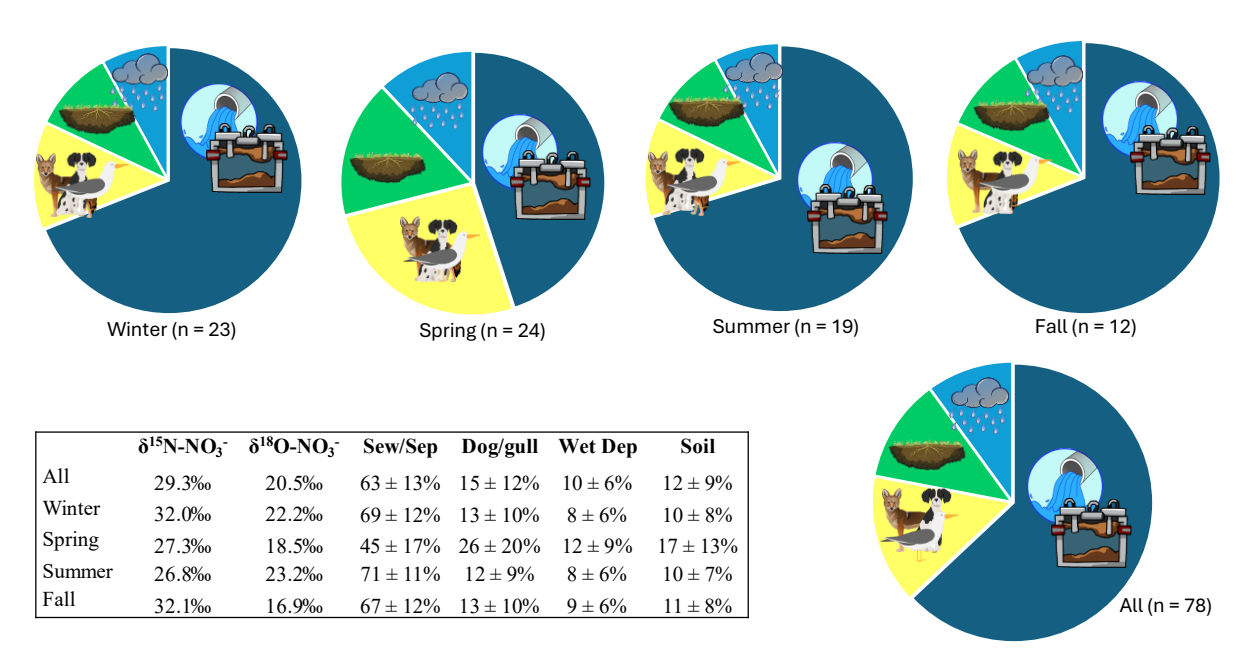


*Figure 5.11.* Ground water NO3- estimated source % contributions throughout duration of sampling and for each season.

# 5.4.2. Ammonium Spatial and Temporal Variations

# 5.4.2.1. Ammonium Surface Water

The average  $NH_4^+$  concentration of surface water samples was  $4.9 \pm 9.4~\mu M$  (n = 300). Averages were lowest in the summer ( $2.2 \pm 2.0~\mu M$ ) and highest in winter ( $3.8 \pm 3.8~\mu M$ ) with the averages being significantly different (p = 0.007) (*Figure 5.12*). There were no significant differences across sites with the exception of S1 ( $11.4 \pm 13.4~\mu M$ ) being significantly higher than a few sites, but it should be noted that this is the only bay surface sample as opposed to all others being Gulf of Mexico surface sites (*Figure 5.13*).

Average  $\delta^{15}$ N-NH<sub>4</sub><sup>+</sup> values were  $13.1 \pm 6.1\%$  (n = 66). There is less data due to the 3  $\mu$ M threshold for isotopic analysis and the minimal data across all surface sites does not allow for a systematic comparison across sites. There are no significant differences across seasons except fall  $16.7 \pm 4.0\%$  is significantly higher than winter (11.2  $\pm 6.3\%$ ) (p = 0.012).

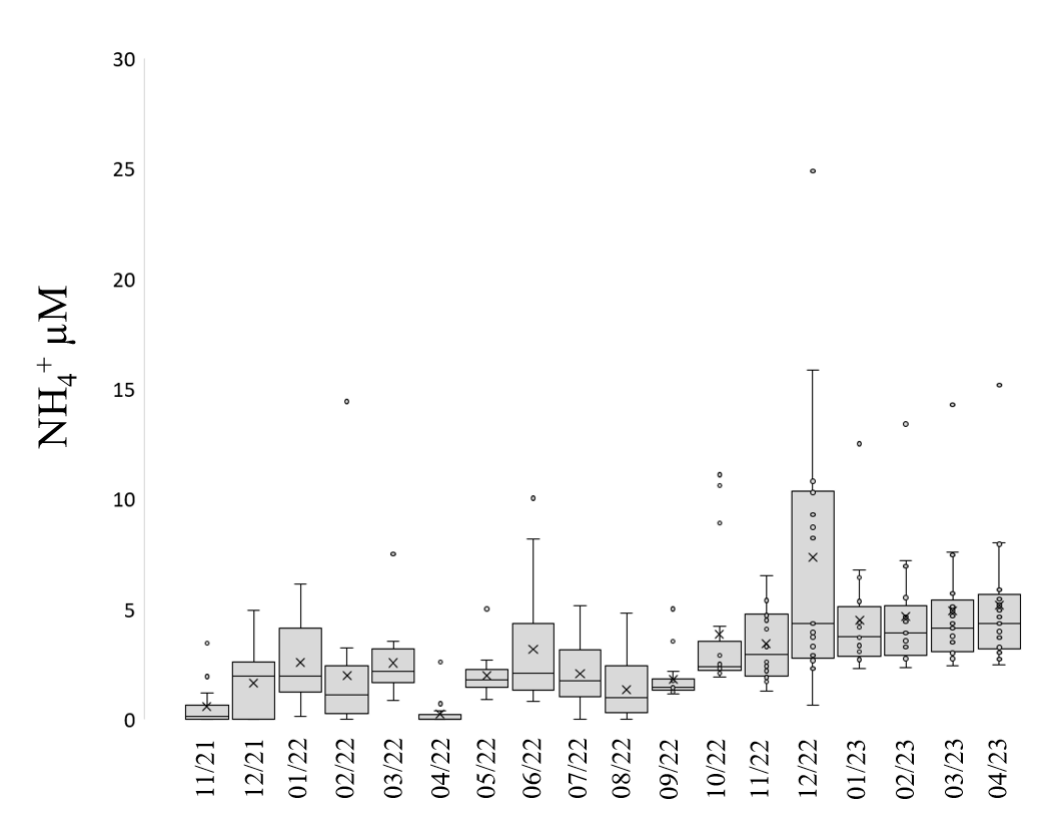


Figure 5.12. Surface water average NH4+ concentrations by month.

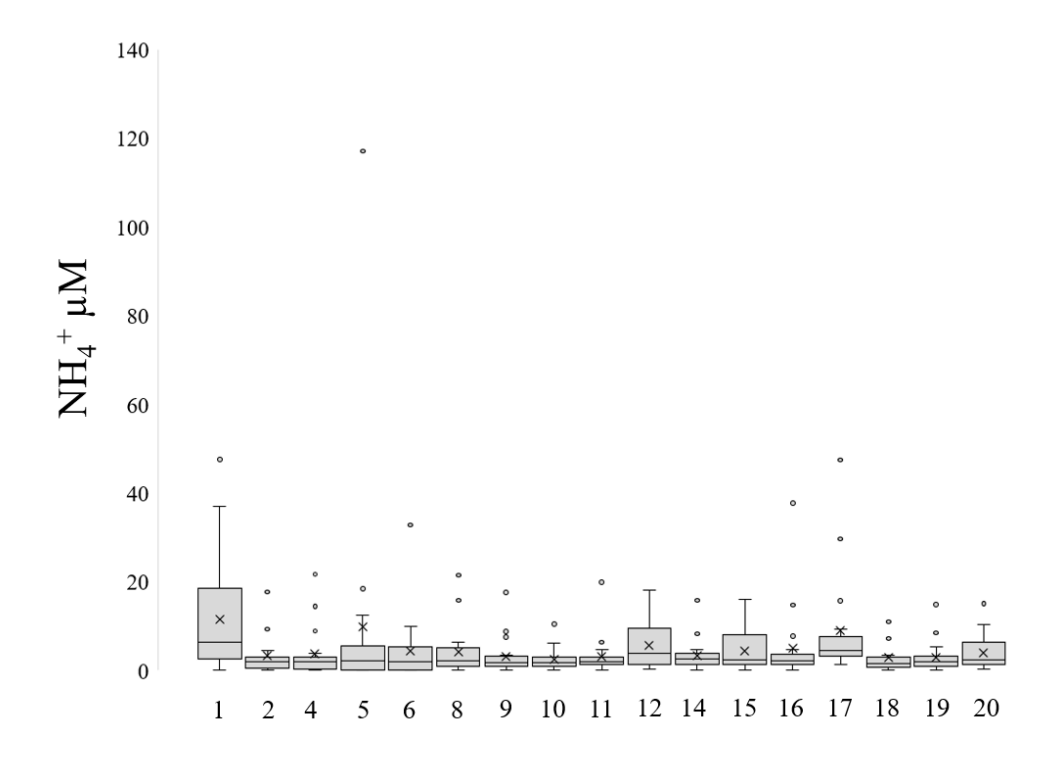


Figure 5.13. Surface water average NH4+ concentrations by site.

#### 5.4.2.2. Ammonium Porewater

The average  $NH_4^+$  concentration of porewater samples was  $27.7 \pm 40.6 \ \mu M$  (n = 192). The three highest porewater sites (i.e., 14, 16, 19) have a significantly higher average concentration (49.9 ± 67.3  $\mu M$ ) than average of the rest of the sites' average concentration (20.7 ± 23.6  $\mu M$ ) (p = 0.00002) (*Figure 5.15*). There were no significant differences between seasons except fall (18.6 ± 26.4  $\mu M$ ) was significantly lower than spring (31.5 ± 28.3  $\mu M$ ) (p = 0.03) (*Figure 5.14*).

Average  $\delta^{15}$ N-NH<sub>4</sub><sup>+</sup> values were  $10.6 \pm 6.3\%$  (n = 138). There was no significant difference between sites except between the highest (site 9:  $12.9 \pm 4.0\%$ ) and the lowest site (site 14:  $7.0 \pm 8.0\%$ ) (p = 0.01). There was no significant difference among seasons except spring is significantly lower than all other seasons ( $7.8 \pm 7.3\%$ ) (p < 0.02).

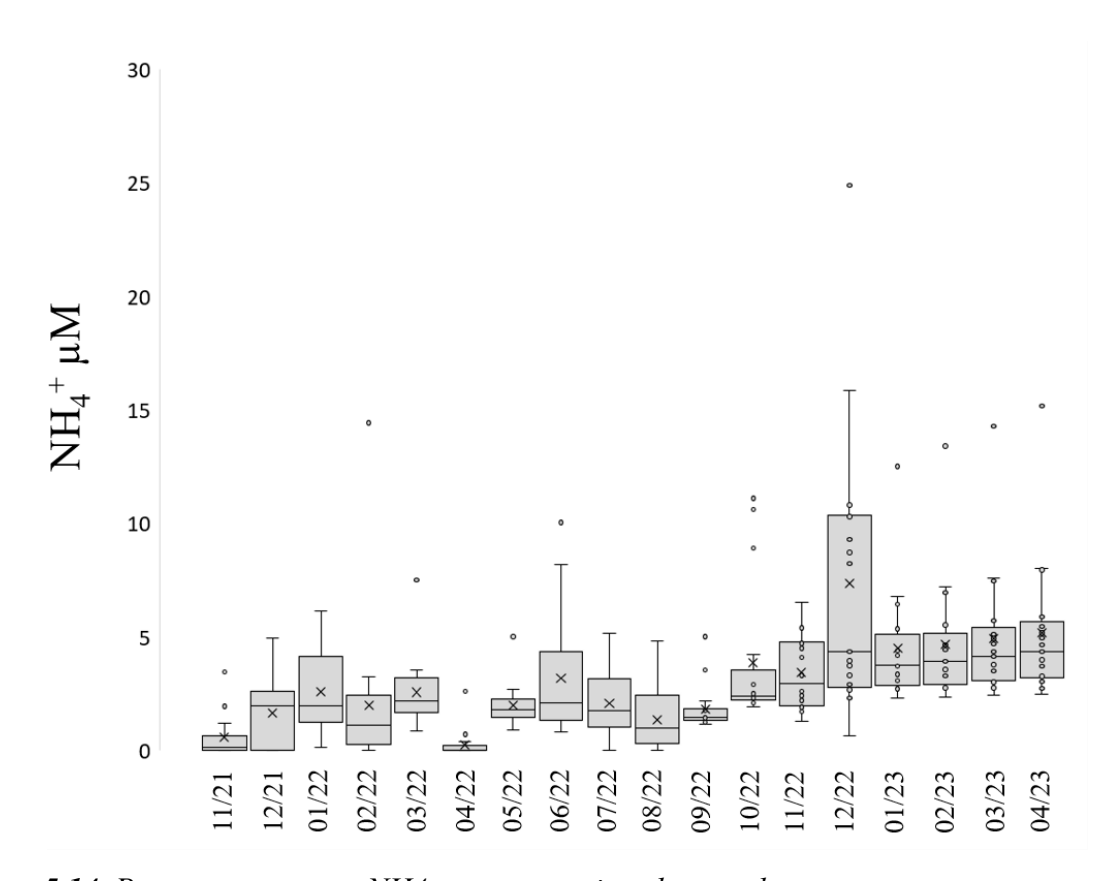
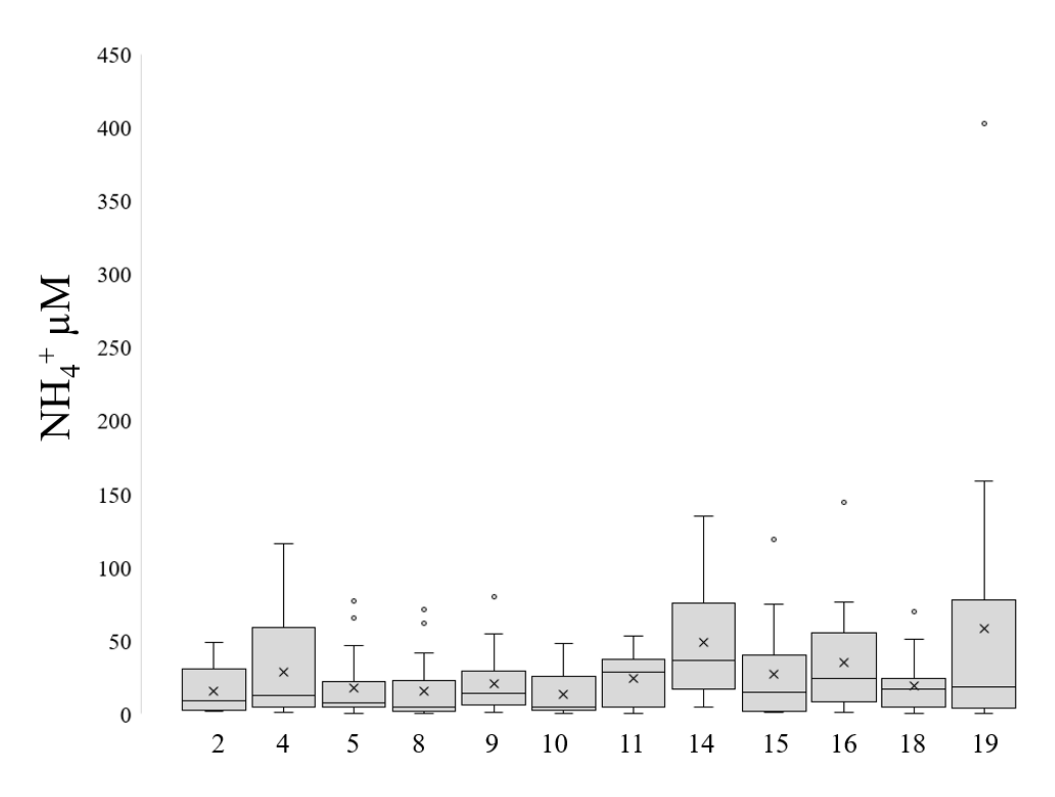


Figure 5.14. Porewater average NH4+ concentrations by month.



*Figure 5.15. Porewater average NH4+ concentrations by site.* 

#### 5.4.2.3. Ammonium Groundwater

The overall average  $NH_4^+$  concentrations of groundwater samples were  $158.9 \pm 345.2$   $\mu M$ . The outlier of 3707  $\mu M$  for the April W11 sample was removed during spatial and temporal analysis (Grubbs test, p < 0.01). The well concentrations fell into three tiers with the W5 and W7 average (507.8  $\pm$  335.8  $\mu M$ ) being significantly higher than the average for wells 3, 10 and 11 (118.4  $\pm$  108.1  $\mu M$ ) and those wells being significantly higher than wells 1, 2, 4, 8, 9, 13, and 14 (41.7  $\pm$  123.4  $\mu M$ ) (ANOVA; p < 0.0001) (**Figure 5.17**). The highest tier had high concentrations in the summer (726.1  $\pm$  580.0  $\mu M$ ) as did the second tier (179.4  $\pm$  210.4  $\mu M$ ) but summer concentrations were not significantly different from other seasons (**Figure 5.16**). The lowest concentration tier had very significantly higher concentrations in the summer (156.1  $\pm$  264.2  $\mu M$ ), specifically driven by the month of June.

Average  $\delta^{15}$ N-NH<sub>4</sub><sup>+</sup> values were  $10.9 \pm 8.3\%$  (n = 116). Spring (7.6  $\pm$  7.8%) was significantly lower than all other seasons (p < 0.02) and winter (10.3  $\pm$  9.4%) is significantly lower than fall (14.9  $\pm$  6.2%)(p = 0.02).  $\delta^{15}$ N-NH<sub>4</sub><sup>+</sup> values for the three tiers were 6.8  $\pm$  5.1% (highest concentration tier),  $10.5 \pm 8.8\%$  (next highest),  $15.0 \pm 8.1\%$  (lowest) with all three tiers being significantly different (p < 0.05).

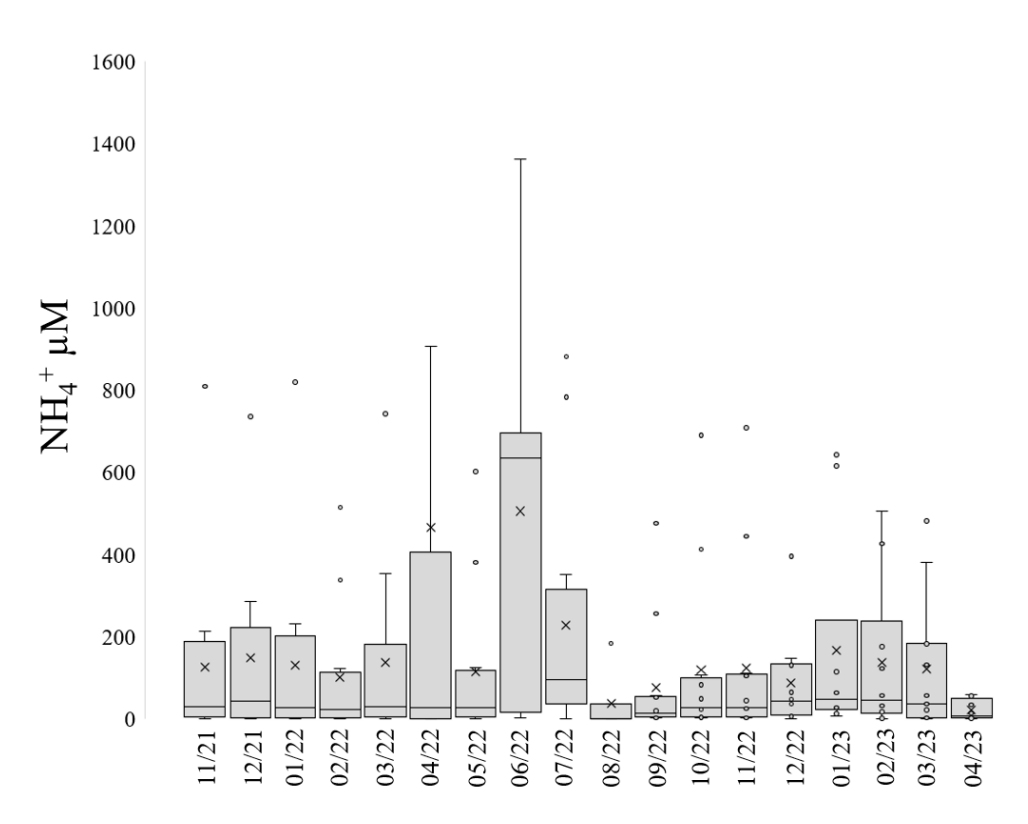


*Figure 5.16.* Groundwater average NH4+ concentrations by month. \*Outlier 3707  $\mu$ M at well 11 not pictured.

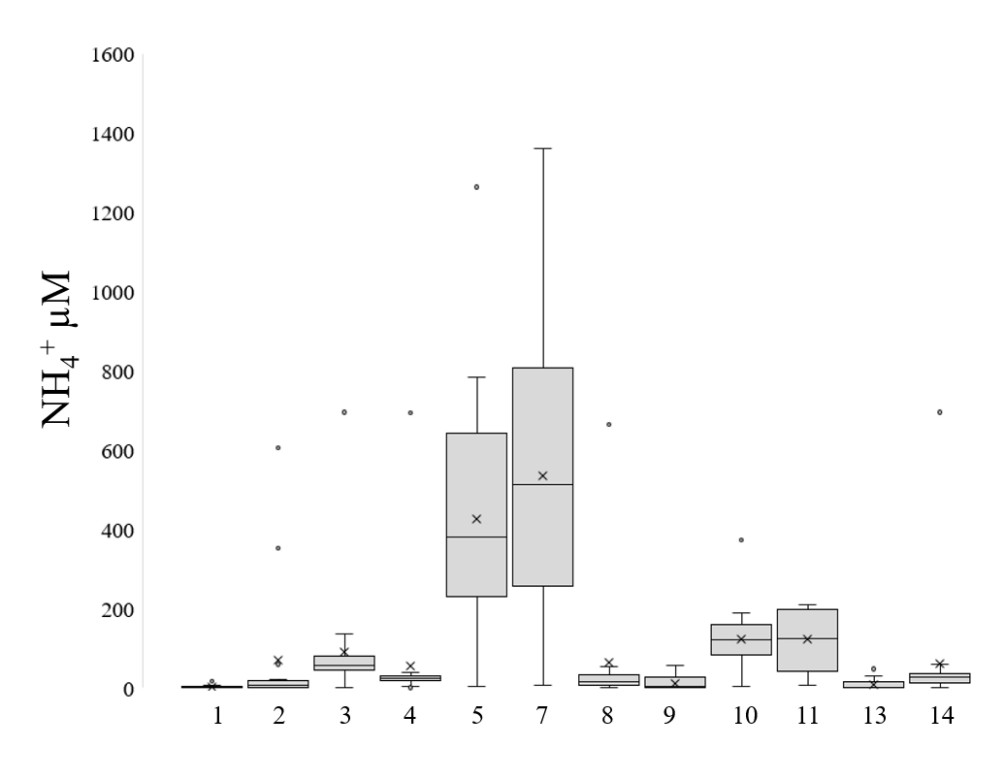


*Figure 5.17.* Groundwater average NH4+ concentrations by site. \*Outlier 3707  $\mu$ M at well 11 not pictured.

## 5.4.3. DON Spatial and Temporal Variations

### 5.4.3.1. DON Surface Water

The average surface water DON concentrations were  $7 \pm 5~\mu M$  (n = 300). Fall ( $10 \pm 4~\mu M$ ) and summer ( $9 \pm 4~\mu M$ ) had significantly higher concentrations than winter ( $5 \pm 5~\mu M$ ) and spring ( $7 \pm 6~\mu M$ ) p < 0.01) (*Figure 5.18*). Site 1 was the only bay surface water site and had the highest average concentration ( $12 \pm 9~\mu M$ ). Surface water sites 14 and 2 were the highest ( $9 \pm 6~\mu M$ ) and lowest ( $4 \pm 4~\mu M$ ) concentrations of Gulf surface water, respectively but were not significantly different (*Figure 5.19*).

Surface water samples had average  $\delta^{15}$ N-DON isotopic values of  $5 \pm 5\%$  (n = 208). Summer values (7 ± 3%) are significantly higher than fall (4 ± 3%) and winter (4 ± 4%) (p < 0.0001). Most sites had average values which were not significantly different but the highest value site 2 (7 ± 12%) and lowest value site 6 (2 ± 3%) were significantly different than several sites.

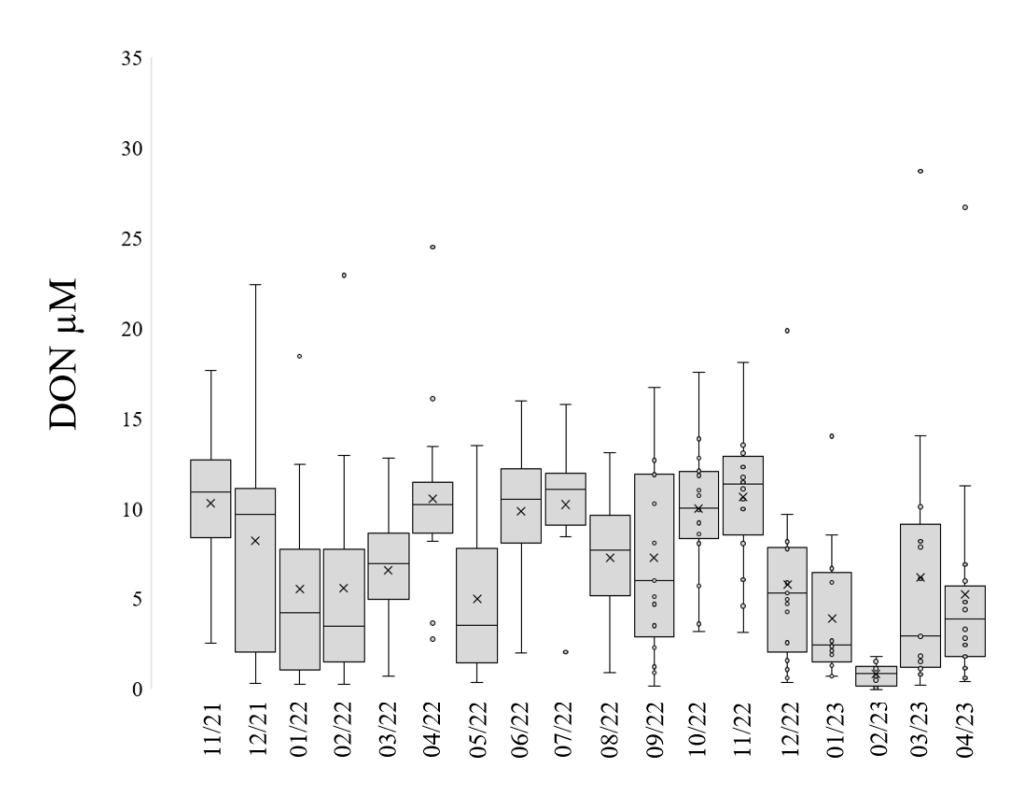


Figure 5.18. Surface water average DON concentrations by month.

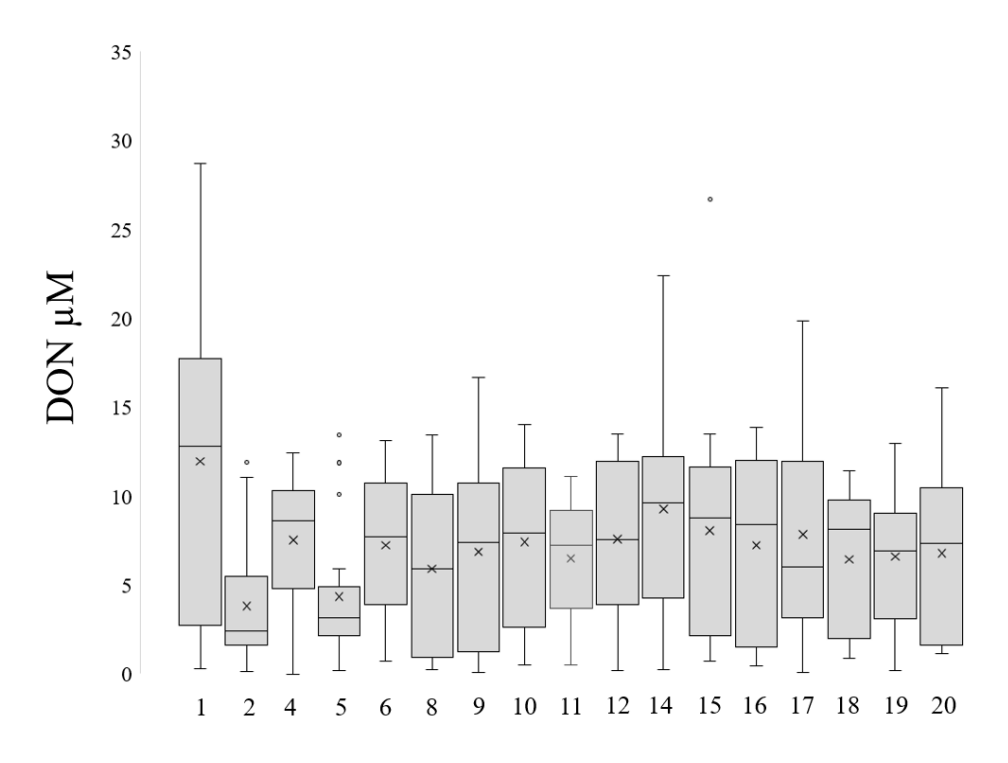


Figure 5.19. Surface water average DON concentrations by site.

## 5.4.3.2. DON Porewater

Average porewater DON concentrations were  $7\pm 8~\mu M$  (n = 192). There were no significant differences between fall (8 ± 8  $\mu M$ ), winter (8 ± 10  $\mu M$ ), spring (7 ± 8  $\mu M$ ), and summer (7 ± 7  $\mu M$ ) seasons (*Figure 5.20*). Most sites had average concentrations which were not significantly different but the highest value site 10 (14 ± 13  $\mu M$ ) and lowest value site 15 (1 ± 2  $\mu M$ ) were significantly different than several sites (*Figure 5.21*) (p < 0.05).

Porewater samples had average  $\delta^{15}$ N-DON isotopic values of  $5 \pm 5\%$  (n = 113). There were no significant differences between seasons. Most sites had average values which were not significantly different but the highest value site 19 (8 ± 10‰) and lowest value site 15 (4 ± 3‰) were significantly different than several sites (p < 0.05).

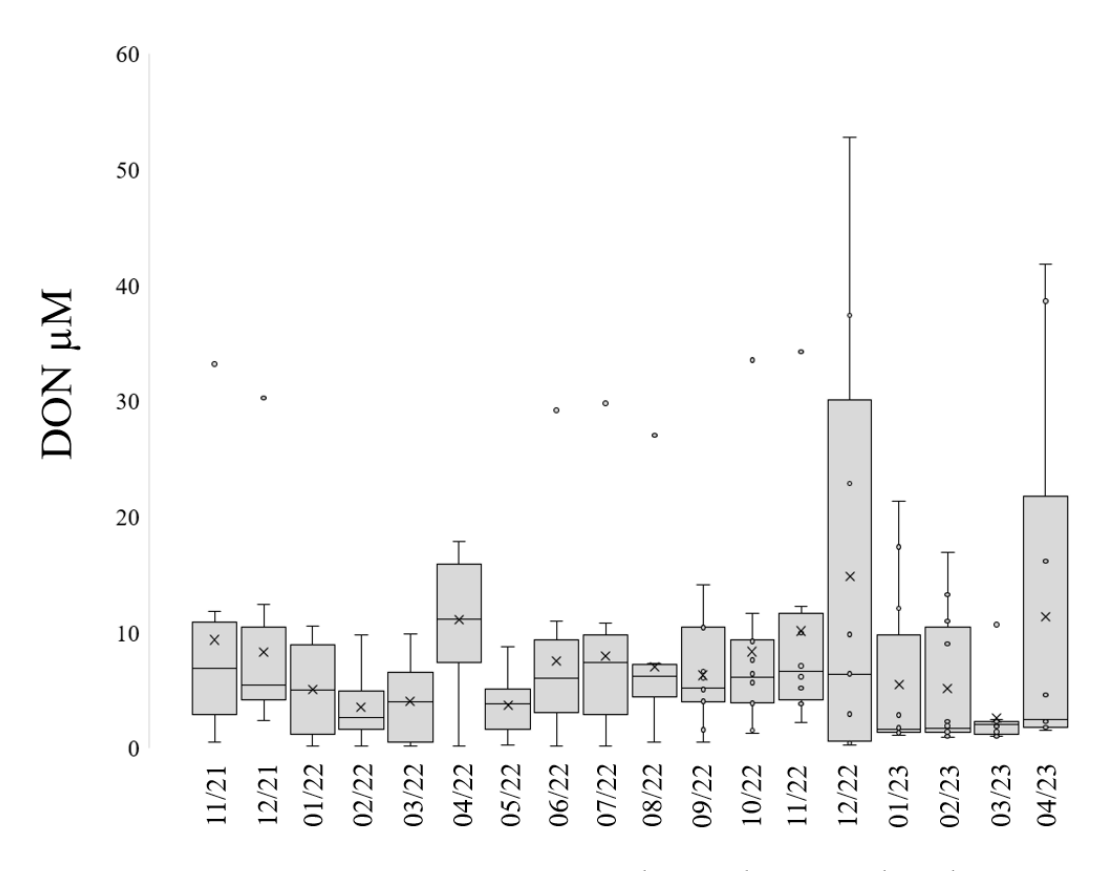


Figure 5.20. Porewater average DON concentrations by month. Moving line shows averages.

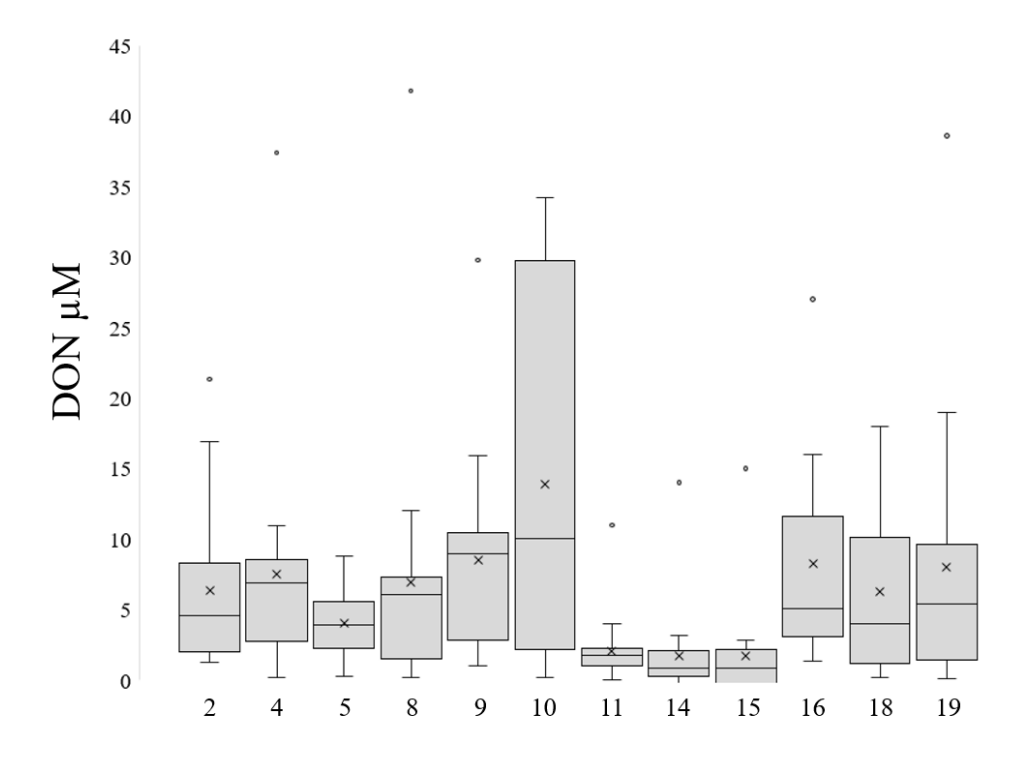
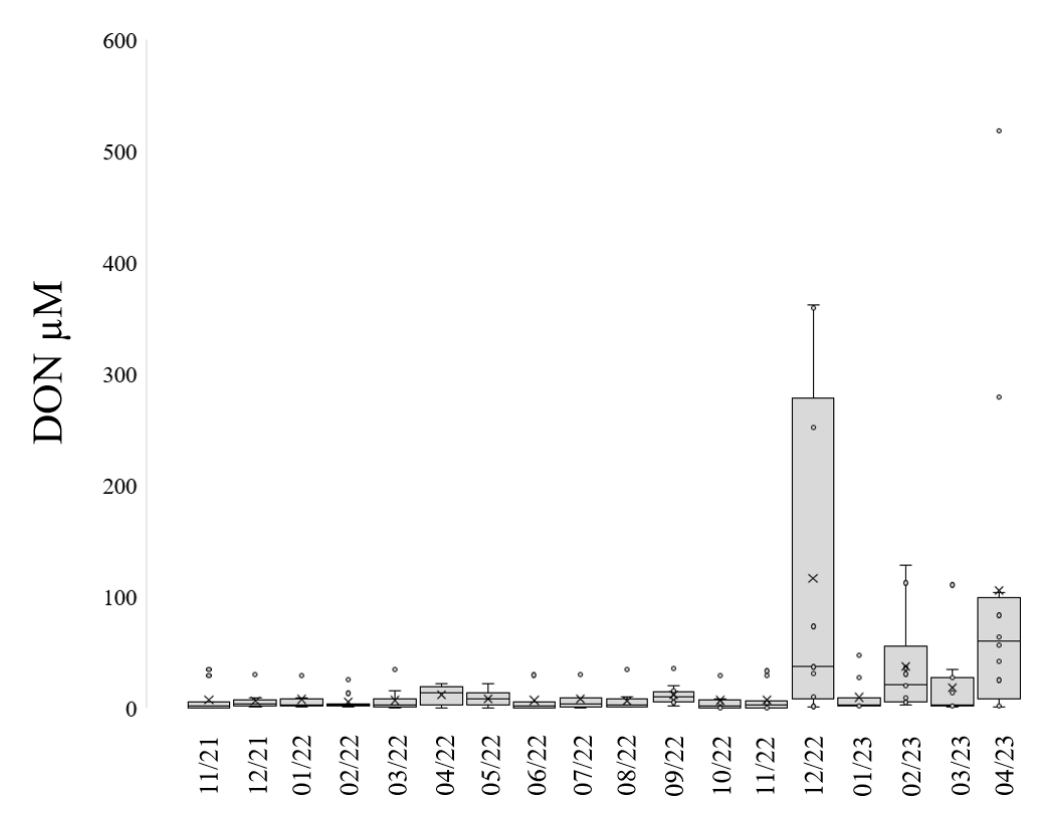


Figure 5.21. Porewater average DON concentrations by month site.

## 5.4.3.3. DON Groundwater

Average DON groundwater concentrations were  $21 \pm 58 \,\mu\text{M}$  (n = 207). Well concentrations were separated into two tiers, with wells 5 and 7 having significantly higher average concentrations  $(48 \pm 123 \,\mu\text{M})$  than the other wells  $(15 \pm 29 \,\mu\text{M})$  (p = 0.002) (**Figure 5.23**). Despite winter  $(29 \pm 71 \,\mu\text{M})$  and spring  $(30 \pm 77 \,\mu\text{M})$  averages being noticeably higher than summer  $(7 \pm 10 \,\mu\text{M})$  and fall  $(8 \pm 10 \,\mu\text{M})$ , the large range in each season leads to no significant difference across seasons. (**Figure 5.22**). The wide ranges are driven by high concentrations in some wells in December 2022 and April 2023.

The average  $\delta^{15}$ N-DON values of groundwater samples were  $3 \pm 11\%$  (n = 92). Many samples did not have high enough concentrations for isotope analysis (> 3  $\mu$ M). In addition, samples that had [NO<sub>3</sub>-]/[TDN] over 80% were not included in isotope analysis due to enhanced error in  $\delta^{15}$ N-DON back calculation at these ratios. Although winter values were noticeably higher, the range in values led there to be no significant difference across seasons. Site 4 had the highest average value (9 ± 15‰) and site 11 had the lowest value (-3 ± 8‰) and were significantly different from each other p = 0.03.



*Figure 5.22. Groundwater average DON concentrations by month.* 

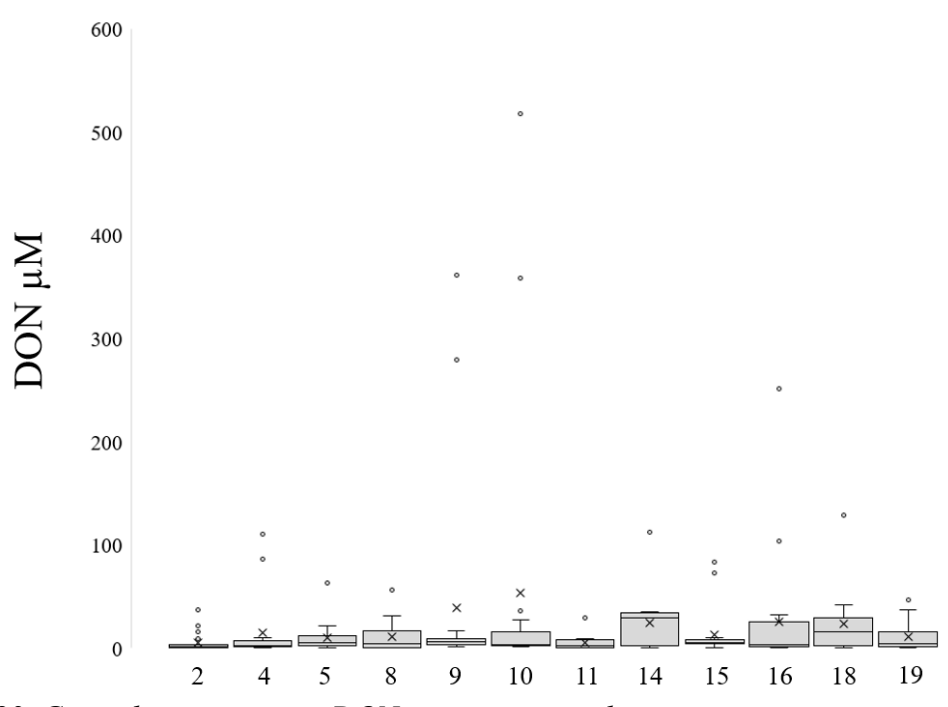


Figure 5.23. Groundwater average DON concentrations by site.

# 5.4.4. Ancillary Data

Nitrate, ammonium and dissolved organic nitrogen concentrations data were investigated with respect to ancillary measurements (e.g.,) Correlation matrix and p significance matrix are included as **Table 5.9**, **Table 5.10**, **Table 5.11**, **Table 5.12**, **Table 5.13**, and **Table 5.14** and organized by matrix – surface water, pore water, and groundwater.

**Table 5.9.** Correlation matrix for surface water. Numbers in each cell represent the correlation coefficient "R" and a positive or negative relationship. DTW is depth to water and DO is dissolved oxygen.

	$NO_3$	$NO_2$	$NH_4^+$	δ <sup>15</sup> N-	δ <sup>18</sup> O-	$\delta^{15}$ N-	δ <sup>15</sup> N-	DON	Temp	DO	Salinity
				$NO_3$	$NO_3$	$NH_4^+$	DON				
NO <sub>3</sub> -	1.00										
$NO_2$	0.07	1.00									
$NH_4^+$	0.10	0.17	1.00								
$\delta^{15}$ N-NO <sub>3</sub>	-0.03	0.06	0.003	1.00							
$\delta^{18}\text{O-NO}_3$	-0.22	-0.22	-0.04	0.54	1.00						
$\delta^{15}$ N-NH <sub>4</sub> <sup>+</sup>	-0.75	-0.30	0.19	0.20	0.07	1.00					
$\delta^{15}$ N-DON	0.04	0.69	0.16	0.06	-0.14	0.38	1.00				
DON	-0.14	-0.05	-0.24	0.09	-0.01	-0.19	0.02	1.00			
Temp	-0.16	0.08	-0.13	0.29	-0.02	0.06	0.20	0.19	1.00		
DO	0.16	0.00	0.14	-0.31	-0.13	-0.12	-0.17	0.03	-0.63	1.00	
Sal	-0.19	-0.14	-0.26	0.08	0.11	0.24	0.08	-0.16	0.28	-0.52	1.00
pН	0.03	-0.01	-0.03	-0.17	-0.17	0.13	-0.07	0.15	-0.24	0.40	-0.12

**Table 5.10.** Probability (p) value correlation significance matrix for surface water. Numbers in each cell represent the p-value of the correlation. Numbers in each cell represent the p-value of the correlation. Light blue to dark blue values indicate significant negative correlations increasing in magnitude with darkness. Light purple to dark purple values indicate significant positive correlations increasing in magnitude with darkness.

	NO <sub>3</sub> -	NO <sub>2</sub> ·	$NH_4^+$	$\delta^{15}$ N-	δ <sup>18</sup> O-	δ <sup>15</sup> N-	δ <sup>15</sup> N-	DON	Temp	DO	Salinity
				NO <sub>3</sub> -	NO <sub>3</sub> -	$\mathrm{NH_4}^+$	DON				
NO <sub>3</sub> -											
NO <sub>2</sub> -	0.2200										
$NH_4^+$	0.0900	0.0033									
$\delta^{15}$ N-NO <sub>3</sub> -	0.7600	0.3030	0.9570								
				<							
$\delta^{18}\text{O-NO}_3^-$	0.0220	0.0220	0.6810	0.0001							
	<				0.574						
$\delta^{15}$ N-NH <sub>4</sub> <sup>+</sup>	0.0001	0.0136	0.1240	0.1047	0						
		<			0.148						
δ <sup>15</sup> N-DON	0.5700	0.0001	0.0220	0.5370	0	0.0015					
			<		0.918						
DON	0.0160	0.3900	0.0001	0.3540	0	0.1240	0.7770				
					0.827						
Temp	0.0058	0.1700	0.0250	0.0020	0	0.6300	0.0041	0.0010			
					0.180				<		
DO	0.0058	1.0000	0.0159	0.0011	0	0.3330	0.0151	0.6070	0.0001		
			<		0.257				<	<	
Sal	0.0010	0.0159	0.0001	0.4110	0	0.0504	0.2550	0.0058	0.0001	0.0001	
					0.078					<	
pН	0.6850	0.8920	0.6850	0.0786	6	0.2940	0.2680	0.3440	0.0010	0.0001	0.1037

**Table 5.11.** Correlation matrix for pore water. Numbers in each cell represent the correlation coefficient "R" and a positive or negative relationship. DTW is depth to water and DO is dissolved oxygen.

	$NO_3$	$NO_2$	$NH_4^+$	$\delta^{15}$ N-	δ <sup>18</sup> O-	δ <sup>15</sup> N-	$\delta^{15}$ N-	DON	Temp	DO	Salinity
				$NO_3$	$NO_3$	$NH_4^+$	DON				
$NO_3^-(\mu M)$	1.00										
$NO_2^-(\mu M)$	0.36	1.00									
$NH_4^+(\mu M)$	-0.20	-0.15	1.00								
$\delta^{15}$ N-NO <sub>3</sub> -	-0.11	-0.05	0.32	1.00							
$\delta^{18}\text{O-NO}_3$	-0.25	-0.16	0.35	0.86	1.00						
$\delta^{15}$ N-NH <sub>4</sub> <sup>+</sup>	-0.06	0.28	-0.03	-0.39	-0.50	1.00					
$\delta^{15}$ N-DON	0.33	0.17	-0.19	0.01	-0.10	0.10	1.00				
DON	-0.06	0.03	-0.07	0.00	-0.07	-0.18	0.23	1.00			
(µM)	-0.00	0.03	-0.07	0.00	-0.07	-0.16	0.23	1.00			
Temp	-0.19	0.15	-0.10	0.13	0.10	-0.05	0.00	0.08	1.00		
DO	0.28	-0.02	-0.32	-0.46	-0.44	0.00	-0.02	-0.10	-0.25	1.00	
Sal	-0.04	0.12	-0.22	-0.05	-0.10	0.09	-0.03	0.09	0.37	0.14	1.00
pН	0.03	-0.17	-0.10	-0.30	-0.35	-0.18	-0.09	0.16	-0.12	0.12	-0.16

**Table 5.12.** Probability (p) value correlation significance matrix for pore water. Numbers in each cell represent the p-value of the correlation. Numbers in each cell represent the p-value of the correlation. Light blue to dark blue values indicate significant negative correlations increasing in magnitude with darkness. Light purple to dark purple values indicate significant positive correlations increasing in magnitude with darkness.

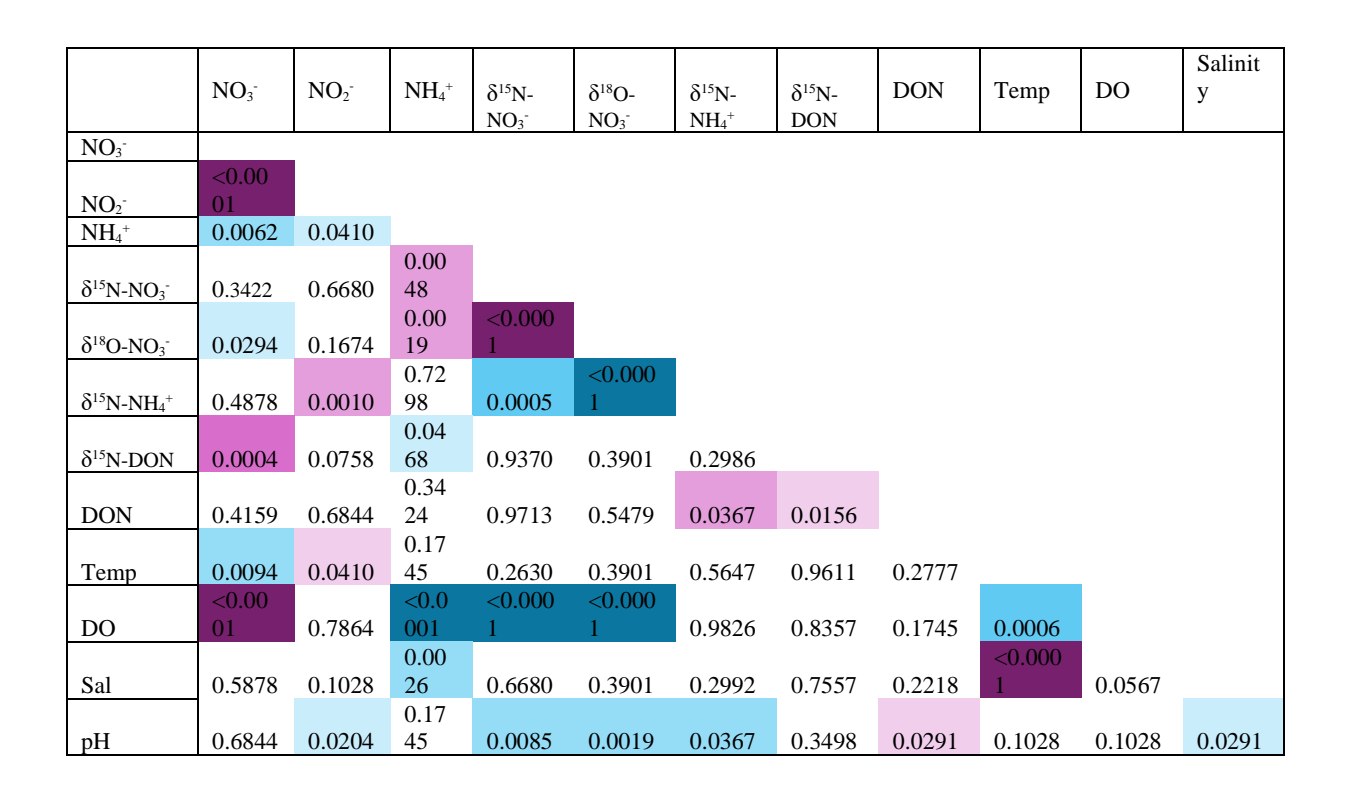


**Table 5.13.** Correlation matrix for groundwater. Numbers in each cell represent the correlation coefficient "R" and a positive or negative relationship. DTW is depth to water and DO is dissolved oxygen.

	$NO_3$	$NO_2$	$NH_4^+$	$\delta^{15}$ N-	δ <sup>18</sup> O-	$\delta^{15}$ N-	$\delta^{15}$ N-	DON	DTW	Temp	DO	Sal
				$NO_3$	$NO_3$	$NH_4^+$	DON					
NO <sub>3</sub> -	1.00											
$NO_2$	0.42	1.00										
$NH_4^+$	-0.11	-0.11	1.00									
$\delta^{15}$ N-NO <sub>3</sub>	0.18	0.01	-0.39	1.00								
$\delta^{18}\text{O-NO}_3$	-0.35	-0.30	0.13	0.22	1.00							
$\delta^{15}N-NH_4^+$	0.18	0.00	-0.12	0.00	-0.24	1.00						
$\delta^{15}$ N-DON	0.25	0.08	-0.13	0.22	-0.18	-0.06	1.00					
DON	-0.01	0.02	-0.06	-0.17	-0.15	-0.39	0.05	1.00				
DTW	0.10	0.03	-0.21	0.62	-0.11	0.37	0.18	-0.19	1.00			
Temp	-0.12	-0.12	-0.04	-0.07	-0.03	0.26	0.07	-0.13	0.18	1.00		
DO	-0.05	-0.14	-0.06	0.21	0.04	0.12	-0.07	0.01	0.26	0.12	1.00	
Sal	-0.13	-0.09	0.34	-0.08	0.24	-0.30	-0.20	0.11	-0.36	0.01	0.01	1.00
pН	0.14	-0.03	-0.04	0.14	0.03	-0.18	-0.16	-0.06	0.14	-0.08	-0.02	-0.05

**Table 5.14.** Probability (p) value correlation significance matrix for groundwater. Numbers in each cell represent the p-value of the correlation. Numbers in each cell represent the p-value of the correlation. Light blue to dark blue values indicate significant negative correlations increasing in magnitude with darkness. Light purple to dark purple values indicate significant positive correlations increasing in magnitude with darkness.

Ī										DTW	Tem		
		$NO_3$	$NO_2$	$NH_4^+$	$\delta^{15}$ N-	δ <sup>18</sup> O-	$\delta^{15}$ N-	$\delta^{15}$ N-			p	DO	Sal
					$NO_3$	NO <sub>3</sub> -	$\mathrm{NH_4}^+$	DON	DON				
	$NO_3$												

	< 0.00											
$NO_2$	01											
$NH_4^+$	0.1090	0.1224										
$\delta^{15}$ N-NO <sub>3</sub> -	0.1148	0.9182	0.0004									
$\delta^{18}\text{O-NO}_3$	0.0017	0.0076	0.2566	0.0529								
$\delta^{15}N\text{-}NH_4^+$	0.0542	0.9999	0.2015	0.9999	0.0343							
$\delta^{15}$ N-DON	0.0157	0.4459	0.2142	0.0529	0.1148	0.5241						
						< 0.00						
DON	0.9148	0.7756	0.3916	0.1367	0.1899	01	0.6341					
				< 0.00		< 0.00		0.006				
DTW	0.1372	0.6701	0.0026	01	0.3377	01	0.0843	5				
								0.062	0.009			
Temp	0.0842	0.0858	0.5681	0.5425	0.7943	0.0050	0.5049	5	6			
								0.886	0.000	0.085		
DO	0.5005	0.0447	0.3916	0.0650	0.7281	0.2015	0.5049	6	2	8		
			< 0.00					0.115	< 0.00	0.886		
Sal	0.0636	0.1983	01	0.4863	0.0343	0.0011	0.0546	5	01	6	0.886	
								0.391	0.044	0.198		
pН	0.1094	0.6686	0.5681	0.2215	0.7943	0.0542	0.1255	6	7	3	0.776	0.475

#### 5.5. Discussion

#### 5.5.1. Nitrate

## 5.5.1.1. Nitrate surface water

The average  $NO_3^-$  concentrations in surface water samples were  $3.4 \pm 5.2 \mu M$ . While few studies have extensively measured nutrients along the shorelines of barrier islands, these concentrations are slightly higher than those observed offshore in the northern Gulf of Mexico  $(1.46 \pm 6.04 \,\mu\text{M}; \text{Cardona et al., } 2016)$  and fall within the range of global ocean  $(0-35 \,\mu\text{M})$  and coastal ocean concentrations (0-5 µM; Garcia et al., 2024). Seasonal trends revealed significantly higher concentrations during winter ( $5.2 \pm 7.2 \mu M$ ), likely due to reduced assimilation. However, the  $\delta^{15}$ N-NO<sub>3</sub><sup>-</sup> to  $\delta^{18}$ O-NO<sub>3</sub><sup>-</sup> slope of 1.04 suggests active assimilation and/or denitrification processes during this period. Marine nitrification, which tends to increase in winter as phytoplankton experience greater light limitation and create less competition for nitrate, may contribute to this signal (Zakem et al., 2018). However, the higher nitrate concentrations observed in winter are more likely attributable to source loading. November and December 2022 experienced relatively high precipitation (~20 cm), which may have resulted in nitrate input via terrestrial or groundwater sources. A lag in delivery from groundwater could explain the distinct peak in nitrate concentrations observed in January 2023 (14.7  $\pm$  13.8  $\mu$ M). In other seasons, lower nitrate concentrations likely resulted from increased assimilation due to higher phytoplankton activity, as well as enhanced denitrification. Warmer temperatures and reduced dissolved oxygen (DO) levels, which create prime conditions for denitrification, likely contributed to these trends. Notably, nitrate concentrations were negatively correlated with both DO and temperature (p = 0.006). DO levels were significantly lower during spring, summer, and fall, with the lowest values observed in summer. Although nitrification can occur in the euphotic zone alongside these processes and potentially decouple the expected ~1:1 ratio from denitrification and assimilation (Casciotti and Buchwald, 2012; Granger and Wankel, 2016), the combination of low DO and low nitrate concentrations in warmer months likely dominates. This is consistent with reports of marine denitrification slopes as low as 0.5 in such conditions.

Surface water sites were statistically similar for the most part (average 3.2  $\mu$ M) but sites 1 12 14, 19, and 14 had the highest average NO<sub>3</sub><sup>-</sup> concentrations. Site 1 is the only site on the

Trinity Bay is in a more densely populated area and is subject to loading from the San Jacinto River and Houston Ship channel. The other high sites are adjacent to channels accessing the Gulf of Mexico. Dredging can weaken NO<sub>3</sub><sup>-</sup> removal from a system for several years (Dong Jing et al., 2013). Multiple studies have confirmed increased total dissolved solids and NO<sub>3</sub><sup>-</sup> concentrations after dredging has occurred, where dredged sediment can release heavy metal and organic contaminants and bury benthic organisms, which can cause long-term effects like eutrophication and pollution (Zhang et al., 2010; Liu et al., 2019). Inlets themselves exchange nutrients with the ocean and can deliver move concentrated nutrients to the coastal ocean.

 $\delta^{15}$ N values were higher in spring and summer, with the source apportionment model indicating a greater relative contribution of septic and sewage loading during these seasons. This is consistent with increased population density in tourist destinations during spring and summer, which likely strains septic and wastewater infrastructure. Overburdened or malfunctioning systems may contribute to elevated nitrate loading during these high-tourism periods. Interestingly, contributions from dog manure and gull guano were highest in winter. According to the Houston Audubon Society, fall migration along the Texas upper coast begins as early as July and continues through November for shorebirds and gulls, many of which overwinter in this region (Houston Audubon Society, 2023). The elevated contribution of dog and gull waste during winter likely reflects the culmination of migration and the presence of overwintering birds that make the Texas Coast their temporary home. Sites 4 and 5 exhibited the highest average percentage of septic/sewage contribution. Although linking inland activities to adjacent offshore water quality is challenging due to the heterogeneity of groundwater flow, it is notable that these sites are in direct transects that include a condominium complex and a large RV park, both of which utilize septic systems. Sites 6 through 12 and site 17 showed the highest relative contributions from dog and gull waste (~30%), suggesting stretches of beach where bird populations may be concentrated. Previous studies have shown that dogs and gulls can contribute significant amounts of fecal bacteria to surface and pore waters, an issue that has been increasingly observed along beaches in California and Florida (Goodwin et al., 2016; Converse et al., 2012). Despite these contributions, nitrate concentrations at these sites generally remain within the range of typical marine levels, suggesting that contamination from these sources may not be severe.

**Table 5.15.** Seasonal surface, pore, and groundwater nitrate  $\delta 15N$  vs  $\delta 18O$  plot characteristics including number of samples (n), correlation coefficient (R), probability value (p) and likely nitrate processes associated with these characteristics.

Season	Slope	n	R	p	Primary processes indicated
Surface wa	iter				
Fall	Not avai	lable (n =	3)		
Winter	1.04	54	0.59	< 0.0001	denitrification/assimilation/nitrification
Spring	0.76	29	0.73	< 0.0001	denitrification/nitrification/assimilation
Summer	0.58	22	0.52	0.0091	denitrification/nitrification/assimilation
Porewater					
Fall	1.18	10	0.68	0.015	denitrification/DNRA
Winter	1.38	32	0.90	< 0.0001	denitrification/DNRA
Spring	0.77	16	0.85	< 0.0001	denitrification/nitrification
Summer	1.5	19	0.91	< 0.0001	denitrification/DNRA
Groundwa	ter high c	oncentrat	ions		

Fall Winter Spring Summer	0.25 0.25 0.32 -0.12	10 12 11 9	0.85 0.71 0.87 0.39	0.0005 0.0044 <0.0001 0.2357	anammox; denitrification/nitrification anammox; denitrification/nitrification anammox; denitrification/nitrification anammox; denitrification/nitrification	
	ater low co					
Fall	Not avai	lable (n =	2)			
Winter	0.95	11	0.82	0.0003	denitrification/nitrification	
Spring	0.33	13	0.50	0.0577	nitrification/denitrification	
Summer	0.24	11	0.56	0.0515	nitrification/denitrification	

## 5.5.1.2. Nitrate porewater

The overall average porewater  $NO_3^-$  concentration was  $4.3 \pm 7.1 \,\mu\text{M}$ , slightly higher than the surface water average of  $3.4 \pm 5.2 \,\mu\text{M}$ . Elevated  $NO_3^-$  concentrations in porewater relative to surface waters are often attributed to the nitrification of  $NO_3^-$  derived from re-mineralized  $NH_4^+$  in sediments, which is subsequently assimilated in surface waters (Ahrens et al., 2020). The observed negative correlation between  $NO_3^-$  and  $NH_4^+$  (p = 0.0062) supports this process, as  $NH_4^+$ decreases while  $NO_3^-$  increases. Additionally, the strong correlation between  $NH_4^+$  and dissolved oxygen (DO; p < 0.0001) in porewater further suggests active nitrification. However, the similarity in  $NO_3^-$  concentrations between porewater and surface water points to continued circulation and exchange between these two reservoirs, particularly in the dynamic shore break zone where samples were collected. This is further corroborated by the  $\delta^{15}N-NO_3^-$  values in porewater (14.7 ± 4.3‰), which were closely aligned with those in surface water (13.5 ± 3.2‰).

As in surface waters, porewater  $NO_3^-$  concentrations were highest in winter (7.6  $\pm$  12.5  $\mu$ M). This may be linked to nutrient inputs from groundwater discharge, driven by high rainfall in November and December 2022.

Interestingly the slope of  $\delta^{15}N$  and  $\delta^{18}O$  in fall winter and summer was higher than the expected denitrification associated slopes which normally do not exceed 1. Dissimilatory nitrate reduction to ammonium (DNRA) may be a contributing factor, particularly under more anoxic conditions in sandy coastal sediments, where it can account for over 50% of total  $NO_3^-$  reduction (Wankel et al., 2007; Hellemann et al., 2020). However, the isotope effects of DNRA remain uncertain (Inamdar et al., 2024). A similar competition between nitrification and denitrification in marine systems can produce  $\Delta\delta^{18}O$ : $\Delta\delta^{15}N$  slopes greater than 1, particularly when the difference between the  $\delta^{18}O$  of subsurface  $NO_3^-$  and seawater is small. This occurs because, at any given fractionation factor, the  $\delta^{18}O$  of nitrified  $NO_3^-$  is greater than the  $\delta^{18}O$  of  $NO_3^-$  removed by denitrification (Granger and Wankel, 2016). This may also be the case when the  $\delta^{18}O$  of the of DNRA-processed  $NO_3^-$  is greater than the  $\delta^{18}O$  of  $NO_3^-$  removed by denitrification. In summer, however, the slope was below 1 (0.77), likely reflecting a shift toward marine denitrification as the dominant process. The lack of significant differences in  $NO_3^-$  concentrations across porewater sites suggests general homogeneity in porewater conditions or continuous mixing with well-circulated Gulf waters.

 $\delta^{15}$ N values were lowest in fall and winter (13.2 ± 2.3% and 14.0 ± 6.8%, respectively) and highest in summer (16.3 ± 2.7%). These seasonal trends align with surface water patterns, where higher septic/sewage contributions in summer are associated with increased human populations, and elevated dog/gull contributions in fall and winter reflect migratory patterns. Sites 8, 9, 10, 11, and 15 exhibited the highest average dog/gull contributions (~30%), which were consistent with co-located surface water sampling results. Additionally, porewater site 4 showed the highest septic/sewage contribution (60%), with co-located surface water displaying

similar source contributions. This further underscores the potential for continued nitrate exchange between surface and pore waters. The  $\delta^{15}N$  source contribution mixing model indicates that septic/sewage was the primary nitrogen source, both spatially and temporally, across the study region. This suggests that wastewater mitigation strategies could be the most effective approach for reducing  $NO_3$ -loading in the area.

## 5.5.1.3. Nitrate groundwater

The average  $NO_3$  concentration across all wells was  $34.4 \pm 113.5 \,\mu\text{M}$ ; however, three wells (W1, W9, and W13) exhibited significantly higher concentrations, averaging  $115.4 \pm 197.6$  $\mu$ M, compared to the remaining wells, which averaged just  $6.0 \pm 32.9 \mu$ M. According to the EPA, low levels of NO<sub>3</sub><sup>-</sup> occur naturally in groundwater, but concentrations above 16 μM are indicative of human activities, while levels exceeding 48.4 µM suggest contamination (Chaudhuri et al., 2012). The EPA's maximum contaminant level (MCL) for NO<sub>3</sub> in drinking water is 161.3 µM, above which groundwater is considered unsafe for consumption and poses a risk for methemoglobinemia (Powlson et al., 2008). This is particularly concerning in regions reliant on private wells for water, as they are not federally regulated, especially in rural areas with poor water quality (Knobeloch et al., 2000). The three high-concentration wells exceeded the MCL. While these wells are shallow and not intended for personal use, their contamination raises concerns for nearby private well owners, who should exercise caution. Interestingly, the high-concentration wells showed significantly elevated NO<sub>3</sub> levels in winter, with the lowest concentrations observed in summer. This seasonal trend may be rainwater driven, as seen with elevated porewater and surface water NO<sub>3</sub> concentrations during winter. The extremely high concentrations in January 2023 likely reflect groundwater flow influenced by heavy rainfall in November and December 2022. Well 1, located inland along the bay coastline and serviced by municipal sewage, displayed high NO<sub>3</sub>-levels following rain events. This may suggest the municipal infrastructure's inability to handle heavy rainfall, potentially indicating leakage or other vulnerabilities. Wells W9 and W13, situated near septic fields, may have experienced septic system saturation from the heavy rains, compromising drainage and reducing the septic system's ability to effectively treat sewage.

Plotting  $\delta^{15}N$  vs.  $\delta^{18}O$  data revealed two distinct processing categories in the wells: one associated with  $\delta^{15}N$  values over 30‰ and another with  $\delta^{15}N$  values below 30‰. Samples with  $\delta^{15}N$  values under 30‰ showed no significant correlation between  $\ln(NO_3^-)$  and  $\delta^{15}N$ -  $NO_3^-$ , but their  $\delta^{15}N$  vs.  $\delta^{18}O$  slope was 0.89, indicating a primarily denitrification-driven process. In contrast, samples with  $\delta^{15}N$  values over 30‰ had a very low  $\delta^{15}N$  vs.  $\delta^{18}O$  slope (0.13), suggestive of competing processes: nitrate production through oxidation and nitrate loss through reduction.

Given the low DO levels in the wells  $(3.2 \pm 2.1 \text{ mg/L})$ , the oxidation process is likely dominated by anammox, a significant oxidation pathway in aquifers (Clark et al., 2008; Erler et al., 2008; Robertson et al., 2012; Granger and Wankel, 2016). Anammox can result in substantial fractionation, potentially explaining the high  $\delta^{15}N$  values. Brunner et al. (2013) proposed that nitrate production via anammox exhibits an inverse kinetic fractionation effect of -31‰. Furthermore, anammox processes can decouple oxygen and nitrogen isotopes (Dähnke et al., 2015), which could explain the anomalously low  $\delta^{15}N$  vs.  $\delta^{18}O$  slope observed in the >30‰ samples.

After correcting the well sample  $\delta^{15}N$  values for their respective processing isotope effects, these corrected values were incorporated into the isotope source apportionment model. Results indicated that sewage/septic systems were the primary nitrate source (~63%) across both high-

and low-concentration wells. Again, this suggests that wastewater mitigation strategies could be the most effective approach for reducing NO<sub>3</sub>-loading in the area.

## 5.5.2. Ammonium

## 5.5.2.1. Surface water NH<sub>4</sub><sup>+</sup>

The average  $NH_4^+$  concentration in surface water samples was  $4.9 \pm 9.4~\mu M$ , notably higher than levels typically found in open ocean environments (approximately 1  $\mu M$ ). In such environments,  $NH_4^+$  is rapidly assimilated by primary producers or oxidized through nitrification almost as quickly as it is produced (Altabet, 2006). Seasonal trends in  $NH_4^+$  concentrations were observed, with the lowest averages in summer ( $2.2 \pm 2.0~\mu M$ ) and the highest in winter ( $3.8 \pm 3.8~\mu M$ ), likely driven by changes in primary producer populations and associated assimilation. Spatially, no significant differences were observed across sites, except for S1, which had a high average concentration of  $11.4 \pm 13.4~\mu M$ . S1 is unique as it is located on Trinity Bay rather than the Gulf of Mexico. It is influenced by higher population densities, inputs from the San Jacinto River, and activities associated with the Houston Ship Channel.

The average  $\delta^{15}$ N-NH<sub>4</sub><sup>+</sup> value was  $13.1 \pm 6.1\%$ . Isotopic data for NH<sub>4</sub><sup>+</sup> in surface waters are generally limited due to analytical challenges, but studies with sufficient NH<sub>4</sub><sup>+</sup> concentrations for isotopic analysis suggest  $\delta^{15}$ N-NH<sub>4</sub><sup>+</sup> values in marine environments typically range from +10% to +29%. These elevated values, combined with low NH<sub>4</sub><sup>+</sup> concentrations, often indicate fractionation from consumptive processes such as nitrification or ammonium assimilation (Sigman and Casciotti, 2001). Seasonal differences in  $\delta^{15}$ N-NH<sub>4</sub><sup>+</sup> were minimal, except for fall (16.7 ± 4.0%), which was significantly higher than winter (11.2 ± 6.3%). The lower winter  $\delta^{15}$ N-NH<sub>4</sub><sup>+</sup> values may reflect reduced fractionation due to a lack of uptake and nitrification activity during this period.

#### 5.5.2.2 Porewater NH<sub>4</sub><sup>+</sup>

Ammonium (NH<sub>4</sub><sup>+</sup>) was the dominant nitrogen species in porewater, with average concentrations of  $27.7 \pm 40.6 \mu M$ . This is consistent with findings from other barrier island studies, such as Ahrens et al. (2020), which reported porewater NH<sub>4</sub><sup>+</sup> concentrations ranging from 0 to 163 µM. NH<sub>4</sub><sup>+</sup> dominance in most anoxic sediment porewaters is attributed to the degradation of organic nitrogen through remineralization and dissimilatory nitrate reduction to ammonium (DNRA) (Zhao et al., 2023). Remineralized nutrients in porewater are subsequently nitrified and assimilated by primary producers in surface waters. Generally, fine sediments promote NH<sub>4</sub><sup>+</sup>generation due to their low oxygen levels and high organic matter content (USEPA). Porewater NH<sub>4</sub><sup>+</sup> concentrations were significantly higher than those in surface waters. While this contrasts with the nitrate discussion, which suggested consistent recirculation between porewater and surface water, it may indicate high turnover rates of NH<sub>4</sub><sup>+</sup> once in the water column. Three porewater sites (14, 16, and 19) exhibited higher average NH<sub>4</sub><sup>+</sup> concentrations  $(49.9 \pm 67.3 \mu M)$  compared to the remaining sites  $(20.7 \pm 23.6 \mu M)$ . These sites' proximity to channels likely exposes them to direct nutrient inputs. Seasonally, NH<sub>4</sub><sup>+</sup> concentrations were highest in summer and spring, potentially due to increased temperatures and higher primary productivity, which provide more organic matter for microbial degradation into NH<sub>4</sub><sup>+</sup>. Spring also had significantly lower  $\delta^{15}$ N-NH<sub>4</sub><sup>+</sup> values (7.8 ± 7.3%), likely reflecting direct remineralization from phytoplankton (5.1  $\pm$  1.1%) (Sachs et al., 1999), which typically exhibit  $\delta^{15}$ N values consistent with this range. The minimal fractionation (+1 to -2.3%) associated with remineralization further supports this interpretation. When examining the relationship between  $ln(NH_4^+)$  and  $\delta^{15}N-NH_4^+$  by season, no significant correlation was observed in spring or winter.

However, both summer and fall displayed a strong positive correlation (p < 0.0001), with higher  $\delta^{15}$ N-NH<sub>4</sub><sup>+</sup> values corresponding to higher NH<sub>4</sub><sup>+</sup> concentrations. The steep slope or isotope effect ( $\epsilon$  = 13.6‰) suggests a process like DNRA as the dominant mechanism, consistent with interpretations from nitrate data. If DNRA is the primary process, this provides valuable insight into the yet-uncertain isotope effects associated with DNRA.

No significant differences were observed between sites, except for the highest (site 9:  $12.9 \pm 4.0\%$ ) and lowest (site 14:  $7.0 \pm 8.0\%$ )  $\delta^{15}$ N-NH<sub>4</sub><sup>+</sup> values. This variation may reflect the degree of processing the NH<sub>4</sub><sup>+</sup> pool has undergone. For example, site 9 exhibited much lower NH<sub>4</sub><sup>+</sup> concentrations ( $21.5 \pm 20.8 \, \mu M$ ) compared to site 14 ( $51.0 \pm 40.3 \, \mu M$ ). If the lower concentration at site 9 is due to more extensive processing of NH<sub>4</sub><sup>+</sup>, the remaining NH<sub>4</sub><sup>+</sup> pool at this site would be expected to be enriched in  $\delta^{15}$ N.

## 5.5.2.3. Groundwater NH<sub>4</sub><sup>+</sup>

Groundwater in this study exhibited unusually high  $NH_4^+$  concentrations, averaging 158.9  $\pm$  345.2  $\mu$ M. For comparison, a similar study of two coastal wells in the Baffin Bay, Texas watershed found much lower concentrations ( $1.6 \pm 2.3 \mu$ M). High  $NH_4^+$  concentrations can occur during tourist seasons in coastal areas, often leading to the formation of a wastewater plume (Potsma et al., 1992; Lapointe et al., 1990; O'Driscoll et al., 2014). Under aerobic conditions, groundwater typically has  $NH_4^+$  concentrations of less than 11  $\mu$ M. However, in anaerobic environments, concentrations can increase by more than 10 times, and salinization of groundwater can further raise ion concentrations, including  $NH_4^+$  (Rusydi et al., 2020). When  $NH_4^+$  dominates in suboxic or anaerobic aquifers, it suggests the intrusion of wastewater or the mineralization and decomposition of organic matter under anaerobic conditions (Szymczycha et al., 2012). Increased salinity in groundwater in coastal areas has also been linked to seawater intrusion or contamination from sewage or septic effluent (Bronders et al., 2012).

Groundwater concentrations in this study were grouped into three tiers. Wells W5 and W7, which had significantly higher concentrations (507.8  $\pm$  335.8  $\mu M$ ), were in the highest tier, while wells 3, 10, and 11 (118.4  $\pm$  108.1  $\mu M$ ) were in the middle tier, and wells 1, 2, 4, 8, 9, 13, and 14 (41.7  $\pm$  123.4  $\mu M$ ) were in the lowest tier. The highest tier wells were located near a condominium complex septic field and a residential area served by on-site sewage facilities (OSSFs), suggesting septic influences. The  $\delta^{15}N\text{-NH}_4^+$  values for these three tiers were 6.8  $\pm$  5.1% (highest concentration tier), 10.5  $\pm$  8.8% (middle tier), and 15.0  $\pm$  8.1% (lowest tier), indicating a relationship between  $\delta^{15}N\text{-NH}_4^+$  values and NH<sub>4</sub><sup>+</sup> concentrations. For comparison, wastewater effluent directly sampled had a  $\delta^{15}N\text{-NH}_4^+$  value of +3.9  $\pm$  2.8% (Cox, 2023), which closely matches the  $\delta^{15}N\text{-NH}_4^+$  value of 6.8% for the high-concentration wells, suggesting a direct source impact with minimal processing. As NH<sub>4</sub><sup>+</sup> is processed, for example through nitrification or assimilation, microorganisms preferentially utilize the lighter  $^{14}N$  isotope. This results in the remaining NH<sub>4</sub><sup>+</sup> becoming enriched in the heavier  $^{15}N$  isotope, thereby increasing the  $\delta^{15}N\text{-NH}_4^+$  values due to increased NH<sub>4</sub><sup>+</sup> processing before reaching the water table.

#### 5.5.3. **DON**

## 5.5.3.1. Surface Water DON

Surface water average DON concentrations were  $7 \pm 5~\mu M$ , with the highest average concentrations observed in fall and summer ( $10 \pm 4~\mu M$  and  $9 \pm 4~\mu M$ , respectively). These concentrations are similar to typical open ocean values of  $5 \pm 2~\mu M$ , with slightly higher concentrations commonly found in coastal areas (Voss et al., 2013; Knapp et al., 2018). Increased concentrations in summer generally coincide with higher organic matter input from seawater, elevated microbial activity due to warmer temperatures, and increased DON production, as seen in other coastal areas

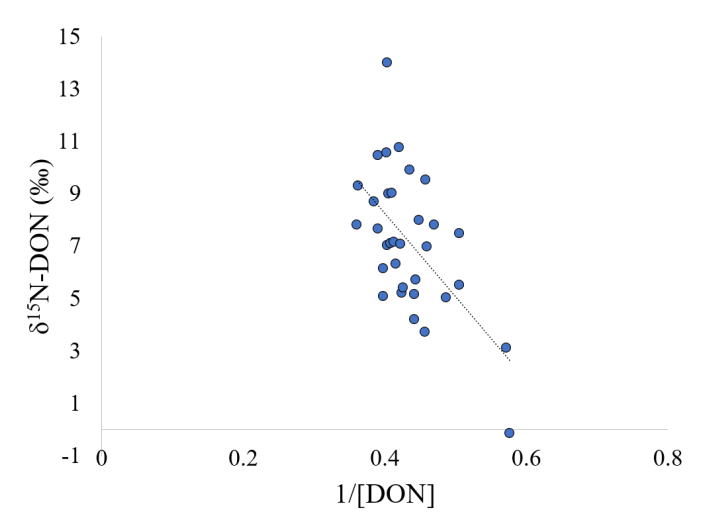


**Figure 5.24.** Surface water 1/[DON] vs  $\delta 15N$ -DON plot portraying potential mixing in the summer.

like the Gulf Coast of Florida (Ahrens et al., 2020; Lamb et al., 2012; Hansell and Carlson, 2001). Open ocean  $\delta^{15}$ N-DON values typically average around 5  $\mu$ M, which aligns well with this study's Gulf water data (5 ± 5‰). However, summer values (7 ± 3‰) and corresponding concentrations (9 ± 4  $\mu$ M) were significantly higher, suggesting an additional source outside of the normal marine nitrogen cycle. To explore potential source mixing behind these summer increases, a plot of 1/DON vs.  $\delta^{15}$ N-DON (with 13% of data excluded as outliers) revealed a significant relationship indicating mixing (p < 0.0001) (*Figure 5.24*). A possible explanation is conservative mixing between a low marine-produced endmember and a higher wastewater-derived endmember (22 ± 7.9‰). Increased wastewater inputs during summer, as discussed in previous sections, could contribute to this trend. Fall also showed higher DON concentrations (9 ± 4  $\mu$ M) and a strong 1/DON vs.  $\delta^{15}$ N-DON correlation (p = 0.0003), but with lower  $\delta^{15}$ N-DON values (4 ± 3‰). While this still indicates mixing, the lower  $\delta^{15}$ N-DON values suggest a greater contribution from the marine nitrogen cycle, particularly from the degradation of primary producers in the fall.

Site 1 exhibited the highest average concentration of DON ( $12 \pm 9 \,\mu\text{M}$ ) and was the only bay surface water site, located on Trinity Bay, which is fed by San Jacinto Bay. Bays and estuaries typically have higher concentrations of DON compared to coastal or open ocean waters, and rivers also contribute to DON levels (Voss et al., 2013). Elevated DON concentrations in estuarine systems have been observed in this region (Wetz et al., 2017). For example, San Jacinto Bay, which supplies water to Site 1, has a reported average total Kjeldahl nitrogen concentration of 120  $\mu$ M (Wetz et al., 2019).

#### 5.5.3.2. Porewater DON

Average porewater DON concentrations were  $7\pm 8~\mu M$  with no significant differences between and most sites had average concentrations which were not significantly different from eachother. The very limited previous studies investigating porewater concentrations show similar results. A study conducted in the Gulf of Lawrence reported porewater concentrations between 8-18  $\mu M$ , while another study off the coast of North Carolina also reported that most porewater

samples fell between 5 and 15  $\mu$ M (Alkhatib et al., 2012; Taylor, 2005). These were not seasonal studies.

The average porewater DON concentration was  $7 \pm 8 \mu M$ , with most sites having average concentrations that were not significantly different from one another. Previous studies investigating porewater concentrations report similar findings. For example, a study in the Gulf of Lawrence found porewater concentrations between 8 and 18 µM, while another study off the coast of North Carolina reported that most porewater samples ranged between 5 and 15 µM (Alkhatib et al., 2012; Taylor, 2005), although these studies were not seasonal in nature. The average  $\delta^{15}$ N-DON value in porewater samples was  $5 \pm 5\%$ , consistent with surface water values and values reported for porewater in the Gulf of Lawrence (between 4% and 7%). There were no significant differences across seasons, and most sites had average  $\delta^{15}$ N-DON values that were not significantly different. This suggests a well-mixed and homogeneous porewater environment with respect to DON. Ammonium can be produced from DON through remineralization in sediments. The positive correlation (p = 0.0367) between DON concentrations and  $\delta^{15}$ N-NH<sub>4</sub><sup>+</sup> supports evidence of remineralization in this system—specifically, as DON is consumed, the  $\delta^{15}$ N-NH<sub>4</sub><sup>+</sup> values increase. Additionally, a strong correlation (r = 0.017) between ln[DON] and  $\delta^{15}$ N-DON further corroborates this processing in the sediment. The resulting slope indicates an inverse isotope effect of 1.6%, which is minimal and falls close to the range suggested in the literature (+1 to -2.3%) (Yu et al., 2021; Mobius, 2013; Kendall et al., 2007).

#### 5.5.3.3 Groundwater DON

The average DON concentration in groundwater was 21±58 µM, with no significant differences observed across seasons. DON concentrations in groundwater can be highly variable and are influenced by several factors, such as depth to groundwater, proximity to groundwater mounds, land use, distance to surface water bodies, and soil type (Wang et al., 2018). Concentrations can range from as low as 7 µM to as high as 231 µM in silty and sandy loam areas, with significantly higher concentrations observed in highly forested areas (Liu et al., 2022; Xin et al., 2019). A study of groundwater DON in coastal aquifers of Massachusetts, with similar land use (primarily residential or vegetated), found highly variable concentrations ranging from 5 to 182 µM (Kroeger et al., 2006). Another study in Baffin Bay, TX, located south of this study region, reported an average DON concentration of  $29.9 \pm 19.0 \,\mu\text{M}$  (Qiu et al., 2024). Groundwater concentrations in this study were categorized into two tiers: wells 5 and 7 had significantly higher average concentrations (48  $\pm$  123  $\mu$ M) compared to other wells (15  $\pm$  29 uM). Ammonium and DON are the primary nitrogen species discharged into septic fields, and wells 5 and 7 are located in a condominium complex serviced by OSSFs and in the backyard of a home in a neighborhood also serviced by OSSFs, suggesting that septic systems may contribute to the elevated concentrations. However, the isotopic signature of septic waste is typically high  $(22 \pm 7.9\%)$ , while the  $\delta^{15}$ N-DON values in wells 5  $(2 \pm 5\%)$ , 7  $(1 \pm 6\%)$ , and all other wells (3  $\pm$  11‰) are lower. This suggests the presence of other sources and potential processing.

Some studies from estuaries in China have shown that samples with very low  $\delta^{15}$ N-DON values (<1‰) are derived from soil-derived organic matter, which is depleted in  $\delta^{15}$ N-DON (Yan et al., 2021). Additionally, low  $\delta^{15}$ N values in particulate organic matter can be converted to DON through decomposition, leading to a depletion of around 5‰ (Casciotti et al., 2003). The negative correlation between  $\delta^{15}$ N-NH<sub>4</sub><sup>+</sup> and [DON], along with the positive correlation with ln[DON], further supports the occurrence of remineralization (ammonification) in the groundwater, leading to the production of NH<sub>4</sub><sup>+</sup>.

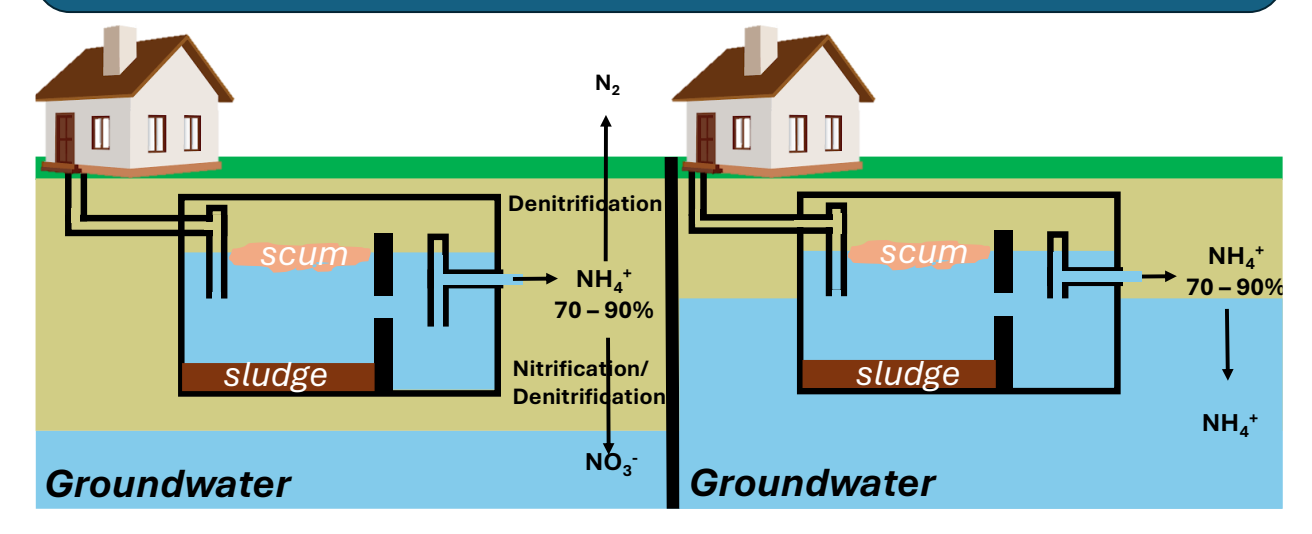
## 5.5.4 Nitrogen Species, Water Levels, and Implications

Septic system malfunctions are increasingly linked to varying sea levels and more frequent heavy precipitation events, both associated with fecal and nitrogen pollution (Powers et al., 2021; Elmir, 2018). Rising water tables reduce the amount of unsaturated soil available for wastewater filtration, diminishing the effectiveness of onsite sewage facilities (OSSFs). This trend is supported by findings from this study, where [NO<sub>3</sub>] was positively (though insignificant) correlated with depth to water (DTW),  $\delta^{15}$ N-NO<sub>3</sub> was positively correlated with DTW,  $[NH_4^+]$ was negatively correlated (p = 0.0026) with DTW, and  $\delta^{15}$ N-NH<sub>4</sub><sup>+</sup> was positively correlated with DTW. Septic discharge typically contains 70-90% NH<sub>4</sub><sup>+</sup>, and when there is more space between the septic discharge field and the water table (i.e., greater DTW), there is more opportunity for  $NH_4^+$  to be nitrified to  $NO_3^-$ , which can then be denitrified to harmless  $N_{2(g)}$ . In this scenario, NH<sub>4</sub><sup>+</sup> is processed before it reaches the water table, and any residual NO<sub>3</sub><sup>-</sup> that is not denitrified to  $N_2$  would enter the groundwater with high  $\delta^{15}N-NO_3^-$  values due to partial denitrification. In contrast, when DTW is low, septic discharge may directly reach the water table, causing unprocessed NH<sub>4</sub><sup>+</sup> to enter the groundwater at high concentrations with an isotopic signature reflective of the septic source. This scenario likely explains the high NH<sub>4</sub><sup>+</sup> concentration wells with low  $\delta^{15}$ N-NH<sub>4</sub>+values, similar to the wastewater NH<sub>4</sub>+ isotopic signature (+3.9 ± 2.8%) (Cox 2023). The evidence suggests that the high NH<sub>4</sub><sup>+</sup> concentrations, along with the lowest DTW values, indicate compromised OSSFs, likely due to sea level variations, which could be a significant issue in this region. For instance, while the exact depth of the OSSF units is unknown, they must be at least 3 feet (0.9 m) from the soil's surface. The average DTW of the monitoring wells on the barrier island was approximately 1 m, with the high NH<sub>4</sub><sup>+</sup> concentration wells having an average DTW of around 0.7 m. This suggests that in some cases, the water table was at or above the level of the septic drain field, allowing effluent to easily percolate into the groundwater.

Coastal communities face increased risks of OSSF failures due to factors such as sandy, porous soils, erosion, severe weather events, and the effects of sea level variations (Mallin, 2013). Furthermore, many OSSFs are old or undocumented, as permits were not required before the Clean Water Act of 1972. These aging systems are more prone to malfunctions, which can lead to contamination of groundwater and drinking water supplies with pathogens, nutrients, and other harmful substances. While fecal indicator bacteria (FIB) can serve as indicators of failing systems, it is crucial to identify and trace all potential sources of contamination, including OSSFs, to fully understand their role in nonpoint source pollution. One effective approach is the analysis of stable nitrogen isotopes in co-migrating nitrogen species within impacted waters. This method can help determine the specific contribution of OSSFs to nutrient pollution.

#### Nitrogen and groundwater level relationships

- $[NH_4^+]$  is significantly negatively correlated to depth to water (p = 0.0026)
- $[\delta^{15}N-NH_4^+]$  is significantly positively correlated with depth to water (p <= 0.0001)
- [DON] is significantly negatively correlated to depth to water (p = 0.007)
- [NO<sub>3</sub>] is positively correlated with depth to water but the relationship is insignificant(p = 0.137)
- $[\delta^{15}N-NO_3]$  is significantly positively correlated with depth to water (p < = 0.0001)



Conceptual Diagram. High and low water table scenarios and their relationships to nitrogen processing with respect to a septic field. Blue box provides specific details between water level, salinity, and nitrogen species.

#### References

- Ahrens, J., Beck, M., Marchant, H. K., Ahmerkamp, S., Schnetger, B., & Brumsack, H. J. (2020). Seasonality of organic matter degradation regulates nutrient and metal net fluxes in a high energy sandy beach. *Journal of Geophysical Research: Biogeosciences*, 125(2), e2019JG005399.
- Alejandra, P. S., Clara, D., Anja, W., Bernhard, M., Stefanie, S., Schloter, M., & Florian, E. (2022). Seasonal dynamics of anaerobic oxidation of ammonium and denitrification in a dimictic lake during the stratified spring–summer period. *Limnology and Oceanography*, 67(5), 1194-1210.
- Alkhatib, M., Lehmann, M. F., & Del Giorgio, P. A. (2012). The nitrogen isotope effect of benthic remineralization-nitrification-denitrification coupling in an estuarine environment. *Biogeosciences*, 9(5), 1633-1646.
- Altabet, M. A. (2006). Isotopic tracers of the marine nitrogen cycle: present and past. *Marine organic matter: biomarkers, isotopes and DNA*, 251-293.
- Anderson, D. M., Burkholder, J. M., Cochlan, W. P., Glibert, P. M., Gobler, C. J., Heil, C. A., & Vargo, G. A. (2008). Harmful algal blooms and eutrophication: examining linkages from selected coastal regions of the United States. *Harmful algae*, 8(1), 39-53.
- Andrisoa, A., Stieglitz, T. C., Rodellas, V., & Raimbault, P. (2019). Primary production in coastal lagoons supported by groundwater discharge and porewater fluxes inferred from nitrogen and carbon isotope signatures. *Marine Chemistry*, 210, 48-60.

- Anglès, S., Jordi, A., Henrichs, D. W., & Campbell, L. (2019). Influence of coastal upwelling and river discharge on the phytoplankton community composition in the northwestern Gulf of Mexico. *Progress in Oceanography*, 173, 26-36.
- Anornu, G., Gibrilla, A., & Adomako, D. (2017). Tracking nitrate sources in groundwater and associated health risk for rural communities in the White Volta River basin of Ghana using isotopic approach (δ15N, δ18ONO3 and 3H). *Science of the total environment*, 603, 687-698.
- Ardón, M., Morse, J. L., Colman, B. P., & Bernhardt, E. S. (2013). Drought-induced saltwater incursion leads to increased wetland nitrogen export. *Global change biology*, *19*(10), 2976-2985.
- Brereton, R. (2007). DIN vs. DON in Groundwater: Their Roles in Estuarine Eutrophication.
- Bronders, J., Tirez, K., Desmet, N., Widory, D., Petelet-Giraud, E., Bregnot, A., & Boeckx, P. (2012). Use of compound-specific nitrogen (d15N), oxygen (d18O), and bulk boron (d11B) isotope ratios to identify sources of nitrate-contaminated waters: a guideline to identify polluters. *Environmental Forensics*, 13(1), 32-38.
- Brown, R. B. (1998). *Soils and septic systems*. University of Florida Cooperative Extension Service, Institute of Food and Agriculture Sciences, EDIS.
- Brunner, B., Contreras, S., Lehmann, M.F., Matantseva, O., Rollog, M., Kalvelage, T., Klockgether, G., Lavik, G., Jetten, M.S., Kartal, B. and Kuypers, M.M., 2013. Nitrogen isotope effects induced by anammox bacteria. *Proceedings of the National Academy of Sciences*, 110(47), pp.18994-18999.
- Bugica, K., Sterba-Boatwright, B., & Wetz, M. S. (2020). Water quality trends in Texas estuaries. *Marine Pollution Bulletin*, 152, 110903.
- Cao, H. T. T.; Nakamura, T.; Toyama, T.; Nishida, K., A protocol for nitrogen isotopic measurement of dissolved organic nitrogen with a combination of oxidation-denitrification and gas phase diffusion methods. *Isotopes in Environmental and Health Studies* **2021**, *57*, (6), 576-584.
- Castro, M. S., Driscoll, C. T., Jordan, T. E., Reay, W. G., & Boynton, W. R. (2003). Sources of nitrogen to estuaries in the United States. *Estuaries*, 26(3), 803-814.
- Chaudhuri, S., Ale, S., DeLaune, P., & Rajan, N. (2012). Spatio-temporal Variability of Groundwater Nitrate Concentration in Texas: 1960 to 2010. *Journal of Environmental Quality*, 41(6), 1806-1817.
- Chen, F., Lao, Q., Zhang, S., Bian, P., Jin, G., Zhu, Q., & Chen, C. (2020). Nitrate sources and biogeochemical processes identified using nitrogen and oxygen isotopes on the eastern coast of Hainan Island. *Continental Shelf Research*, 207, 104209.
- Cho, S., Kambey, C., & Nguyen, V. K. (2019). Performance of anammox processes for wastewater treatment: a critical review on effects of operational conditions and environmental stresses. *Water*, 12(1), 20.
- Choi, W. J., Han, G. H., Lee, S. M., Lee, G. T., Yoon, K. S., Choi, S. M., & Ro, H. M. (2007). Impact of land-use types on nitrate concentration and δ15N in unconfined groundwater in rural areas of Korea. *Agriculture, ecosystems & environment, 120*(2-4), 259-268.
- Choi, W. J., Kwak, J. H., Lim, S. S., Park, H. J., Chang, S. X., Lee, S. M., ... & Kim, H. Y. (2017). Synthetic fertilizer and livestock manure differently affect δ15N in the agricultural landscape: a review. *Agriculture, ecosystems & environment, 237*, 1-15.
- Clark, I. (2015). Groundwater geochemistry and isotopes. CRC press.

- Clark, I., Timlin, R., Bourbonnais, A., Jones, K., Lafleur, D., & Wickens, K. (2008). Origin and fate of industrial ammonium in anoxic ground water—15N evidence for anaerobic oxidation (anammox). *Groundwater Monitoring & Remediation*, 28(3), 73-82.
- Cole, M. L., Kroeger, K. D., McClelland, J. W., & Valiela, I. (2006). Effects of watershed land use on nitrogen concentrations and δ15 nitrogen in groundwater. *Biogeochemistry*, 77(2), 199-215.
- Cooper, J. A., Loomis, G. W., & Amador, J. A. (2016). Hell and high water: Diminished septic system performance in coastal regions due to climate change. *PloS one*, *11*(9), e0162104.
- Cox, A., 2023. Dissolved Inorganic Nitrogen Concentrations and Isotopic Values of Wastewater Treatment Plants in a Semi-Arid Region (Master's thesis, Texas A&M University-Corpus Christi).
- Craine, J. M., Brookshire, E. N. J., Cramer, M. D., Hasselquist, N. J., Koba, K., Marin-Spiotta, E., & Wang, L. (2015). Ecological interpretations of nitrogen isotope ratios of terrestrial plants and soils. *Plant and Soil*, *396*(1), 1-26.
- Davidson, K., Gowen, R. J., Harrison, P. J., Fleming, L. E., Hoagland, P., & Moschonas, G. (2014). Anthropogenic nutrients and harmful algae in coastal waters. *Journal of environmental management*, 146, 206-216.
- Denk, T. R., Mohn, J., Decock, C., Lewicka-Szczebak, D., Harris, E., Butterbach-Bahl, K., & Wolf, B. (2017). The nitrogen cycle: A review of isotope effects and isotope modeling approaches. *Soil Biology and Biochemistry*, 105, 121-137.
- Detenbeck, N. E., You, M., & Torre, D. (2019). Recent Changes in Nitrogen Sources and Load Components to Estuaries of the Contiguous United States. *Estuaries and coasts : journal of the Estuarine Research Federation*, 42(8), 2096–2113.
- Di Lorenzo, T., Brilli, M., Del Tosto, D., Galassi, D. M., & Petitta, M. (2012). Nitrate source and fate at the catchment scale of the Vibrata River and aquifer (central Italy): an analysis by integrating component approaches and nitrogen isotopes. *Environmental Earth Sciences*, 67(8), 2383-2398.
- Dong Jing, L., Xi Wu, C., Tong Liu, J., Guang Wang, H., & Yi Ao, H. (2013). The effects of dredging on nitrogen balance in sediment-water microcosms and implications to dredging projects. *Ecological Engineering*, *52*, 167-174.
- Elmir, S. (2018). Septic Systems Vulnerable to Sea Level Rise. *Miami-Dade County Water and Sewage Department, Florida Department of Health: Miami, FL, USA*.
- Erler, D.V., Eyre, B.D. and Davison, L., 2008. The contribution of anammox and denitrification to sediment N2 production in a surface flow constructed wetland. Environmental Science & Technology, 42(24), pp.9144-9150.
- Faramarzmanesh, S., Mashal, M., & Ebrahim Hashemi Garmdareh, S. (2021). Effect of saline drainage water on performance of denitrification bioreactors. *Water Supply*, 21(1), 98-107.
- Felix, J., Elliott, E.M., Gish, T.J., McConnell, L.L. & Shaw, S.L. (2013). Characterizing the isotopic composition of atmospheric ammonia emission sources using passive samplers and a combined oxidation-bacterial denitrifier approach. *Rapid Communications in Mass Spectrometry* 27(20), 2239-2246.
- Gao, Z., Weng, H., & Guo, H. (2021). Unraveling influences of nitrogen cycling on arsenic enrichment in groundwater from the Hetao Basin using geochemical and multi-isotopic approaches. *Journal of Hydrology*, 595, 125981.

- Garcia, H.E., Bouchard, C., Cross, S.L., Paver, C.R., Reagan, J.R., Boyer, T.P., Locarnini, R.A., Mishonov, A.V., Baranova, O.K., Seidov, D. and Wang, Z., 2024. World Ocean Atlas 2023, Volume 4: Dissolved Inorganic Nutrients (Phosphate, Nitrate, and Silicate).
- Giblin, A. E., Tobias, C. R., Song, B., Weston, N., Banta, G. T., & H. RIVERA-MONROY, V. I. C. T. O. R. (2013). The importance of dissimilatory nitrate reduction to ammonium (DNRA) in the nitrogen cycle of coastal ecosystems. *Oceanography*, 26(3), 124-131.
- Gleeson, J., Santos, I. R., Maher, D. T., & Golsby-Smith, L. (2013). Groundwater—surface water exchange in a mangrove tidal creek: evidence from natural geochemical tracers and implications for nutrient budgets. *Marine Chemistry*, 156, 27-37.
- Goodridge, B. M., & Melack, J. M. (2014). Temporal evolution and variability of dissolved inorganic nitrogen in beach pore water revealed using radon residence times. *Environmental science & technology*, 48(24), 14211-14218.
- Gotkowska-Płachta, A., Gołaś, I., Korzeniewska, E., Koc, J., Rochwerger, A., & Solarski, K. (2016). Evaluation of the distribution of fecal indicator bacteria in a river system depending on different types of land use in the southern watershed of the Baltic Sea. *Environmental Science and Pollution Research*, 23(5), 4073-4085.
- Granger, J., & Wankel, S. D. (2016). Isotopic overprinting of nitrification on denitrification as a ubiquitous and unifying feature of environmental nitrogen cycling. *Proceedings of the National Academy of Sciences*, 113(42), E6391-E6400.
- Guo, H., Li, G., Zhang, D., & Zhang, X. (2006). Effects of water table and fertilization management on nitrogen loading to groundwater. *Agricultural Water Management*, 82(1-2), 86-98.
- Hellemann, D., Tallberg, P., Aalto, S. L., Bartoli, M., & Hietanen, S. (2020). Seasonal cycle of benthic denitrification and DNRA in the aphotic coastal zone, northern Baltic Sea. *Marine Ecology Progress Series*, 637, 15-28.
- Herrero, A., Flores, E., & Imperial, J. (2019). Nitrogen assimilation in bacteria.
- Holmes, R. M., Aminot, A., Kérouel, R., Hooker, B. A., & Peterson, B. J. (1999). A simple and precise method for measuring ammonium in marine and freshwater ecosystems. *Canadian Journal of Fisheries and Aquatic Sciences*, *56*(10), 1801-1808.
- Howe, S., Miranda, C., Hayes, C.T., Letscher, R.T. and Knapp, A.N., 2020. The dual isotopic composition of nitrate in the Gulf of Mexico and Florida Straits. *Journal of Geophysical Research: Oceans*, 125(9), p.e2020JC016047.
- Humphrey Jr, C. P., Iverson, G., & O'Driscoll, M. (2017). Nitrogen treatment efficiency of a large onsite wastewater system in relation to water table dynamics. *Clean–Soil, Air, Water*, 45(12), 1700551.
- Ji, X., Xie, R., Hao, Y., & Lu, J. (2017). Quantitative identification of nitrate pollution sources and uncertainty analysis based on dual isotope approach in an agricultural watershed. *Environmental Pollution*, 229, 586-594.
- Jiang, W., Wang, G., Sheng, Y., Zhao, D., Liu, C., & Guo, Y. (2016). Enrichment and sources of nitrogen in groundwater in the Turpan-Hami area, northwestern China. *Exposure and Health*, *8*, 389-400.
- Jung, H., Koh, D. C., Kim, Y. S., Jeen, S. W., & Lee, J. (2020). Stable isotopes of water and nitrate for the identification of groundwater flowpaths: A review. *Water*, 12(1), 138.
- Junk, G., & Svec, H. J. (1958). The absolute abundance of the nitrogen isotopes in the atmosphere and compressed gas from various sources. *Geochimica et cosmochimica acta*, 14(3), 234-243.

- Kallistova, A., Nikolaev, Y., Grachev, V., Beletsky, A., Gruzdev, E., Kadnikov, V., ... & Mardanov, A. (2022). New Insight Into the Interspecies Shift of Anammox Bacteria Ca. "Brocadia" and Ca. "Jettenia" in Reactors Fed With Formate and Folate. *Frontiers in Microbiology*, 12, 802201.
- Kartal, B., Kuenen, J. V., & Van Loosdrecht, M. C. M. (2010). Sewage treatment with anammox. *Science*, 328(5979), 702-703.
- Kendall, C., & Aravena, R. (2000). Nitrate isotopes in groundwater systems. In *Environmental tracers in subsurface hydrology* (pp. 261-297). Springer, Boston, MA.
- Kendall, C., Elliott, E. M., & Wankel, S. D. (2007). Tracing anthropogenic inputs of nitrogen to ecosystems. *Stable isotopes in ecology and environmental science*, *2*(1), 375-449.
- Kimura, Y., Isaka, K., & Kazama, F. (2011). Tolerance level of dissolved oxygen to feed into anaerobic ammonium oxidation (anammox) reactor. *Journal of Water and Environment Technology*, 9(2), 169-178.
- Knapp, A. N., Sigman, D. M., & Lipschultz, F. (2005). N isotopic composition of dissolved organic nitrogen and nitrate at the Bermuda Atlantic Time-series Study site. *Global Biogeochemical Cycles*, 19(1).
- Knobeloch, L., Salna, B., Hogan, A., Postle, J., & Anderson, H. (2000). Blue babies and nitrate-contaminated well water. *Environmental health perspectives*, 108(7), 675-678.
- Krause, S., Heathwaite, L., Binley, A., & Keenan, P. (2009). Nitrate concentration changes at the groundwater-surface water interface of a small Cumbrian River. *Hydrological Processes: An International Journal*, 23(15), 2195-2211.
- Kroeger, K. D., Cole, M. L., & Valiela, I. (2006). Groundwater-transported dissolved organic nitrogen exports from coastal watersheds. *Limnology and Oceanography*, 51(5), 2248-2261.
- Lamb, K., Swart, P. K., & Altabet, M. A. (2012). Nitrogen and carbon isotopic systematics of the Florida reef tract. *Bulletin of Marine Science*, 88(1), 119-146.
- Li, W., Ye, X., & Du, X. (2022). Imputation of ammonium nitrogen concentration in groundwater based on a machine learning method. *Water*, 14(10), 1595.
- Li, X., Masuda, H., Koba, K., & Zeng, H. (2007). Nitrogen isotope study on nitrate-contaminated groundwater in the Sichuan Basin, China. *Water, air, and soil pollution*, 178(1), 145-156.
- Liu, W., Wang, P., Zhou, B., Chen, Q., Ma, J., Li, Q., & Zhang, J. (2019). Experimental simulation of nitrogen and phosphorus release during marine dumping of dredged sediment. In *E3S Web of Conferences* (Vol. 118, p. 03031). EDP Sciences.
- Liu, X. L., Han, G., Zeng, J., Liu, M., Li, X. Q., & Boeckx, P. (2021). Identifying the sources of nitrate contamination using a combined dual isotope, chemical and Bayesian model approach in a tropical agricultural river: Case study in the Mun River, Thailand. *Science of the Total Environment*, 760, 143938.
- Liu, X. Y., Xiao, H. W., Xiao, H. Y., Song, W., Sun, X. C., Zheng, X. D., ... & Koba, K. (2017). Stable isotope analyses of precipitation nitrogen sources in Guiyang, southwestern China. *Environmental Pollution*, 230, 486-494.
- Liu, Y., Jiao, J. J., Liang, W., & Luo, X. (2017). Tidal pumping-induced nutrients dynamics and biogeochemical implications in an intertidal aquifer. *Journal of Geophysical Research: Biogeosciences*, 122(12), 3322-3342.
- Liu, Y., Xin, J., Wang, Y., Yang, Z., Liu, S., & Zheng, X. (2022). Dual roles of dissolved organic nitrogen in groundwater nitrogen cycling: Nitrate precursor and denitrification promoter. *Science of The Total Environment*, 811, 151375.

- Lusk, M. G., Toor, G. S., Yang, Y. Y., Mechtensimer, S., De, M., & Obreza, T. A. (2017). A review of the fate and transport of nitrogen, phosphorus, pathogens, and trace organic chemicals in septic systems. *Critical Reviews in Environmental Science and Technology*, 47(7), 455-541.
- Macías-Tapia, A., Mulholland, M. R., Selden, C. R., Loftis, J. D., & Bernhardt, P. W. (2021). Effects of tidal flooding on estuarine biogeochemistry: Quantifying flood-driven nitrogen inputs in an urban, lower Chesapeake Bay sub-tributary. *Water Research*, 201, 117329.
- Maeda, K., Toyoda, S., Yano, M., Hattori, S., Fukasawa, M., Nakajima, K., & Yoshida, N. (2016). Isotopically enriched ammonium shows high nitrogen transformation in the pile top zone of dairy manure compost. *Biogeosciences*, *13*(4), 1341-1349.
- Marchant, H. K., Ahmerkamp, S., Lavik, G., Tegetmeyer, H. E., Graf, J., Klatt, J. M., ... & Kuypers, M. M. (2017). Denitrifying community in coastal sediments performs aerobic and anaerobic respiration simultaneously. *The ISME journal*, *11*(8), 1799-1812.
- Mayer, P. M., Groffman, P. M., Striz, E. A., & Kaushal, S. S. (2010). Nitrogen dynamics at the groundwater–surface water interface of a degraded urban stream. *Journal of Environmental Quality*, 39(3), 810-823.
- Middelburg, J. J., & Nieuwenhuize, J. (2001). Nitrogen isotope tracing of dissolved inorganic nitrogen behaviour in tidal estuaries. *Estuarine, Coastal and Shelf Science*, 53(3), 385-391.
- Mizota, C., 2009. Nitrogen isotopic patterns of vegetation as affected by breeding activity of Black-tailed Gull (Larus crassiostris): A coupled analysis of feces, inorganic soil nitrogen and flora. Applied Geochemistry, 24(11), pp.2027-2033.
- Möbius, J. (2013). Isotope fractionation during nitrogen remineralization (ammonification): Implications for nitrogen isotope biogeochemistry. *Geochimica et Cosmochimica Acta*, 105, 422-432.
- Mueller, D. K. (1995). *Nutrients in ground water and surface water of the United States: An analysis of data through 1992* (Vol. 95, No. 4031). US Department of the Interior, US Geological Survey.
- Murgulet, D., & Tick, G. R. (2013). Understanding the sources and fate of nitrate in a highly developed aquifer system. *Journal of contaminant hydrology*, 155, 69-81.
- Nakagawa, K., Amano, H., Persson, M., & Berndtsson, R. (2021). Spatiotemporal variation of nitrate concentrations in soil and groundwater of an intensely polluted agricultural area. *Scientific reports*, *11*(1), 1-13.
- Negrin, V. L., Spetter, C. V., Asteasuain, R. O., Perillo, G. M., & Marcovecchio, J. E. (2011). Influence of flooding and vegetation on carbon, nitrogen, and phosphorus dynamics in the pore water of a Spartina alterniflora salt marsh. *Journal of Environmental Sciences*, 23(2), 212-221.
- Omani, N., Srinivasan, R., & Lee, T. (2012). Estimating sediment and nutrient loads of Texas Coastal Watersheds with SWAT. In *2012 Dallas, Texas, July 29-August 1, 2012* (p. 1). American Society of Agricultural and Biological Engineers.
- Pastén-Zapata, E., Ledesma-Ruiz, R., Harter, T., Ramírez, A. I., & Mahlknecht, J. (2014). Assessment of sources and fate of nitrate in shallow groundwater of an agricultural area by using a multi-tracer approach. *Science of the Total Environment*, 470, 855-864.
- Powers, N. C., Pinchback, J., Flores, L., Huang, Y., Wetz, M. S., & Turner, J. W. (2021). Long-term water quality analysis reveals correlation between bacterial pollution and sea level rise in the northwestern Gulf of Mexico. *Marine Pollution Bulletin*, 166, 112231.

- Powlson, D. S., Addiscott, T. M., Benjamin, N., Cassman, K. G., de Kok, T. M., van Grinsven, H., ... & Van Kessel, C. (2008). When does nitrate become a risk for humans?. *Journal of environmental quality*, 37(2), 291-295.
- Qiu, Y., Felix, J.D., Murgulet, D., Wetz, M. and Abdulla, H., 2024. Isotopic compositions of organic and inorganic nitrogen reveal processing and source dynamics at septic influenced and undeveloped estuary sites. *Science of The Total Environment*, 925, p.171749.
- Rebich, R. A., Houston, N. A., Mize, S. V., Pearson, D. K., Ging, P. B., & Evan Hornig, C. (2011). Sources and Delivery of Nutrients to the Northwestern Gulf of Mexico from Streams in the South-Central United States 1. *JAWRA Journal of the American Water Resources Association*, 47(5), 1061-1086.
- Ribot, M., Von Schiller, D., & Martí, E. (2017). Understanding pathways of dissimilatory and assimilatory dissolved inorganic nitrogen uptake in streams. *Limnology and Oceanography*, 62(3), 1166-1183.
- Robertson, W.D., Moore, T.A., Spoelstra, J., Li, L., Elgood, R.J., Clark, I.D., Schiff, S.L., Aravena, R. and Neufeld, J.D. (2012). Natural attenuation of septic system nitrogen by anammox. *Groundwater*, *50*(4), 541-553.
- Rose, L. A., Yu, Z., Bain, D. J., & Elliott, E. M. (2019). High resolution, extreme isotopic variability of precipitation nitrate. *Atmospheric Environment*, 207, 63-74.
- Rusydi, A. F., Onodera, S. I., Saito, M., Hyodo, F., Maeda, M., Sugianti, K., & Wibawa, S. (2021). Potential sources of ammonium-nitrogen in the coastal groundwater determined from a combined analysis of nitrogen isotope, biological and geological parameters, and land use. *Water*, 13(1), 25.
- Ryabenko, E. (2013). Stable isotope methods for the study of the nitrogen cycle. *Topics in oceanography*, 1-40.Ryabenko, Evgenia. Stable Isotope Methods for the Study of the Nitrogen Cycle. *Topics in Oceanography*.
- Sachs, J.P., Repeta, D.J. and Goericke, R., 1999. Nitrogen and carbon isotopic ratios of chlorophyll from marine phytoplankton. *Geochimica et Cosmochimica Acta*, 63(9), pp.1431-1441.
- Sadat-Noori, M., & Glamore, W. (2019). Porewater exchange drives trace metal, dissolved organic carbon and total dissolved nitrogen export from a temperate mangrove wetland. *Journal of environmental management*, 248, 109264.
- Sankoh, A. A., Derkyi, N. S. A., Frazer-williams, R. A., Laar, C., & Kamara, I. (2021). A review on the application of isotopic techniques to trace groundwater pollution sources within developing countries. *Water*, *14*(1), 35.
- Santos, I. R., Burnett, W. C., Dittmar, T., Suryaputra, I. G., & Chanton, J. (2009). Tidal pumping drives nutrient and dissolved organic matter dynamics in a Gulf of Mexico subterranean estuary. *Geochimica et Cosmochimica Acta*, 73(5), 1325-1339.
- Sharp, Z. (2017). Principles of stable isotope geochemistry.
- Sigman, D. M., Casciotti, K. L., Andreani, M., Barford, C., Galanter, M. B. J. K., & Böhlke, J. K. (2001). A bacterial method for the nitrogen isotopic analysis of nitrate in seawater and freshwater. *Analytical chemistry*, 73(17), 4145-4153.
- Snow, Daniel. (2018). Nitrate-N Isotope Results and Interpretation. *University of Nebraska, Eastern Research Group*.

- Strauss, B., Tebaldi, C., Kulp, S., Cutter, S., Emrich, C., Rizza, D., Yawitz, D. (2014). Texas and the Surging Sea: a vulnerability assessment with projections for sea level rise and coastal flood risk. *Climate Central Research*.
- Szymczycha, B., Vogler, S., & Pempkowiak, J. (2012). Nutrient fluxes via submarine groundwater discharge to the Bay of Puck, southern Baltic Sea. *Science of the Total Environment*, 438, 86-93.
- Taylor, K. L. (2005). Beach sediments: a Source of Dissolved Organic Carbon and Nitrogen Species to the Coastal Ocean (Doctoral dissertation, University of North Carolina at Wilmington).
- Texas Groundwater Protection Committee (TGPC), Groundwater Issues Subcommittee. (2019). How is Groundwater Quality Affected by Failing On-Site Sewage Facilities (OSSFs)?
- Toor, G. S., Lusk, M., & Obreza, T. (2011). Onsite sewage treatment and disposal systems: Nitrogen. Document SL348 prepared by the Department of Soil and Water Sciences at the University of Florida Institute of Food and Agricultural Sciences Extension.
- Tsikas, D. (2007). Analysis of nitrite and nitrate in biological fluids by assays based on the Griess reaction: appraisal of the Griess reaction in the L-arginine/nitric oxide area of research. *Journal of Chromatography B*, 851(1-2), 51-70.
- Tsunogai, U., Kido, T., Hirota, A., Ohkubo, S. B., Komatsu, D. D., & Nakagawa, F. (2008). Sensitive determinations of stable nitrogen isotopic composition of organic nitrogen through chemical conversion into N2O. *Rapid Communications in Mass Spectrometry:* An International Journal Devoted to the Rapid Dissemination of Up-to-the-Minute Research in Mass Spectrometry, 22(3), 345-354.
- Vieillard, A. M., & Fulweiler, R. W. (2012). Impacts of long-term fertilization on salt marsh tidal creek benthic nutrient and N2 gas fluxes. *Marine Ecology Progress Series*, 471, 11-22.
- Vitòria, L., Soler, A., Canals, À., & Otero, N. (2008). Environmental isotopes (N, S, C, O, D) to determine natural attenuation processes in nitrate contaminated waters: example of Osona (NE Spain). *Applied Geochemistry*, 23(12), 3597-3611.
- Vitousek, S., Barnard, P. L., Fletcher, C. H., Frazer, N., Erikson, L., & Storlazzi, C. D. (2017). Doubling of coastal flooding frequency within decades due to sea-level rise. *Scientific reports*, 7(1), 1-9.
- Voss, M., Bange, H. W., Dippner, J. W., Middelburg, J. J., Montoya, J. P., & Ward, B. (2013). The marine nitrogen cycle: recent discoveries, uncertainties and the potential relevance of climate change. *Philosophical Transactions of the Royal Society B: Biological Sciences*, 368(1621), 20130121.
- Wang, B., Hipsey, M. R., Ahmed, S., & Oldham, C. (2018). The impact of landscape characteristics on groundwater dissolved organic nitrogen: Insights from machine learning methods and sensitivity analysis. *Water Resources Research*, 54(7), 4785-4804.
- Wankel, S. D., Kendall, C., Pennington, J. T., Chavez, F. P., & Paytan, A. (2007). Nitrification in the euphotic zone as evidenced by nitrate dual isotopic composition: Observations from Monterey Bay, California. *Global Biogeochemical Cycles*, 21(2).
- Weissman, D. S., & Tully, K. L. (2020). Saltwater intrusion affects nutrient concentrations in soil porewater and surface waters of coastal habitats. *Ecosphere*, 11(2), e03041.
- Wetz, M.S., Cira, E.K., Sterba-Boatwright, B., Montagna, P.A., Palmer, T.A. and Hayes, K.C., 2017. Exceptionally high organic nitrogen concentrations in a semi-arid South Texas estuary susceptible to brown tide blooms. *Estuarine, Coastal and Shelf Science*, 188, pp.27-37.

- Wetz, M.S., 2019. Long-term water quality trends in Texas estuaries: relationships with climatic variability and watershed land use change.
- Wong, W. W., Cartwright, I., Poh, S. C., & Cook, P. (2022). Sources and cycling of nitrogen revealed by stable isotopes in a highly populated large temperate coastal embayment. *Science of The Total Environment*, 806, 150408.
- Xin, J., Liu, Y., Chen, F., Duan, Y., Wei, G., Zheng, X., & Li, M. (2019). The missing nitrogen pieces: A critical review on the distribution, transformation, and budget of nitrogen in the vadose zone-groundwater system. *Water research*, 165, 114977.
- Xiong, D., Williams, I. D., Hudson, M. D., Osborne, P. E., & Zapata-Restrepo, L. M. (2023). The impact of an annual major recreational boating event on water quality in the Solent Strait. *Marine Pollution Bulletin*, 186, 114450.
- Yang, X., Wei, X., Xu, X., Zhang, Y., Li, J., & Wan, J. (2019). Characteristics of Dissolved Organic Nitrogen in the Sediments of Six Water Sources in Taihu Lake, China. *International journal of environmental research and public health*, 16(6), 929.
- Yu, L., Zheng, T., Hao, Y., & Zheng, X. (2021). Determination of the nitrogen isotope enrichment factor associated with ammonification and nitrification in unsaturated soil at different temperatures. *Environmental Research*, 202, 111670.
- Zhang, L., Altabet, M.A., Wu, T. & Hadas, O. (2007). Sensitive Measurement of NH4+ 15N/14N (δ15NH4+) at Natural Abundance Levels in Fresh and Saltwaters. *Analytical Chemistry* 79(14), 5297-5303.
- Zhang, S., Zhou, Q., Xu, D., Lin, J., Cheng, S., & Wu, Z. (2010). Effects of sediment dredging on water quality and zooplankton community structure in a shallow of eutrophic lake. *Journal of Environmental Sciences*, 22(2), 218-224.
- Zhao, R., Babbin, A. R., Roerdink, D. L., Thorseth, I. H., & Jørgensen, S. L. (2023). Nitrite accumulation and anammox bacterial niche partitioning in Arctic Mid-Ocean Ridge sediments. *ISME communications*, *3*(1), 1-14.
- Zhou, Z., Ge, L., Huang, Y., Liu, Y., & Wang, S. (2021). Coupled relationships among anammox, denitrification, and dissimilatory nitrate reduction to ammonium along salinity gradients in a Chinese estuarine wetland. *Journal of Environmental Sciences*, 106, 39–46.

# 6. INTEGRATED ASSESSMENT: GROUNDWATER TRACERS, BACTERIA, AND NUTRIENT INTERACTIONS

Prepared by Roya Narimani, Ph.D., Allie Watson, Dorina Murgulet, Ph.D.

## 6.1. Analysis of FIB Behavior in the Studied Environments

Fecal indicator bacteria (FIB) loading hotspots in surface water tend to appear consistently along coastal and inland water bodies, with some seasonal variations observed. For example, in Figure 6.1, summer months (e.g., June through August) show a higher presence of bacteria, possibly linked to increased rainfall, runoff, and tourism. Additionally, the higher population density at the beach during these months may contribute to increased bacterial contamination as more people visit the area, potentially leading to higher pollution levels. Conversely, cooler months like February, November, and December display lower contamination levels. Understanding these spatial and temporal patterns is critical for identifying sources of bacteria, assessing environmental conditions, and implementing mitigation strategies to improve water quality in the region (Figures 6.2 and 6.3).

# 6.1.1. Surface water relationships

Beyond seasonal variations in bacteria loading, another critical factor influencing bacterial presence in surface waters is dissolved oxygen (DO), which exhibits strong negative correlations with bacterial counts in certain areas. DO consistently showed a negative correlation with bacteria counts in surface water across all areas and regardless of the type of data transformations, with various strengths. For instance, DO was found to be important in predicting bacteria counts after Boruta analysis in areas 1 and 4 after the data underwent BOXCOX and logarithmic transformations. In area 1, DO showed a strong negative correlation (p-value: 0.01; p-value: 0.01) with bacteria counts after BOXCOX and logarithmic transformations, respectively. In area 4, DO showed a strong negative correlation with bacteria after BOXCOX and logarithmic transformations (p-value << 0.01; p-value << 0.01). While DO was an important predicting variable in these areas, it was not as significant in areas 2 and 3. In area 2, with BOXCOX, logarithmic, and no transformation, DO had a weak negative correlation with bacteria (p-value: 0.05; p-value: 0.06; p-value: 0.05, respectively), in addition to a rejected status after Boruta analysis. Across all transformations in area 3, DO also negatively correlated with bacteria and was rejected after Boruta analysis. The consistent negative correlation between DO and FIB across all areas, especially in the warmer months, can be explained by metabolic, decomposition, and nutrient-rich environmental processes. Higher temperatures reduce oxygen solubility, leading to lower dissolved oxygen levels that can trigger algal blooms, which support the growth of E. coli and enterococci in surface water (Tiefenthaler et al., 2008). In addition, FIB consume oxygen during respiration and are often associated with elevated organic matter, which amplifies microbial decomposition that depletes DO in areas with a high bacteria load. The difference in the strength of correlations and predictive capability of DO for bacteria counts across the surface water of different areas highlights that DO and FIB relationships can be locality-specific and may be influenced by other environmental factors, such as nutrient levels, salinity, and organic matter content (Badgley et al., 2019). Variability in land use, hydrology, and water chemistry across areas can lead to differing strengths in the correlation between DO and bacterial counts.

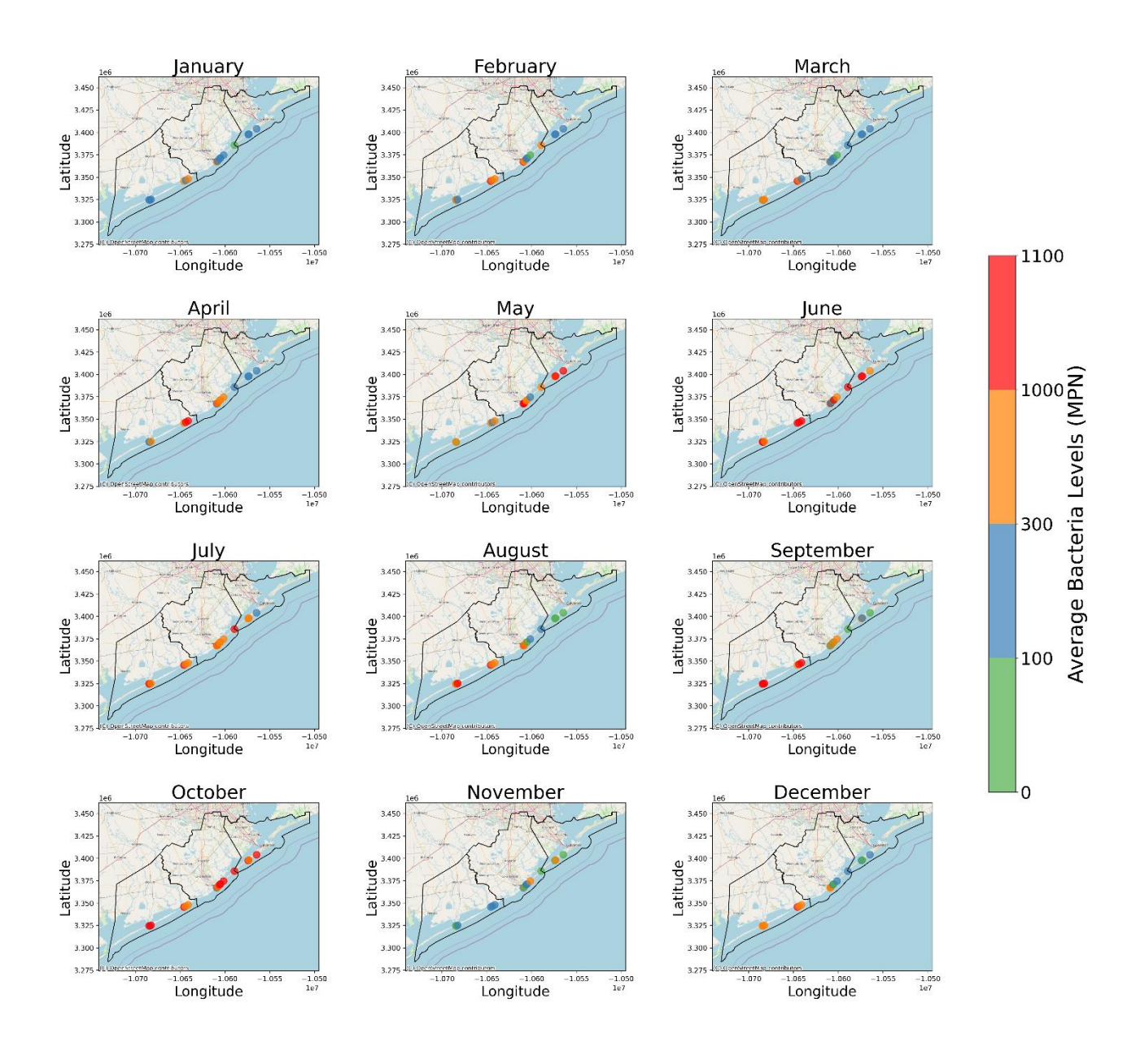


**Figure 6.1.** Monthly bacteria contamination levels in surface Water. The average bacteria levels across various monitoring locations are shown with color gradients. Red and orange markers represent higher contamination levels.

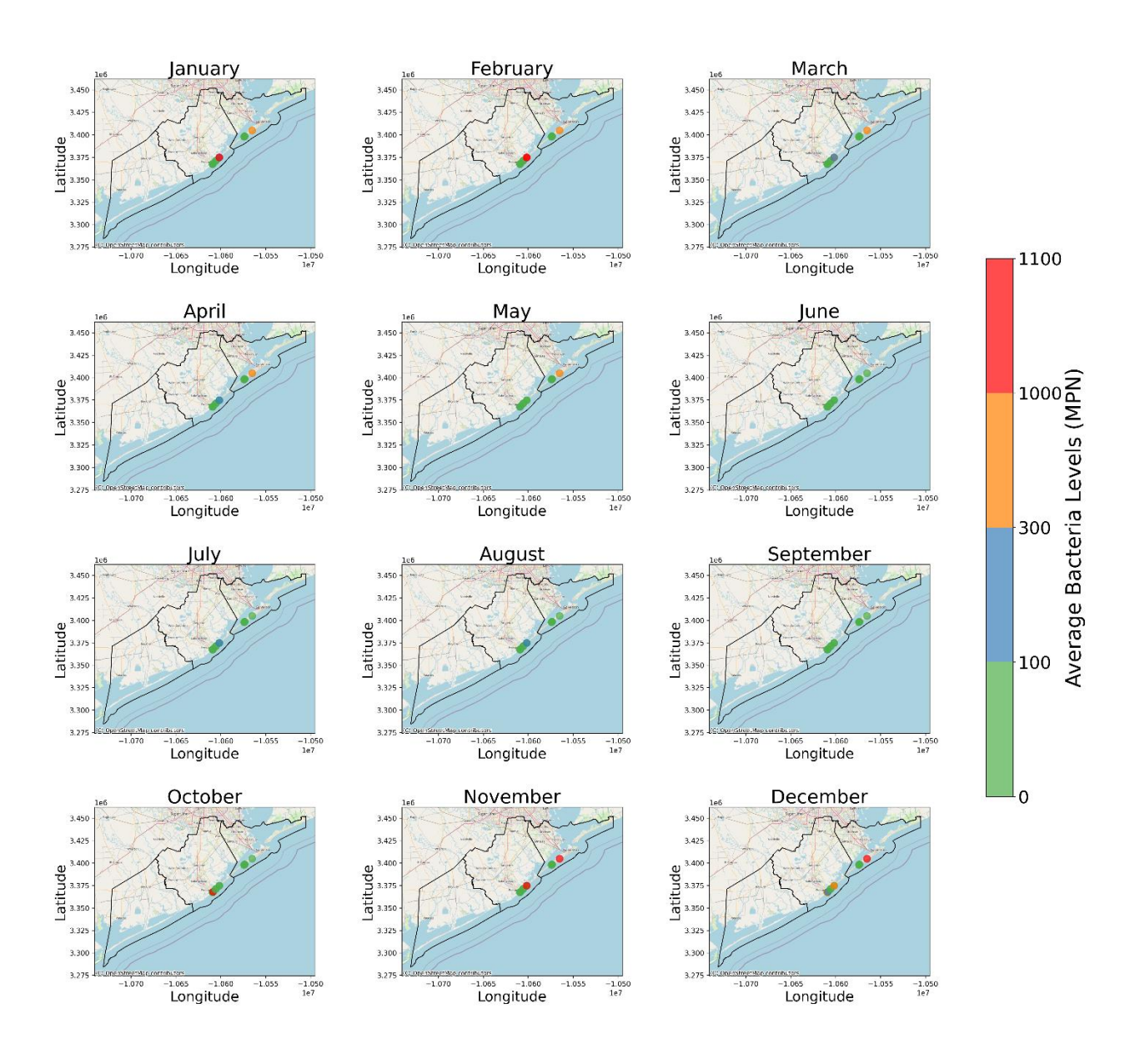


*Figure 6.2.* Monthly bacteria levels in groundwater. Higher concentrations are represented by the blue, orange, and red colors.

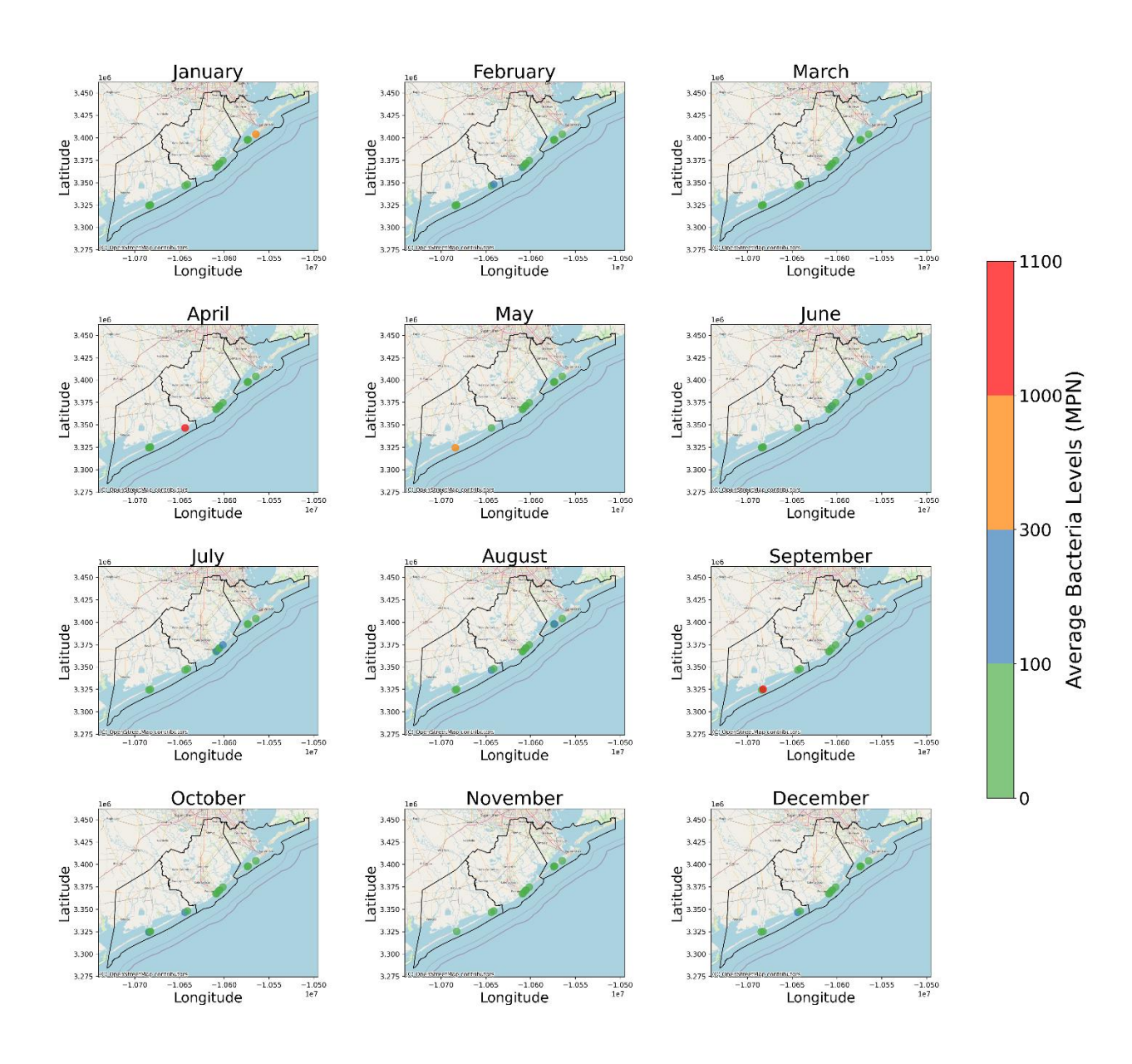


**Figure 6.3**. Monthly bacteria levels in porewater. Higher concentrations are represented by the blue, orange, and red colors.

Another variable influencing FIB dynamics is chlorophyll-a (*chl-a*), which demonstrated positive correlations with bacteria in surface water in specific areas. *Chl-a* was a weak significant predictor of FIB in surface water in multiple areas (area 1 and area 3) with positive correlations under different transformations. In area 1, *chl-a* positively correlated with bacteria after undergoing both BOXCOX, logarithmic and no transformations (p-value: 0.05; p-value: 0.05, respectively). In area 3, *chl-a* positively correlated with bacteria counts after a logarithmic transformation (p-value: 0.05). Across both areas, *chl-a* was confirmed through Boruta analysis, showing that the variable could be a significant predictor of FIB in these areas. The positive correlation between FIB and *chl-a* may be attributed to nutrient-rich waters and untreated surface water or subsurface runoff to the gulf, which can contribute to algae blooms (source of *chl-a*) and elevated enterococci levels (Kelly et al., 2020).

In contrast, other environmental factors exhibited unique correlations in different areas. Some areas exhibited unique variables that correlated with FIB and/or exhibited a predictive potential for FIB in surface water. Unique to area 2, the logarithmically transformed dataset showed relationships between FIB and radium isotopes (223Ra, 226Ra). 223Ra had a strong negative correlation (p-value << 0.01) with bacteria and <sup>226</sup>Ra had a weaker negative correlation (r=-0.8, pvalue: 0.04). However, the above variables were rejected after undergoing Boruta analysis, indicating that the variables are unimportant for predicting bacteria counts in this area. Distinct to area 3, salinity consistently correlated positively with bacteria counts and a confirmed status after Boruta analysis across all transformations (BOXCOX, logarithmic, and none). After undergoing a BOXCOX transformation, salinity had a correlation of 0.5 (p-value << 0.01), a correlation of 0.5 (p-value << 0.01) after a logarithmic transformation, and a correlation of 0.4 (p-value << 0.01) when no transformation was performed. In the original dataset with no transformations, <sup>226</sup>Ra had a weak positive correlation ( $R^2=0.8$ , p-value: 0.02) with bacteria counts in area 4, as well as the predictive potential for bacteria counts (Boruta status confirmed). In area 1, DIN was found to have a moderate negative correlation with bacteria after undergoing BOXCOX and logarithmic transformations. After the BOXCOX transformation was performed, the correlation of DIN with bacteria was -0.5 (p-value: 0.03). After the data was transformed logarithmically, the correlation of DIN with bacteria was -0.5 (p-value: 0.04). Despite the correlation between the two variables, Boruta analysis rejected DIN, indicating that it was not considered an important feature in the model for predicting bacteria counts. The spatially specific correlations observed herein underscore the complexity of bacterial dynamics across regions.

After bacteria data underwent a logarithmic transformation, surface water chemistry variables had several significant correlations. DO showed a strong negative correlation with FIB (p-value<<0.01), while ORP had a weak positive correlation with FIB (p-value: 0.04). Like in groundwater and pore water, salinity exhibited a strong positive correlation with bacteria in surface water (p-value<<0.01). In surface water, only the nitrogen species NO<sub>2</sub><sup>-</sup> showed a significant relationship with bacteria, with a strong positive correlation (p-value<<0.01).

#### 6.1.2. Groundwater relationships

Groundwater also exhibited distinct temporal and spatial patterns (Figure 15). Nitrogen species likely play a prominent role in bacterial dynamics in groundwater. Both areas 3 and 4, where well monitoring was available, a negative correlation between bacterial counts in groundwater and nitrogen species was observed. In area 3, NO<sub>3</sub><sup>-</sup> and NO<sub>3</sub><sup>-</sup>+NO<sub>2</sub><sup>-</sup> exhibited negative correlations across BOXCOX and logarithmic transformations. After a BOXCOX

transformation, NO<sub>3</sub><sup>-</sup> had a weak correlation of -0.3 (p-value: 0.04), and NO<sub>3</sub><sup>-</sup>+NO<sub>2</sub><sup>-</sup> had a weak correlation of -0.4 (p-value: 0.02) in area 3. Similar relationships were found after a logarithmic transformation was performed on the area 3 dataset, with a NO<sub>3</sub><sup>-</sup> correlation of -0.4 (p-value: 0.03) and a NO<sub>3</sub><sup>-</sup>+NO<sub>2</sub><sup>-</sup> correlation of -0.4 (p-value: 0.03). The status of significant organic nitrogen species in area 3 was rejected after Boruta analysis, indicating that these variables are not significant for predicting FIB values in groundwater. In area 4, NH<sub>4</sub><sup>+</sup> and DIN consistently showed negative correlations in both transformed datasets. After a BOXCOX transformation, NH<sub>4</sub><sup>+</sup> and DIN showed a significant negative correlation to bacteria (p-value<<0.01 and p-value<<0.01) with a confirmed Boruta status after analysis, highlighting the variables' predictive ability for bacteria in this area. Similar to the BOXCOX transformed dataset, a logarithmic transformation indicated a significant negative correlation between NH<sub>4</sub><sup>+</sup> and DIN with bacteria (p-value<<0.01 and p-value<<0.01) and a confirmed Boruta status. This indicates that nitrogen species, while varying in form, are inversely related to bacterial levels in groundwater across both areas. Analysis also indicates that while nitrogen species have a negative correlation with bacteria in both areas, only inorganic nitrogen species are significant in predicting bacteria values in area 4 groundwater.

While both areas demonstrate the relationship between nitrogen species and bacteria in groundwater, the two study areas have their unique significant variables. Area 3 is characterized by broader geochemical influences, including salinity, ORP, depth to water, and radium isotopes. In contrast, area 4 is dominated by strong nitrogen-bacteria interactions, with a narrower range of significant variables.

After bacteria underwent a BOXCOX and a logarithmic transformation, a weak negative correlation between depth to water and bacteria was found in the groundwater (r=0.3, p-value: 0.04; r=0.3, p-value: 0.04). After Boruta analysis, the BOXCOX-transformed dataset had a confirmed status, but the logarithmically transformed dataset yielded a rejected status. Salinity exhibited a weak positive correlation with bacterial counts in area 3 across both transformations, BOXCOX and logarithmic (r=0.4, p-value: 0.03; r=0.4, p-value: 0.03). After Boruta analysis for both transformations of bacteria against salinity, the status was rejected, indicating that salinity is not significant for predicting bacteria counts. Variability between the strength, significance, and Boruta status of salinity and bacteria between the two areas indicates that correlations likely reflect other environmental conditions of the area, such as fortnightly tidal variability (Boehm and Weisberg, 2005), which impact the input, transport, and distribution of fecal indicator bacteria (Knee et al., 2008). Despite the observed correlation, salinity itself plays a limited role in FIB levels; instead, tidal variations, which influence both salinity and FIB transport, are the primary factor (Boehm and Weisberg, 2005). Additionally, oxidation-reduction potential (ORP) showed a weak negative correlation in the logarithmically transformed dataset (r=-0.3, p-value: 0.05), however, ORP had a rejected status after Boruta analysis. A weak positive correlation with <sup>223</sup>Ra was observed in the logarithmic dataset (r=0.3, p-value: 0.04) with a rejected status after Boruta analysis, showing that the variable is insignificant for predicting bacteria values.

In contrast to area 3, no additional parameters (e.g., salinity, ORP, radium isotopes) showed significant correlations with bacterial counts, suggesting that nitrogen species are the primary drivers of bacterial variation in the groundwater in area 4. In area 4, strong negative correlations with NH<sub>4</sub><sup>+</sup> and DIN were observed across BOXCOX and logarithmic datasets (p-value<<0.01 for both variables after BOXCOX and logarithmic transformations). These variables were also confirmed as significant predictors through Boruta analysis, emphasizing their role in predicting bacteria counts in area 4. Ammonium toxicity on FIB like *E. coli, B. subtilis*, and *Enterococcus* 

often depends on the concentration, the bacterial species present, the initial bacterial density, and the specific environmental conditions. High ammonium concentrations can be lethal to FIB, however, mortality is attributed to ionic or osmotic stress rather than directly to ammonium toxicity (Muller et al., 2006). In addition, a study done in 2023 by Pereira et al. found that Enterococcus exhibits a higher mortality rate in the presence of in-use quaternary ammonium compounds (QACs) and lack QAC tolerance genes. QACs are commonly found in disinfectants, antiseptics, preservatives, food production products, and consumer products (Pereira et al., 2023), which can make their way into the environment through wastewater treatment plant discharge and leaching sewage (Arnold et al., 2023).

After the bacteria dataset underwent a logarithmic transformation, various factors were found to be significant across all systems, including groundwater, pore water, and surface water. DO and ORP demonstrated a strong positive correlation with FIB (p-value << 0.01 and pvalue << 0.01), highlighting their significance across all systems. Additionally, salinity and pH displayed strong positive correlations across all systems (p-value << 0.01 for both variables). FIB, like enterococci, tend to be more sensitive to acidic environments (Hubbart et al., 2022), indicating that more neutral and alkaline environments are conducive to bacterial survival across all systems. Radium isotopes and radon presented mixed relationships with FIB. Radon (Rn) exhibited a strong negative correlation (p-value << 0.01) with bacteria counts. A negative correlation between Rn and FIB could be found in environments with high wind conditions, which cause the increased degassing of Rn in surface water (Lefebvre et al., 2015) and an increase in wave action, resulting in sediment suspension that can prolong FIB survival (Bradshaw et al., 2021). Radium isotopes <sup>223</sup>Ra and <sup>224</sup>Ra also showed negative correlations. However, the correlation was stronger between FIB and <sup>224</sup>Ra (p-value << 0.01) and weaker between FIB and <sup>223</sup>Ra (p-value = 0.02). These radon/radium patterns with FIB could arise from various conditions. Dilution of bacteria by radon/radium-rich groundwater with longer residence times (Hwang et al., 2019) could cause an inverse relationship between FIB and radon/radium to be observed. In addition, environmental factors favoring bacterial growth, such as increased organic matter, stagnant waters, or reduced flow (Evanson and Ambrose, 2006), in radon/radium-poor areas could explain these patterns. Biogeochemical factors could also play a role, such as sediment interactions reducing radon/radium levels while promoting bacterial activity. Additionally, human or animal and surface runoff inputs could disproportionately elevate bacteria in areas with low radon/radium influence.

Bacteria data was log-transformed and compared against groundwater chemistry data to identify possible relationships. DO showed a strong positive correlation with FIB concentrations (p-value<<0.01) Like DO, salinity exhibited a significant positive correlation (p-value<<0.01). Radium isotopes <sup>223</sup>Ra and <sup>224</sup>Ra showed strong positive correlations with bacteria (p-value<<0.01; p-value<<0.01, respectively). The <sup>224</sup>Ra/<sup>226</sup>Ra activity ratio (e.g., AR224:226) also had a strong positive correlation with bacteria (p-value<<0.01). This indicates that bacterial inputs are associated with very recent nearshore inputs since 224Ra is a short-lived isotope (half-life of 3.6 days). Nitrogen species consistently exhibited negative correlations with FIB concentrations in groundwater. TDN showed a strong negative correlation (p-value<<0.01), while NO<sub>3</sub><sup>-</sup> and the NO<sub>3</sub><sup>-</sup> + NO<sub>2</sub><sup>-</sup> had weaker but still significant negative correlations (p-value = 0.016 and p-value = 0.011, respectively).

Few groundwater variables showed significant correlations with fecal indicator bacteria (FIB) in the untransformed dataset. DO and salinity both showed weaker positive correlations with fecal indicator bacteria, with DO being the stronger of the two (p-value: 0.016 and p-value: 0.05,

respectively). Radium isotopes <sup>223</sup>Ra and <sup>224</sup>Ra exhibited strong positive correlations with FIB in groundwater (p-value: 0.004 and p-value<<0.01, respectively). Contrasting against the log-transformed bacteria dataset, surface water DO was found to have a strong negative correlation with bacteria in the untransformed dataset (p-value<<0.01). Like the log-transformed dataset, surface water salinity had a strong positive correlation with bacteria (p-value<<0.01). A weak positive correlation between <sup>226</sup>Ra and bacteria (p-value: 0.03) was found. Additionally, unique to the untransformed surface water when compared to other untransformed systems, NO<sub>2</sub><sup>-</sup> was found to have a strong negative correlation with FIB (p-value: 0.009).

## 6.1.3. Porewater relationships

The analysis of pore water chemistry revealed several significant correlations with logtransformed FIB data, highlighting the intricate relationships between geochemical conditions and microbial dynamics in nearshore environments. DO exhibited a weak positive correlation with FIB concentrations (p-value: 0.041), suggesting oxygen availability may slightly enhance bacterial persistence or mobilization. Still, this relationship is less pronounced than other factors. This indicates that areas with moderate flushing, where oxygenated waters are present, could still pose a risk of microbial contamination if other environmental conditions are favorable. Salinity, on the other hand, showed a strong positive correlation with FIB (p-value << 0.01), underscoring its significant role in bacterial persistence. Elevated salinity levels in porewater indicate stagnant, poorly flushed sediments, which create an environment conducive to the concentration and survival of bacteria. Enteric bacteria have shown increased survival in sediments, as particulates provide microhabitats that offer unique protection, nutrients, and more moisture (Gerba and McLeod, 1976; Pommepuy et al., 1992; Davies et al., 1995; Howell et al., 1996; Desmarais et al., 2002). Additionally, suitable microhabitats for Enterococcus and other fecal bacteria can be provided by biofilm formation (Piggot et al., 2012). Microbes and bacteria are protected by physical and biological challenges and stressors along shorelines such as fluctuations in temperature, desiccation, ion concentration, predation, ultraviolet radiation, and wave action by extracellular polymeric substances (EPS), which allow for microbes to adhere to surfaces and each other (Piggot et al., 2012). Such conditions are likely exacerbated by tidal forcing or saltwater intrusion, particularly in areas where septic system backflow or sewage line failures introduce additional nutrient loads, further enhancing bacterial persistence.

Radium isotopes, <sup>223</sup>Ra and <sup>224</sup>Ra, demonstrated strong positive correlations with FIB, with p-values of 0.007 and 0.004, respectively. These correlations suggest that radium activities, often associated with SGD and sediment-water interactions, are reliable indicators of bacterial transport and contamination pathways. Elevated radium activities likely reflect zones, where contaminated groundwater or sediment-water exchanges, facilitate the mobilization of FIB from sediments into nearshore environments, particularly in areas affected by failing infrastructure. Contrary to the trends observed in groundwater, the activity ratio of <sup>224</sup>Ra/<sup>226</sup>Ra (AR224:226) displayed a weaker positive correlation with FIB concentrations (p-value: 0.027) with the log-transformed data. However, when using the untransformed dataset for pore water. The AR224:226 correlated significantly with FIB (p-value: 0.0084) in pore water and was the only significant correlated variable. Specific hydrodynamic or geochemical processes govern the relative contributions of short-lived and long-lived radium isotopes. Higher AR224:226 values likely reflect recent SGD or sediment-water exchange events where <sup>224</sup>Ra is readily desorbed from sediments due to its short-lived nature and dynamic hydrodynamic conditions (Gonneea et al., 2008). These events can act as conduits for FIB transport, as SGD and sediment disturbance mobilize bacteria and other

contaminants from sediments into the overlying water column. In contrast, areas dominated by longer residence times or limited exchange processes may exhibit lower AR224:226 ratios and reduced FIB mobilization.

Thus, the correlation between AR224:226 and FIB concentrations underscores the interplay between radium mobility, sediment-water interactions, and microbial contamination. Monitoring these isotopic ratios can provide valuable insights into recent SGD dynamics and associated bacterial transport pathways, particularly in nearshore environments with complex hydrological and geochemical conditions.

## 6.1.4. Combined groundwater, porewater, and surface water relationships

When considering the <u>data from all three environments</u>, including groundwater, surface water, and porewater, nitrogen species showed significant negative correlations with FIB concentrations. TDN had a significantly strong negative correlation (p<<0.01), as did DON (p-value = 0.006). DIN and its components,  $NO_3^-$ ,  $NO_2^-$ , and the combined measure of nitrate and nitrite, all showed strong negative correlations with FIB concentrations (p-value<<0.01 for listed variables).  $NH_4^+$  also exhibited a strong negative correlation (p<<0.01).

In the untransformed dataset, FIB showed relationships with several variables across all systems (groundwater, porewater, and surface water). Like in the logarithmically transformed bacteria dataset, bacteria showed a strong positive correlation with DO (p-value << 0.01). Strong positive correlations were also observed between bacteria and salinity, pH, and ORP (pvalue << 0.01 for listed variables). Radon and radium isotopes (223Ra and 224Ra) showed negative correlations with bacteria at varying strengths. Radon had a strong negative correlation with FIB (p-value << 0.01). <sup>223</sup>Ra exhibited a weaker negative correlation with bacteria (p-value: 0.02), while <sup>224</sup>Ra had a strong negative correlation with bacteria (p-value << 0.01). The activity ration of <sup>224</sup>Ra to <sup>223</sup>Ra (AR224:223) had a weak negative correlation with FIB (p-value: 0.04). All nitrogen species showed negative correlations with fecal indicator bacteria (FIB), indicating that these species may play a role in inhibiting bacterial growth. Total dissolved nitrogen (TDN) had a strong negative correlation with bacteria (p-value << 0.01). Dissolved organic nitrogen (DON) and its species, nitrate (NO<sub>3</sub><sup>-</sup>), nitrite + NO<sub>2</sub><sup>-</sup>, and the combined measurement of the two (NO<sub>3</sub><sup>-</sup> + NO<sub>2</sub><sup>-</sup>) exhibited significant negative correlations with FIB (p-value << 0.01 for DON and its components). Dissolved inorganic nitrogen (DIN) and ammonium (NH<sub>4</sub><sup>+</sup>) had strong negative correlations with bacteria across all systems (p-value << 0.01 and p-value << 0.01).

# 6.2. Analysis of Chemical Data Using Deep Learning and Principal Component Analyses

The results of the Variational Autoencoder (VAE) for surface sample chemicals, focusing on the two highest latent dimensions, are shown in **Figure 6.4**. Latent Dimension 1 accounts for 21.21% of the total variance, Latent Dimension 2 accounts for 32.60%, Latent Dimension 3 accounts for 25.39%, and Latent Dimension 4 accounts for 20.80%.

The red arrows in the plot indicate statistically significant chemical variables with a p-value of less than 0.05, demonstrating a significant correlation with the bacteria dataset. These arrows were highlighted to emphasize the chemicals that have a notable relationship with bacteria levels. Additionally, when arrows are aligned in the same direction, it suggests a positive correlation between those chemicals, while arrows in opposite directions indicate a negative correlation.

The results of the Variational Autoencoder (VAE) for surface sample chemicals, focusing on the two highest latent dimensions with log-transformed bacteria is shown in **Figure 6.5**. Latent Dimension 1 accounts for 26.85% of the total variance, Latent Dimension 2 accounts for 7.17%, Latent Dimension 3 accounts for 28.18%, and Latent Dimension 4 accounts for 37.81%. The remaining figures display the chemical datasets across different systems, including groundwater and pore water, with both the original and log-transformed Bacteria datasets. These visualizations provide a comprehensive view of the relationships and correlations between the chemical variables and the Bacteria dataset in various water systems. **Figure 6.6**, **Figure 6.7**, **Figure 6.8**, and **Figure 6.9** illustrate the results of the Variational Autoencoder (VAE) for pore sample chemicals with original bacteria, pore sample chemicals with log-transformed bacteria, ground sample chemicals with original bacteria, and ground sample chemicals with log-transformed bacteria, respectively.

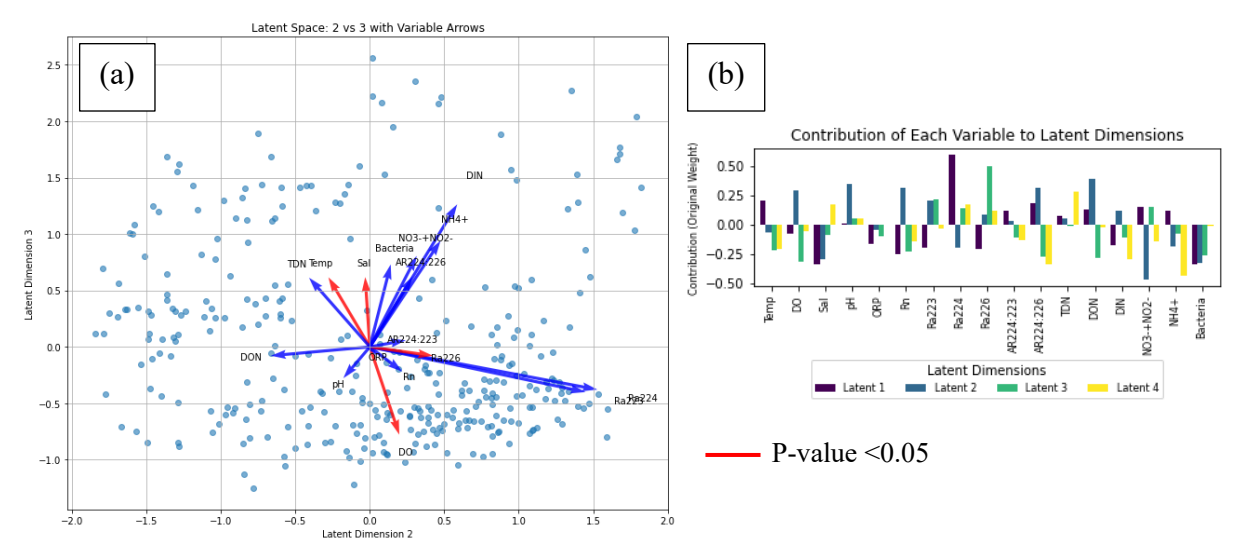


**Figure 6.4.** Results of the Variational Autoencoder (VAE) for surface sample chemicals with the original Bacteria dataset. (a) The relationship between Latent Dimension 2 (32.60%) and Latent Dimension 3 (25.39%), with red arrows highlighting variables with a p-value less than 0.05. (b) Contribution of each variable to the respective latent dimensions.

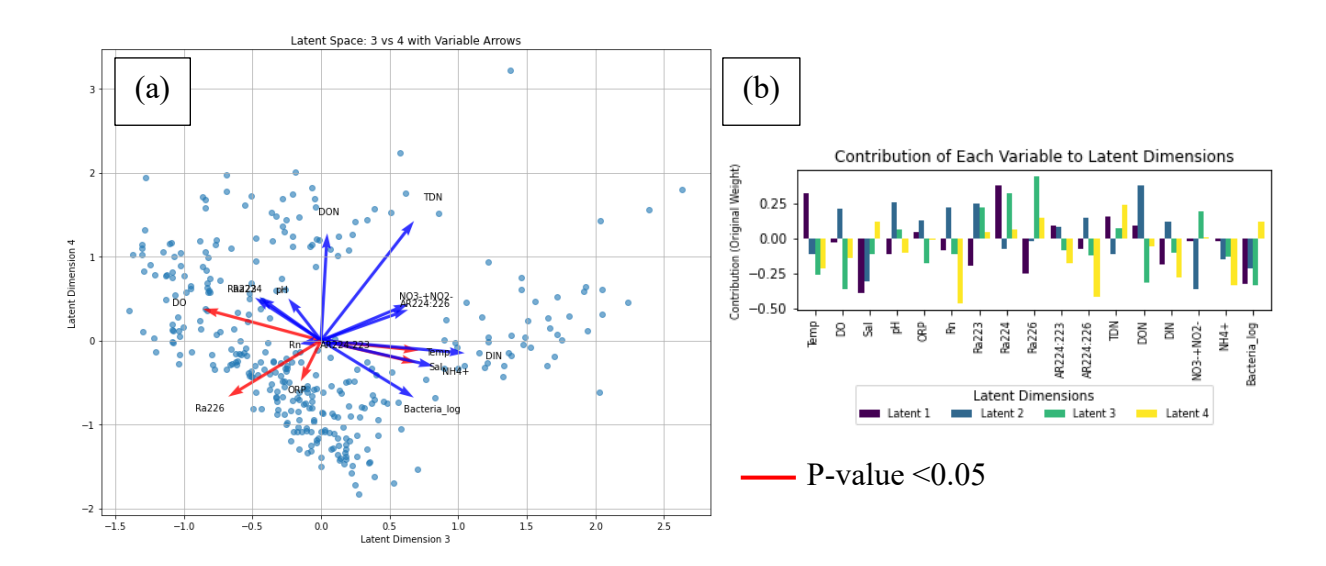


**Figure 6.5.** Results of the Variational Autoencoder (VAE) for surface sample chemicals with log-transformed Bacteria dataset, focusing on the highest latent dimensions. (a) The relationship between Latent Dimension 3 (28.18%) and Latent Dimension 4 (37.81%), with red arrows highlighting variables with a p-value less than 0.05. (b) Contribution of each variable to the respective latent dimensions.

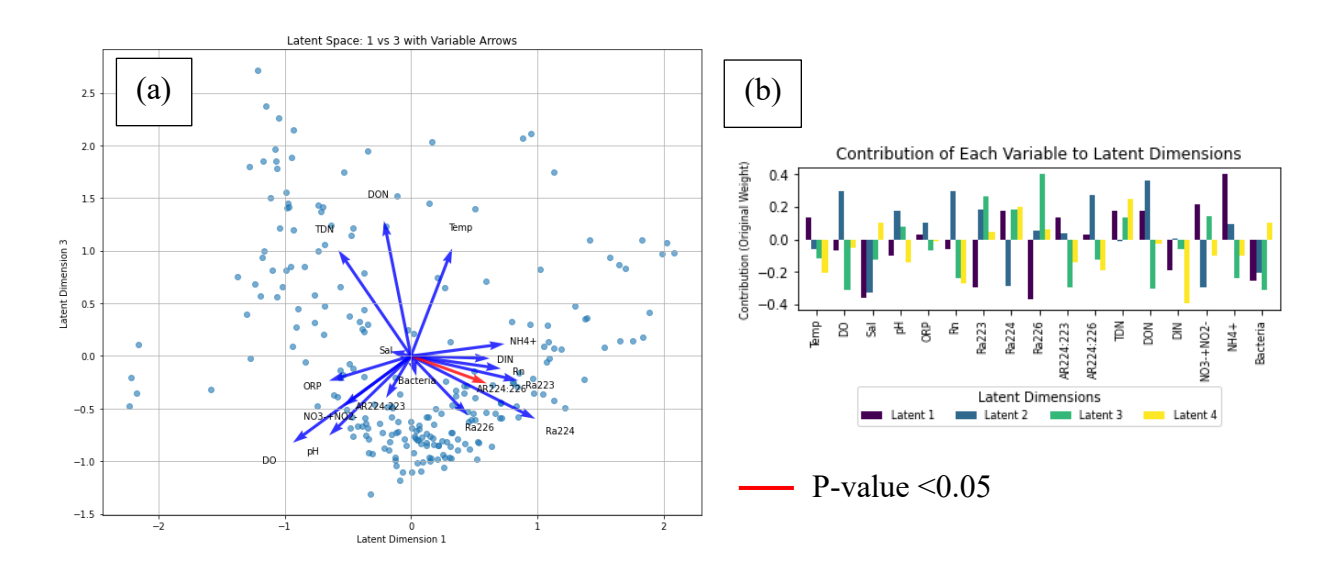


**Figure 6.6.** Results of the Variational Autoencoder (VAE) for pore sample chemicals with the original Bacteria dataset, focusing on the highest latent dimensions. (a) The relationship between Latent Dimension 1 (35.41%) and Latent Dimension 3 (42.18%), with red arrows highlighting variables with a p-value less than 0.05. (b) Contribution of each variable to the respective latent dimensions.

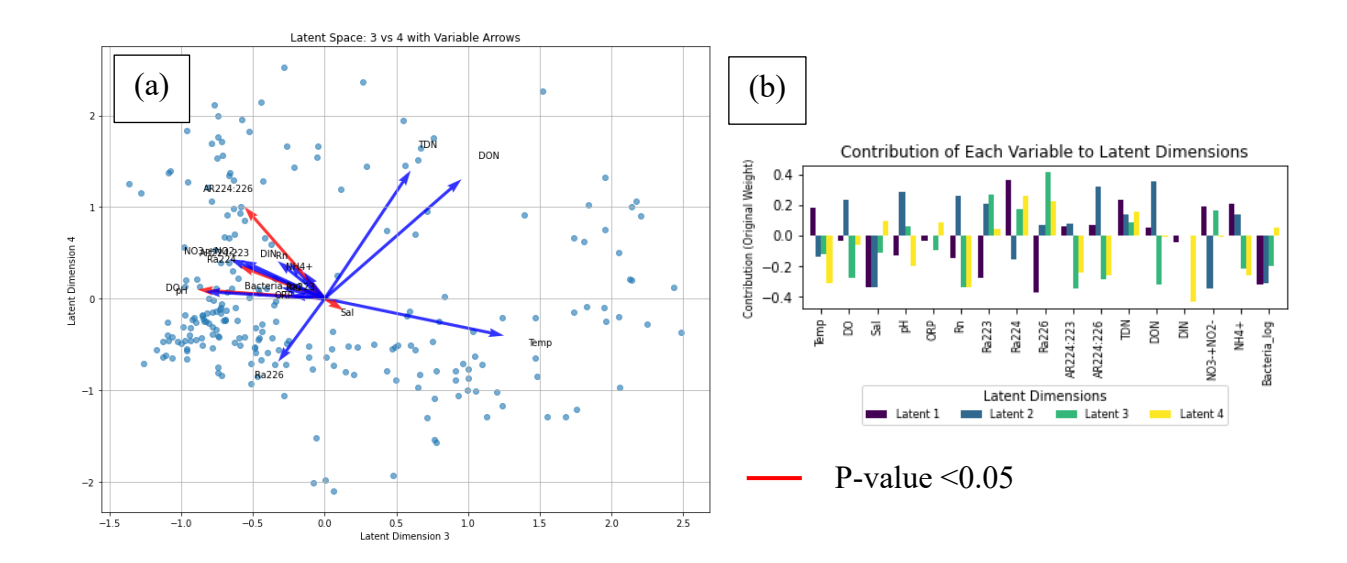


**Figure 6.7.** Results of the Variational Autoencoder (VAE) for pore sample chemicals with log-transformed Bacteria dataset, focusing on the highest latent dimensions. (a) The relationship between Latent Dimension 3 (44.46%) and Latent Dimension 4 (40.45%), with red arrows highlighting variables with a p-value less than 0.05. (b) Contribution of each variable to the respective latent dimensions.

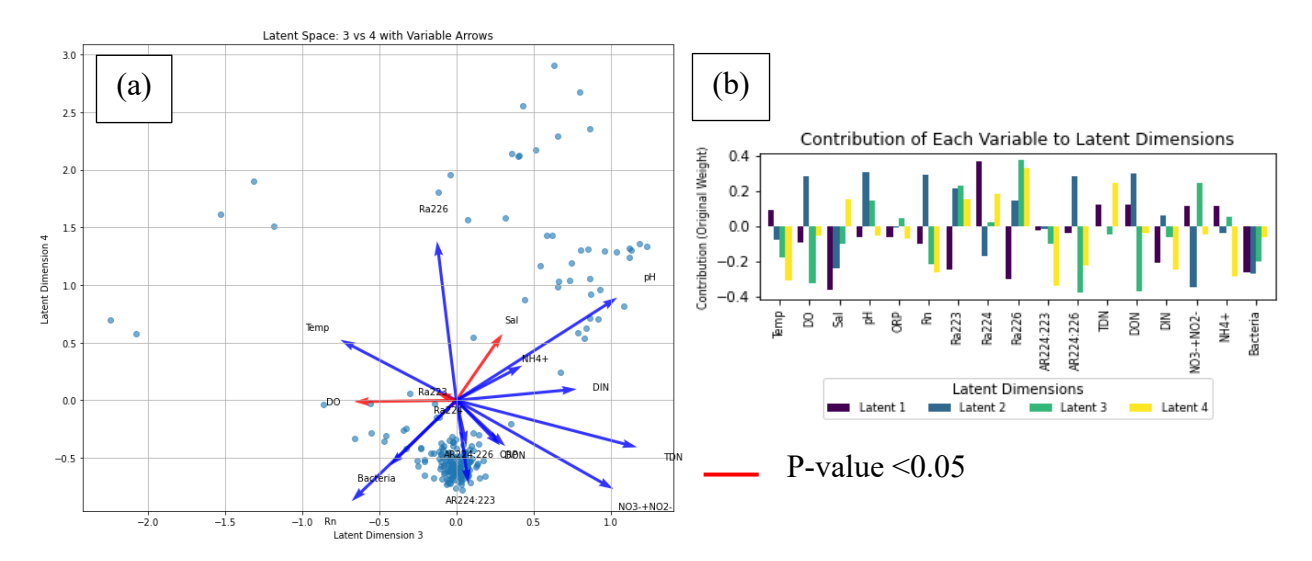


**Figure 6.8.** Results of the Variational Autoencoder (VAE) for ground sample chemicals with the original Bacteria dataset, focusing on the highest latent dimensions. Results of the Variational Autoencoder (VAE) for ground sample chemicals with the original Bacteria dataset, focusing on the highest latent dimensions. (a) The relationship between Latent Dimension 3 (20.64%) and Latent Dimension 4 (73.59%), with red arrows highlighting variables with a p-value less than 0.05. (b) Contribution of each variable to the respective latent dimensions.

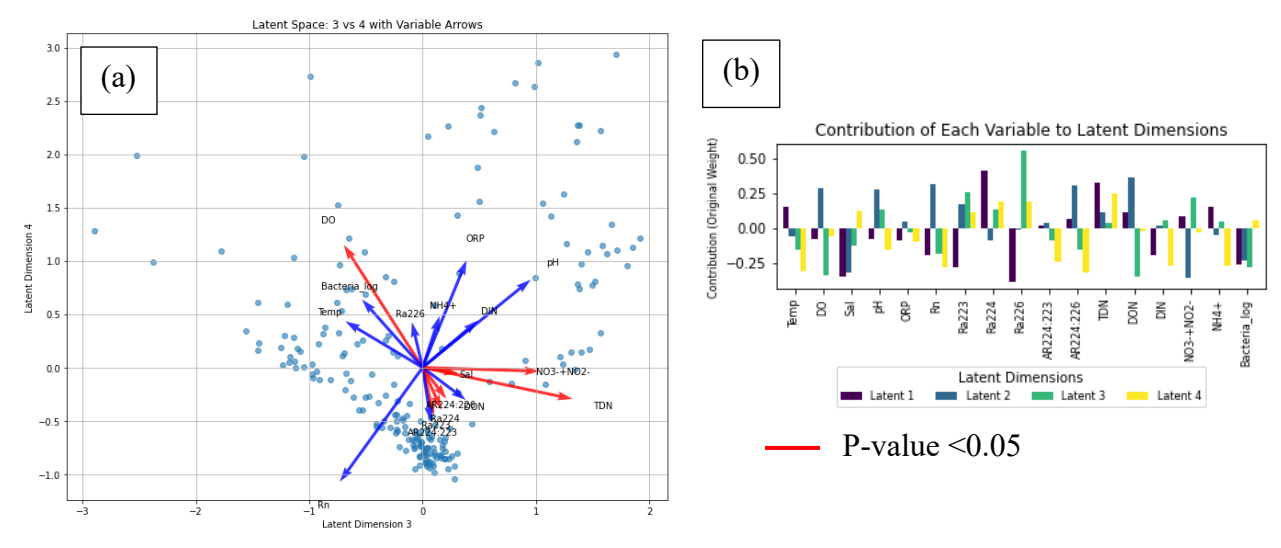
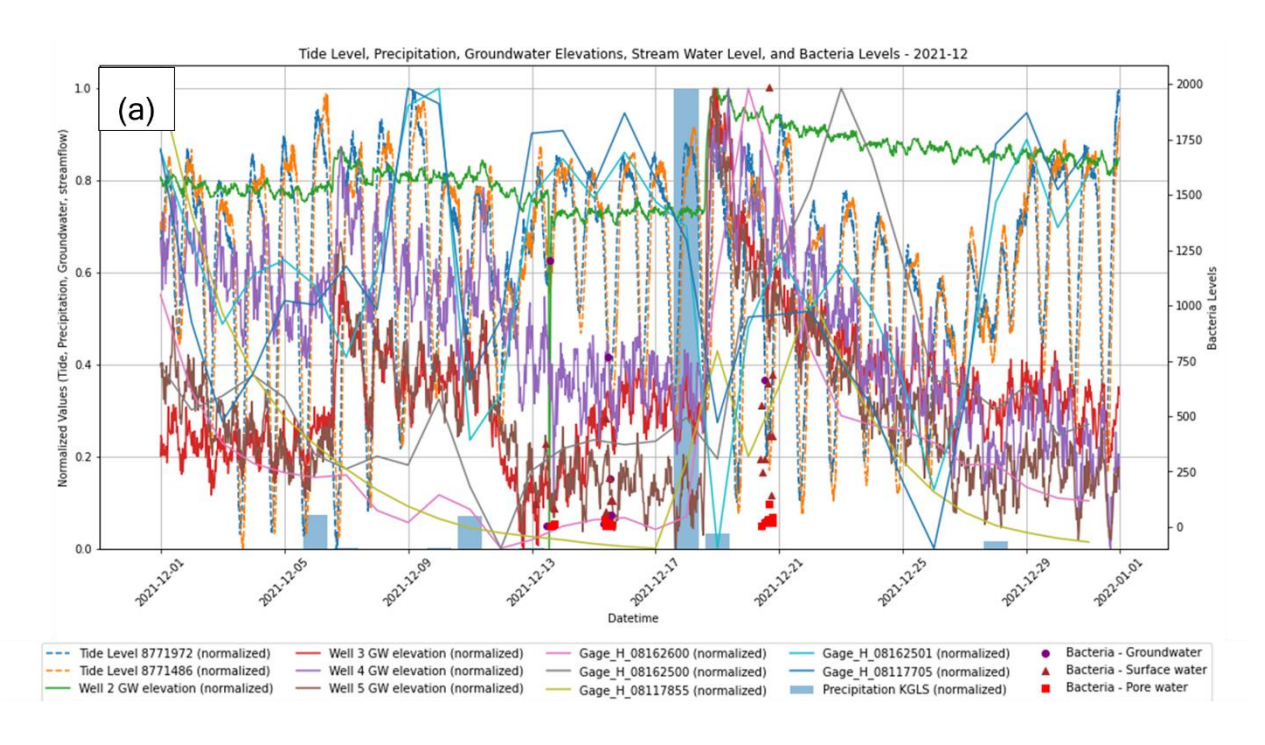


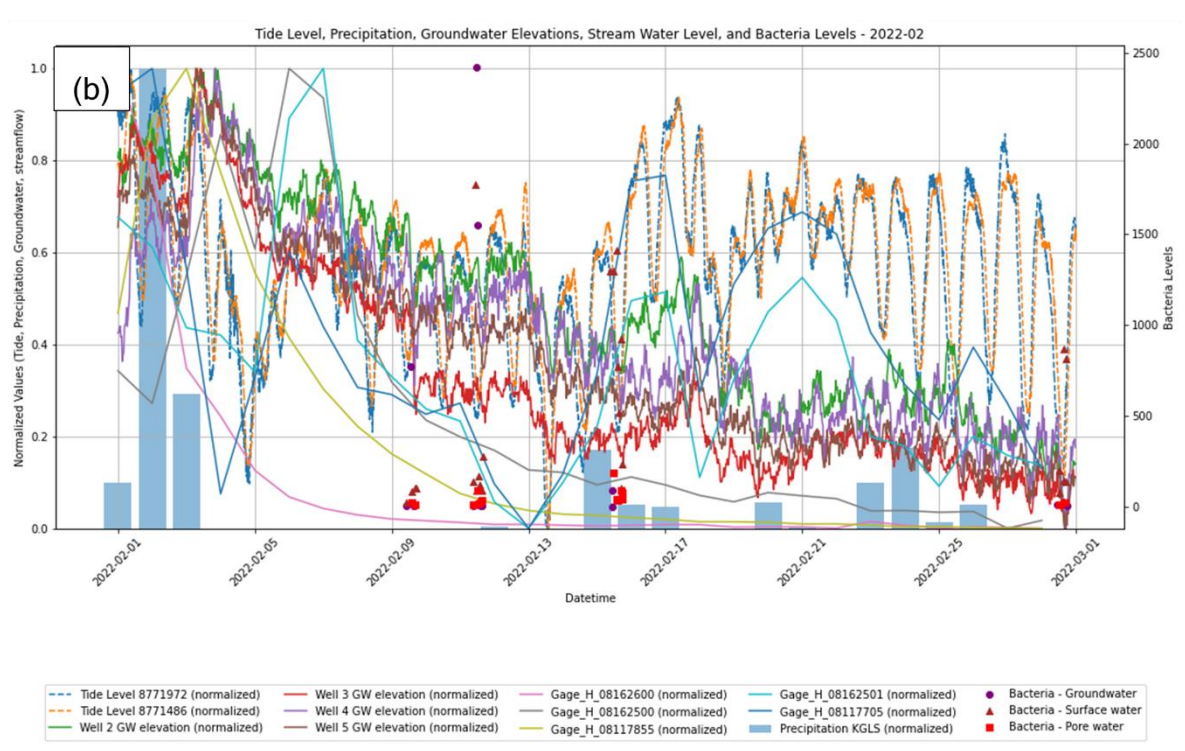
**Figure 6.9.** Results of the Variational Autoencoder (VAE) for ground sample chemicals with log-transformed Bacteria dataset, focusing on the highest latent dimensions. (a) The relationship between Latent Dimension 3 (38.81%) and Latent Dimension 4 (50.74%), with red arrows highlighting variables with a p-value less than 0.05. (b) Contribution of each variable to the respective latent dimensions.

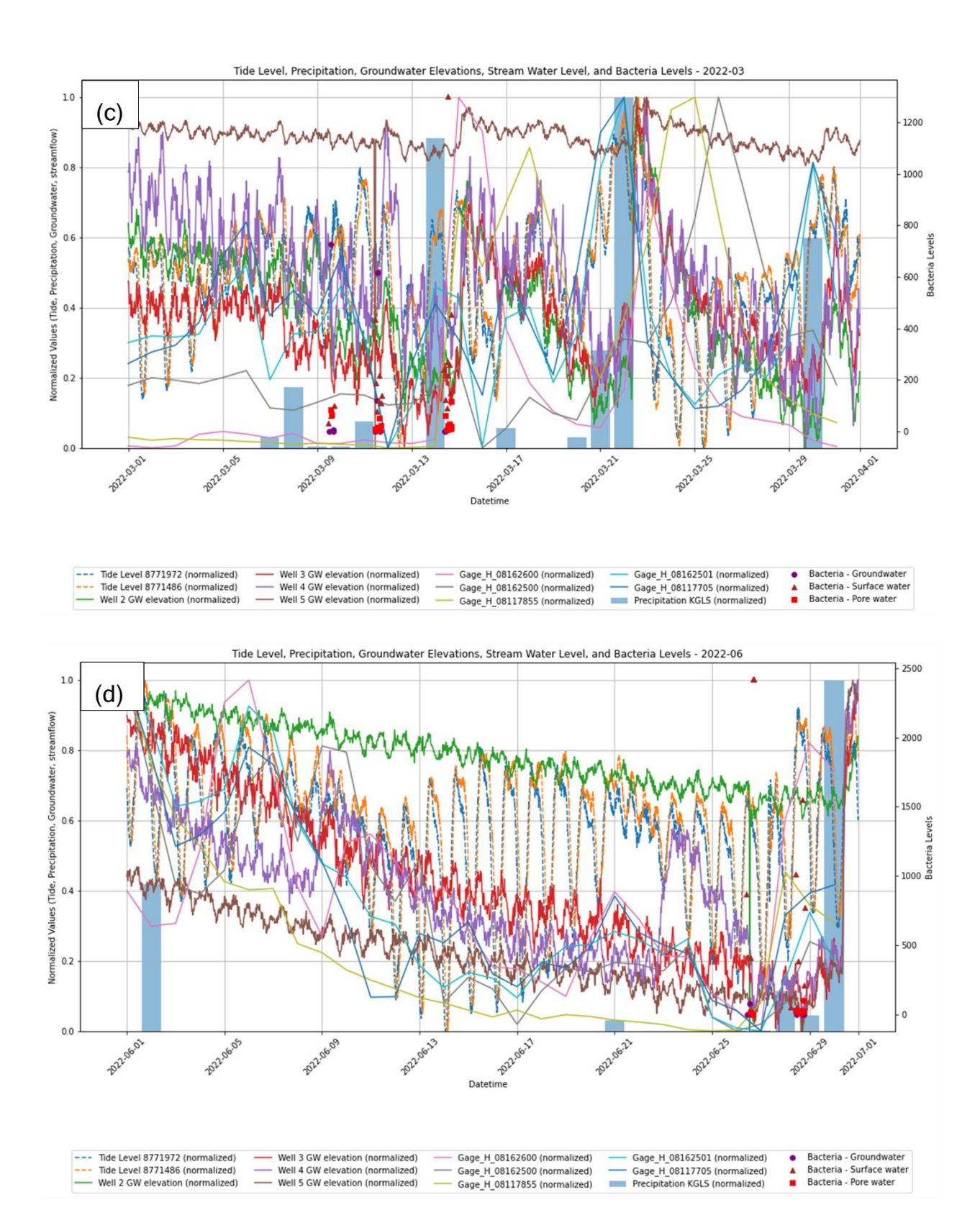
# 6.3. Relationships Between Bacteria Levels, Groundwater Elevation, and Environmental Factors using Machine Learning Techniques

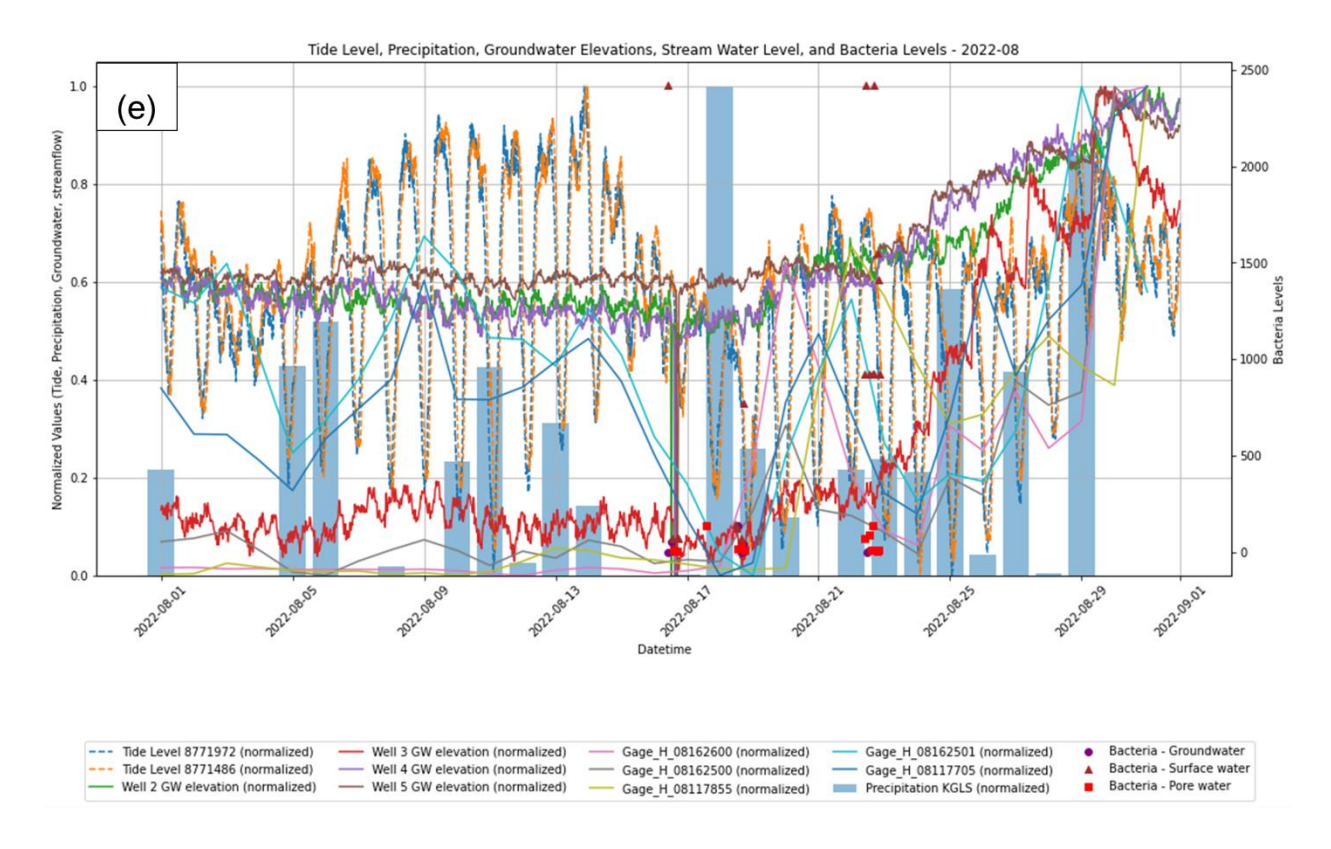
# 6.3.1. Analysis of environmental and hydrological datasets, preprocessing of data, and variables selection for machine learning models

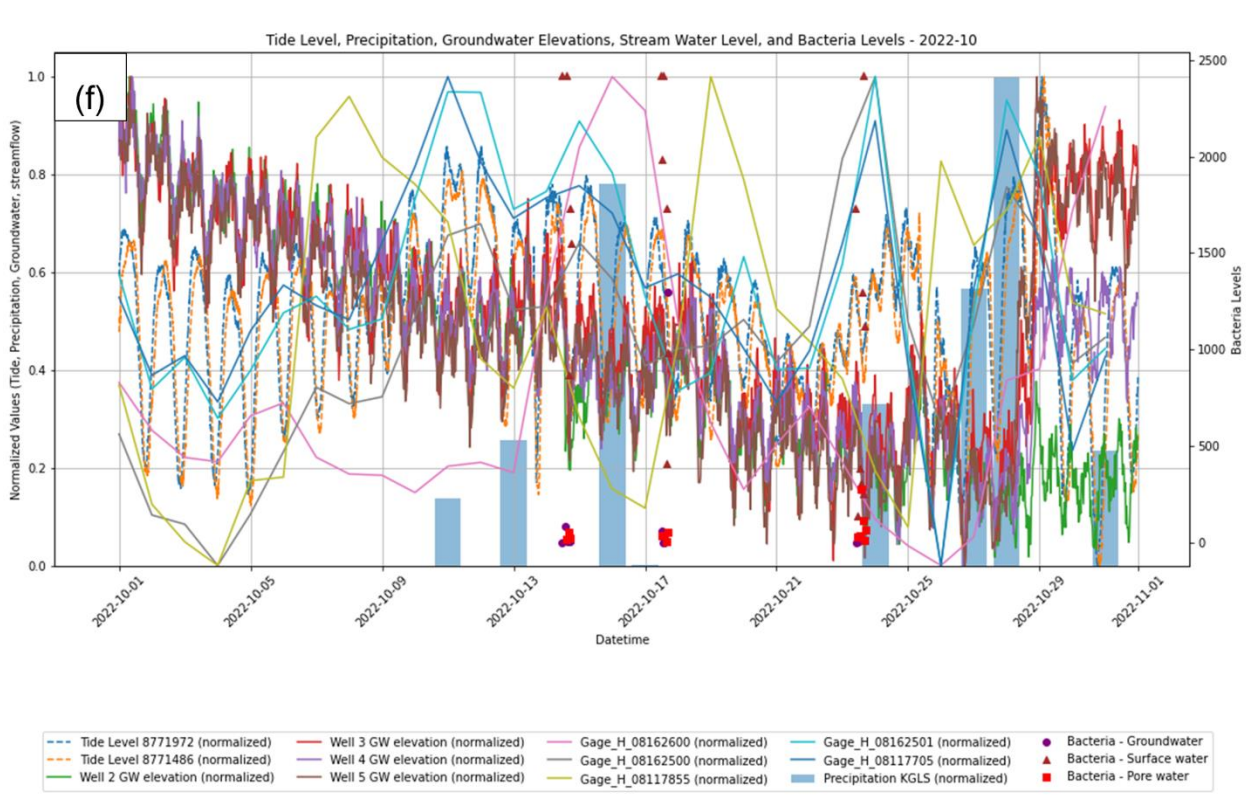
The study area spans three counties: Matagorda, Brazoria, and Galveston. It was divided into distinct regions based on different watersheds, with the dataset extracted using GIS for each specific area. The tables below present the datasets utilized for each region. This approach categorizes the study area into four locations according to watershed type. This analysis investigates the relationship between environmental factors and bacteria across various areas, including surface, pore, and groundwater samples. It examines how key environmental variables, such as tide level, groundwater elevation, streamflow, and precipitation, correlate with bacterial levels in each water system. The aim is to understand the influence of environmental and hydrological factors on bacterial distribution and behavior across different areas, ultimately identifying the most significant factors for optimizing the machine learning model. For instance, Figure 6.10 Figure 6.10. Analysis of Environmental Factors and Bacteria in Area 4 in different months: (a) 2021-12; (b) 2022-02; (c) 2022-03; (d) 2022-06; (e) 2022-08; (f) 2022-10; (g) 2022-11; (h) 2022-12; (i) 2023-01; (j) 2023-02; (k) 2023-04.illustrates the variation in tide level, precipitation, groundwater elevation, streamflow, and bacteria levels during December 2021 for Galveston County (Area 4). Bacteria levels exhibit notable fluctuations, with significant increases observed during certain peaks. These spikes are frequently associated with rainfall events (indicated by blue bars), as well as changes in tide levels and groundwater elevation.

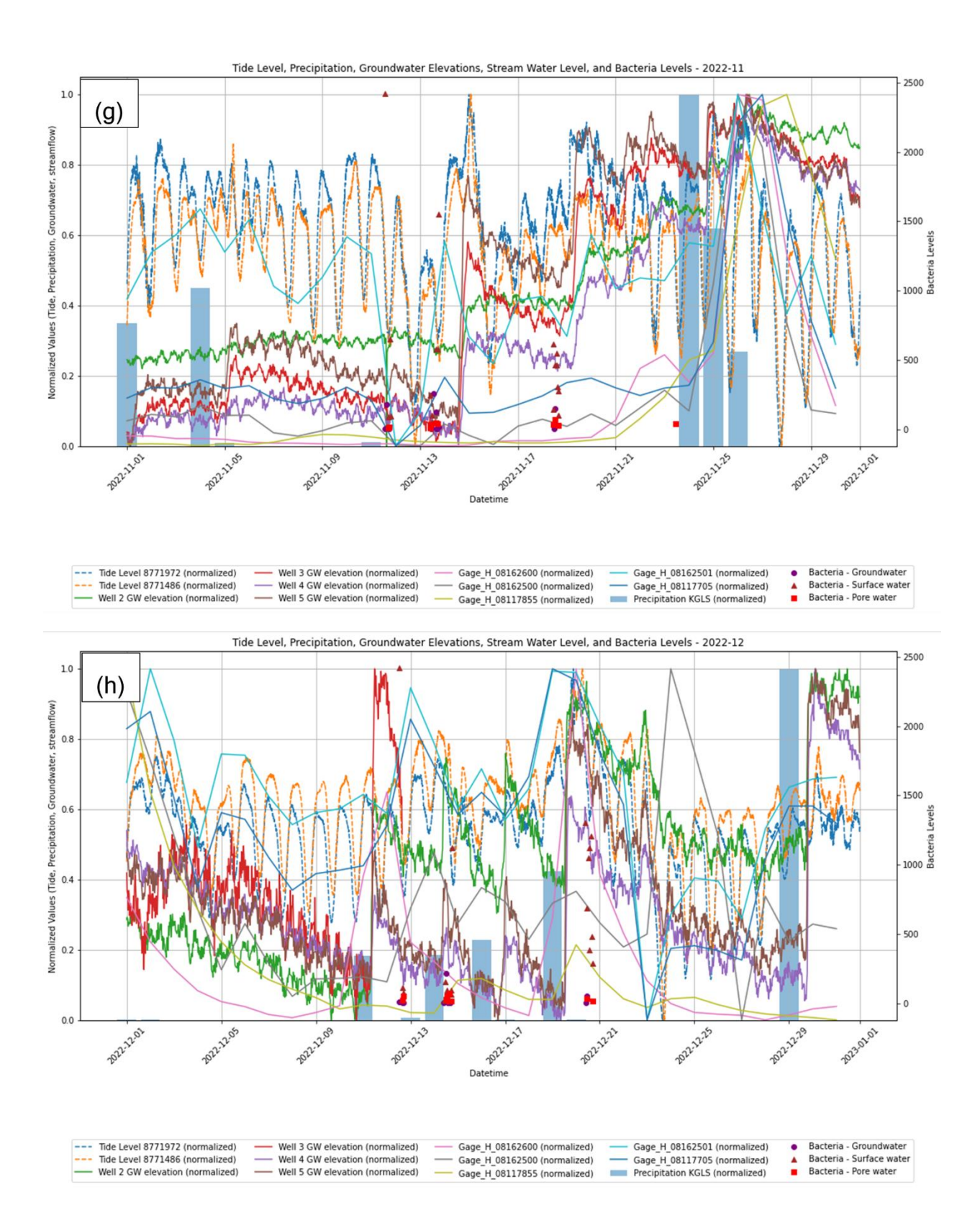


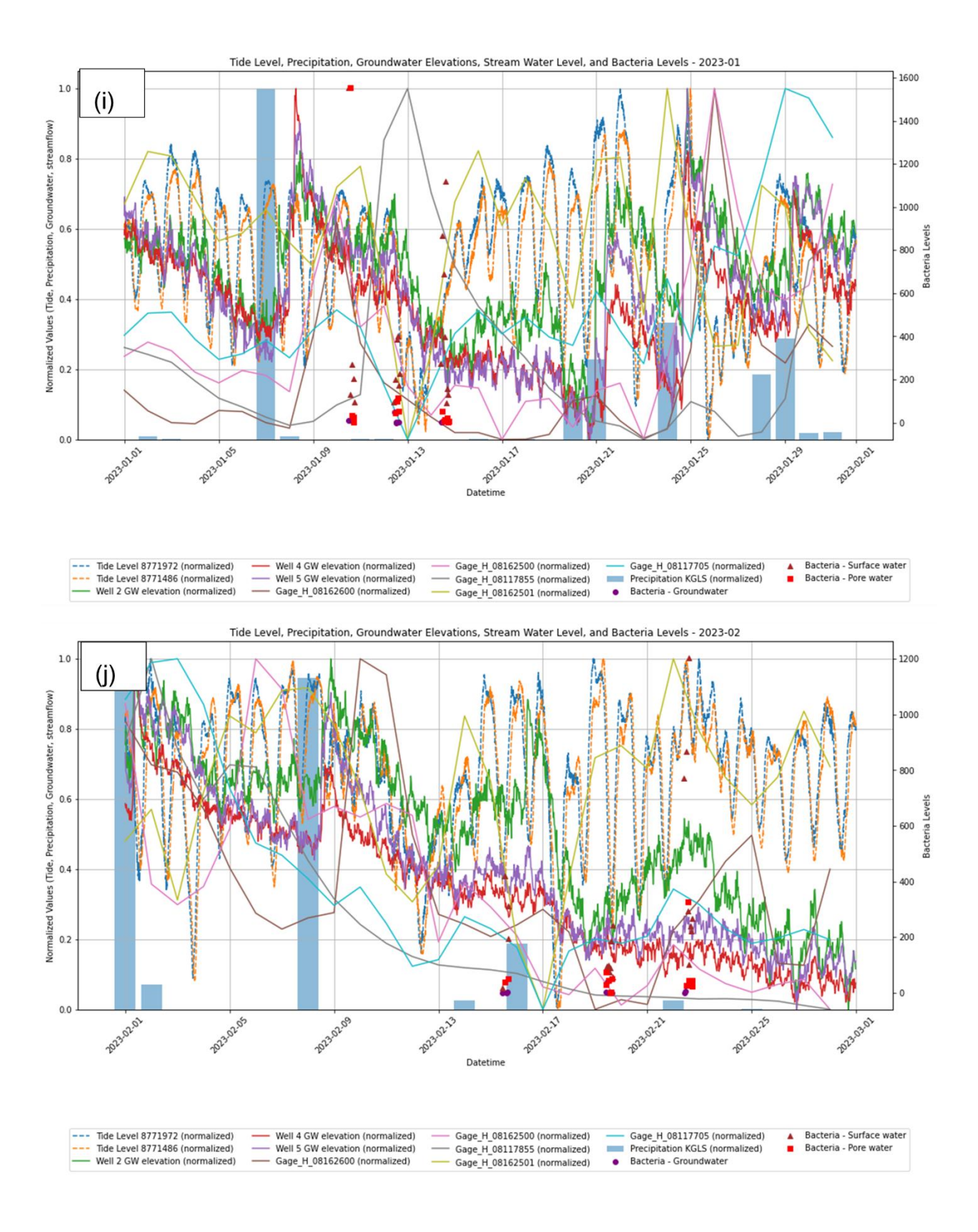












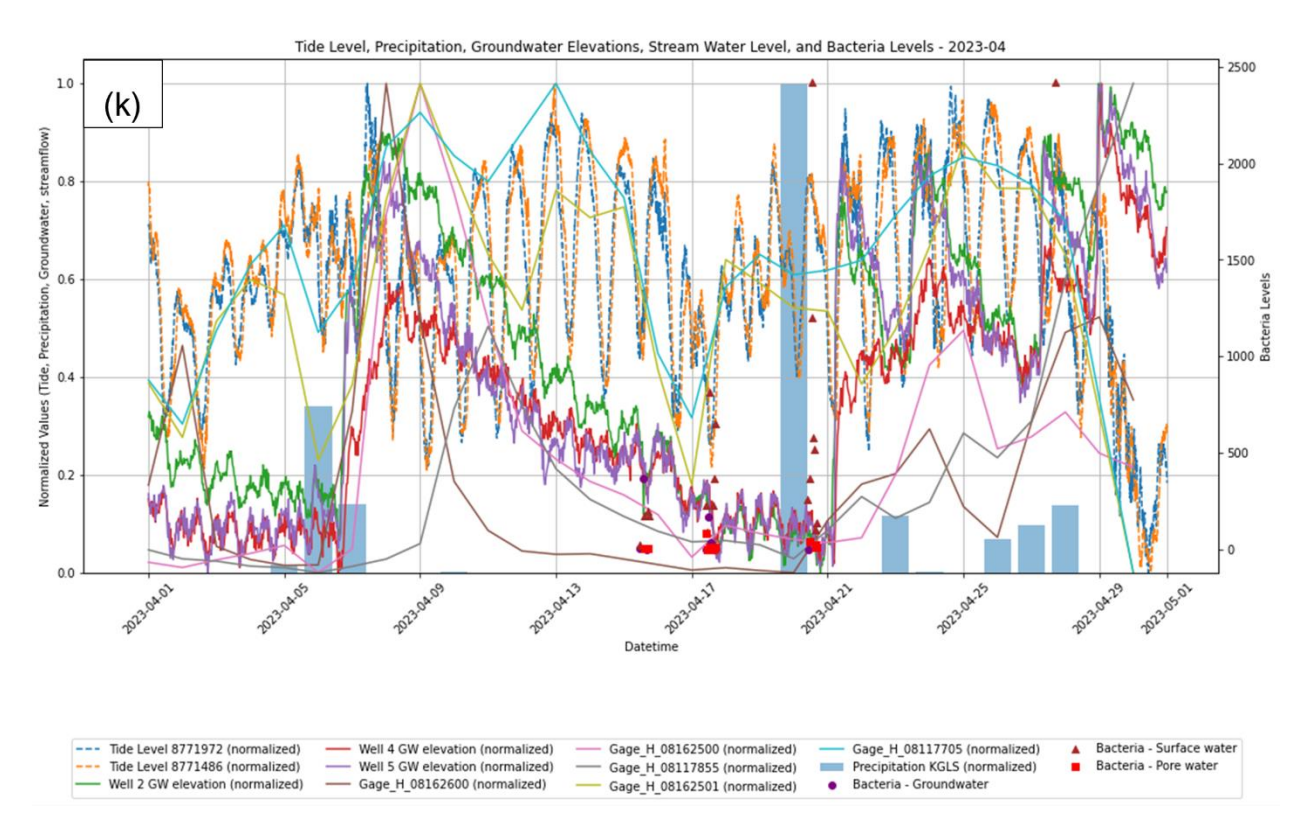


**Figure 6.10.** Analysis of Environmental Factors and Bacteria in Area 4 in different months: (a) 2021-12; (b) 2022-02; (c) 2022-03; (d) 2022-06; (e) 2022-08; (f) 2022-10; (g) 2022-11; (h) 2022-12; (i) 2023-01; (j) 2023-02; (k) 2023-04.

The figures presented below (**Figure 6.11** and **Figure 6.12**) illustrate the statistical significance of various transformed environmental factors in relation to bacteria levels in the dataset. These visualizations highlight which factors have a significant impact on bacteria concentrations, helping to identify key drivers of bacterial increases in different areas and systems. By analyzing the relationships between these transformed factors and bacteria levels, we can gain valuable insights into the underlying environmental conditions contributing to bacterial growth and contamination in areas 1 and 2. This information is crucial for understanding the dynamics of bacteria proliferation and for informing strategies aimed at mitigating contamination.

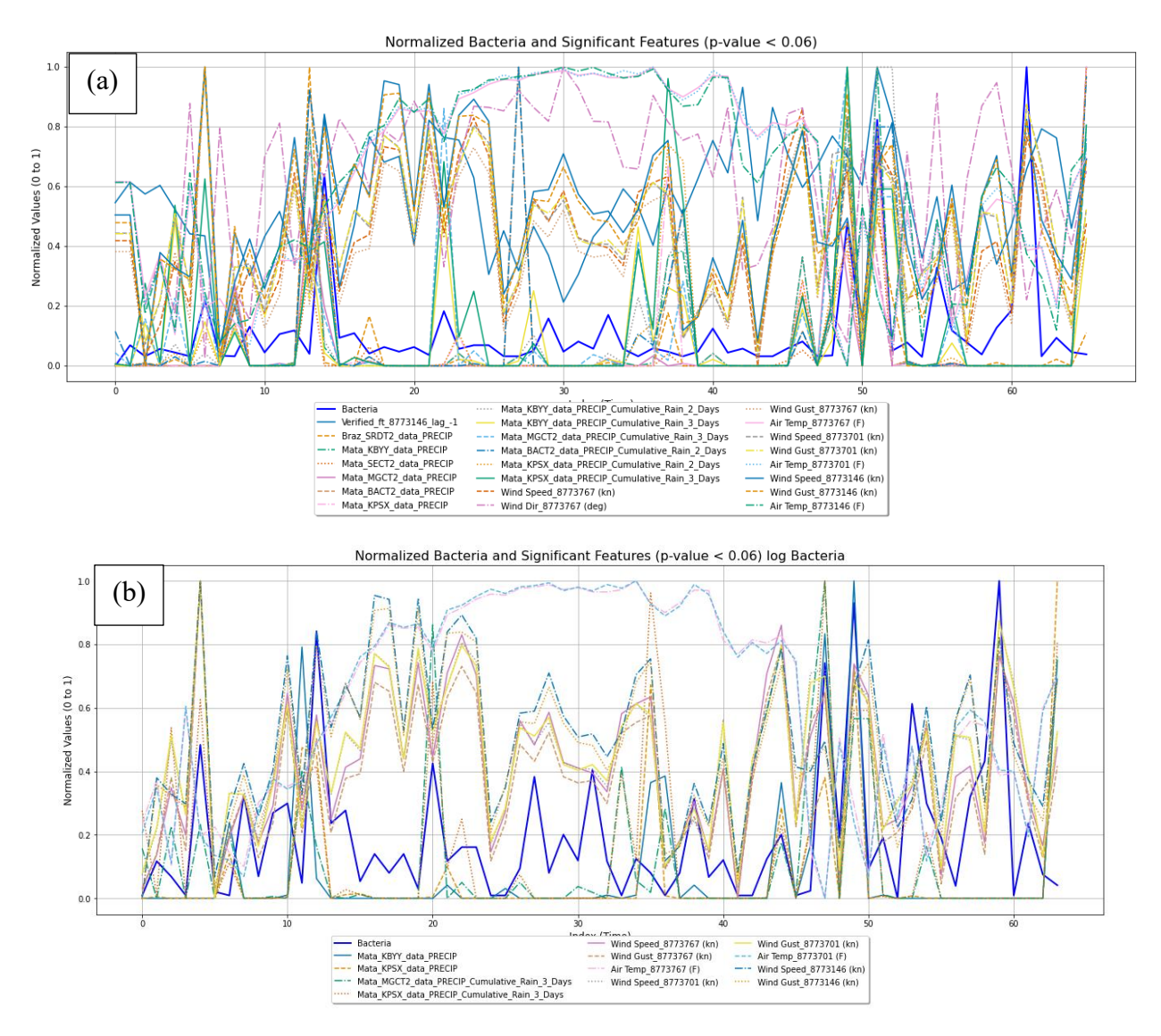


**Figure 6.11.** Area 1: Normalized Bacteria in surface water and significant environmental factors: (a) original bacteria data; (b) log-transformed bacteria data.

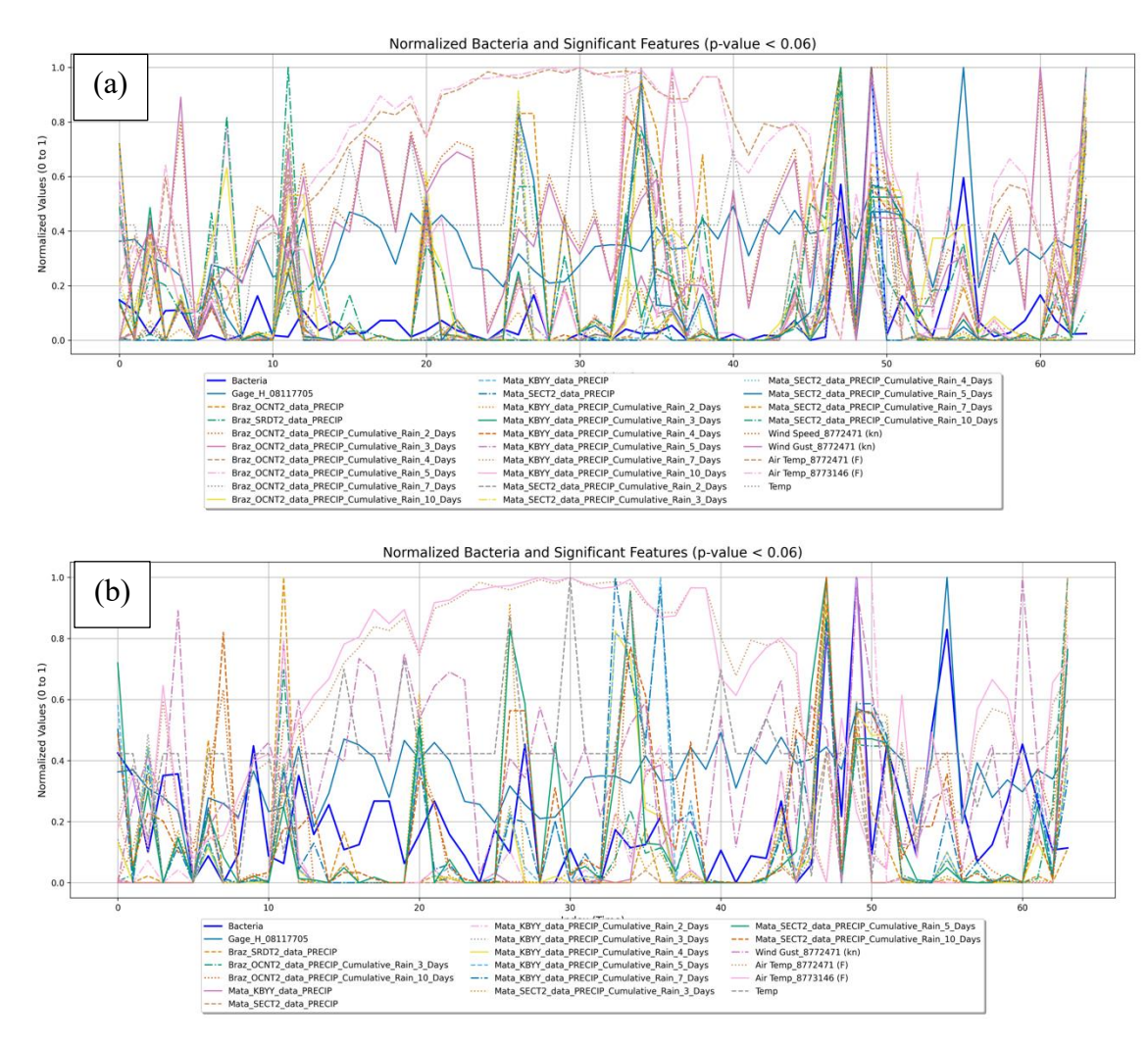


**Figure 6.12**. Area 2: Normalized Bacteria in surface water and significant environmental factors: (a) original bacteria data; (b) log-transformed bacteria data.

# 6.3.2. Surface water bacteria level predictions using machine learning techniques

A machine learning model was developed for modeling surface bacteria levels using environmental factors, including streamflow, tide level, three sources of precipitation, wind direction, sea level pressure, soil moisture, terrestrial water storage, wind speed, water temperature, air temperature, surface runoff, root-soil moisture, and sampled data for groundwater elevation. To ensure data readiness, a thorough cleaning and preprocessing step was conducted, focusing on removing inconsistencies, addressing missing data, and preparing the dataset for robust analysis. Additionally, data was normalized to ensure that all features were on a similar scale. Normalization was particularly important to prevent dominance by features with larger numerical ranges, improving model stability, convergence speed, and overall performance.

One of the key preprocessing steps involved the handling of missing data to ensure the dataset's integrity and suitability for analysis. Next, we focused on feature selection to identify the most relevant variables influencing surface bacteria levels. Additionally, feature selection was

employed to identify the most relevant variables influencing surface Bacteria levels, such as precipitation, tides, and other environmental factors. This targeted approach enhanced the model's efficiency by reducing dimensionality, mitigating overfitting risks, and focusing computational resources on impactful predictors. Data augmentation was implemented to address this limitation because the bacteria dataset was insufficient to develop a robust model due to its lack of continuous temporal coverage. Synthetic samples were generated using Gaussian noise to augment the dataset and improve model generalization, allowing the model to learn from a more diverse dataset and reducing overfitting risks.

A combined dataset (X\_combined) was created by appending the labels column to the augmented data. The data was then split into training and testing sets. The training set included both original and synthetic data to enhance the model's exposure to variability, while the testing set was restricted to original data only to maintain unbiased evaluation metrics. To evaluate the model's performance exclusively on the original data, the testing set was filtered to include only the original samples and their corresponding labels to ensure that synthetic data did not interfere with the testing phase, preserving the integrity of the results. Finally, XGBoost model was developed by selecting the most influential features, leading to better generalization when applied to unseen data. Hyperparameter tuning was done to identify the optimal settings that minimize prediction error and improve model robustness.

As shown in **Figure 6.13**, for area 3, the model achieved an RMSE of 0.4340, an R<sup>2</sup> value of 0.90, and an MAE of 0.122. In comparison, area 4 demonstrated an even stronger performance with an RMSE of 0.242, an R<sup>2</sup> value of 0.96, and an MAE of 0.110. These results highlight the model's robustness and strong predictive capability across different areas.

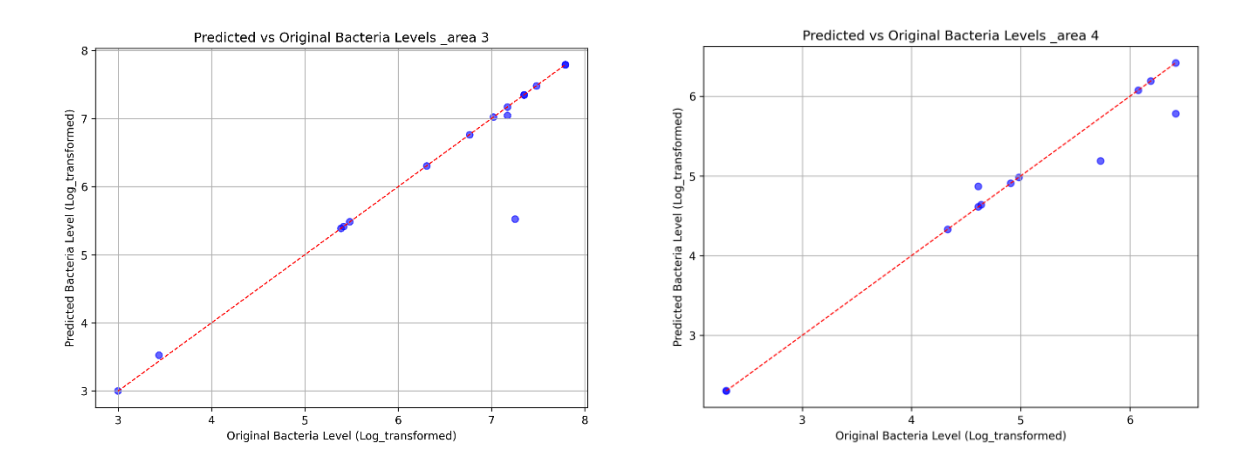


*Figure 6.13.* Scatter plot of the model's predictions for both areas using transformed log bacteria data.

As shown in **Figure 6.14a**, the most influential factors contributing to surface bacteria contamination in area 3 include streamflow (station: 8117210), 15-day precipitation accumulation (station: DNCT2), groundwater elevation in well 10, wind direction (EW) at station 8771972, tide level (station: 8771486) with a 5-day lag, and tide level at station 8771013 with a -3-day lag, among others. The combination of these hydrological and meteorological variables reflects a

strong interplay between surface water inputs and groundwater fluctuations, driving bacteria levels in this area. In contrast, for area 4, as illustrated in **Figure 6.14b**, the primary factors are tide level (station: 8771013) with lags of -3, -10, and 3 days, 7-day precipitation accumulation (station: BZRT2), streamflow (station: 08117301), groundwater elevation in well 2 with lags of -4 and 1 days, average sea level pressure, and salinity. The dominance of tide-related features highlights the significant influence of coastal processes on bacteria dynamics in Area 4, while interactions with groundwater and precipitation provide additional pathways for contamination.

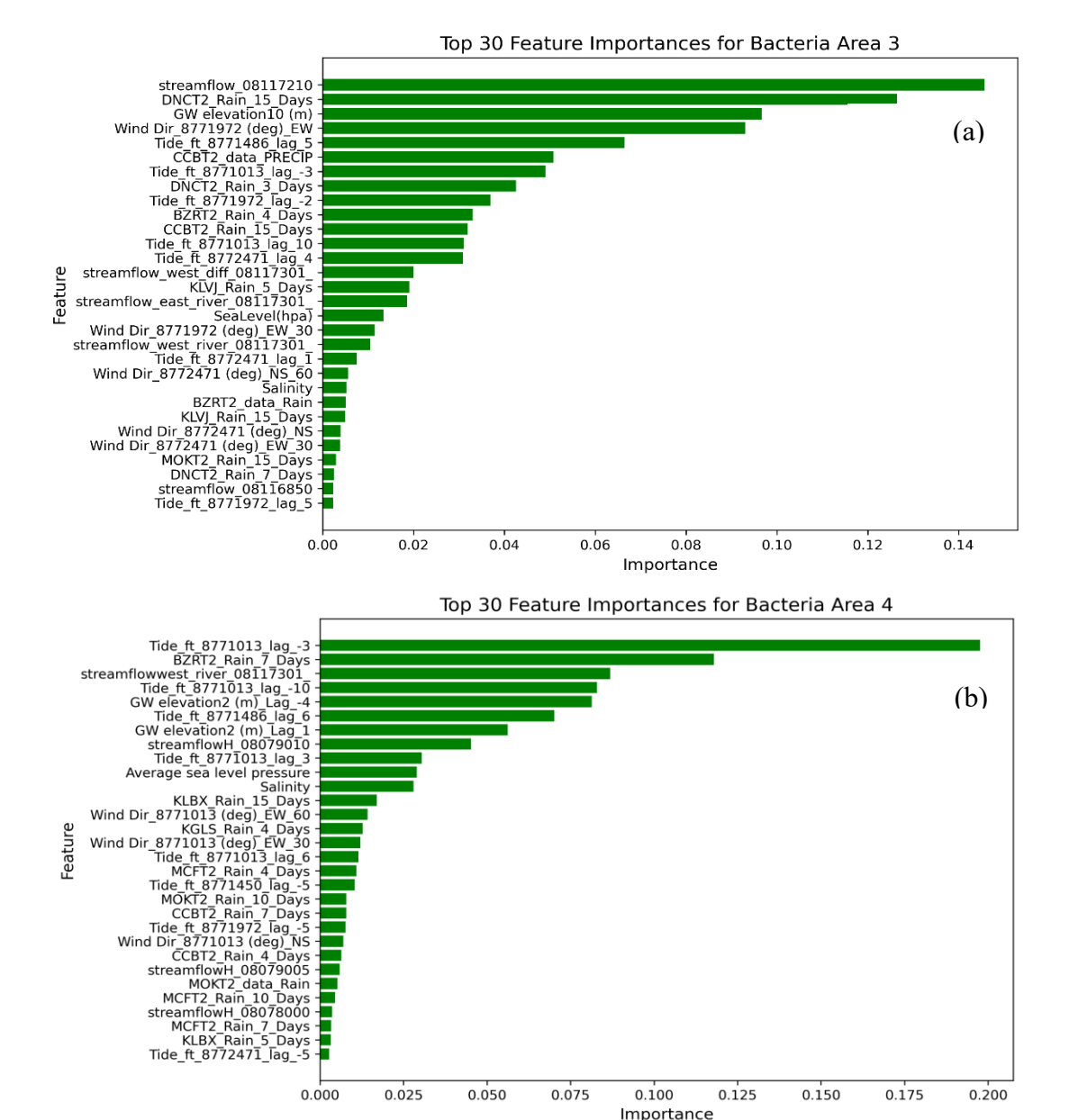


**Figure 6.14.** Feature importance for (a) Area 3 and (b) Area 4, illustrating the top 30 most consistent important features based on the weight metric for predicting surface bacteria levels using environmental and hydrological factors.

Each subplot represents a specific area, with features ordered by their contribution to reduce the model's error. The bars indicate the relative importance of each feature, with the values on the bars representing their importance scores.

#### 6.4 References

Arnold, W. A., Blum, A., Branyan, J., Bruton, T. A., Carignan, C. C., Cortopassi, G., Datta, S., DeWitt, J., Doherty, A., Halden, R. U., Harari, H., Hartmann, E. M., Hrubec, T. C., Iyer, S., Kwiatkowski, C. F., LaPier, J., Li, D., Li, L., Muñiz Ortiz, J. G., . . . Zheng, G. (2023). Quaternary ammonium compounds: A chemical class of emerging concern.

- *Environmental Science & Technology, 57*(20), 7645-7665. https://doi.org/10.1021/acs.est.2c08244
- Badgley, B. D., Steele, M. K., Cappellin, C., Burger, J., Jian, J., Neher, T. P., Orentas, M., & Wagner, R. (2019). Fecal indicator dynamics at the watershed scale: Variable relationships with land use, season, and water chemistry. *The Science of the Total Environment*, 697, 134113-134113. https://doi.org/10.1016/j.scitotenv.2019.134113
- Boehm, A. B., & Weisberg, S. B. (2005). Tidal forcing of enterococci at marine recreational beaches at fortnightly and semidiurnal frequencies. *Environmental Science & Technology*, 39(15), 5575-5583. <a href="https://doi.org/10.1021/es048175m">https://doi.org/10.1021/es048175m</a>
- Bradshaw, J. K., Snyder, B., Spidle, D., Sidle, R. C., Sullivan, K., & Molina, M. (2021). Sediment and fecal indicator bacteria loading in a mixed land use watershed; contributions from suspended sediment and bedload transport. *Journal of Environmental Quality*, 50(3), 598-611. <a href="https://doi.org/10.1002/jeq2.20166">https://doi.org/10.1002/jeq2.20166</a>
- Davies, C. M., Long, J. A., Donald, M., & Ashbolt, N. J. (1995). Survival of fecal microorganisms in marine and freshwater sediments. *Applied and environmental microbiology*, 61(5), 1888–1896. <a href="https://doi.org/10.1128/aem.61.5.1888-1896.1995">https://doi.org/10.1128/aem.61.5.1888-1896.1995</a>
- Desmarais, T. R., Solo-Gabriele, H. M., & Palmer, C. J. (2002). Influence of soil on fecal indicator organisms in a tidally influenced subtropical environment. *Applied and environmental microbiology*, 68(3), 1165–1172. <a href="https://doi.org/10.1128/AEM.68.3.1165-1172.2002">https://doi.org/10.1128/AEM.68.3.1165-1172.2002</a>
- Dimova, N., Burnett, W. C., Horwitz, E. P., & Lane-Smith, D. (2007). Automated measurement of 224Ra and 226Ra in water. *Applied Radiation and Isotopes*, 65(4), 428-434. <a href="https://doi.org/10.1016/j.apradiso.2006.10.005">https://doi.org/10.1016/j.apradiso.2006.10.005</a>
- Evanson, M., & Ambrose, R. F. (2006). Sources and growth dynamics of fecal indicator bacteria in a coastal wetland system and potential impacts to adjacent waters. *Water Research* (Oxford), 40(3), 475-486. <a href="https://doi.org/10.1016/j.watres.2005.11.027">https://doi.org/10.1016/j.watres.2005.11.027</a>
- Fetter, C. W. (2001). Applied hydrogeology (4th;4; ed.). Prentice Hall.
- Gerba, C. P., & McLeod, J. S. (1976). Effect of sediments on the survival of Escherichia coli in marine waters. *Applied and environmental microbiology*, *32*(1), 114–120. <a href="https://doi.org/10.1128/aem.32.1.114-120.1976">https://doi.org/10.1128/aem.32.1.114-120.1976</a>
- Gonneea, M. E., Morris, P. J., Dulaiova, H., & Charette, M. A. (2008). New perspectives on radium behavior within a subterranean estuary. *Marine Chemistry*, 109(3-4), 250-267. https://doi.org/10.1016/j.marchem.2007.12.002
- Howell, J.M., Coyne, M.S. and Cornelius, P.L. (1996), Effect of Sediment Particle Size and Temperature on Fecal Bacteria Mortality Rates and the Fecal Coliform/Fecal Streptococci Ratio. *Journal of Environmental Quality*, 25(6), 1216-1220. https://doi.org/10.2134/jeq1996.00472425002500060007x
- Hubbart, J. A., Kellner, E., & Petersen, F. (2022). A 22-site comparison of land-use practices, Ecoli and enterococci concentrations. *International Journal of Environmental Research and Public Health*, 19(21), 13907. https://doi.org/10.3390/ijerph192113907
- Hwang, H., Frey, S. K., Park, Y., Pintar, K. D. M., Lapen, D. R., Thomas, J. L., Spoelstra, J., Schiff, S. L., Brown, S. J., & Sudicky, E. A. (2019). Estimating cumulative wastewater treatment plant discharge influences on acesulfame and escherichia coli in a highly impacted watershed with a fully-integrated modelling approach. *Water Research* (Oxford), 157, 647-662. https://doi.org/10.1016/j.watres.2019.03.041

- Kelly, E., Gidley, M., Sinigalliano, C., Kumar, N., Brand, L., Harris, R. J., & Solo-Gabriele, H. M. (2020, March). Proliferation of microalgae and enterococci in the Lake Okeechobee, St. Lucie, and Loxahatchee watersheds. *Water Research*, 171, 115441. <a href="https://doi.org/10.1016/j.watres.2019.115441">https://doi.org/10.1016/j.watres.2019.115441</a>
- Knee, K. L., Layton, B. A., Street, J. H., Boehm, A. B., & Paytan, A. (2008). Sources of nutrients and fecal indicator bacteria to nearshore waters on the north shore of Kaua'i (Hawai'i, USA). *Estuaries and Coasts*, 31(4), 607-622. https://doi.org/10.1007/s12237-008-9055-6
- Lefebvre, K., Barbecot, F., Larocque, M., & Gillon, M. (2015). Combining isotopic tracers (222Rn and δ13C) for improved modelling of groundwater discharge to small rivers. *Hydrological Processes*, 29(12), 2814-2822. <a href="https://doi.org/10.1002/hyp.10405">https://doi.org/10.1002/hyp.10405</a>
- Müller, T., Walter, B., Wirtz, A., & Burkovski, A. (2006). Ammonium toxicity in bacteria. *Current Microbiology*, 52(5), 400-406. <a href="https://doi.org/10.1007/s00284-005-0370-x">https://doi.org/10.1007/s00284-005-0370-x</a>
- Null, K. A., Knee, K. L., Crook, E. D., de Sieyes, N. R., Rebolledo-Vieyra, M., Hernandez-Terrones, L., & Paytan, A. (2014). Composition and fluxes of submarine groundwater along the caribbean coast of the yucatan peninsula. *Continental Shelf Research*, 77, 38-50. <a href="https://doi.org/10.1016/j.csr.2014.01.011">https://doi.org/10.1016/j.csr.2014.01.011</a>
- Pereira, A.P., Antunes, P., Bierge, P., Willems, R.J.L., Corander, J., Coque, T.M., Pich, O.Q., Peixe, L., Freitas, A.R., Novais, C. (2023). Unraveling Enterococcus susceptibility to quaternary ammonium compounds: genes, phenotypes, and the impact of environmental conditions. *Microbiology Spectrum*, 11(5), e02324-23. <a href="https://doi.org/10.1128/spectrum.02324-23">https://doi.org/10.1128/spectrum.02324-23</a>
- Piggot, A. M., Klaus, J. S., Johnson, S., Phillips, M. C., & Solo-Gabriele, H. M. (2012). Relationship between enterococcal levels and sediment biofilms at recreational beaches in South Florida. *Applied and environmental microbiology*, 78(17), 5973–5982. <a href="https://doi.org/10.1128/AEM.00603-12">https://doi.org/10.1128/AEM.00603-12</a>
- Pommepuy, M., Guillaud, J. F., Dupray, E., Derrien, A., Guyader, F. L., & Cormier, M. (1992). Enteric bacteria survival factors. *Water Science and Technology*, 25(12), 93-103. <a href="https://doi.org/10.2166/wst.1992.0341">https://doi.org/10.2166/wst.1992.0341</a>
- Tiefenthaler, L. L., Stein, E. D., & Lyon, G. S. (2009). Fecal indicator bacteria (FIB) levels during dry weather from southern california reference streams. *Environmental Monitoring and Assessment*, 155(1-4), 477-492. https://doi.org/10.1007/s10661-008-0450-z
- Webster, I. T., Hancock, G. J., & Murray, A. S. (1995). Modelling the effect of salinity on radium desorption from sediments. *Geochimica Et Cosmochimica Acta*, 59(12), 2469-2476. https://doi.org/10.1016/0016-7037(95)00141-7

#### 7. OVERALL CONCLUSION

This study highlights the essential need for interdisciplinary and thorough measurements in addressing the complex hydrological, ecological, and infrastructural challenges facing the Texas Gulf Coast. By combining various methods such as groundwater monitoring, sediment analysis, microbial source tracking (MST), groundwater tracers, and predictive modeling, we gain a deeper insight into the factors influencing water table fluctuations, the transport of nutrients and microbes, and their effects on both human health and the environment. Our results indicate a significant connection between upstream hydrological systems and the groundwater dynamics of barrier islands. This connection underscores the importance of coordinated management approaches across the region to effectively tackle issues related to flooding, contamination, and ecological degradation.

The research found that groundwater recharge from upstream streamflow, alongside local rainfall and tidal effects, notably elevates water tables in the barrier islands from late winter to early spring. This elevation increases the risk of flooding, especially in areas with permeable sediments and shallow water tables, which can lead to septic system failures, sewage backflow, and the transport of fecal indicator bacteria and nutrients into nearshore waters. Such incidents pose immediate health risks to beachgoers due to bacterial contamination and can result in long-term ecological challenges like nutrient enrichment, eutrophication, and harmful algal blooms. Furthermore, our use of radium isotopes as tracers revealed critical areas of nutrient-rich groundwater discharge, further illustrating the interconnected nature of coastal water quality, regional hydrology, and the resilience of infrastructure.

The predictive modeling aspect of our research identified key factors influencing water table fluctuations, including streamflow, soil moisture, rainfall, and terrestrial water storage. These models have demonstrated strong effectiveness in predicting groundwater behavior, equipping coastal managers with the tools to foresee high-risk periods and implement proactive measures to minimize flooding and contamination risks. The findings stress the importance of predictive tools in enhancing decision-making processes, especially for issuing advisories to safeguard recreational users, strengthening infrastructure resilience, and protecting coastal ecosystems.

#### Recommendations

- 1. Hydrological Monitoring and Early Warning Systems:
  - Establish long-term, regionally integrated monitoring programs that focus on groundwater levels, upstream streamflow, precipitation, and tidal influences. These data should be used to refine predictive models for better forecasting of water table fluctuations and flood risks.
  - Implement real-time early warning systems for beach advisories, using bacterial contamination thresholds and predictive indicators such as water table levels, rainfall, and streamflow dynamics.

# 2. Infrastructure Improvements:

- Upgrade and maintain septic systems and sewage infrastructure in vulnerable areas, particularly in zones prone to shallow water tables and tidal influences. Consider the adoption of more resilient, watertight designs that minimize infiltration and backflow during high water table periods.
- Develop policies and funding mechanisms to retrofit or replace failing septic systems, especially in coastal communities with older infrastructure.

# 3. Nutrient and Contaminant Mitigation:

- o Introduce land-use policies that regulate nutrient and contaminant runoff, particularly upstream, to reduce inputs into regional hydrological systems. Encourage sustainable agricultural practices and reduce impervious surfaces to improve groundwater recharge and minimize nutrient loading.
- Promote the use of green infrastructure, such as vegetated buffers and constructed wetlands, to filter contaminants and nutrients before they enter groundwater or surface water systems.

# 4. Public Health and Recreational Safety:

- Establish standardized protocols for monitoring and reporting fecal indicator bacteria levels in recreational waters. This includes integrating microbial source tracking into routine assessments to identify contamination sources and inform targeted interventions.
- Conduct public education campaigns on the risks of bacterial contamination and the importance of compliance with advisories to protect health during high-risk periods.

#### 5. Coastal Ecosystem Resilience:

- Prioritize the protection and restoration of coastal ecosystems, which play a key role in mitigating the impacts of nutrient loading and supporting biodiversity. Efforts should focus on preserving natural buffers such as wetlands and dunes to improve coastal resilience against flooding and contamination.
- o Develop conservation strategies for areas identified as hotspots of submarine groundwater discharge to balance ecological health with groundwater management needs.

#### 6. Integrated Management Strategies:

- Foster collaboration between upstream water resource managers and coastal stakeholders to develop cohesive management plans that address the interconnectedness of regional hydrological and coastal systems.
- Incorporate climate variability projections into planning efforts to account for potential shifts in precipitation patterns, sea-level rise, and increasing storm intensity, ensuring long-term sustainability and resilience of coastal resources.

This research highlights the complexity and interconnectivity of coastal groundwater systems and underscores the need for an integrated, science-driven approach to managing these dynamic environments. By addressing the hydrological, ecological, and infrastructural

challenges collectively, coastal managers can enhance resilience and sustainability, protecting both human and environmental health in the face of evolving climate and development pressures.

#### 8. TASK 4: EDUCATION AND OUTREACH

TAMUCC has successfully trained graduate and undergraduate students to collect, organize, analyze, and interpret data. This project has effectively integrated research findings and supportive materials into the curricula and developed hands-on educational activities primarily targeting undergraduate and graduate students. TAMUCC has incorporated data visualization techniques, such as concentration maps and groundwater fluxes, into classroom education and made these visualizations available to the research community through exhibits at national meetings and workshops. Principal investigators and their graduate students have participated in and presented results at local and regional conferences.

#### 8.1. List of all Communications

None to report.

# 8.2. List of Student Training Opportunities

TAMUCC Undergraduate/Graduate Education: Dr. Roya Narimani trained both graduate and undergraduate students in data analysis and machine learning techniques from the ground up, preparing them to handle big data effectively. She has served as a co-instructor for the Big Data Blitz course during the summer semester, providing an intensive overview of big data analysis, and as an instructor for the Environmental Forecasting course in the fall semester, where students apply machine learning to real-world environmental forecasting challenges. Cody Lopez, Laura Button, Mahima Yogesh, Remi Labeille, Amanda Burton, Ifeanyi Anyanwu, Quincy Walker, Allyson Girard, Justin Elliott, Rostam Mirzadi, Meehan Skylar, and Lillian Pedraza are part of this group who participated in these classes.

Cody Lopez has trained students Joy Brown, Brittney Ortega, Cindy Vaquero, Victoria Rivera, Sarah Martinez, Karol Ramirez-Prado, Mikaiel Khan, Annelyz Garza, Allie Watson, Laura Button, McKenna Reinsch, Sean Majors, Ahmed Eid, Meehan Skylar, Jesicca Palitza, and Ifeanyi Anyanwu on field work, sample collection and processing as well as measurements of nutrients, anions, radon and radium.

Erin Taylor trained undergraduate students, Kristen Lincoln, Paulina Caro, and Sofia Miatello, in general water quality and sample processing techniques.

Dr. Audrey Douglas has trained students on processing, measurement and analysis radium and radon, data entry, and other standard operating procedures.

<u>UTSA Undergraduate Education</u>: The project was introduced to the undergraduate students enrolled in CE 2633 Environmental Engineering. A presentation was developed covering the basics of fecal source tracking, study sites and methods, and the importance of the study for Texas Coastal areas and delivered as part of regular lecture in the Water and Wastewater Module. The class was enthusiastic about the project and several students approached Dr. Kapoor afterwards to learn more about the project and seek opportunities to be involved in such studies.

<u>UTSA Graduate Education</u>: The project was introduced to the students enrolled in the course CE 5683 Biological Phenomenon in Environmental Engineering. A presentation covering the basics of fecal source tracking, study sites and methods, and the study's importance for Texas Coastal areas was developed and delivered as part of a regular lecture in the Microbial Water Quality section. The class was enthusiastic about the project, and several students approached Dr. Kapoor afterwards to learn more about it and seek opportunities to be involved in such studies.

# **TAMUCC Students trained:**

Graduate students – Laura Button, McKenna Reinsch, Sean Majors, Ahmed Eid, Ifeanyi Anyanwu, Meehan Skylar, Erin Taylor, Cody Lopez

Undergraduate students – Joy Brown, Brittney Ortega, Cindy Vaquero, Victoria Rivera, Sarah Martinez, Karol Ramirez-Prado, Mikaiel Khan, Annelyz Garza, Allie Watson, Kristen Lincoln, Paulina Caro, Sofia Miatello

#### **UTSA Students trained:**

Graduate students – Dipti Anik Dhar, Carlos Romero Vazquez, Arash Jafarzadeh Undergraduate students – Camila Sandoval, Alexandria Bowdoin, Jazmin Carothers

# 8.3. List of Conferences, Publications, and Public Presentations

- ❖ 2025, Dhar, Dipti Anik; Vadde, Kiran; Narimani, Roya; Murgulet, Dorina; Felix, Joseph; Matta, Akanksha; Pinchback, Jason; Kapoor, Vikram. Occurrence of fecal indicator bacteria and microbial source tracking markers along the Texas Gulf Coast adjoining two barrier islands. Environmental Science & Technology, Manuscript ID es-2024-144015, status: with Editor.
- ❖ 2024, Narimani, R\*., Murgulet, D. Drivers of Water Table Dynamics in Barrier Islands: A GIS-Ensemble Machine Learning Model Using Multivariate Environmental Data. American Geophysical Union (AGU), Washington, December 2024.
- ❖ 2024, Dr. Dorina Murgulet presented on clean water Texas on February 15th.
- ❖ 2023, Dhar, D., Murgulet, D., & Kapoor, V. Quantitative Detection of Gen. Fecal Indicator Bacteria and Host-Specific Source Tracking Markers to Determine Fecal Contamination in the Texas Gulf Coast. Poster presentation at *ASM Microbe 2023*, Houston, TX, U.S.A.
- ❖ 2023, \* Eid, A., Narimani, R., Taylor, E., Dhar, D., Lopez, C.V., Felix, J.D.D., Kapoor, V., Murgulet, D. Septic System Failure, and Water Quality in Coastal Regions- A Study of Bacterial Contamination and Nutrient Concentrations in the Northwestern Gulf of Mexico. American Geophysical Union (AGU), San Francisco, December 2023.
- ❖ 2023, \*Taylor, E., Felix, J. D., Murgulet, D., Determining Nitrogen Loading and Processing Along the Texas Coast and Potential Impacts Due to Sea Level Variations. 18th Annual TAMUS Pathways Student Research Symposium, Galveston, TX, March 2023.

*	2023, Felix, J. D., Investigating Nitrogen in Coastal Bend Waters. Texas General Land Office Lunch and Learn Speaker Series. March 2023. Corpus Christi, TX